Title
Micromechanical Damage Models for Continuous Fiber Reinforced Composite Materials

Author
Wu, Yi

Publication Date
2013

Peer reviewed|Thesis/dissertation

UNIVERSITY OF CALIFORNIA

Los Angeles

Micromechanical Damage Models for Continuous Fiber Reinforced Composite Materials

A dissertation submitted in partial satisfaction

of the requirement for the degree Doctor of Philosophy

in Civil Engineering

by

Yi Wu

2013

ABSTRACT OF THE DISSERTATION

Micromechanical Damage Models for Continuous Fiber Reinforced Composite Materials

by

Yi Wu

Doctor of Philosophy in Civil Engineering

University of California, Los Angeles, 2013

Professor Jiann-Wen Ju, Chair

The primary objective of this research work is to investigate the effective mechanical responses of continuous fiber reinforced composites by modifying and extending the available micromechanical framework. A major part of the work conducted involves the investigation of the effective damage responses due to damage evolutions of matrix microcracks and fiber breakages.

Chapter 3 presents the effective elastic damage behavior of continuous fiber reinforced composites with evolutionary matrix microcracks. A cohesive penny-shape microcrack model is proposed within a two-step homogenization framework to achieve the effective elastic damage behavior of continuous fiber reinforced composites. In the proposed model, the size and the number density of microcracks are defined as two damage parameters to control the matrix microcrack evolution. In addition, the thermal effect is taken into account by taking advantage of the thermal eigenstrain and the Eshelby's equivalent inclusion principle. The overall coefficient of thermal expansion (CTE) of the composite is systematically derived under the framework of micromechanics to describe the overall damage behavior of composites due to matrix microcrack evolution under temperature changes.

Chapter 4 proposes a micromechanical evolutionary damage framework capable of predicting the overall mechanical behavior of and damage evolution in continuous fiber reinforced composites. In the framework, the effective stress fields in a single fiber due to an embedded penny-shaped fiber breakage are systematically derived by applying the double-inclusion theory. The notion of effective length denoting the distance between two adjacent breakages is introduced as a damage parameter while determining the damage evolution within a single fiber. This enables the modeling of the effective damage behavior of a single-fiber reinforced composite. As an application of the proposed framework, a micromechanical damage model is further proposed to simulate the fiber-dominated failure mechanism within a multi-fiber composite. A Weibull probability function is adopted to estimate the varying volume fractions of damaged fibers and intact fibers. Numerical simulations are presented to demonstrate the effectiveness of the proposed methodology.

In Chapter 5, based on the linear elastic fracture mechanics (LEFM) and ensemble-volume averaging technique, an effective eigenstrain is newly proposed to quantify the homogenized stress fields in a single fiber due to multiple fiber breakages. In the proposed model, the number density evolution of fiber breakages is characterized by a two-parameter Weibull statistic with the temperature effect implicitly enclosed by properly adjusting the Weibull parameters. The damage criterion in the evolutionary damage model is theoretically derived. Utilization of the proposed damage framework, a homogeneous damage evolution model capable of simulating the material behavior of multi-fiber reinforced composite materials is developed.

Chapter 6 presents two stochastic risk-competing models to simulate the fiber breakage evolution in a multi-fiber composite with an inhomogeneous fashion by considering different load sharing mechanisms. A unit cell model is adopted with each cell being assigned an initial weakness based on a normal distribution. Damage evolution inside each cell structure follows the micromechanical model presented in Chapter 5. Two risk-competing models are introduced subsequently to determine the damage sequence within the multi-fiber composite by computing the fracture probability based on the weakness of cells at each time step. It is observed that one risk-competing model tends to generate a concentrated damage pattern with broken fibers clustering in a T-shape or a cross-shape, while the other model yields a more diffused damage pattern. Finally, the overall stress-strain responses and the fiber breakage evolution are predicted and verified against experimental data.

Chapter 7 examines the effective elastoplastic behavior of metal matrix composites (MMCs) containing unidirectionally aligned continuous fibers. A homogenization procedure is utilized to

derive the overall yield function for the composite based on the probabilistic spatial distribution of aligned inclusions. Based on continuum plasticity, a plastic flow rule and a hardening law are postulated. These laws together with the proposed overall yield function then characterized the macroscopic elastoplastic behavior of the composite under three-dimensional arbitrary loading/unloading histories. The overall uniaxial elastoplastic stress-strain behavior of MMCs with aligned continuous fibers is investigated. Comparisons between theoretical predictions and experimental data for the composite are performed to illustrate the capability of the proposed method.

Chapter 8 concludes the present research on micromechanics and effective elastic and elastoplastic behavior of continuous fiber reinforced MMCs. Finally, related future research topics are discussed briefly.

The dissertation of Yi Wu is approved.

Jian Zhang

Stanley B. Dong

Yingnian Wu

Jiann-Wen Ju, Chair

University of California, Los Angeles

2013

DEDICATION

To my mom and dad

TABLE OF CONTENTS

LIST OF FIGURES

LIST OF TABLES

ACKNOWLEDGMENTS

First of all, I would like to express my sincere appreciation to Professor Jiann-Wen Ju, advisor and committee chair, for the advice guidance, support, and encouragement he provided during the studies, research, and preparation of this manuscript. This work could not have been done without his enthusiasm, knowledge, and dedication toward the success of his students.

In addition, I would like to express my immense gratitude to, Professor Jian Zhang, Professor Stanley Dong, Professor Yingnian Wu, members of the committee, for their time and valuable input towards this research work. I would also like to thank Professor Ajit Mal, for his help and suggestions during my Ph.D. candidacy exam.

Moreover, my profound thanks to all my colleagues, Dr. Prechaporn Suwatnodon, Dr. Kuo-Yao Yuan, Professor Keiji Yanase, Dr. Yu-Kai Wang, Ms. Hsuan-Ju Hung, Mr. Chung-Wen Chuang, Mr. Chia-So Chuang, and Mr. Seongwon Hong, with whom I have the great luxury of working.

I would like to express my special thanks to Dr. Chung-Hao Lee, for always being so supportive to me.

Last but not least, this thesis could not have been done without the selfless love and the generous support from my dearest parents and all my family members. To my family, I extend my deepest appreciation.

VITA OF YI WU

2003–2007	B.S., Water Resource and Ocean Engineering,
	Zhejiang University, Hangzhou, China
2007–2008	M.S., Civil and Environmental Engineering,
	University of California, Los Angeles, U.S.A.
2010	Candidate in Doctor of Philosophy Degree,
	University of California, Los Angeles, U.S.A.
2012	M.S., Statistics
	University of California, Los Angeles, U.S.A.
2008–2010	Teaching Assistant, Civil and Environmental Engineering,
	University of California, Los Angeles, U.S.A.
2008–2013	Research Assistant, Civil and Environmental Engineering,
	University of California, Los Angeles, U.S.A.
2011–2013	Teaching Fellow, Civil and Environmental Engineering,
	University of California, Los Angeles, U.S.A.

CHAPTER 1 INTRODUCTION

1.1 Composite Materials – Definition and Application

The word ‘composite’ in the term ‘composite material’ signifies that two or more materials are combined on a macroscopic scale to form a third useful material. In general, a two-phase composite material needs to satisfy the following criteria. First, both constituents have to present in reasonable proportions. The major component of the composite is termed ‘the matrix’, whereas the minor component, that is, the constituent present in small amount is called ‘the reinforcement’. Secondly, the two constituent phases need to exhibit different properties, so the properties of the composite are noticeably different from those of the original constituents. Generally speaking, reinforcements are adopted to enhance and improve the mechanical properties of the composite. Lastly, a man-made composite is usually produced by mixing and combining the constituents by various means.

The history of composites can be traced back to ancient Egypt, where the straw reinforced bricks are known to be the very first composites used in ancient civilizations. Due to the continuing quest for improved performance, composites have been studied and investigated extensively over the past few decades. Today, composite materials are routinely designed, manufactured and used in the military, aerospace, automobile, leisure, electronic and medical industries because of their outstanding mechanical properties such as high strength-to-weight and stiffness-to-weight ratios, low coefficients of thermal expansion, and superior ductility. The

resulting extensive applications have motivated in-depth studies of composites from various interdisciplinary viewpoints.

1.2 Classification of Composite Materials

There are various ways of classifying composite materials. For instance, in terms of their reinforcement profiles, composites can be classified as, being particle-reinforced or continuous fiber reinforced. Particle-reinforced composites have reinforcements with dimensions that are approximately equal in all directions. Such reinforcements effectively constrain the deformation of the surrounding matrix material as a result of their higher stiffness compared with that of the matrix. Although particle reinforcements can carry some loads, their load-sharing capability is inferior to that of continuous fiber reinforcements. Therefore, particle reinforcement is more effective in enhancing the stiffness than in increasing the strength of composites. In practice, particle reinforcements are frequently used to improve the mechanical properties of matrix materials, for example, modify thermal and electrical conductivities, improve composite performance at elevated temperatures, reduce friction, increase wear and abrasion resistance, reduce shrinkage, and increase surface hardness. By contrast, continuous fiber reinforcement is characterized by fiber length being much greater than its cross-sectional dimensions. Unlike particles, continuous fibers possess superb load sharing capability. This results in an effective increase of the strength of composites. In addition to enhancing of the composite's overall moduli, continuous fibers can also significantly improve the fracture resistance of the matrix by bridging cracks. Because of these advantages, continuous fiber reinforced composites are one of the most commonly used composites in the engineering field.

Composites can also be classified on the basis the matrix material: polymer matrix composites (PMCs), metal matrix composites (MMCs) and ceramic matrix composites (CMCs). In general, PMCs have low strengths and Young's moduli; CMCs are strong, stiff and brittle; MMCs have intermediate strengths and moduli together with good ductility. In terms of decreasing temperature-bearing capabilities, the three types can be ordered as CMCs, MMCs and PMCs. Thus, each type has its own unique advantages and corresponding application fields.

1.3 Damage Mechanisms in Continuous Fiber Reinforced MMCs

1.3.1 Continuous fiber Reinforced Metal Matrix Composites

Continuous fiber reinforced metal matrix composites have numerous practical applications in a variety of industries including the aerospace industry for airframe and spacecraft structures, automotive, electronic, and leisure industries. In general, the matrix phase of MMCs consists of one contiguous metallic material, such as aluminum, titanium, magnesium, copper, and the like. In essence, the matrix phase provides protection and support for the reinforcements, as well as transfers the local stresses of reinforcements from one to another. More importantly, the metal matrix material can dissipate energy in the form of plastic deformation, which, in turn, lowers the evolution rate of other damage mechanisms, such as fiber breaking and fiber/matrix interfacial debonding. On the other hand, the fiber reinforcing constituent is normally a ceramic (e.g., silicon carbide, silicon nitride, and alumina) although a refractory metal is preferred sometimes. Such reinforcements are used primarily to enhance the mechanical properties of the matrix. As a consequence, a combination of a metal matrix with the ceramic fibers can provide the following

properties, which make the continuous fiber reinforced metal matrix composite, an attractive structural material candidate (Arsenault, 1984):

- High strength, elastic modulus, fracture toughness and impact properties,
- High electrical and thermal conductivity,
- High vacuum environment resistance,
- High surface durability and low sensitivity to surface flaws, and
- Low sensitivity to temperature changes or thermal shock.

1.3.2 Interfacial Layer in MMCs

An interfacial layer is a thin region formed between the fiber and the matrix as a result of the chemical reactions. Although interfacial layers may be formed during service, but they are more commonly formed during fabrication. This is particularly true with regard to metals like titanium and aluminum. Owing to their high chemical reactivity, interfacial layers form more easily in them. However, whether or not interfacial layers are encountered depends also on many factors besides the material's chemical reactivity. One important factor is the composition of the matrix material. For instance, there is negligible reaction between aluminum alloy matrices and most alumina fibers, except when the matrix contains lithium or magnesium. As a result, no noticeable interfacial layer will be observed in this case. Thermal effects can also influence the interfacial layer thickness. Composites in the as-fabricated state do not exhibit excessive chemical interactions. However after thermal exposure, composites undergo extensive chemical interaction thus inducing thicker interfacial layers.

Interfacial reactions are of special concern as they can adversely affect the mechanical performance of an MMC. Both the strength and toughness of a composite get degraded by the presence of the interfacial layer. Experimental evidence reveals that the fiber strength is closely related to the thickness of the interfacial layer. Fiber-matrix chemical reactions create notches on the fiber surface, leading to degradation of fiber strength. The level of degradation depends on the thickness of the reaction zone. If the reaction zone is thin, the notch formed due to cracking in the reaction zone is smaller than the intrinsic defects of the fiber. As a consequence, the fiber is more likely to maintain its original strength. Nevertheless, if the reaction zone thickness exceeds a critical value, the fiber strength decreases as the reaction zone thickness increases. The fiber strength then becomes a function of the geometry and Young's modulus of the fiber, the critical energy release rate, and most importantly, the thickness of the reaction zone. When the reaction zone is extremely thick, the failure of the reaction zone will cause the fiber to fracture immediately. In other words, the fiber strength is dependent on the fracture strain of the reaction layer. Although a reaction layer is generally inevitable during fabrication, as a general rule, extensive interfacial reactions should be avoided if optimum mechanical performance is to be achieved with MMCs.

1.3.3 Damage Mechanisms in Continuous fiber Reinforced Composites

Many studies have shown that the homogeneity of reinforcement dispersion, the properties of the reinforcement (the surface properties in particular), the cleanness of the matrix, and the magnitude and inhomogeneity of the internal stress level all play some role in controlling the failure mechanisms in a continuous fiber reinforced composite system. Nevertheless, although it

occupies a vanishing fraction of the total composite volume, the interface layer between the fibers and the matrix plays a key role in determining the overall composite properties and stress-strain relations associated with damage (He et al., 1993; Curtin, 1998). The composition and mechanical properties of the interface layer and the bonding conditions between adjacent layers are critical in controlling the damage mechanisms.

Consider a unidirectionally aligned continuous fiber reinforced composite subject to tensile loading in the longitudinal direction. Microcracks usually initiate in the interfacial region, primarily due to the relatively lower fracture strength of the interfacial reaction region compared to that of the fiber and matrix. Subsequently, stress concentrations are induced near the crack tips which lead to the initiation of various damage modes. Different combinations of interfacial bonding conditions and material properties of the fiber, matrix and interface layer result in different damage mechanisms.

- **Interfacial Debonding**

In reality, a typical interface region possesses functionally graded multi-layer structure, which is formed primarily due to the chemical reaction between the fiber and the matrix. Moreover, the carbon coating technique, which is a commonly used to protect the fiber from strength degradation during fabrication, e.g., the double-layer carbon coating, will also introduce additional layers between the fiber and interfacial layer. Taking a SCS-6-Ti_3Al composite for instance, titanium, aluminum and niobium are all involved in the reaction with SCS-6 fiber and formed multiple layers of complex carbides and silicides. The layer consists of (Ti, Nb)$C_{(1-x)}$ and

(Ti, Nb, Al)$_5$Si$_3$ in the inner reaction zone and (Ti, Nb)$_3$AlC and (Ti, Nb, Al)$_5$Si$_3$ in the outer reaction zone. Since microcracks usually initiate in the interfacial region, cracks propagate along the weakest interface if the interfacial bonding strength is low. As a result, fiber/matrix interfacial debonding may take place at different locations including the interfaces between the two carbon coating layers, the outer carbon layer and reaction zone, and the reaction zone and matrix alloy. Experimental evidence reveals that both complete debonding and partial debonding can exist simultaneously and most of the partial fiber/matrix debonding takes place in a symmetric fashion under uniaxial or biaxial transverse mechanical loading. It is general agreed that the damage mechanism of debonding is related directly to the nonlinear behavior of the stress-strain relations.

- **Fiber Breakage**

Consider a composite made of a tough matrix and high interfacial bonding strength. In this case, microyielding of the matrix occurs which leads to blunting of the crack. If the fiber is strong, the crack neither propagates through the fiber nor debonds along the carbon coating layer. Upon further loading, owing to the presence of good interfacial bonding, the load is transferred back to the reaction zone, which in turn leads to multiple cracks in the reaction zone. As the loading is increased further, fiber fracture occurs at random locations in the fiber due to the statistical scatter of the fiber strength. The cracks resulting from the fiber breakage induce further stress concentration in the fibers adjacent to the broken fibers. This can lead to the fracture of other intact fibers as well as matrix yielding if the matrix is ductile. The failure of several fibers in the same plane may be sufficient to initiate failure of the composite. As a result, the composite exhibits a non-linear stress-strain behavior accompanied by a relatively flat facture surface.

- **Matrix Cracking**

In case a composite possesses a relatively brittle matrix with high interfacial bonding strength, microcracks initiated at the interface reaction layer are able to extend into the matrix causing matrix microcracks. These microcracks accumulate as the loading increases. This leads to the formation of macrocracks within the composite. Upon further loading of a composite with high interfacial bonding strength, the crack can propagate easily across the fibers with little deflection along the fiber-matrix interface. As a result, the composite exhibits a linear elastic stress-strain behavior up to the final fracture. The fracture surface is relatively flat with no significant amount of fiber full-outs. However, if the interfacial bonding strength is low, the shear stress concentration at the crack tip induces debonding along the fiber-matrix interface. Therefore, upon further loading, the tensile and shear stress concentration at the debonded crack tip causes the debonding crack to propagate along the fiber-matrix interface, extends into the matrix, and causes multiple matrix cracking. The advancement of the crack depends on the matrix shear failure strengths. As a result, the composite shows a bilinear stress-strain behavior while the fracture surface exhibits fiber pull-out.

- **Matrix Yielding**

Consider a continuous fiber reinforced composite made of a ductile matrix and brittle reinforcements. Damage initiated in the interface layer induces stress concentration. This leads to microyielding of the matrix which results in blunting of the crack. If the adjacent material layers possess low to medium interfacial bonding strength, the fiber will be debonded easily from the matrix or fractured. The result is a loss in fibers' load-sharing capability and the load carried by

the damaged fibers is transfer to the matrix. Upon further loading, global inelastic deformation in the matrix is triggered which may continue until the composite system fails.

1.4 Objective and Scope of the Dissertation

The primary objective of this research work is to investigate the effective mechanical responses of continuous fiber reinforced composites by modifying and extending the available micromechanical framework. A major part of the work conducted involves the investigation of the effective damage responses due to damage evolutions of matrix microcracks and fiber breaks.

Chapter 2 introduces the fundamentals of micromechanics theory. The concepts of the representative volume element, the Eshelby's equivalent principle, eigenstrains, and homogenization methods are reviewed first. Next, a literature review on the subject of continuous fiber reinforced MMCs with particular reference to various damage mechanisms is presented. The literature reviewed includes different analytical and numerical approaches and experimental results provided by various researchers.

Chapter 3 presents the effective elastic damage behavior of continuous fiber reinforced composites with evolutionary matrix microcracks. A cohesive penny-shape microcrack model is proposed within a two-step homogenization framework to achieve the effective elastic damage behavior of fibrous composites. In the present model, the number density and the size of microcracks are defined as two parameters controlling the damage evolution. Moreover, the

thermal effect is incorporated in the proposed model by taking advantage of the thermal eigenstrain and the Eshelby's equivalent inclusion principle. The overall coefficient of thermal expansion (CTE) of a composite is then derived under the framework of micromechanics to describe the overall damage behavior of composites due to the matrix microcrack evolution under temperature changes.

Chapter 4 proposes a micromechanical evolutionary damage framework capable of predicting the overall mechanical behavior of and damage evolution in continuous fiber reinforced composites. In the presented framework, the effective stress fields in a single fiber due to an embedded penny-shaped fiber break are systematically derived by applying the double-inclusion theory. An effective length denoting the distance between two adjacent cracks is then introduced as a damage parameter while determining the damage evolution within a single fiber. This enables the modeling of the effective damage behavior of a single fiber-reinforced composite. As an application of the proposed framework, a micromechanical damage model is further proposed to simulate the fiber-dominated failure mechanism within a continuous fiber reinforced composite. A Weibull probability function is adopted to estimate the varying volume fractions of damaged fibers and intact fibers. Numerical simulations are presented to demonstrate the effectiveness of the proposed methodology.

In Chapter 5, based on the linear elastic fracture mechanics (LEFM) and ensemble-volume averaging technique, an effective eigenstrain is newly proposed to quantify the homogenized stress fields in a single fiber due to multiple breaks. In the proposed model, the number density evolution of fiber breaks is characterized by a two-parameter Weibull statistic with the

temperature effect implicitly enclosed by properly adjusting the Weibull parameters. In particular, the damage criterion in the evolutionary model is theoretically. Base on the proposed damage framework, a homogeneous damage evolution model capable of simulating the material behavior of multi-fiber reinforced composite materials is developed.

Chapter 6 presents two stochastic risk-competing models to simulate the fiber breaking evolution in a multi-fiber composite in an inhomogeneous fashion by considering different load sharing mechanisms. A unit cell model is adopted with each cell being assigned an initial weakness based on a normal distribution. Damage evolution inside each individual cell structure follows the micromechanical model presented in Chapter 5. Two risk competing models are then introduced to determine the damage sequence within the multi-fiber composite by computing the fracture probability based on the weakness of cells at each time step. It is observed that one risk-competing model tends to generate a concentrated damage pattern with broken fibers clustering in a T-shape or a cross-shape, while the other model yields a more diffused damage pattern. Finally, the overall stress-strain responses and the fiber break evolution are s predicted and verified against experimental data.

Chapter 7 examines the effective elastoplastic behavior of MMCs containing unidirectionally aligned continuous fibers. A homogenization procedure is utilized to derive the overall yield function for the composite based on the probabilistic spatial distribution of aligned inclusions. Based on continuum plasticity, a plastic flow rule and a hardening law are postulated. These laws together with the proposed overall yield function then characterized the macroscopic elastoplastic behavior of the composite under three-dimensional arbitrary loading/unloading

histories. The overall uniaxial elastoplastic stress-strain behavior of MMCs with aligned continuous fibers is investigated. Comparisons between theoretical predictions and experimental data for the composite are performed to illustrate the capability of the proposed method.

Chapter 8 concludes the present research on micromechanics and effective elastic and elastoplastic behavior of continuous fiber reinforced MMCs. Finally, related future research topics are discussed briefly.

Table 1.1 Comparison of room temperature properties of ceramics, metals and polymers

	Density (Mg/m^3)	*Young's modulus* (GPa)	*Strength* (MPa)	*Ductility* (%)	*Toughness* K_{IC} ($MPa\ m^{1/2}$)	*Specific modulus* [(GPa)/ (Mg/m^3)]	*Specific strength* [(MPa)/ (Mg/m^3)]
CERAMICS							
Alumina AI_2O_3	3.87	382	332	0	4.9	99	86
Magnesia MgO	3.60	207	230	0	1.2	58	64
Silicon Nitride Si_3N_4		166	210	0	4.0		
Zirconia ZrO_2	5.92	170	900	0	8.6	29	152
β-Sialon	3.25	300	945	0	7.7	92	291
Glass-ceramic Silceram	2.9	121	174	0	2.1	42	60
METALS							
Auminium	2.70	69	77	47		26	29
Auminium-3%Zn-0.7%Zr	2.83	72	325	18		25	115
Brass Cu-30%Zn	8.50	100	550	70		12	65
Nickel-20%Cr-15%Co	8.18	204	1200	26		25	147
Steel mild	7.86	210	460	35		27	59
Titanium-2.5% Sn	4.56	112	792	20		24	174
POLYMERS							
Epoxy	1.12	4	50	4	1.5	4	36
Melamine formaldehyde	1.50	9	70			6	47
Nylon 6.6	1.14	2	70	60		18	61
Polyetheretherketone	1.30	4	70			3	54
Polymethylmethacrylate	1.19	3	50	3	1.5	3	42
Polystyrene	1.05	3	50	2	1.0	3	48
Polyvinylchloride rigid	1.70	3	60	15	4.0	2	35

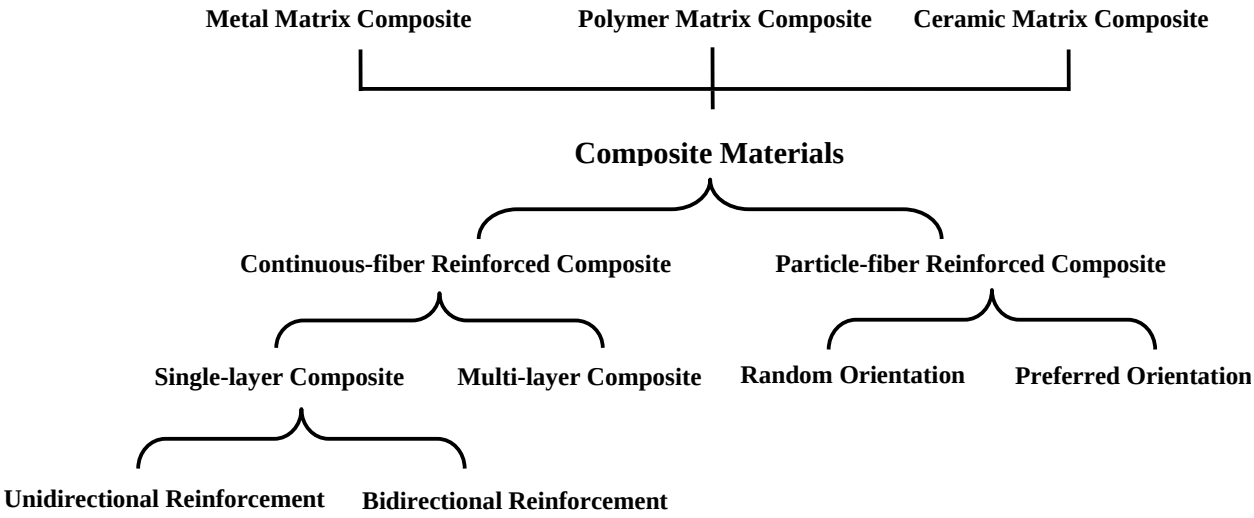

Figure 1.1 Classification of composite materials.

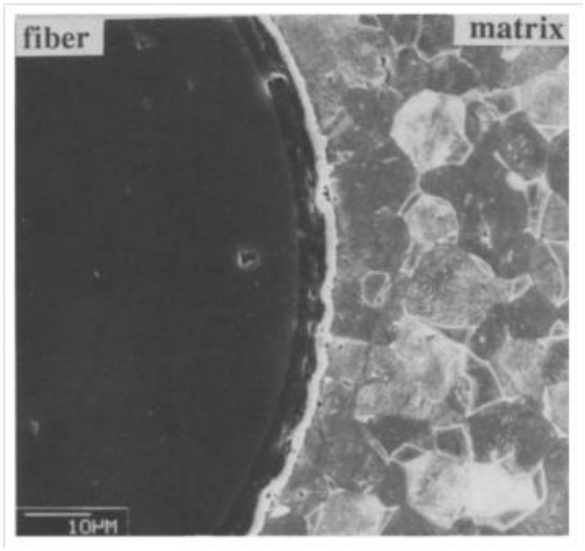

Microstructure of the interfacial region
in the SCS-6-Ti-6-4 composite

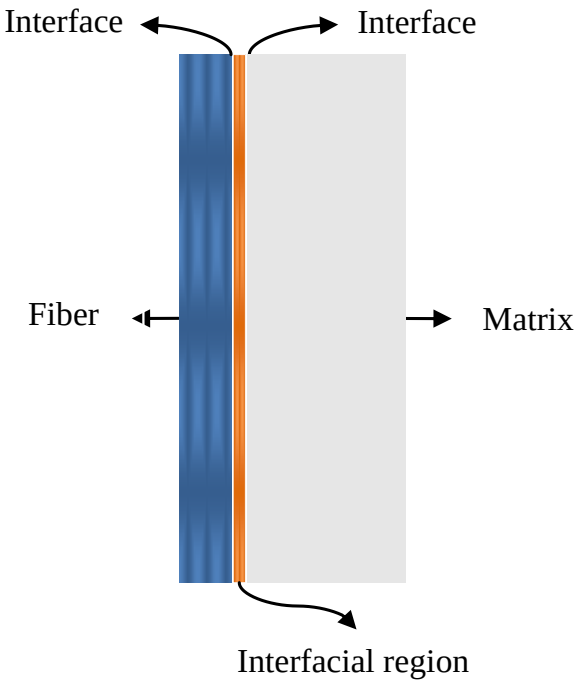

Figure 1.2 Schematic of the interfacial region microstructure of a fiber reinforced composite.

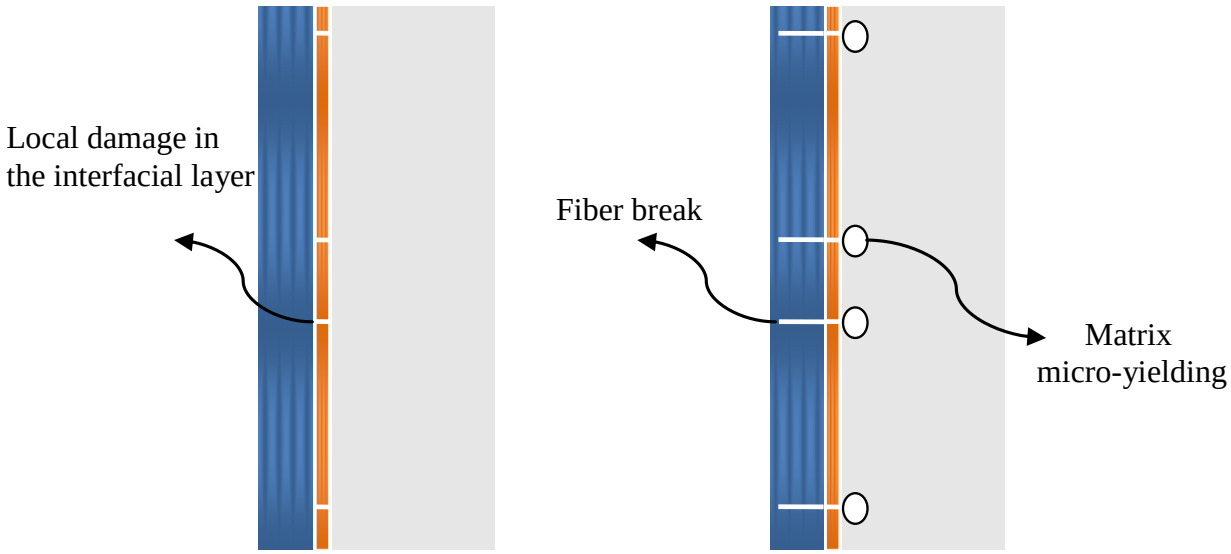

Figure 1.3 Schematic of the fiber breakage damage mechanism in a fiber reinforced composite.

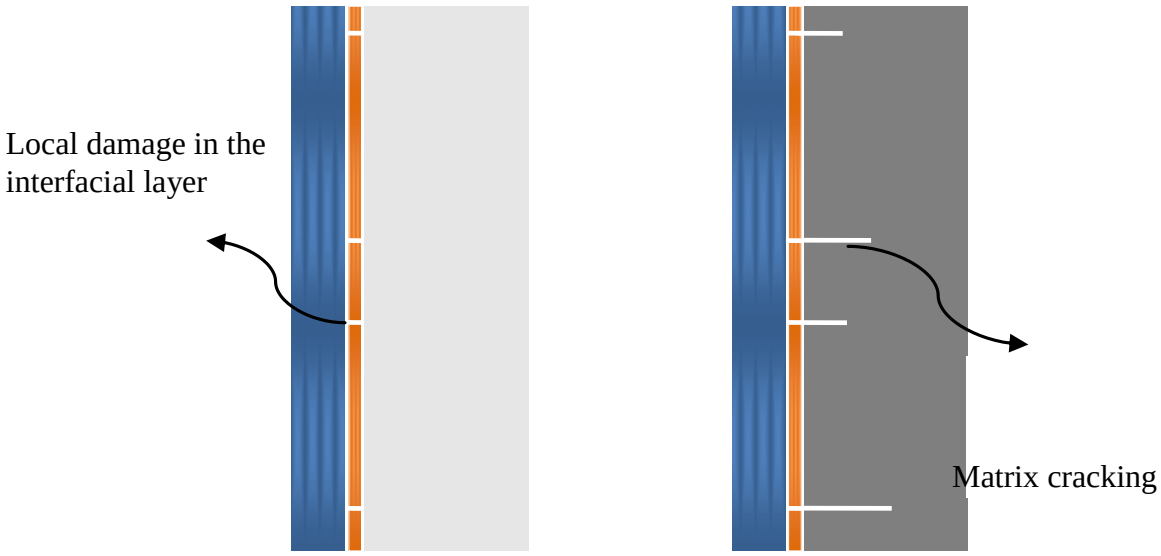

Figure 1.4 Schematic of the matrix microcrack damage mechanism in a fiber reinforced composite.

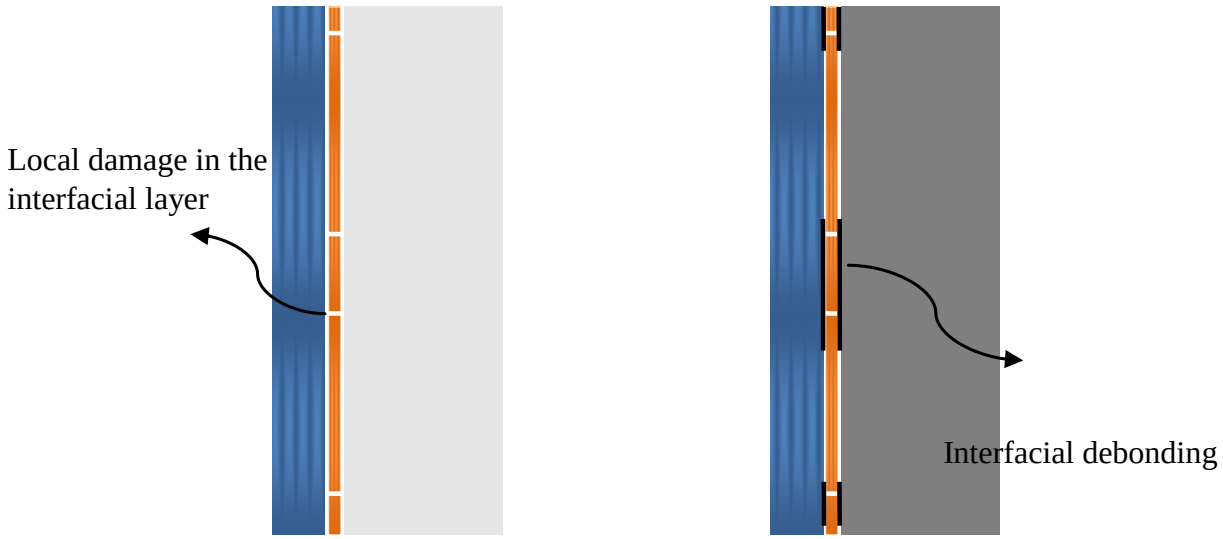

Figure 1.5 Schematic of the interfacial debonding damage mechanism in a fiber reinforced composite.

CHAPTER 2 LITERATURE REVIEW

2.1 Theories of Micromechanics

Traditional continuum mechanics deals with idealized materials under the assumptions of (1) the elastic properties of a solid at a material point are the same in every direction (isotropy); (2) the material property is the same at all points within the solid (homogeneity). These two assumptions render a uniform stress/strain distribution within an infinitesimal material element. However, optical morphology reveals that microscopic structures of a solid are complex; consist of inclusions, grains separated by grain boundaries, and local damage such as microcavities, cracks and dislocations. Consequently, the stress/strain fields within such a material element are not uniform at the microscopic level. In addition, it is impractical, or even impossible to comprehensively account for the factors of the microstructure in engineering design and analysis. Nevertheless, the field of micromechanics seeks to provide a rigorous framework for studying the overall material behavior by taking material microstructures and local damage into consideration. It also enables one to examine the interaction of constituent materials at a microscopic scale and determine the interaction effect on the overall composite properties at a macroscopic scale.

2.1.1 Representative Volume Element (RVE)

The prediction and estimation of the overall mechanical properties of random heterogeneous materials is of great interest to researchers and engineers in many science and engineering disciplines. In micromechanics, the so-called 'effective' properties of a heterogeneous composite can be obtained by certain volume and ensemble averaging processes over a representative volume element (RVE). An RVE for a material point of the continuum mass defines a material volume that statistically represents the infinitesimal material in the neighborhood of that material point. In other words, an RVE features the 'mesoscopic' length scale that is much larger than the characteristic length scale of inhomogeneity/inclusion but is smaller than the characteristic length scale of the 'macroscopic' specimen.

2.1.2 Eshelby's Equivalence Principle and Eigenstrain

In studying heterogeneous solids, it is convenient and effective to consider the equivalent homogeneous solids (Eshelby, 1957). In accounting for the mismatch of the material properties between the matrix and inclusion, the notion of stress-free strain $\boldsymbol{\varepsilon}^*$ is introduced within the inclusion domain so that, under the applied force or displacement, the equivalent homogeneous solid has the same stress and strain fields as the actual heterogeneous solid. As a result of this artifact, the following equation can be obtained on the basis of an integral representation of elasticity:

$$\mathbf{C}_1 : \left(\boldsymbol{\varepsilon}^0 + \boldsymbol{\varepsilon}'\right) = \mathbf{C}_0 : \left(\boldsymbol{\varepsilon}^0 + \boldsymbol{\varepsilon}' - \boldsymbol{\varepsilon}^*\right) \tag{2.1}$$

where $\mathbf{C}_1$ and $\mathbf{C}_0$ are the elasticity tensors of the inhomogeneity phase and matrix phase, respectively, and $\boldsymbol{\varepsilon}'$ and $\boldsymbol{\varepsilon}^0$ signify the perturbed strain due to the presence of the inhomogeneity and the far-field strain, respectively.

Eigenstrain, $\boldsymbol{\varepsilon}^*$, (Mura, 1987) is a generic name introduced in micromechanics to represent inelastic strains such as thermal strains, phase transformation strains initial strains, plastic strains, misfit strains, and the like. In literature, other names have been used for eigenstrains by various authors, e.g., stress-free transformation strains (Eshelby, 1957). On the other hand, eigenstress is a generic name for the self-equilibrated internal stresses caused by one or more of these eigenstrains in bodies, which are free from any external force and surface constraints. The eigenstress is a consequence of the incompatibility of the eigenstrain. For micromechanical modeling of elastic heterogeneous solids, Eshelby highlighted the following results:

if

1) the matrix is homogeneous, linearly elastic and extended infinitely;
2) the inclusion domain is ellipsoid,

then

1) the eigenstrain is uniformly distributed within the inclusion domain;
2) the perturbed strain $\boldsymbol{\varepsilon}'$ and perturbed stress $\boldsymbol{\sigma}'$ caused by the presence of the inclusions are also uniform within the inclusion domain;
3) the perturbed strain in the inclusion domain is demonstrated by $\boldsymbol{\varepsilon}'_{ij} = \mathbf{S}_{ijkl}\boldsymbol{\varepsilon}^*_{kl}$.

Since the perturbed strain is evaluated in the inclusion domain, **S** tensor is called the interior-point Eshelby's tensor. The key features of **S** tensor are:

1) it is independent of material properties of the inclusion,
2) it depends on the shape of ellipsoidal inclusion and Poisson's ratio of the isotropic matrix material.

2.1.3 Homogenization Methods

In micromechanics, the procedure related to the ensemble-volume averaging process is called 'homogenization'. It is a methodology applied in estimating the effective material properties. A number of homogenization methods have been developed in literature to predict the overall properties and behavior of heterogeneous materials. The first school utilizes the variational principle to arrive at the mathematical lower and upper bounds for the effective elastic moduli of composites. With this perspective, Hashin and Shtrikman (1962a, b) gave the mathematical lower and upper bounds for the effective moduli of isotropic composite materials with prescribed volume fractions of inclusions with arbitrary shapes. Later, Hill (1963) and Hashin (1965) determined the bounds for the fiber-reinforced composites. Castenada and Wills (1988), and Talbot and Wills (1985) introduced a general method for deriving the bounds on the overall potentials of nonlinear composites. In addition, Castenada (1991) proposed a new and conceptually simple variational procedure that leads to more general bounds for the nonlinear composites. The second school is known as the effective medium theory which includes the self-consistent method (Budiansky, 1965), the differential scheme (Hashin, 1988; McLaughlin, 1977), the generalized self-consistent method (Christensen and Lo, 1979; Christensen, 1990) and the

Mori-Tanaka method (Mori and Tanaka, 1973; Weng, 1990). In the effective medium theory, particle locations or their relative configurations are not taken into consideration. The third school aims at direct micromechanical determination of effective properties of the composite materials by incorporating the interactions amongst the inclusions and the geometric effect due to the configurations of the inclusions dispersed within the matrix material. Important works along this line, include Ju and Chen (1994a, b), Ju and Lee (2000), Li et al. (2004), Ju and Ko (2006), Ju and Yanase (2009).

Numerical methods, such as the finite element method (FEM) are also used widely for predicting the overall behavior of composites. For example, Christman et al. (1989 a, b) and Tvergard (1990) calculated the effective elastoplastic behavior of aligned short-fiber reinforced MMCs using the axisymmetric unit cell model. To determine the effective response of the MMCs, Levy and Papazian (1990) used the unit cell model while applying the three-dimensional finite element method.

Both analytical and numerical treatments have their advantages and disadvantages (Dunn and Ledbetter, 1996). In general, analytical approaches assume an idealized geometry to predict the properties of the RVE. For the sake of mathematical simplicity, the reinforcing phases are assumed to be ellipsoidal inclusions. In such cases, the celebrated Eshelby's equivalence principle (Eshelby, 1957) is applicable. Plastic flow is typically constructed according to the effective-medium approach (continuum plasticity), which does not rigorously consider the micromechanical local plastic flow initiated at the interface between the reinforcement and the matrix. On the other hand, numerical approaches are based on a pre-defined geometry, so the

local elastic and plastic stress/strain fields can be analyzed. However, the periodic boundary conditions introduce a periodicity in the inclusion distribution, which does not exist in actual composite materials. Therefore, the resulting local fields must be interpreted with caution.

2.2 Theoretical Damage Models

- **Interfacial Debonding**

The symmetric debonding model is employed extensively in literature for both the analytical analyses (cf. Takahashi and Chou, 1988; Zhao and Weng, 2002) and the numerical analyses (cf. Nimmar et al., 1991; Warrier et al., 1999; Naboulsi, 2003). A series of comprehensive studies on the damage behavior of fiber-reinforced composites due to fiber/matrix interfacial debonding is performed by Ju and his coworkers. Various damage models are proposed by considering particle-shaped reinforcements (Ju and Lee, 2000; Liu et al., 2004, 2006) and continuous fibers (Ju and Ko, 2006; Ju and Yanase, 2009) with evolutionary complete debonding (Ju and Ko, 2006) and progressive partial debonding (Sun et al. 2003; Ju and Ko, 2008; Ju et al., 2008). In particular, the geometric effect of the fiber cross section shape on the overall damage behavior is studied. For instance, continuous reinforcements with circular-shaped (Ju and Ko, 2008) and elliptical-shaped cross-sections (Ju et al., 2009; Ju and Yanase, 2009) are systematically investigated. In their study, an interfacial debonding angle is introduced as the damage parameter based on the symmetric debonding model. Moreover, debonding is assumed to propagate instantly in the fiber direction once the interfacial damage is activated. As a result, the three dimensional problem can be effectively solved as a two-dimensional problem and the partially debonded isotropic elliptical fibers can be replaced by equivalent orthotropic yet perfectly

bonded elliptical fibers. The Weibull probabilistic function is employed to describe the progressive fiber debonding process in the composite system. As an extension of the framework, thermal residual stresses have also been taken into account successfully through the concept of thermal eigenstrain to simulate the effects of the manufacturing process-induced residual stresses (Ju and Yanase, 2008). The primary advantage of these models is that they provide the explicit form of the effective moduli of the composite. However, these models only consider the influence of far-field interactions on the overall deformation behavior of a composite with a moderate fiber volume fraction.

- **Fiber Breaking**

There are several schools of theories for estimating the damage effect of fiber breaks in multi-fiber composites. The shear lag theory (Cox, 1952) involving various load transferring mechanisms is one of the means. For example, the global load shearing (GLS) model assumes that the load originally borne by the broken fiber is equally redistributed over all the remaining intact fibers on the cross-session. Every cross-sects becomes statistically identical, thus, a multi-fiber composite problem can be treated as an equivalent single-fiber composite problem (Curtin, 1998). The primary advantage of such models is simplicity of application. However, in reality, the load transfer mechanism within the local region is far more complicated. Hence, the local load shearing (LLS) model is proposed assuming that the extra load associated with the failed fibers is transferred to the neighboring fibers (Smith, 1980; He et al., 1993; Zhou and Curtin, 1995; Ibnabdeljalil and Curtin, 1997; Okabe and Takeda, 2002). This group of models is mainly concerned with the local microstructure and how the load transfers from the broken fiber to the intact fibers. Both the GLS and LLS models lead to a qualitative understanding of the

mechanisms of forming discontinuities, as well as the interaction among the material phases. However, none of these approaches allows straightforward incorporation of the nonlinear models to describe the complicated material behaviors (Mishnaevsky and Brøndsted, 2009).

Another school aims at formulating the explicit forms of the overall constitutive laws for heterogeneous materials considering various local damage modes (Ju, 1991; Ju and Tseng, 1992; Sun et al., 2003; Lee and Ju, 2008). Following the concept of eigenstrain introduced by Eshelby (1957, 1961), the effective properties of heterogeneous composites containing inhomogeneities and local damage are derived based on an ensemble-volume averaging process within a representative volume element (RVE). In particular, Sun and Ju (Sun et al., 2003) applied the double-inclusion theory (Hori and Nemat-Nasser, 1993; Shodia and Sarvestani, 2001) to investigate the particle-shaped fiber cracking problem. They explicitly derived the perturb stress field associated with a single crack embedded in a single fiber. Utilizing the innovative governing ensemble-volume average field equations developed by Ju and Chen (1994), the explicit form of the overall constitutive relations for short fiber reinforced composites with progressive fiber breaks was realized. Ko and Ju (2013) further extended the application of the double-inclusion theory to predict the overall material behavior associated with fiber cracking in continuous fiber-reinforced composites, with the local cracking damage propagating along the longitudinal direction. The primary advantage of micromechanics is that these models consider the explicit form of the overall constitutive relations of composites considering different material phases and various damage modes. However, since the crack opening displacement of the breakage is neglected in the double-inclusion model, the ensemble volume-averaged total eigenstrain depends only on material properties of the fiber phase.

Numerical techniques have also been applied extensively to simulate the fiber breaking process in MMCs. Finite element simulation is one of the most commonly-used methods (Nickolas and Ahmad, 1994; Shodja and Sarvestni, 2001; Xia et al., 2002; Ohno et al., 2004). Another widely adopted technique for the prediction of the strength of the composite materials is the Monte Carlo simulation (Landis, 2000; Meyer et al., 2003; Liu and Zheng, 2006; Nazari et al., 2011). Most computational models are based on a pre-defined micro-structural layout, which has the advantage of high accuracy of solutions by taking into account the geometry of reinforcements and local interactions among reinforcements. However, numerical models do not yield explicit forms for the overall constitutive relations. This makes them difficult to be implemented in the stress analyses at the macroscopic level.

- **Matrix Cracking**

The penny-shaped microcrack model is extensively employed in theoretical models to study the damage behavior of composites due to matrix cracks. In addition, the crack number density is widely adopted as the damage parameter that governs the degradation of composites. Kaechele and Tetelman suggested that the crack number density increases as the ninth power of normal stress across the cleavage plane. A number of models based on the penny-shaped crack models and the concept of crack density evolution, have been developed to simulate the matrix cracking problem in composite materials. Based on the theory of micromechanics, Ju and his coworkers conducted a series of studies to systematically investigate the influence of microcracks on the effective moduli of the composites. A three-dimensional statistical micromechanical framework considering the first-order microcrack interaction was proposed by Ju and Tseng (1992) to investigate effective elastic moduli of brittle solids with randomly located, penny-shaped

microcracks. The higher-order pair-wise microcrack interaction was later taken into account (Ju and Chen, 1994 d, e). Moreover, Ju and Lee applied the highly accurate Legendre and Tchebycheff orthogonal polynomials to solve the randomly located and oriented two-crack interaction problem in a two-dimensional space. A three-dimensional elastic stress analysis was later performed on an infinite solid to study the interaction between a penny-shaped crack and a spherical inclusion (Lee and Ju, 2007). The primary advantage of these models is that the microstructural statistical information is embedded implicitly in the ensemble-averaged equations and, therefore, no Monte Carlo simulations are needed.

In reality, there exists an atomic bonding force near the crack tip, which provides a cohesive closing pressure on the crack and resists further crack propagation. Since the pioneering works of Dugdale (1960) and Barenblatt (1962), cohesive cracks have been studied widely and employed to investigate the failure mechanisms. Keer and Mura (1965) used the Tresca yield criterion to link the cohesive strength with the microscale yield stress. Later, Keer and his coworkers (1966, 1991, and 1993) performed a series of studies to investigate the cohesive crack in various materials under different loading conditions. Li et al. (2004) proposed a cohesive microcrack model based on the homogenization of the Dugdale-Bilby-Cottrell-Swinden type microcracks in a two dimensional elastic representative volume element. In addition to the analytical models, numerical techniques, such as the finite element method, are also widely used to simulate the damage evolution of cohesive cracks. For instance, Belytschko and his coworkers (2002) utilized the extended finite element method (XFEM) to predict the growth of arbitrary cohesive cracks.

- **Matrix Yielding**

The matrix material tends to yield at a relatively low stress around the interface between the matrix and inclusion due to the high stress concentration induced by the mismatched stiffness of those materials (Christman et al., 1989a, b). However, the resulting local plastic yielding does not control the onset of global yielding. The overall yield stress of metal matrix composites is governed not so much by the premature local yielding of the matrix, but rather by the attainment of an average stress in the matrix that is sufficient for the global yielding (Clyne and Withers, 1993). Moreover, due to the similarity of the yield criteria developed for monolithic materials which reflect the tri-axial state of stress, it seems reasonable to take this tri-axial state of stress into account for metal matrix composites. A number of models use the von Mises and Tresca type yield criteria. They assume that overall plastic flow of the composite occurs when the average stress in the matrix exceeds certain threshold value. Therefore, the matrix material plays a crucial role in determining the overall composite yielding (Nieh and Chellman, 1984).

In literature, there are several schools of theories regarding the prediction of the elastoplastic behavior of MMCs due to matrix plastic deformation. A number of models have focused on the prediction of effective elastoplastic behavior of MMCs from their microstructural characteristics. These microstructural characteristics include the mechanical properties of constituent phases, volume fractions, spatial distributions, and micro-geometries (shapes, orientations, and sizes) of inhomogeneities. For instance, Tandon and Weng (1988) employed the Mori-Tanaka method (Mori and Tanaka, 1973) and the secant moduli method (Berveiller and Zaoui, 1979) to predict the effective elastoplasticity of MMCs. Subsequently, Zhao and Weng (1990) considered the overall elastoplasticity of aligned spheroid reinforced MMCs. An improved method was

proposed by Qiu and Weng (1991, 1992, 1995), using the energy criterion for the effective stress of the ductile matrix while estimating the strain potential and the overall stress-strain relations of two-phase composites containing spherical or spheroidal inclusions. Ju and his research group proposed an elastoplastic micromechanical framework, in which the local stress field at any matrix point can be computed directly by using the exterior-point Eshelby's tensor. The ensemble-area-averaging method can be employed directly to obtain the effective yield function for the fiber reinforced metal matrix composites with evolutionary multi-level damage.

Emanating from the continuum mechanics approach, another group of researchers treats MMCs as single-phase anisotropic materials exhibiting properties along different directions. Naturally, the behavior of the aligned fiber reinforced MMCs exhibit at least transverse isotropy. Important works along this line include, the continuum model of Mulhern et al. (1967), the failure criteria of Hashin (1980), and the bimodal plasticity analysis of Dvorak and Bahei-El-Din (1987) and Dvorak (1988) for fiber reinforced MMCs. Hansen et al. (1991) and Schmidt et al. (1993) also proposed a modified model of Hill (1948) to calculate the plastic behavior of transversely isotropic composites. Further, Voyiadjis and Thiagarajan (1995) proposed a new anisotropic pressure-dependent continuum yield surface model for directional fiber-reinforced MMCs.

Numerical techniques are also used widely for modeling the mechanical behavior of MMCs. For instance, Christman et al. (1989a, b) and Tvergaard (1990) calculated the effective elastoplastic behavior of short-fiber reinforced MMCs by using an axisymmetric unit cell model under the finite element framework. Similarly, Levy and Papazian (1990) and Hom (1992)

utilized a unit cell model together with the three-dimensional finite element analysis to determine the effective elastoplastic responses of short-fiber reinforced MMCs. Moreover, Bao et al. (1991) combined the finite element analysis with a theoretical investigation.

CHAPTER 3 MICROMECHANICAL MODELING OF CONTINUOUS FIBER REINFORCED COMPOSITES WITH PENNY-SHAPED COHESIVE MATRIX MICROCRACKS AND THERMAL EFFECTS

3.1 Introduction

Continuous fiber reinforced composites have been investigated extensively because of their superb mechanical properties. Experimental results indicate that chemical reactions between the fiber and the matrix during fabrication normally form a brittle interfacial layer. In general, this layer possesses a lower fracture strength comparing to that of the fiber and the matrix. Upon the tensile loading along the fiber longitudinal direction, microcracks initiate in the interfacial layer with the crack opening surfaces perpendicular to the loading direction. As a consequence, stress concentrations are induced near crack tips. Different damage modes can be triggered near the interfacial region depending on the combination of the constituents' properties and the interfacial bonding conditions. Consider a composite with a brittle matrix and perfect interfacial bonding conditions. Microcracks that initiated in the interface layer can further extend into the brittle matrix, leading to the formation of matrix microcracks. As the load increases, the size and the number density of microcracks increase as well. This leads to the nonlinear stress-strain behaviors of the overall material behavior.

In literature, the effective properties of an isotropic elastic matrix material containing microcracks have been investigated extensively. Famous works along this line include the self-

consistent model (Budiansky 1965; Ju and Lee 1991a, 1991b), the variational bounds (Talbot and Willis, 1985), the differential scheme (Hashin 1988), the Mori-Tanaka method (Zhao et al. 1989), the deterministic microcrack interaction model (Krasnikovs and Megnis 2005), and the statistical microcrack interaction model (Ju and Tseng 1992). Moreover, numerical techniques have also been applied widely in studying microcracks and crack propagation problems. For example, Belytschko and his coworkers (1991) developed a finite element model for crack growth without re-meshing.

In reality, a small area termed the 'cohesive zone' exists near the crack tip, where the atomic bonding force applies a closing pressure on the crack tip and resists the crack from further propagation. The presence of the cohesive zone complicates the local microstructures and the corresponding theoretical study. A number of research works have taken account of the cohesive effect while investigating the matrix crack initiation and crack propagation problems. The early contribution was made by L. Keer and T. Mura (1965), who used the Tresca yield criterion linking the cohesive strength with the microscale yield stress. In their study, only uniaxial tension loading was considered. More recently, Chen and Keer (1993) re-examined the problem, and they obtained the general solutions for a penny-shaped cohesive crack under mixed-mode loadings. Later, Li and his coworkers (2003) proposed a micromechanical framework to incorporate the cohesive effect under hydrostatic loading condition. The overall damaged material properties were derived analytically. In addition, numerical models have also been developed to take the cohesive effect into account. For example, Belytschko and his co-works (Moës and Belytschko 2002) modified their crack model by using the extended finite element method (XFEM) to simulate the growth of arbitrary cohesive cracks.

3.2 Micromechanical Formulation

In order to render a tractable homogenization solution, the following assumptions are made in this study: 1) the overall damage due to the permanent crack opening is only associated with the average hydrostatic stress state in an RVE; and 2) the overall damage effect due to the average deviatoric stress is negligible (Wang and Li, 2004). These assumptions enable us to investigate the damage behavior that is only susceptible to macro hydrostatic stress state.

A three dimensional penny-shaped Dugdale crack model with an inner radius a and outer radius b is adopted to represent a cohesive microcrack. The ring-shaped zone with width $b-a$ denotes the cohesive zone as illustrated in Figure 3.2. Consider an RVE with microcracks randomly dispersed within it and a uniform triaxial tension stress σ_0 is applied at the remote boundary of the RVE. The traction conditions on the remote boundary ∂V_∞ and the symmetric displacement boundary conditions can be expressed in the cylindrical coordinate as

$$\sigma_{zz}\,|_{\partial V_\infty} = \sigma_{\theta\theta}\,|_{\partial V_\infty} = \sigma_{rr}\,|_{\partial V_\infty} = \sigma_0 \tag{3.1}$$

$$u_z(r,\theta,0) = 0 \quad \text{for } b \le r,\ 0 \le \theta \le 2\pi \tag{3.2}$$

Utilizing the concept of superposition, the problem of a matrix material containing one penny-shaped cohesive microcrack under hydrostatic stress state can be treated as two sub-problems as shown in Figure 3.3. One is an intact material under the hydrostatic stress and the other is a crack problem with the crack surface traction distribution. The stresses on the crack surface and the cohesive zone are

$$\sigma_{zz}(r,\theta,0) = \sigma_{co} H(r-a) \quad \text{for} \quad 0 \le r \le b,\ 0 \le \theta \le 2\pi \tag{3.3}$$

where $H(r-a)$ is the Heaviside function, and σ_{co} is the cohesive strength of the matrix phase.

In the second sub-problem, the crack opening displacement u_z can be solved analytically as

$$u_z(r)=\begin{cases}\dfrac{2}{\pi}\left(\dfrac{1-\nu^*}{\mu^*}\right)\left(\sigma_0\sqrt{b^2-r^2}-\sigma_{co}\displaystyle\int_a^b\sqrt{t^2-a^2}\,/\sqrt{t^2-r^2}\,dt\right), & 0<r<a\\ \dfrac{2}{\pi}\left(\dfrac{1-\nu^*}{\mu^*}\right)\left(\sigma_0\sqrt{b^2-r^2}-\sigma_{co}\displaystyle\int_r^b\sqrt{t^2-a^2}\,/\sqrt{t^2-r^2}\,dt\right), & a<r<b\end{cases} \tag{3.4}$$

The averaged strain field $\overline{\boldsymbol{\varepsilon}}$ is related to the averaged stress $\overline{\boldsymbol{\sigma}}$ through the overall complementary energy density $\overline{W}_c$ of the RVE

$$\overline{\boldsymbol{\varepsilon}}=\frac{\partial\overline{W}_c}{\partial\overline{\boldsymbol{\sigma}}} \tag{3.5}$$

The averaged strain $\overline{\boldsymbol{\varepsilon}}$ and the far-field stress $\boldsymbol{\sigma}_0$ can be related by introducing an effective compliance tensor $\overline{\mathbf{D}}$ of the damaged RVE through

$$\overline{\boldsymbol{\varepsilon}}=\overline{\mathbf{D}}:\boldsymbol{\sigma}_0 \tag{3.6}$$

where the averaged stress $\overline{\boldsymbol{\sigma}}=\boldsymbol{\sigma}_0$ according to the average theorem.

Similarly, the averaged strain $\overline{\boldsymbol{\varepsilon}}$ can be divided into two parts, with each part associated with a sub-problem. Then,

$$\overline{\boldsymbol{\varepsilon}}=\boldsymbol{\varepsilon}^{(0)}+\boldsymbol{\varepsilon}^{(a)} \tag{3.7}$$

where $\boldsymbol{\varepsilon}^{(a)}$ is termed as additional strain tensor representing the damage effect. This additional strain can be expressed in terms of the averaged stress $\overline{\boldsymbol{\sigma}}$ as

$$\boldsymbol{\varepsilon}^{(a)} = \mathbf{H} : \bar{\boldsymbol{\sigma}} \tag{3.8}$$

where $\mathbf{H}$ is the additional compliance tensor due to the presence of microcracks. Once $\mathbf{H}$ is derived, the effective elastic compliance moduli $\bar{\mathbf{D}} = \mathbf{D} + \mathbf{H}$ can be deduced subsequently.

Assume that the total energy release of a cohesive crack is completely consumed in the surface separation. This may or may not be true in cohesive fracture due to the plastic dissipation in the cohesive zone. As a consequence, the upper bound estimation of the total energy release rate of an RVE with a single penny-shaped cohesive microcrack can be expressed as

$$R = \int_{\Omega} \Sigma_m [u_z] dS - \int_{\Omega_2} \sigma_{co} [u_z] dS \tag{3.9}$$

Carrying out the integration using crack displacement solutions, the energy release estimate can be written as the following expression:

$$R = \frac{16(1-\nu^*)}{3\mu^*} \sigma_{co}^2 a_\alpha^3 \left(1 - \sqrt{1 - (\Sigma_m / \sigma_{co})^2}\right) \tag{3.10}$$

where the cohesive microcrack volume fraction can be expressed as

$$f = \sum_{\alpha=1}^{N} \frac{4\pi a_\alpha^3}{3V} \beta \tag{3.11}$$

where a_α is the radius of the αth crack, and $4\pi a_\alpha^3 / 3$ is the volume of a sphere with radius a_α, N is the number density of microcracks in the RVE, and β is the ratio between the volume of permanent crack opening and the volume of total crack opening of a cohesive microcrack. For simplicity, we assumed that this ratio is fixed with the value $\beta = 0.95$ for every crack inside the RVE. Hence, the density of energy release of the RVE is estimated as

$$\begin{aligned}\frac{R}{V} &= \frac{16(1-\nu^*)}{3\mu^*\beta}\sigma_0^2\sum_{\alpha=1}^{N}\left(\frac{4\pi a_\alpha^3}{3V}\beta\right)\times\frac{3}{4\pi}\left(1-\sqrt{1-(\Sigma_m/\sigma_0)^2}\right)\\ &= \frac{4(1-\nu^*)}{\pi\mu^*\beta}\sigma_0^2 f\left(1-\sqrt{1-(\Sigma_m/\sigma_0)^2}\right)\end{aligned} \tag{3.12}$$

The overall complementary energy density, therefore, may be expressed as the sum of complementary energy of corresponding virgin material and the density of energy release estimate due to microcrack distribution,

$$\begin{aligned}\bar{W}^c &= W^c + \frac{R}{V}\\ &= \frac{1}{2}\boldsymbol{\sigma}_0 : \mathbf{D} : \boldsymbol{\sigma}_0 + \frac{4\left(1-\nu^*\right)}{\beta\pi\mu^*}\sigma_{co}^2 f\left(1-\sqrt{1-\left(\Sigma_m/\sigma_{co}\right)^2}\right)\end{aligned} \tag{3.13}$$

For a given microcrack volume fraction f , the averaged strain tensor can be obtained as

$$\begin{aligned}\boldsymbol{\varepsilon} &= \frac{\partial\bar{W}^c}{\partial\boldsymbol{\Sigma}} = \frac{\partial\bar{W}^c}{\partial\boldsymbol{\sigma}_0} = \mathbf{D}:\boldsymbol{\sigma}^\infty + \frac{\partial\left(R/V\right)}{\partial\left(\Sigma_m\right)}\frac{\partial\left(\Sigma_m\right)}{\partial\sigma_0}\\ &= \mathbf{D}:\boldsymbol{\sigma}_0 + \frac{4\left(1-\nu^*\right)}{3\beta\pi\mu^*} f\frac{\Sigma_m\mathbf{I}^{(2)}}{\sqrt{1-\left(\Sigma_m/\sigma_{co}\right)^2}}\end{aligned} \tag{3.14}$$

Further, the expression for the additional strain can be derived as

$$\boldsymbol{\varepsilon}^{(a)} = \frac{4\left(1-\nu^*\right)}{3\beta\pi\mu^*} f\frac{\Sigma_m\mathbf{I}^{(2)}}{\sqrt{1-\left(\Sigma_m/\sigma_{co}\right)^2}} \tag{3.15}$$

By imposing the restriction that the relative reduction of the shear modulus is the same as that of the bulk modulus leads to

$$\frac{\bar{K}}{K} = \frac{\bar{\mu}}{\mu} \tag{3.16}$$

By using the following relations:

$$\frac{1}{3K}=\frac{1-2\nu}{E} \quad \text{and} \quad \frac{1}{3\bar{K}}=\frac{1-2\bar{\nu}}{\bar{E}} \tag{3.17}$$

$$\frac{1}{2\mu}=\frac{1+\nu}{E} \quad \text{and} \quad \frac{1}{2\bar{\mu}}=\frac{1+\bar{\nu}}{\bar{E}} \tag{3.18}$$

We can then derive that $\bar{\nu}=\nu$ and

$$\frac{1}{3\bar{K}}=\frac{1}{2\bar{\mu}}\left(\frac{1-2\bar{\nu}}{1+\bar{\nu}}\right)=\frac{1}{2\bar{\mu}}\left(\frac{1-2\nu}{1+\nu}\right) \tag{3.19}$$

$$\frac{1}{3K}=\frac{1}{2\mu}\left(\frac{1-2\nu}{1+\nu}\right) \tag{3.20}$$

Finally, the effective elastic moduli can be estimated as:

$$\frac{\bar{K}}{K}=\frac{\bar{\mu}}{\mu}=1-\frac{8\left(1-\nu^2\right)}{3\beta\pi\left(1-2\nu\right)}\frac{f}{\sqrt{1-\left(\boldsymbol{\Sigma}_m/\boldsymbol{\sigma}_0\right)^2}} \tag{3.21}$$

3.3 Two-Step Homogenization and Damage Evolution

3.3.1 Homogenization Procedure

Based on the penny-shaped cohesive microcrack model, a two-step homogenization framework is developed to achieve the effective elastic damage behaviors of continuous fiber-reinforced composites associated with matrix microcracks. In the first stop, an intact matrix material is homogenized with the penny-shaped microcracks. Next, the damaged matrix material is homogenized with reinforcements to achieve the effective damaged material properties of the continuous fiber reinforced composite associated with matrix microcracks. In the present

framework, the fiber volume fraction is assumed to be low so that the higher-order interactions among reinforcements and microcracks can be neglected.

3.3.2 Damage Evolution

The crack number density and the crack size are defined as two damage parameters in describing the damage evolution due to matrix microcracks. Upon on loading, the number density of matrix microcracks increases. Assuming that the number evolution of matrix microcracks is governed by the Weibull statistic:

$$n = p_1 \cdot n_{saturated} \tag{3.22}$$

$$p_1 = \begin{cases} 1 - \exp\left[-\left(\dfrac{\sigma - \sigma_{cr}}{S} \right)^M \right] & \text{if } \sigma \geq \sigma_{cr} \\ 0 & \text{if } \sigma < \sigma_{cr} \end{cases}$$

where $n_{saturated}$ and σ_{cr} are the saturated number of matrix microcracks and the stress threshold for microcrack initiation, respectively, σ is the internal stress of the composite, and S and M are the two Weibull parameters, which can be quantitatively characterized from experiment. Here, S is associated with the local fiber breaking strength, whereas M governs the damage evolution rate.

Once a microcrack is triggered, the size of the microcrack increases as the load increases. We define a radius ratio

$$radius\ ratio = \frac{a}{b} = \sqrt{1 - (\frac{\sigma}{\Sigma_m})^2} \tag{3.23}$$

This ratio tends to increase as the loading increases. As a consequence, we compute the current volume fraction of microcracks as $f_{new} = f_{old} * (\frac{ratio_{old}}{ratio_{new}})$. This governs the damage evolution of the cohesive microcracks.

3.4 Numerical Results and Discussion

The following material properties of a fiber-reinforced composite are adopted for demonstration purpose. The Young's Modulus of the matrix and fibers are $E_m = 210$ GPA and $E_f = 245$ GPA, respectively. The Poisson's ratios are $\nu_m = 0.3$ for the matrix and $\nu_m = 0.27$ for the fibers. Assuming the initial volume fraction of microcracks is 0.05.

The stress-strain curves in Figure 3.5 show the nonlinear material behavior due to the microcrack evolution with different values of initial microcrack volume fraction. The greater the initial volume fraction of microcracks, the lower the stiffness of the material will be. From the numerical simulation as shown in Figure 3.6, it is obvious that the existence of microcracks within the composites tends to lower the stiffness of materials. By introducing the cohesive effects into the penny-shaped microcrack model, an increasing of the overall stiffness of the composites is observed. That is, the closing pressure due to the cohesion attempts to stop the growth of the microcracks, thus, requires more energy for further cracks to propagate. Figure 3.7

shows the stress-strain behavior of the fiber-reinforced composite with cohesive microcrack compared against the virgin matrix material and matrix material with cohesive microcracks.

The proposed micromechanical damage model with the two-step homogenization is further implemented in the user subroutine UMAT in ABAQUS. The plate with the same material properties given previously is discretized by 1,200 20-nodes finite element with the prescribed displacements and boundary conditions given in Figure 3.8. General nonlinear analysis with 50 load increments is performed in order to capture the material degradation due to microcrack damage evolution.

The overall stress-strain relations and overall microcrack damage evolution obtained from the analyses in ABAQUS are shown in Figure 3.9 and Figure 3.10, respectively. The corresponding stress-strain relationships and damage evolution curves for the corner and middle points of the plate are given in Figure 3.11–Figure 3.14, which reveals that the damage evolutions are inhomogeneous and position-dependent.

3.5 Microscopic Matrix Cracks with Thermal Effects

The mechanical properties and material behaviors of composites are sensitive to thermal effect. On one hand, the material properties of MMCs are dependent upon temperature (Matthews and Rawlings 1993). On the other hand, thermal residual stresses normally exist in the composites due to the high temperature fabrication/annealing and subsequent cooling process.

While the introduction of rigid inhomogeneity improves the material properties of matrix, their existence induces the thermal residual stresses in composites simultaneously, owing to the mismatch between the coefficients of thermal expansion (CTE) of the matrix and that of the inhomogeneity. Particularly, the combination of the thermal expansion coefficients between the fiber and matrix has significant effect on the behaviors of the matrix cracks triggered by the internal residual stresses. Take continuous fiber reinforced composites for instance. If the CTE of the reinforcements is greater than that of the matrix, the axial tensile stresses induced in the fiber produce an overall net residual compressive stress in the matrix and, as the fibers contract, there is a tendency for them to pull away from the matrix. The stress state is reversed when the CTE of the reinforcements is less than that of the matrix and cracking of the matrix due to the axial tensile stresses occurred in the matrix (Matthews and Rawlings 1993). In reality, thermal stresses and thermal strains can be either beneficial or detrimental to structures depending on the path of temperature changes, boundary conditions, and the CTEs of the fiber and matrix. Therefore, a thorough understanding of the thermal effects of the composites due to the temperature change enables a more accurate prediction of composite behaviors and a better design of the composite structure.

A number of researches aimed at investigating the thermal effect on the overall material behaviors by computing the effective thermal expansion coefficients of a composite. Taya et al. (1985) studied the effects of dispersed microvoids on the thermal expansion behavior of composite material. Their findings indicated that the combination of fiber reinforcements with high elastic modulus and low CTE and disk-shaped voids will remarkably lower the overall CTE of composites. Wakashima et al. (1974) predicted the overall thermal expansion characteristics

of a two-phase composite material containing aligned ellipsoidal inclusions. These works provide the foundation to study the coupling of mechanical properties of composites and thermal effects. Another group of models focused on studying the effect of thermal residual stress on the damage evolution in composites. Research works along this line include Ju and Yanase proposed a micromechanical framework to incorporate the thermal effect by introducing the thermal eigenstrain due to manufacturing defects. Taking advantage of the Eshelby's equivalent principle and Eshelby's solution, the thermal eigenstrain is related to the material properties, far-field strain and the eigenstrain due to the material mismatch. The thermal residual stresses are at equilibrium with their surroundings. However, it will affect the interfacial stress, thus the interfacial damage evolution. Homogenized constitutive equations of composites are then derived systematically in an explicit way so that they can be implemented directly for the structural analysis.

3.5.1 Effective Thermal Expansion Coefficient (CTE)

Consider a two-phase composite reinforced with continuous fibers as shown in Figure 3.15. The matrix phase is linearly elastic with the elastic stiffness tensor denoted by $\mathbf{C}_m$. The fibers are represented by the randomly dispersed yet unidirectionally aligned, linearly elastic cylinders with the elastic stiffness tensor denoted by $\mathbf{C}_f$. The fiber aspect ratio is defined as $\alpha = a_3 / a_1$, where a_3 is the fiber radius and a_1 represents the fiber length. Both the matrix phase and the fiber phase are isotropic with the CTEs designated as $\boldsymbol{\alpha}_m$ and $\boldsymbol{\alpha}_f$, respectively. Let the domains of the composite body and fibers being denoted by D and Ω, respectively. Hence the domain of the matrix phase is represented by $D-\Omega$. The thermal strains of the composite can be treated as a

superposition of a homogeneous thermal deformation $\boldsymbol{\varepsilon}_m^{\Delta T} = \boldsymbol{\alpha}_m \Delta T$ due to the matrix and an additional deformation $\boldsymbol{\varepsilon}_{add}^{\Delta T}$ due to the mismatch between the matrix CTE and overall composite CTE. The local perturbed strain $\boldsymbol{\varepsilon}'$ due to the presence of the fiber inclusion and additional thermal strain $\boldsymbol{\beta}^* = (\boldsymbol{\alpha}_f - \boldsymbol{\alpha}_m)\Delta T$ with respect to the thermal strain of the matrix phase can be related to the total strain as the follows:

$$\begin{cases} \boldsymbol{\varepsilon}^{total} = \boldsymbol{\varepsilon}_{add}^{\Delta T} + \boldsymbol{\varepsilon}' - \boldsymbol{\beta}^* & \text{in } \Omega \\ \boldsymbol{\varepsilon}^{total} = \boldsymbol{\varepsilon}_{add}^{\Delta T} & \text{in } \mathrm{D} - \Omega \end{cases} \tag{3.24}$$

Therefore, the total stresses in both matrix and fiber phases have the form:

$$\begin{cases} \boldsymbol{\sigma}^{total} = \mathbf{C}_f : \left(\boldsymbol{\varepsilon}_{add}^{\Delta T} + \boldsymbol{\varepsilon}' - \boldsymbol{\beta}^* \right) & \text{in } \Omega \\ \boldsymbol{\sigma}^{total} = \mathbf{C}_m : \boldsymbol{\varepsilon}_{add}^{\Delta T} & \text{in } \mathrm{D} - \Omega \end{cases} \tag{3.25}$$

By using the Eshelby's equivalent inclusion principle, the internal stress in Ω can be recast as

$$\boldsymbol{\sigma}^{total} = \mathbf{C}_m : \left(\boldsymbol{\varepsilon}_{add}^{\Delta T} + \boldsymbol{\varepsilon}' - \boldsymbol{\beta}^* - \boldsymbol{\varepsilon}^* \right) \tag{3.26}$$

where

$$\boldsymbol{\varepsilon}' = \mathbf{S} : \left(\boldsymbol{\beta}^* + \boldsymbol{\varepsilon}^* \right) \tag{3.27}$$

Herein, $\mathbf{S}$ is the 4th-rank interior Eshelby tensor depending on the geometry of the inclusion and the Poisson's ratio of the matrix, and $\boldsymbol{\varepsilon}^*$ is the eigenstrain with non-zero values in Ω.

By using the Eshelby's equivalent inclusion method, the internal stress can be expressed as

$$\begin{aligned}\left\langle \boldsymbol{\sigma}^{total} \right\rangle &= (1-f)\cdot \mathbf{C}_m : \boldsymbol{\varepsilon}_{add}^{\Delta T} + f\cdot \mathbf{C}_m : \left(\boldsymbol{\varepsilon}_{add}^{\Delta T} + \boldsymbol{\varepsilon}' - \boldsymbol{\beta}^* - \boldsymbol{\varepsilon}^*\right) \\ &= \mathbf{C}_m : \boldsymbol{\varepsilon}_{add}^{\Delta T} + f\cdot \mathbf{C}_m \bullet (\mathbf{S}-\mathbf{I}) : \left(\boldsymbol{\beta}^* + \boldsymbol{\varepsilon}^*\right) \\ &= 0\end{aligned} \tag{3.28}$$

which leads to the following expression of the additional mismatched deformation as:

$$\boldsymbol{\varepsilon}_{add}^{\Delta T} = f\,(\mathbf{I}-\mathbf{S}) : \left(\boldsymbol{\beta}^* + \boldsymbol{\varepsilon}^*\right) \tag{3.29}$$

The overall disturbance strain in the composite due to thermal effect can be written as

$$\begin{aligned}\boldsymbol{\varepsilon}_{composite}^{\Delta T} = \boldsymbol{\varepsilon}_m^{\Delta T} + \left\langle \boldsymbol{\varepsilon}_{induce}^{\Delta T} \right\rangle &= \boldsymbol{\varepsilon}_m^{\Delta T} + (1-f)\cdot \boldsymbol{\varepsilon}_{add}^{\Delta T} + f\cdot\left(\boldsymbol{\varepsilon}_{add}^{\Delta T} + \boldsymbol{\varepsilon}'\right) \\ &= \boldsymbol{\varepsilon}_m^{\Delta T} + \boldsymbol{\varepsilon}_{add}^{\Delta T} + f\cdot \mathbf{S}\left(\boldsymbol{\beta}^* + \boldsymbol{\varepsilon}^*\right) \\ &= \boldsymbol{\varepsilon}_m^{\Delta T} + f\left(\boldsymbol{\beta}^* + \boldsymbol{\varepsilon}^*\right)\end{aligned} \tag{3.30}$$

Therefore, the overall thermal expansion coefficient of the composite is derived as

$$\boldsymbol{\alpha}_c = \boldsymbol{\varepsilon}_{composite}^{\Delta T} \big/ \Delta T = \boldsymbol{\alpha}_m + f\left(\boldsymbol{\beta}^* + \boldsymbol{\varepsilon}^*\right) \big/ \Delta T \tag{3.31}$$

where the eigenstrain is determined by solving the following equation

$$\mathbf{C}_f : \left[f\,(\mathbf{I}-\mathbf{S}) : \left(\boldsymbol{\beta}^* + \boldsymbol{\varepsilon}^*\right) + (\mathbf{S}-\mathbf{I}) : \boldsymbol{\beta}^* + \mathbf{S} : \boldsymbol{\varepsilon}^* \right] = \mathbf{C}_m : \left[f\,(\mathbf{I}-\mathbf{S}) : \left(\boldsymbol{\beta}^* + \boldsymbol{\varepsilon}^*\right) + (\mathbf{S}-\mathbf{I}) : (\boldsymbol{\beta}^* + \boldsymbol{\varepsilon}^*) \right] \tag{3.32}$$

3.5.2 Effective Moduli of Composites with Microcracks and Thermal Effects

The first-order interaction approximation will be employed to estimate increases in effective compliances of brittle solids with microcracks. Four governing micromechanical ensemble-volume averaged field equations were derived by Ju and Chen (1994a).

$$\bar{\boldsymbol{\sigma}} = \mathbf{C}^o : \left(\bar{\boldsymbol{\varepsilon}} - \sum_{r=1}^{n} \phi_r \bar{\boldsymbol{\varepsilon}}_r^{\,*} \right) \tag{3.33}$$

$$\overline{\boldsymbol{\varepsilon}} = \boldsymbol{\varepsilon}_o + \sum_{r=1}^{n} \phi_r \mathbf{S} : \overline{\boldsymbol{\varepsilon}}_r^{\,*} \tag{3.34}$$

$$\left(-\mathbf{A}_r - \mathbf{s}\right) : \overline{\boldsymbol{\varepsilon}}_r^{\,*} = \boldsymbol{\varepsilon}_o + \overline{\boldsymbol{\varepsilon}}_r'^{p} \tag{3.35}$$

$$\left(1 - \sum_{r=1}^{n} \phi_r\right) \overline{\boldsymbol{\varepsilon}}_r'^{m} + \sum_{r=1}^{n} \phi_r \overline{\boldsymbol{\varepsilon}}_r'^{p} = \sum_{r=1}^{n} \phi_r \left(\mathbf{S} - \mathbf{s}\right) : \overline{\varepsilon}_r^{\,*} = \mathbf{0} \tag{3.36}$$

where $\mathbf{A}_r$ is defined as:

$$\mathbf{A}_r = \left(\mathbf{C}_r - \mathbf{C}_0\right)^{-1} \bullet \mathbf{C}_0 \tag{3.37}$$

If we consider a two-phase composite material with linearly elastic isotropic $\mathbf{C}_0$ and $\mathbf{C}_1$, the effective moduli of it can be derived from the governing equations as the following:

$$\mathbf{C}^* = \mathbf{C}^0 \bullet \left\{ \mathbf{I} + \phi \left[\mathbf{A} + \left(1 - \phi\right) \mathbf{S} \right]^{-1} \right\} \tag{3.38}$$

Unidirectionally aligned penny-shaped microcracks can be regarded as the limiting case of unidirectionally aligned spheroidal voids with the aspect ratio $\rho \to 0$. That is, one can collapse one axis of a spheroidal microvoid to recover a penny-shaped microcrack. In this event, the non-interacting approximation becomes

$$\mathbf{C}^* = \mathbf{C}_0 + \frac{4\pi}{3} n a^3 \mathbf{C}_0 \left[\frac{1}{\rho} \left(\mathbf{S}_1 - \mathbf{I}\right) - \frac{4\pi}{3} n a^3 \mathbf{S}_1 \right]_{\rho \to 0}^{-1} \tag{3.39}$$

If a composite is undergoing a temperature change ΔT, then the total strain $\boldsymbol{\varepsilon}_{total}$ in the composite is the sum of the elastic strain $\boldsymbol{\varepsilon}_{el}$ and the thermal strain $\boldsymbol{\varepsilon}_{th}$. Unlike the elastic strain, the thermal strain $\boldsymbol{\varepsilon}_{th}$ is a stress-free strain. Therefore, if we consider a composite with microcracks under a

given temperature change, the stress-strain relations in the vector form incorporating the thermal effect appear as

$$\boldsymbol{\sigma} = \mathbf{C}^{*} : \boldsymbol{\varepsilon}_{el} - \Delta T \boldsymbol{\alpha}_{c} \tag{3.40}$$

3.5.3 Numerical Results

Let us examine the effective thermal expansion coefficients of the SiC/Al composite and carbon/epoxy composite by the presented model. The thermo-mechanical properties of constituents are given in Table 3.1. Both the effective thermal expansion coefficients in the longitudinal direction and transverse direction are plotted in Figure 3.17 and Figure 3.18 for the SiC/Al and Carbon/Epoxy composites, respectively. Various aspect ratios are adopted herein with the values of 1.5, 4 and 25 for a SiC/Al composite. It is obvious that the effective thermal expansion coefficients in the transverse direction are larger those in the longitudinal direction. The bigger the aspect ratio, the greater the difference of the effective thermal expansion coefficients is in two directions. Figure 3.18 shows the effective thermal coefficients of the Carbon/Epoxy with fiber aspect ratios of 10, 20 and 100. The larger effective transverse thermal expansion coefficients over those in the longitudinal direction are observed again for the Carbon/Epoxy composite. However, the difference between the overall thermal expansion coefficients of the Carbon/Epoxy in the transverse and longitudinal directions tends to be much larger than that of the SiC/Al composite. This is because of the matrix and fibers in SiC/Al share the same thermal expansion coefficients in both the transverse and longitudinal directions while the fibers have much larger thermal expansion coefficients in the transverse direction than that of the longitudinal direction in Carbon/Epoxy composite. Comparing the results of α_T in Figure

3.17 and those in Figure 3.18, α_T for SiC/Al increases monotonically as f increases, whereas that for Carbon/Epoxy has a peal at f around 0.1.

The constitutive relations are plotted in Figure 3.19 and Figure 3.20 for pure matrix material with penny-shaped microcracks with and without cohesive effect under different temperature changes. Figure 3.21 shows the stress-strain relation for the fiber reinforced composite with cohesive microcracks under different temperature changes. Obviously, larger temperature changes will induce the larger thermal strain in the structural component, which further leads to the larger deformation of the composite.

3.6 Conclusion

In this Chapter, a micromechanical damage mechanics framework is proposed to predict the overall elastic damage behaviors of the fibrous composites with the evolution of cohesive microcracks. The concept of cohesion effects is introduced in the proposed model by considering the energy release contribution to the material damage process is estimated in a representative volume element under the macro hydrostatic stress state. A two-step homogenization is implemented to simulate the damage behavior of fibrous composites with the presence of microcrack evolution. From the numerical simulations, the resulting stress-strain relations exhibit nonlinear elastic-damage behaviors, which are computationally governed by the stress-state or strain-state (algorithm) of progressively damaged composite materials. Subsequently, the proposed micromechanical formulation is further implemented in the finite element analysis software ABAQUS with UMAT subroutine. The stress-strain relations and the damage contour

plots are systematically presented to illustrate the predictive capability of proposed probabilistic micromechanical formulation. Moreover, the effective thermal expansion coefficients were derived for the fiber-reinforced composites. Both the constant aspect ratio and the variable aspect ratio of the fibers are taken into consideration in determining the effective thermal expansion coefficients. The effect of variable fiber aspect ratio on the thermo-mechanical properties of a fibrous composite was investigated in the numerical examples as well. With the existence of the thermal effect, the overall effective moduli of a two-phase composite with penny-shaped microcracks were obtained under our micromechanical framework.

Table 3.1 Material properties of composite materials used in the numerical examples.

	Al	SiC	Epoxy	Carbon
Young's modulus (GPA)	68.3	490	3.5	C_{11} = 28.25 C_{33} = 234.23
Poisson's Ratio	0.33	0.17	0.42	C_{12} = 12.13 C_{13} = 12.14 C_{44} = 10.0
CTE Longitudinal (x 10^{-6})	23.6	4.3	80	-1.5
CTE Transverse (x 10^{-6})	23.6	4.3	80	27.0

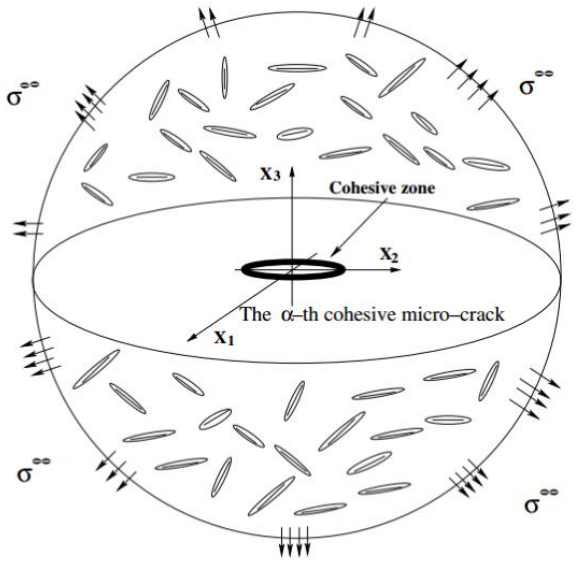

Figure 3.1 Isotropic distribution of microcracks with random orientations.

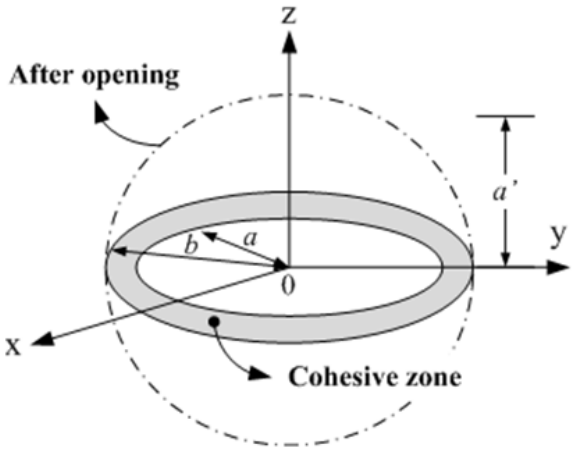

Figure 3.2 Schematic of a penny-shaped microcrack with the cohesive crack zone.

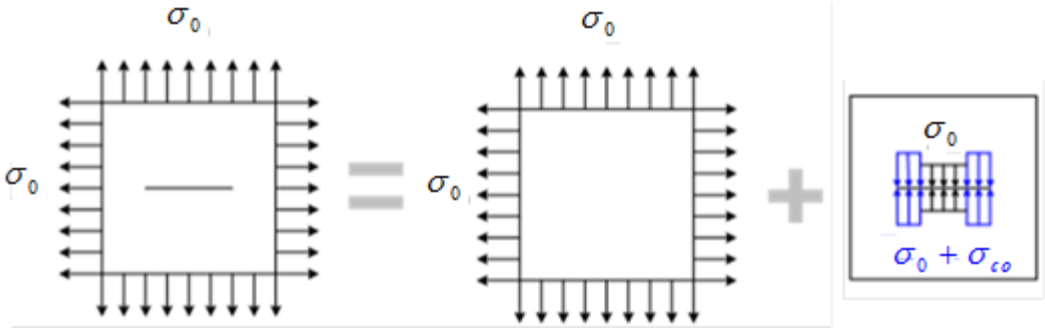

Figure 3.3 Illustration of the superposition of the cohesive microcrack problem.

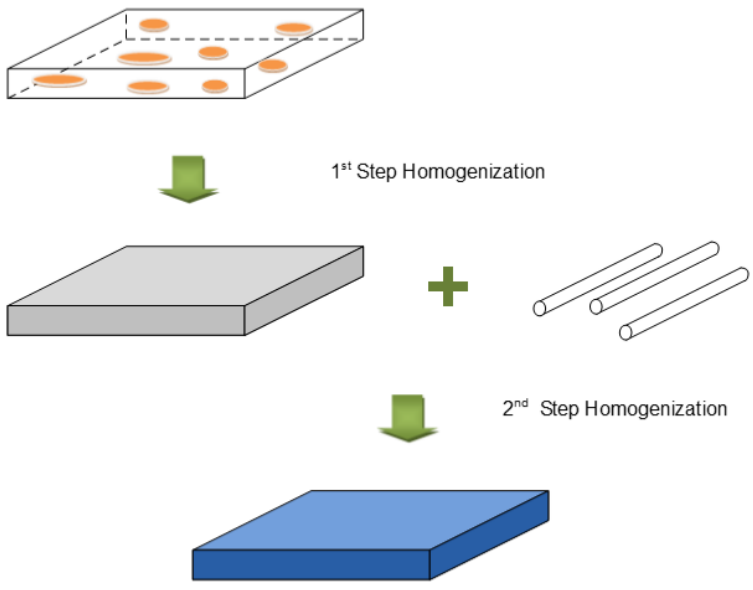

Figure 3.4 Schematic of the two-step homogenization for fiber-reinforced composites with matrix micro-cracking.

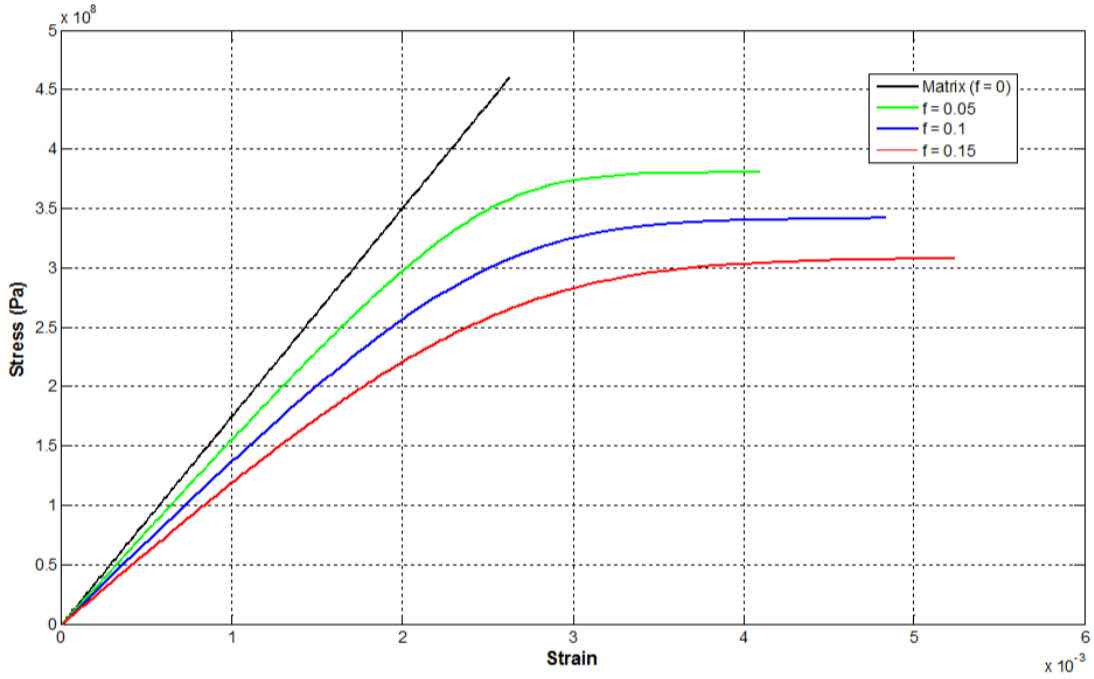

Figure 3.5 Predicted stress-strain relations of matrix with various amounts of initial cohesive microcracks.

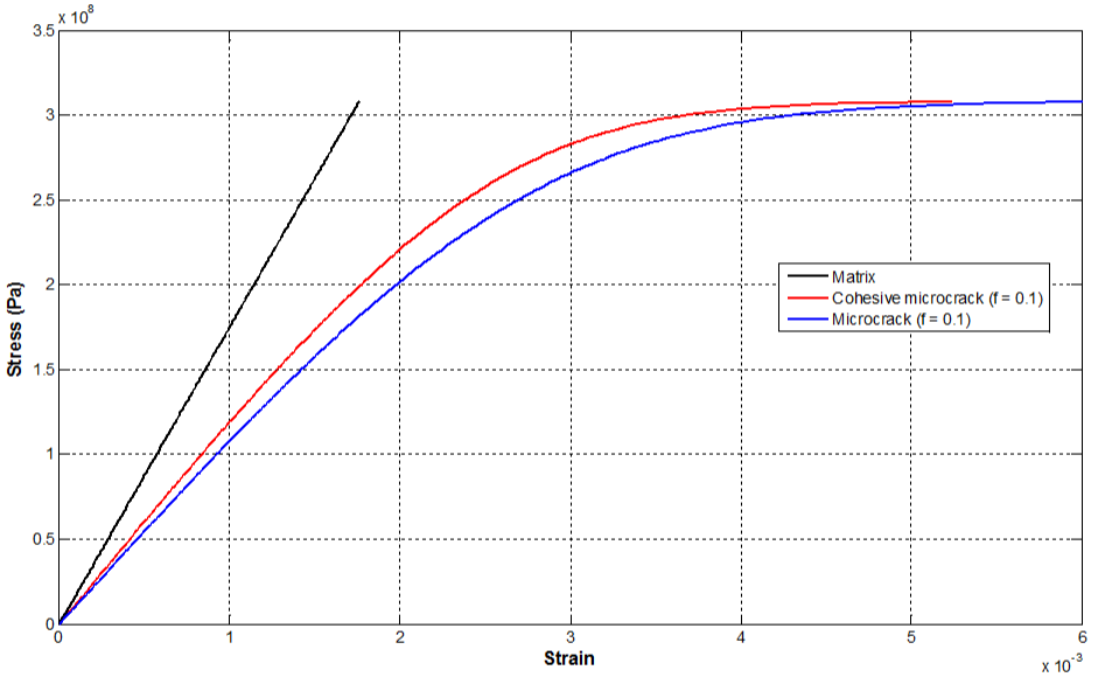

Figure 3.6 Predicted stress-strain relations of matrix with and without consideration of cohesive microcracks.

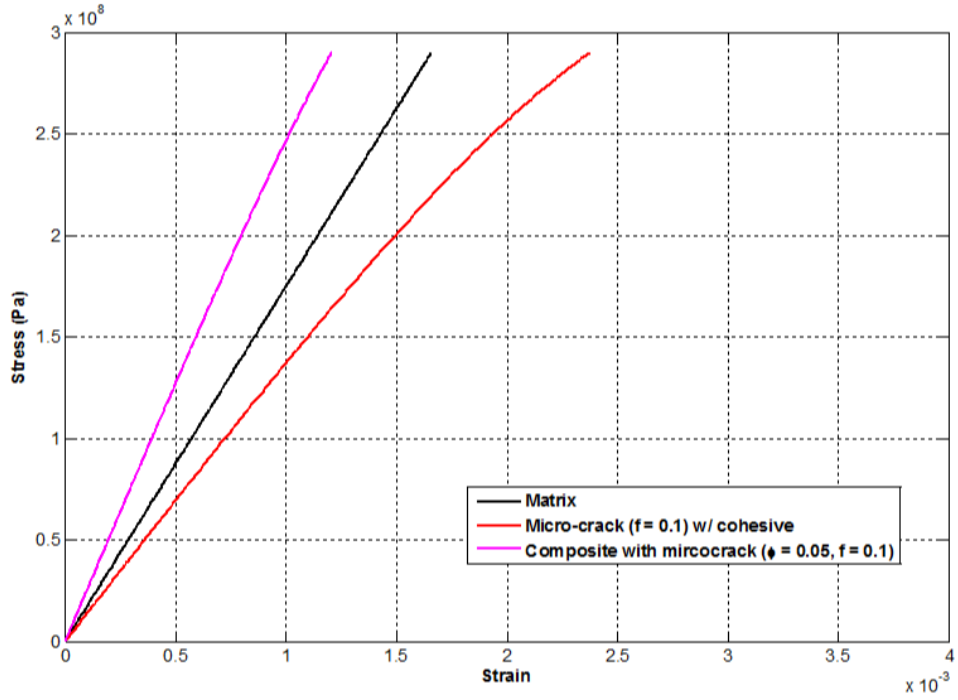

Figure 3.7 Predicted stress-strain relations of fiber-reinforced composites.

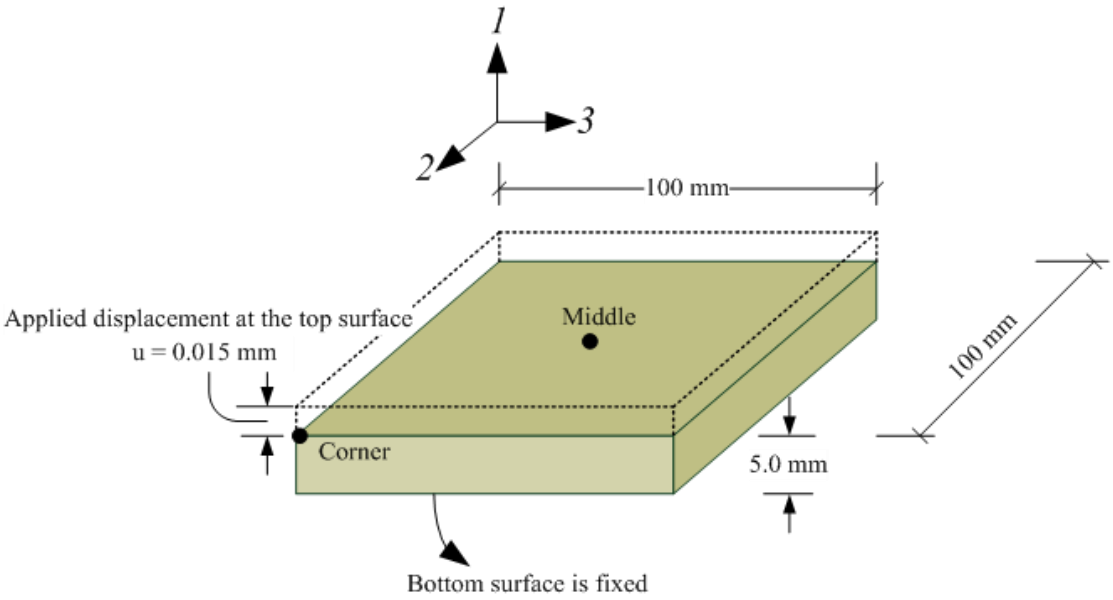

Figure 3.8 Schematic of the dimension of the laminated composite and its boundary conditions.

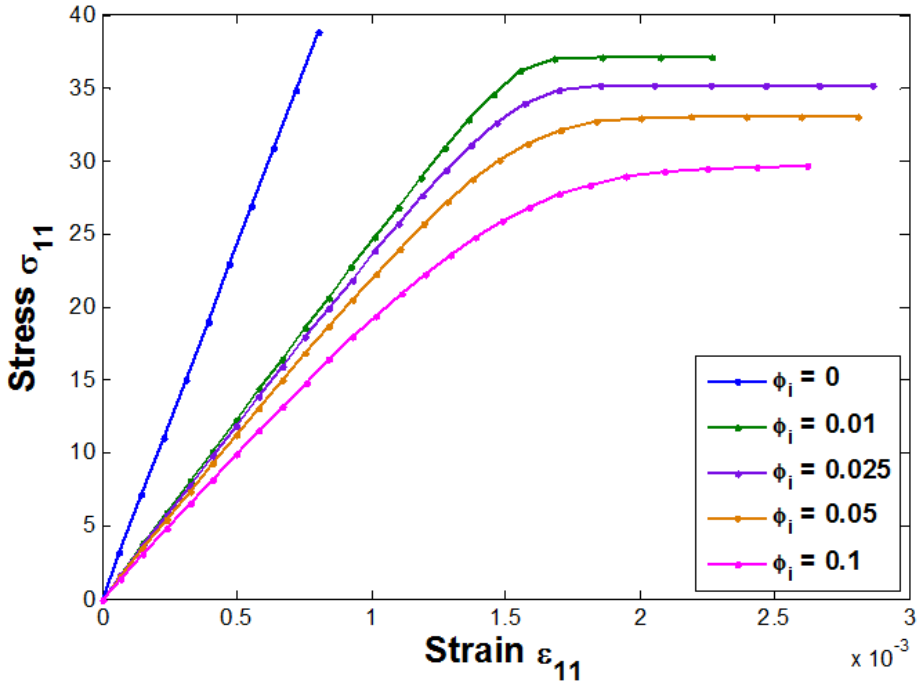

Figure 3.9 Overall stress-strain behaviors of the laminated composite with various amounts of initial cohesive microcracks.

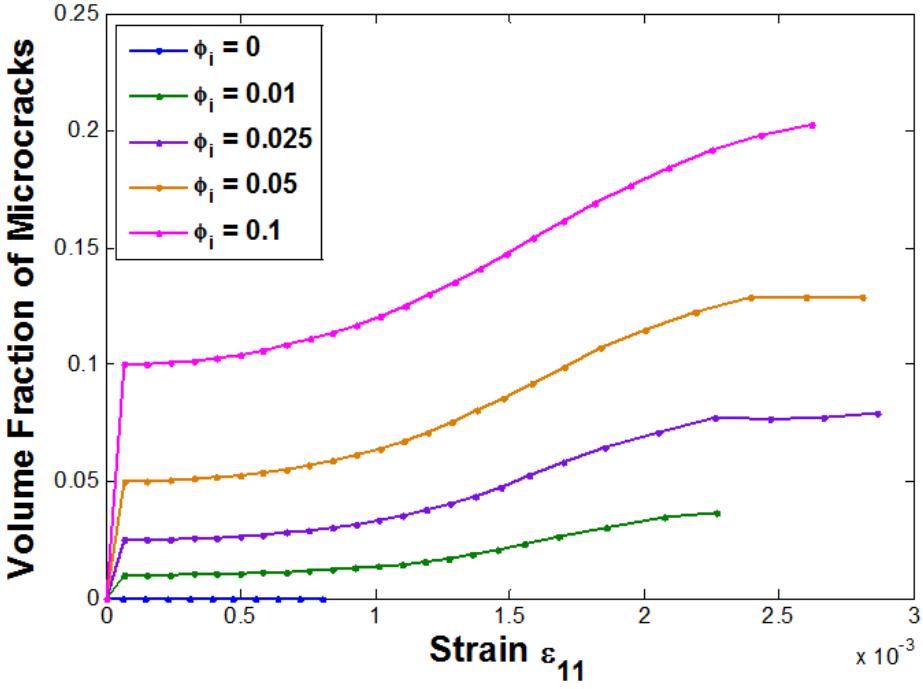

Figure 3.10 Overall microcrack volume fraction evolution with various amounts of initial cohesive microcracks.

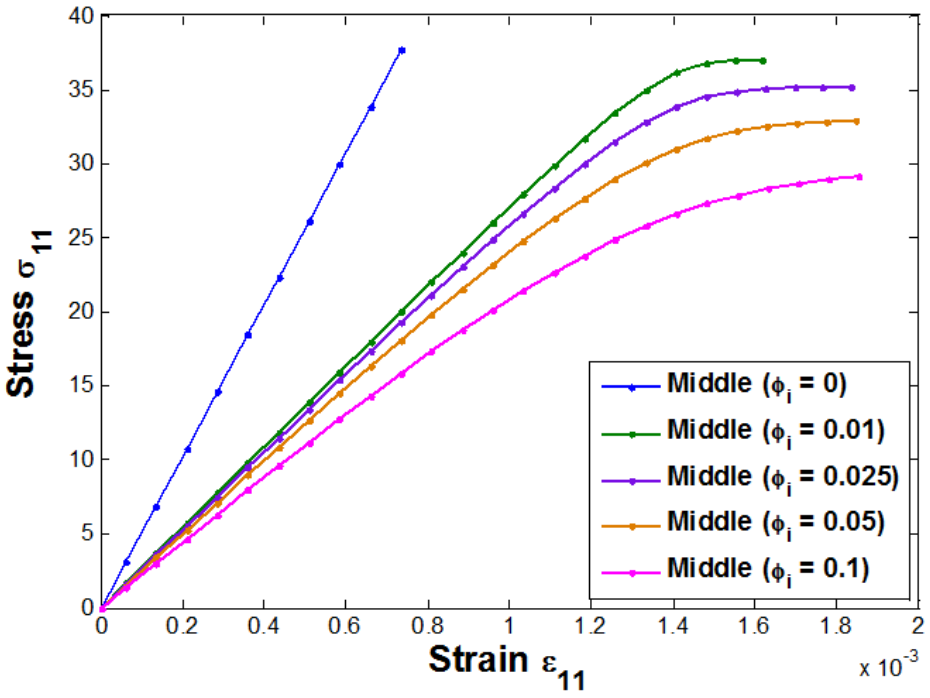

Figure 3.11 Predicted stress-strain relation at the middle point.

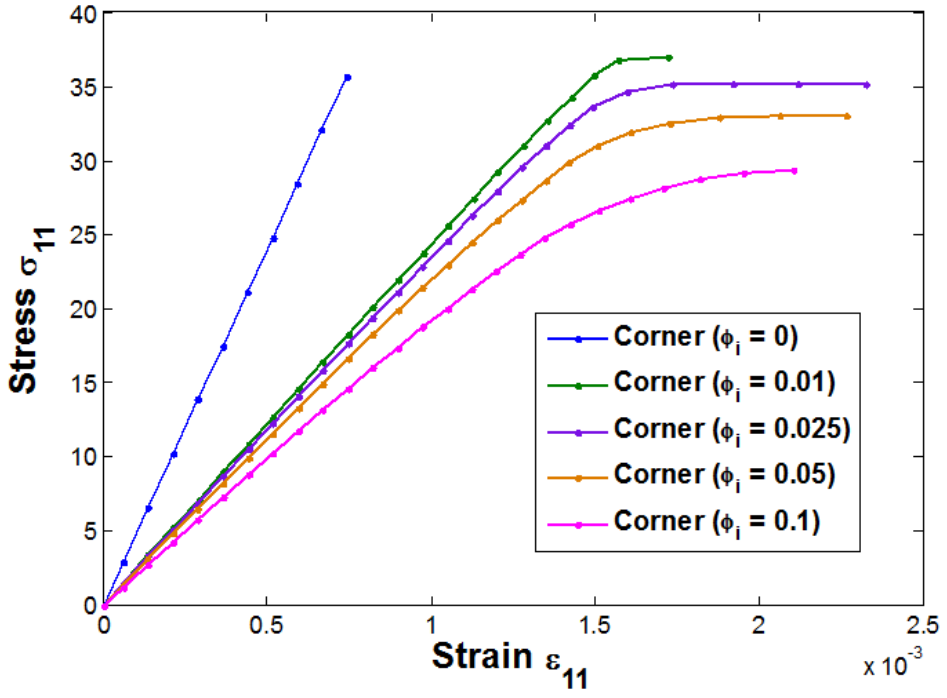

Figure 3.12 Predicted stress-strain relation at the corner point.

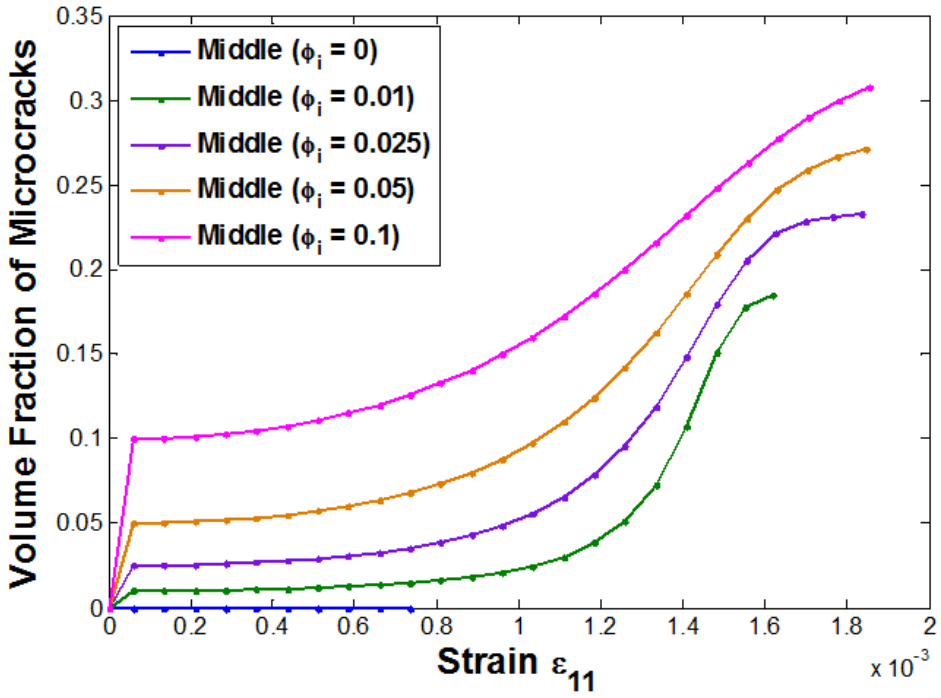

Figure 3.13 Predicted microcrack volume fraction evolution at the middle point.

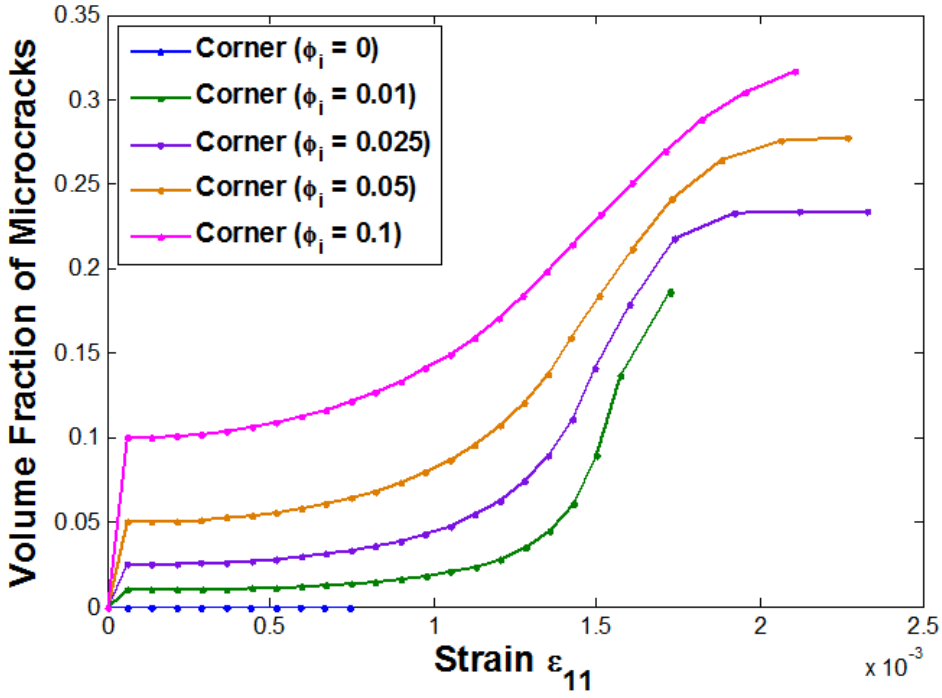

Figure 3.14 Predicted microcrack volume fraction evolution at the corner point.

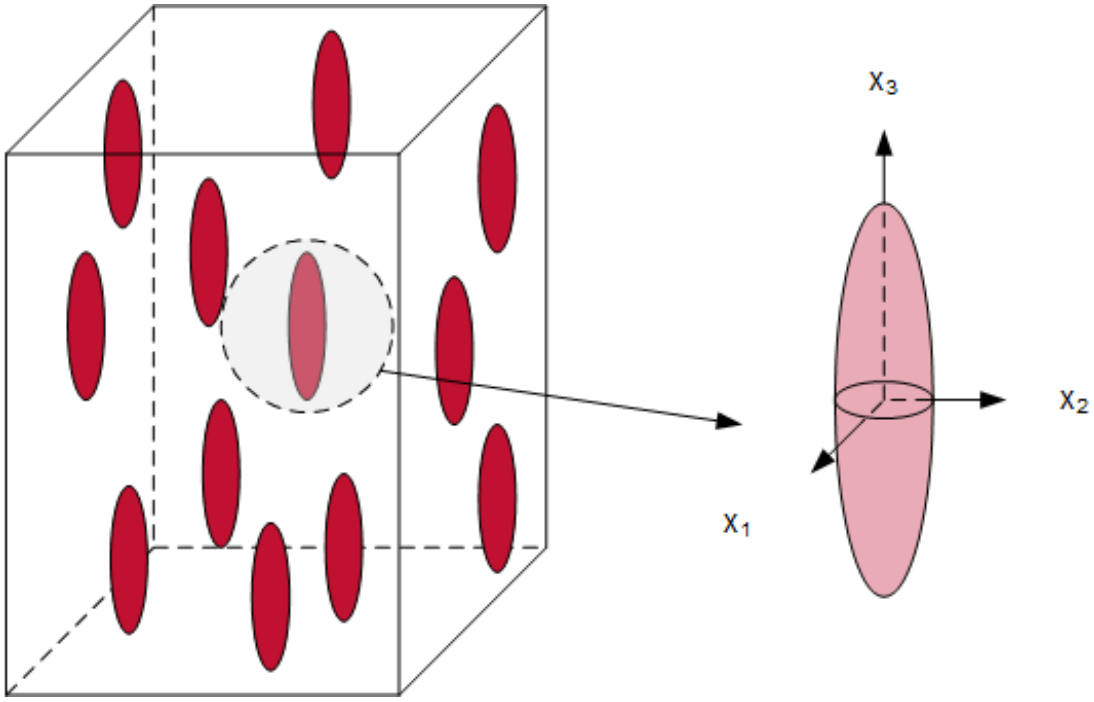

Figure 3.15 Schematic of fibers with constant aspect ratio embedded in the matrix.

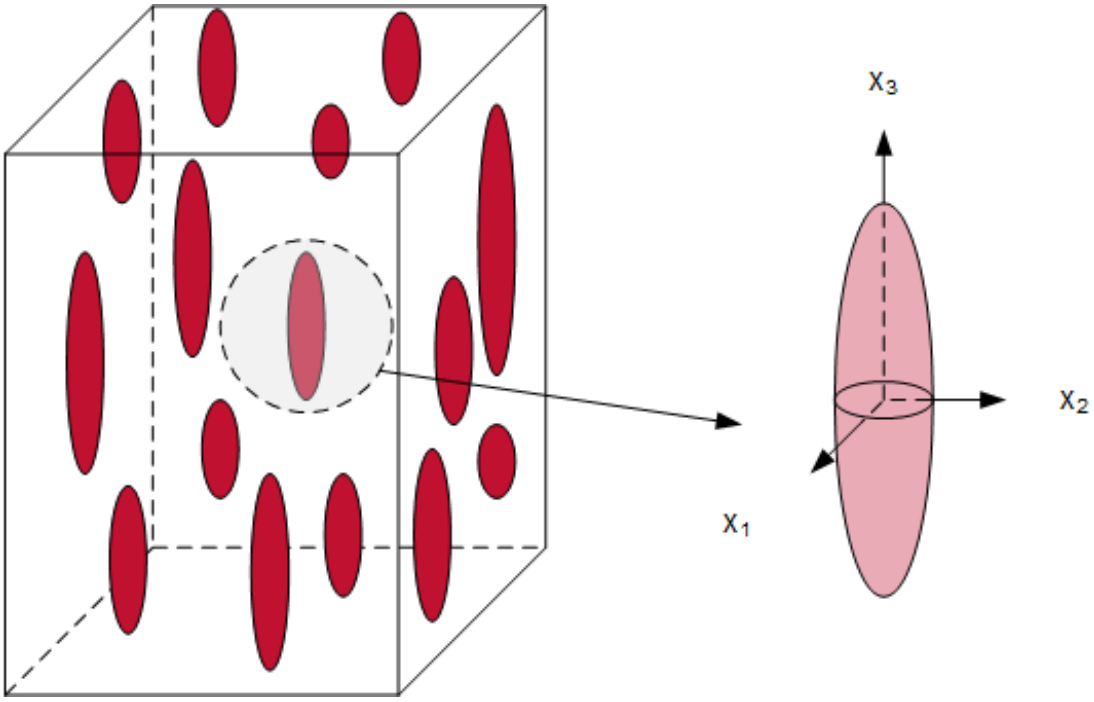

Figure 3.16 Schematic of fibers with variable aspect ratio embedded in the matrix.

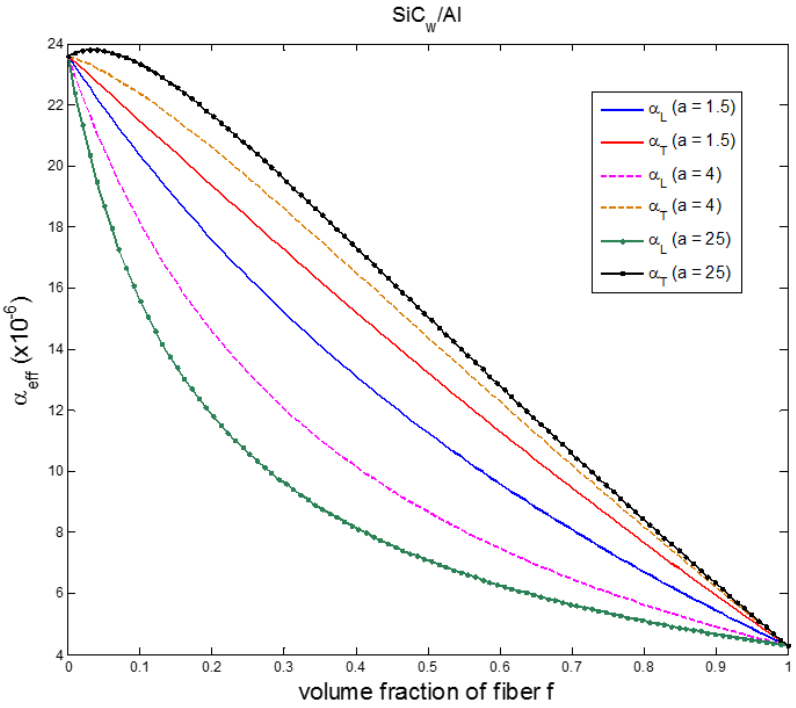

Figure 3.17 Effective CTE of SiC/Al composites with different fiber aspect ratios.

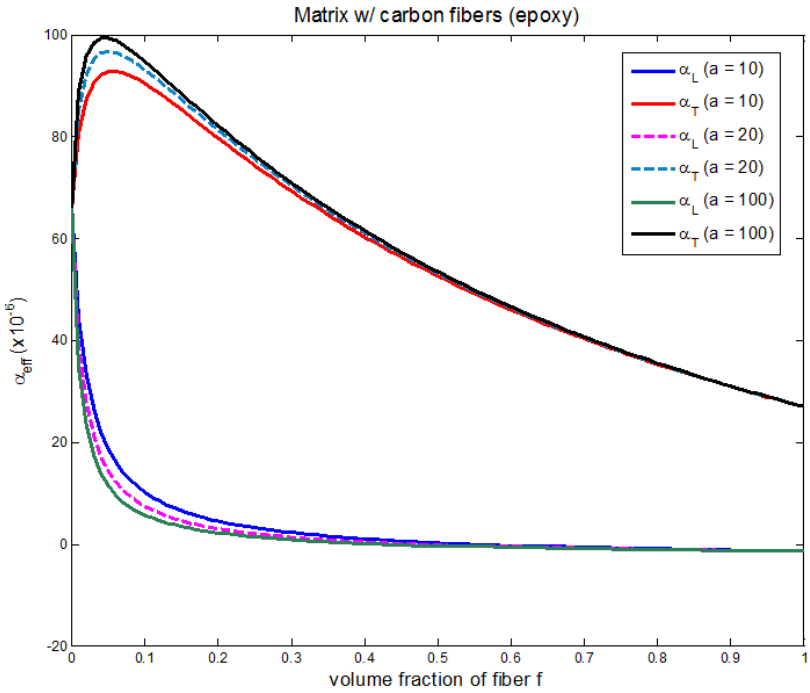

Figure 3.18 Effective CTE of carbon/epoxy composites with different fiber aspect ratios.

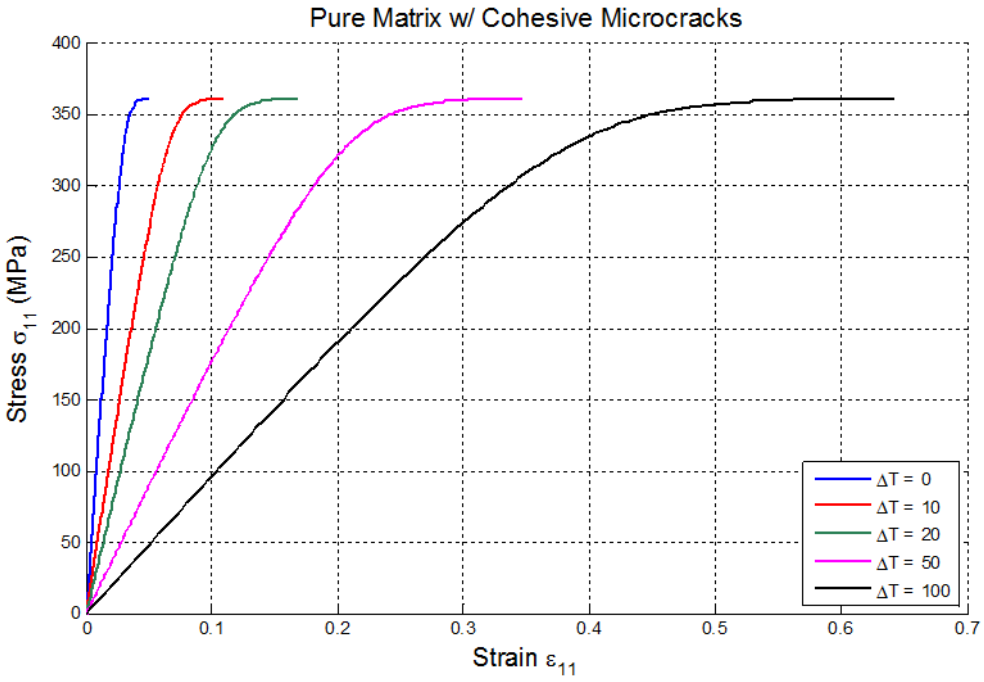

Figure 3.19 Predicted stress-strain relations of the matrix material with cohesive penny-shaped microcracks under different temperature changes.

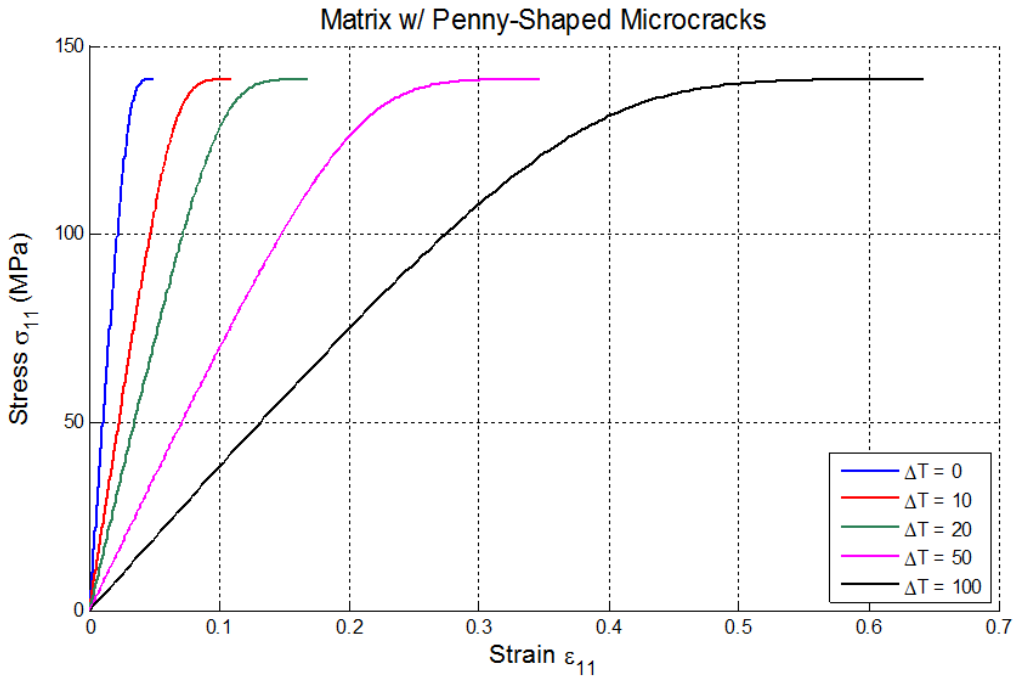

Figure 3.20 Predicted stress-strain relations of the matrix material without cohesive penny-shaped microcracks under different temperature changes.

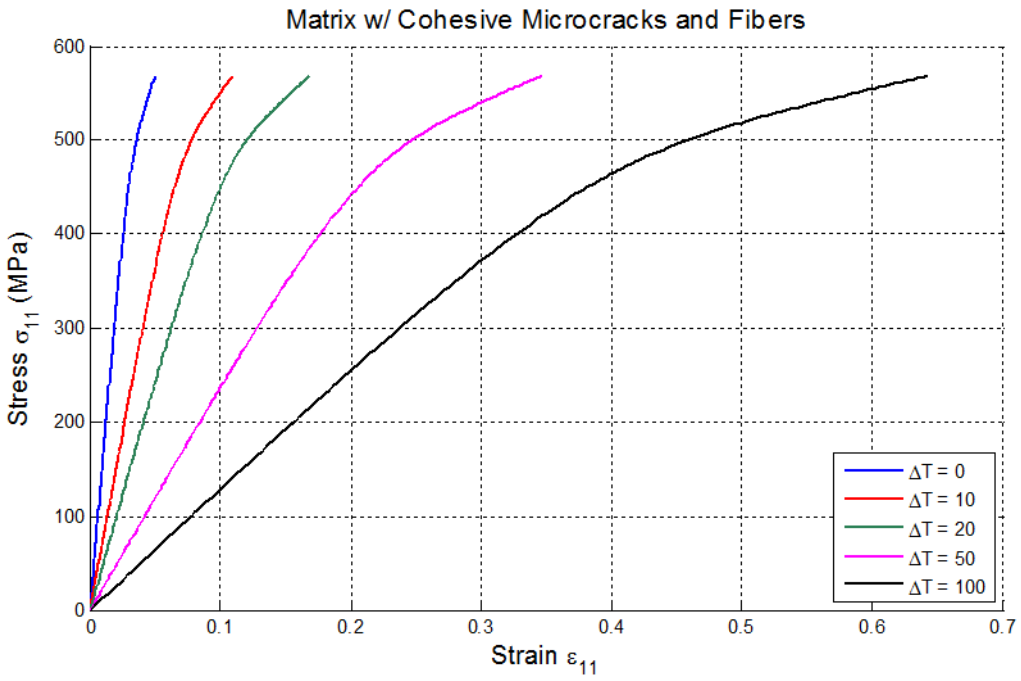

Figure 3.21 Predicted stress-strain relations of the composite material with cohesive penny-shaped microcracks under different temperature changes.

CHAPTER 4 EFFECTS OF FIBER BREAKAGE ON FIBER-DOMINATED DAMAGE BEHAVIOR OF CONTINUOUS FIBER REINFORCED COMPOSITES

4.1 Introduction

Continuous fiber reinforced metal matrix composites (MMCs) have been applied widely as load-bearing materials in various industries due to their superior mechanical properties. Silicon carbide, silicon nitride, carbon, boron, and glass are the commonly-used fiber materials. Ductile metals or alloys with high failure strength, such as aluminum, steel, and titanium, are used extensively as the matrix material for the sake of composites to have a high strength-to-weight ratio and a high stiffness-to-weight ratio. In general, the failure strength of fibers is much lower than that of the matrix in a MMC. If the interfacial bonding strength is high, fiber breakage may occurs before other damage modes while the tensile loading is applied in the fiber direction. The failure of several fibers in the same plane may trigger the failure of the composite before the global onset of plastic deformation in the composite (Jeng et al., 1991). This damage mechanism is termed as the fiber-dominated damage is some literature.

The single-fiber composite (SFC) fragmentation test is an effective means in determining the fiber strength, interface bonding strength, and interface toughness in a composite. During a fragmentation test, a SFC specimen is loaded in tension until the number of fiber breaks reaches saturation. The material properties can be quantified from the measurement of the microscopic damage and the fiber fragmentation at each strain level. Most analytical models of SFC

fragmentation tests assume a constant shear stress for simplicity. Regions around a fiber break are shielded from higher loads by the shearing and the shielded region grows with the applied load until the shielded regions around all the breaks encompass the entire fiber length. Curtin and his coworkers (1998) conducted a series of investigations on SFC fragmentation tests. They proposed several models to calculate the evolving fragment distribution and applied the final saturated fragment distribution data to estimate the interfacial shear stress. Some of the models also evaluated the fragmentation process in the SFC to estimate the fiber strength distribution.

Although the SFC test is instructive in studying the fiber breakage mechanism, the fiber breakage evolution process in multi-fiber composites is far more complicated than that of a SFC. The sequence of the damage modes in composites depends on the material properties of constitutes, the properties of the interface reaction layer, the volume fraction of the reinforcements and the interfacial bonding conditions. Generally, for fiber reinforced composites with brittle matrix materials, the first noticeable damage mode upon tensile loading in the fiber direction is the matrix cracks perpendicular to the loading direction. As the applied load increases, more transverse matrix cracks initiate, accompanied by other damage events such as the fiber/matrix interfacial debonding and the fiber breakage. On the other hand, if the matrix material is ductile while the fibers are relatively brittle, the fiber breakage tends to initiate as the first damage mode (Curtin 1998). As fiber breakages accumulate, other damage modes such as the matrix cracks and the interfacial debonding occur subsequently and further reduce the strength of the composite until the composite reaches its failure criteria. In this sense, the fiber breakage involves in the failure process of a composite at different stages depending on the material properties of material phases and their interfacial bonding conditions.

A number of models have been proposed to predict the strength and the stiffness of continuous fiber-reinforced composites with fiber breakage under various loading conditions. Wang and his co-workers (2008) investigated the effect of multiple cracks on a SFC by the integral equation technique. Steif (1984) studied the stiffness reduction due to fiber breakage by simulating a dilute concentration of broken fibers which were partially debonded from the matrix. Liao and his coworkers (2000) developed a tensile strength model for a unidirectional fiber-reinforced brittle matrix composite, in which a statistical analysis of fiber fracture was performed. Oguni and Ravichandran (2000) worked on an energy-based model to predict the longitudinal splitting in unidirectional fiber-reinforced composites under compression loading condition. Krasnikovs and Megnis (2005) proposed a stochastic fiber break clusters accumulation model for polymer matrix unidirectional fiber-reinforced composites subjected to tension-tension fatigue loading. Most analytical models are based on the linear elasticity and the linear elastic fracture mechanics. On the other hand, most computational models are based on the periodic unit cell models, which have the advantage of high accuracy of solutions by considering realistic geometry of reinforcements and local interactions among reinforcements with the expense of intensive computational cost. Moreover, numerical models do not result in explicit forms for the overall constitutive relations. This makes them difficult to implement in stress analyses at the macroscopic level.

In this Chapter, we focus on studying i) the fiber breakage mechanism in a single-fiber composite; ii) the fiber-dominated damage in a unidirectional reinforced multi-fiber composite under the rigorous micromechanical framework.

4.2 Double-Inclusion Model

A double-inclusion model consists of an ellipsoidal inclusion which contains an ellipsoidal heterogeneity. The double-inclusion is embedded in an infinitely extended homogeneous domain. Comparing to a single-inclusion problem, the local field variables in the double-inclusion are difficult to determine, even for uniform far-field boundary conditions. However, the average field quantities of the inclusion can be calculated analytically and explicitly. The following notations are adopted for this study as illustrated in Figure 4.1: the domains of the outer inclusion, the inner inclusion, and the infinite solid are denoted by R, Ω, and B, respectively; region $R-\Omega$ is denoted by Γ. It is assumed that the domains of Ω, Γ, and $B-R$ are uniform with elastic tensors $\mathbf{C}^{(1)}$, $\mathbf{C}^{(2)}$, and $\mathbf{C}$, respectively. The corresponding constitutive relations can be established thereafter as

$$\boldsymbol{\sigma}(\mathbf{x}) = \begin{cases} \mathbf{C}^{(1)} : \boldsymbol{\varepsilon}(\mathbf{x}), & \text{for } \mathbf{x} \text{ in } \Omega \\ \mathbf{C}^{(2)} : \boldsymbol{\varepsilon}(\mathbf{x}), & \text{for } \mathbf{x} \text{ in } \Gamma \\ \mathbf{C} : \boldsymbol{\varepsilon}(\mathbf{x}), & \text{for } \mathbf{x} \text{ in } B-R \end{cases} \tag{4.1}$$

Suppose that the infinite solid B is subjected to a far-field strain field $\boldsymbol{\varepsilon}^{\infty}$ with an accompanied far-field stress field $\boldsymbol{\sigma}^{\infty} = \mathbf{C} : \boldsymbol{\varepsilon}^{\infty}$. In order to analyze this double-inclusion problem, we consider an auxiliary problem as shown in Figure 4.2. The notations of R^*, Ω^*, Γ^* and B^* denotes the counterparts of R, Ω, Γ and B in the original problem, respectively. Eigenstrains, $\boldsymbol{\varepsilon}^*(x)$, are distributed in the region R^*. Based on the Eshelby's inclusion theory (Eshelby 1957, 1961), the eigenstrain field $\boldsymbol{\varepsilon}^*(x)$ produces the perturbed strains and stresses as follows:

$$\boldsymbol{\varepsilon}'(\mathbf{x};\boldsymbol{\varepsilon}^*) = \int_{R^*} \mathbf{G}(\mathbf{x}-\mathbf{y}) : \boldsymbol{\varepsilon}^*(\mathbf{y})\, dV_y \tag{4.2}$$

$$\boldsymbol{\sigma}'\left(\mathbf{x};\boldsymbol{\varepsilon}^*\right)=\mathbf{C}:\left[\boldsymbol{\varepsilon}'\left(\mathbf{x};\boldsymbol{\varepsilon}^*\right)-\boldsymbol{\varepsilon}^*\left(\mathbf{x}\right)\right] \tag{4.3}$$

where $\boldsymbol{\varepsilon}'\left(\mathbf{x};\boldsymbol{\varepsilon}^*\right)$ and $\boldsymbol{\sigma}'\left(\mathbf{x};\boldsymbol{\varepsilon}^*\right)$ are the perturbed strains and stresses at location **x,** respectively; and **G** is the fourth-order tensor determined by the Green's function associated with the equivalent infinite solid B^* (Mura 1987). Utilization of the Eshelby's equivalent inclusion principle, the following consistency condition is reached

$$\boldsymbol{\sigma}^\infty+\boldsymbol{\sigma}'\left(\mathbf{x};\boldsymbol{\varepsilon}^*\right)=\mathbf{C}:\left[\boldsymbol{\varepsilon}^\infty+\boldsymbol{\varepsilon}'\left(\mathbf{x};\boldsymbol{\varepsilon}^*\right)-\boldsymbol{\varepsilon}^*\left(\mathbf{x}\right)\right]=\begin{cases}\mathbf{C}^{(1)}:\left[\boldsymbol{\varepsilon}^\infty+\boldsymbol{\varepsilon}'\left(\mathbf{x};\boldsymbol{\varepsilon}^*\right)\right], & \text{for } \mathbf{x} \text{ in } \Omega^*\\ \mathbf{C}^{(2)}:\left[\boldsymbol{\varepsilon}^\infty+\boldsymbol{\varepsilon}'\left(\mathbf{x};\boldsymbol{\varepsilon}^*\right)\right], & \text{for } \mathbf{x} \text{ in } \Gamma^*\end{cases} \tag{4.4}$$

Consistency conditions shown in Equation 1.4 can be solved numerically, and the local response of the double inclusion problem can then be analyzed. However, the relative position and orientation of the inclusion Ω must be specifically defined in the numerical analysis. In addition, average field quantities can be estimated analytically and explicitly, yielding the close-form expressions for the overall moduli of the double-inclusion problem. With the aid of the equivalent homogeneous inclusion method (Hori and Nemat-Nasser, 1993), the ensemble-averaged eigenstrains over Ω^* and Γ^* can be determined as follows:

$$\begin{aligned}\boldsymbol{\varepsilon}^{*(\Omega)}=-\Bigg\{&\mathbf{S}^{(\Omega)}+\left[\left(\mathbf{C}^{(1)}-\mathbf{C}\right)^{-1}\bullet\mathbf{C}+\left(\mathbf{S}^{(R)}-\mathbf{S}^{(\Omega)}\right)\right]\bullet\left[\mathbf{S}^{(\Omega)}-\frac{f}{1-f}\left(\mathbf{S}^{(R)}-\mathbf{S}^{(\Omega)}\right)+\left(\mathbf{C}^{(2)}-\mathbf{C}\right)^{-1}\bullet\mathbf{C}\right]^{-1}\\&\bullet\left[\mathbf{S}^{(\Omega)}-\frac{f}{1-f}\left(\mathbf{S}^{(R)}-\mathbf{S}^{(\Omega)}\right)+\left(\mathbf{C}^{(1)}-\mathbf{C}\right)^{-1}\bullet\mathbf{C}\right]^{-1}\Bigg\}:\boldsymbol{\varepsilon}^\infty\end{aligned} \tag{4.5}$$

$$\begin{aligned}\boldsymbol{\varepsilon}^{*(\Gamma)}=-\Bigg\{&\left(\mathbf{S}^{(R)}-\mathbf{S}^{(\Omega)}\right)+\left[\mathbf{S}^{(\Omega)}+\left(\mathbf{C}^{(1)}-\mathbf{C}\right)^{-1}\bullet\mathbf{C}\right]\bullet\left[\mathbf{S}^{(\Omega)}-\frac{f}{1-f}\left(\mathbf{S}^{(R)}-\mathbf{S}^{(\Gamma)}\right)+\left(\mathbf{C}^{(1)}-\mathbf{C}\right)^{-1}\bullet\mathbf{C}\right]^{-1}\\&\bullet\left[\mathbf{S}^{(\Omega)}-\frac{f}{1-f}\left(\mathbf{S}^{(R)}-\mathbf{S}^{(\Omega)}\right)+\left(\mathbf{C}^{(2)}-\mathbf{C}\right)^{-1}\bullet\mathbf{C}\right]^{-1}\Bigg\}:\boldsymbol{\varepsilon}^\infty\end{aligned} \tag{4.6}$$

where $\mathbf{S}^{(R)}$ and $\mathbf{S}^{(\Omega)}$ are the Eshelby's tensors for ellipsoids R^* and Ω^*, respectively; $f = \Omega^* / R^*$ is the volume fraction of the inner inclusion Ω^*. The rest of the average field relations for the double inclusion can be determined by

$$\langle \boldsymbol{\varepsilon} \rangle_{\Omega} = \left(\mathbf{I} + \Delta\mathbf{S} \bullet \boldsymbol{\Phi}^{\Gamma} + \mathbf{S}^{\Omega} \bullet \boldsymbol{\Phi}^{\Omega} \right) : \boldsymbol{\varepsilon}^{\infty} \tag{4.7}$$

$$\langle \boldsymbol{\sigma} \rangle_{\Omega} = \left\{ \mathbf{C} \bullet \left[\mathbf{I} + \Delta\mathbf{S} \bullet \boldsymbol{\Phi}^{\Gamma} + \left(\mathbf{S}^{\Omega} - \mathbf{I} \right) \bullet \boldsymbol{\Phi}^{\Omega} \right] \right\} : \boldsymbol{\varepsilon}^{\infty} \tag{4.8}$$

$$\langle \boldsymbol{\varepsilon} \rangle_{\Gamma} = \left[\mathbf{I} + \left(\mathbf{S}^{R} + \frac{f}{1-f} \Delta\mathbf{S} \right) \bullet \boldsymbol{\Phi}^{\Gamma} + \frac{f}{1-f} \Delta\mathbf{S} \bullet \boldsymbol{\Phi}^{\Omega} \right] : \boldsymbol{\varepsilon}^{\infty} \tag{4.9}$$

$$\langle \boldsymbol{\sigma} \rangle_{\Gamma} = \left\{ \mathbf{C} \bullet \left[\mathbf{I} + \left(\mathbf{S}^{R} - \mathbf{I} - \frac{f}{1-f} \Delta\mathbf{S} \right) \bullet \boldsymbol{\Phi}^{\Gamma} + \frac{f}{1-f} \Delta\mathbf{S} \bullet \boldsymbol{\Phi}^{\Omega} \right] \right\} : \boldsymbol{\varepsilon}^{\infty} \tag{4.10}$$

$$\langle \boldsymbol{\varepsilon} \rangle_{R} = \left(\mathbf{I} + \mathbf{S}^{R} \bullet \boldsymbol{\Phi}^{R} \right) : \boldsymbol{\varepsilon}^{\infty} \tag{4.11}$$

$$\langle \boldsymbol{\sigma} \rangle_{R} = \left\{ \mathbf{C} \bullet \left[\mathbf{I} + \left(\mathbf{S}^{R} - \mathbf{I} \right) \bullet \boldsymbol{\Phi}^{R} \right] \right\} : \boldsymbol{\varepsilon}^{\infty} \tag{4.12}$$

where $\Delta\mathbf{S} = \mathbf{S}^{(R)} - \mathbf{S}^{(\Omega)}$, $\mathbf{I}$ is the fourth-rank identity tensor, and

$$\boldsymbol{\Phi}^{\Gamma} = -\left[\left(\mathbf{S}^{(\Omega)} + \mathbf{A}^{(1)} \right) + \Delta\mathbf{S} \bullet \left(\mathbf{S}^{(\Omega)} - \frac{f}{1-f} \Delta\mathbf{S} + \mathbf{A}^{(2)} \right)^{-1} \bullet \left(\mathbf{S}^{(\Omega)} - \frac{f}{1-f} \Delta\mathbf{S} + \mathbf{A}^{(1)} \right)^{-1} \right] \tag{4.13}$$

$$\boldsymbol{\Phi}^{\Omega} = -\left[\Delta\mathbf{S} + \left(\mathbf{S}^{(\Omega)} + \mathbf{A}^{(1)} \right) \bullet \left(\mathbf{S}^{(\Omega)} - \frac{f}{1-f} \Delta\mathbf{S} + \mathbf{A}^{(1)} \right)^{-1} \bullet \left(\mathbf{S}^{(\Omega)} - \frac{f}{1-f} \Delta\mathbf{S} + \mathbf{A}^{(2)} \right)^{-1} \right] \tag{4.14}$$

$$\boldsymbol{\Phi}^{R} = f \cdot \boldsymbol{\Phi}^{\Omega} + (1-f) \cdot \boldsymbol{\Phi}^{\Gamma} \tag{4.15}$$

Herein, we adopt the following expressions

$$\mathbf{A}^{(1)} = \left(\mathbf{C}^{(1)} - \mathbf{C} \right)^{-1} \bullet \mathbf{C} \tag{4.16}$$

$$\mathbf{A}^{(2)} = \left(\mathbf{C}^{(2)} - \mathbf{C}\right)^{-1} \bullet \mathbf{C} \tag{4.17}$$

4.3 Characterization of Fiber Breakage in a Single-Fiber Composite

Consider a single-fiber composite under an external tensile loading in the longitudinal direction as illustrated in Figure 4.3. The fiber phase is assumed to be isotropic and elastic with elasticity modulus of $\mathbf{C}^{(1)}$. It is embedded in an isotropic and elastic matrix material with a elasticity tensor of $\mathbf{C}^{(0)}$. A penny-shaped microcrack model is adopted to represent a breakage in the fiber. Following the notations defined in the previous section, the domains of the fiber breakage, the intact fiber phase, and the matrix are denoted by R, Ω, and B, respectively, as shown in Figure 4.4. It is assumed that Ω, Γ and $B-R$ possess uniform elastic properties of $\mathbf{C}^{(2)}$, $\mathbf{C}^{(1)}$ and $\mathbf{C}^{(0)}$, respectively. Taking advantage of the double-inclusion model, the problem of a single fiber breakage within a single-fiber composite can be analyzed subsequently. If there is no fiber break in the single-fiber composite, the overall elasticity tensor $\bar{\mathbf{C}}$ can be derived as

$$\bar{\mathbf{C}}_{ijkl} = \mathbf{C}^{(0)}_{ijmn} \bullet \left[\mathbf{I}_{mnkl} + \left(\mathbf{Y}^{-1}_{mnkl} - \mathbf{S}_{mnkl}\right)^{-1}\right],\ i, j, k, l, m, n = 1, 2, 3 \tag{4.18}$$

$$\mathbf{Y}_{mnkl} = \sum_{\beta=1}^{3} \phi^{(\beta)} \left[\mathbf{S}_{mnkl} + \left(\mathbf{C}^{(\beta)}_{mnpq} - \mathbf{C}^{(0)}_{mnpq}\right)^{-1} \bullet \mathbf{C}^{(0)}_{pqkl}\right]^{-1},\ k, l, m, n, p, q = 1, 2, 3 \tag{4.19}$$

where

$$\phi^{(\beta)} = \phi^{(1)} \quad \text{and} \quad \phi^{(2)} = 0 \tag{4.20}$$

where $\phi^{(1)}$ is the initial volume fraction of intact fibers; and $\phi^{(2)}$ is the volume fraction of fractured fibers; and $\mathbf{S}$ is the fourth-rank Eshelby tensor associated with a cylindrical inclusion

for the fiber phase and an spheroidal inclusion for the fiber breakage (void) phase, which has the form (Mura 1984; Ju and Sun 2001):

$$\mathbf{S}_{ijkl} = S_{IK}^{(1)}\delta_{ij}\delta_{kl} + S_{IJ}^{(2)}(\delta_{ik}\delta_{jl} + \delta_{il}\delta_{jk}) \tag{4.21}$$

Cylindrical inclusion (*fiber phase* $\mathbf{S}^{(1)}$):

$$S_{11}^{(1)} = 0, \;\; S_{12}^{(1)} = S_{13}^{(1)} = 0 \tag{4.22}$$

$$S_{21}^{(1)} = S_{31}^{(1)} = \frac{\nu_0}{2(1-\nu_0)} \tag{4.23}$$

$$S_{22}^{(1)} = S_{33}^{(1)} = S_{32}^{(1)} = S_{23}^{(1)} = \frac{4\nu_0 - 1}{8(1-\nu_0)} \tag{4.24}$$

$$S_{11}^{(2)} = 0, \;\; S_{12}^{(2)} = S_{13}^{(2)} = S_{21}^{(2)} = S_{31}^{(2)} = \frac{1}{4}, \;\; S_{22}^{(2)} = S_{33}^{(2)} = S_{23}^{(2)} = S_{32}^{(2)} = \frac{3-4\nu_0}{8(1-\nu_0)} \tag{4.25}$$

Sphoroidal inclusion (*void phase* $\mathbf{S}^{(2)}$):

$$S_{11}^{(1)} = \left[4\nu_0 + \frac{2}{\delta^2 - 1}\right]\mathrm{g}(0) + 4\nu_0 + \frac{4}{3\left(\delta^2 - 1\right)} \tag{4.26}$$

$$S_{12}^{(1)} = S_{13}^{(1)} = \left[4\nu_0 - \frac{2\delta^2 + 1}{\delta^2 - 1}\right]\mathrm{g}(0) + 4\nu_0 - \frac{2\delta^2}{\delta^2 - 1} \tag{4.27}$$

$$S_{21}^{(1)} = S_{31}^{(1)} = \left[-2\nu_0 + \frac{1 + 2\delta^2}{\delta^2 - 1}\right]\mathrm{g}(0) - \frac{2\delta^2}{\delta^2 - 1} \tag{4.28}$$

$$S_{22}^{(1)} = S_{23}^{(1)} = S_{32}^{(1)} = S_{33}^{(1)} = \left[-2\nu_0 + \frac{4\delta^2 - 1}{4\left(\delta^2 - 1\right)}\right]\mathrm{g}(0) + \frac{\delta^2}{2\left(\delta^2 - 1\right)} \tag{4.29}$$

$$S_{11}^{(2)} = \left[-4\nu_0 + \frac{4\delta^2 - 2}{\delta^2 - 1} \right] \mathrm{g}(0) - 4\nu_0 + \frac{12\delta^2 - 8}{3\left(\delta^2 - 1\right)} \tag{4.30}$$

$$S_{12}^{(2)} = S_{13}^{(2)} = S_{21}^{(2)} = S_{31}^{(2)} = \left[-\nu_0 - \frac{\delta^2 + 2}{\delta^2 - 1} \right] \mathrm{g}(0) - 2\nu_0 - \frac{2}{\delta^2 - 1} \tag{4.31}$$

$$S_{22}^{(2)} = S_{23}^{(2)} = S_{32}^{(2)} = S_{33}^{(2)} = \left[2\nu_0 - \frac{4\delta^2 - 7}{4\left(\delta^2 - 1\right)} \right] \mathrm{g}(0) - 2\nu_0 + \frac{\delta^2}{2\left(\delta^2 - 1\right)} \tag{4.32}$$

where $\delta < 1$ is the aspect ratio of the spheroidal inclusion, ν_0 is the Poisson's ratio of the matrix phase, and

$$\mathrm{g}(0) = \frac{\delta}{\left(1 - \delta^2\right)^{3/2}} \left[\delta \left(1 - \delta^2\right)^{1/2} - \cos^{-1} \delta \right] \tag{4.33}$$

Once the fiber breakage occurs, that is $\phi^{(\beta)} = \phi^{(2)}$, and $\phi^{(1)} = 0$, the overall eigenstrain in a single fiber with a single crack can be derived as follows:

$$\left\langle \boldsymbol{\varepsilon}^{*} \right\rangle = f\ \boldsymbol{\varepsilon}^{*(2)} + (1 - f)\boldsymbol{\varepsilon}^{*(1)} = \rho \left[-\mathbf{J}^{*-1} + \mathbf{K}^{-1} \right] : \boldsymbol{\varepsilon}^{\mathrm{o}} - \mathbf{K}^{-1} : \boldsymbol{\varepsilon}^{\mathrm{o}} \tag{4.34}$$

where

$$\boldsymbol{\varepsilon}^{*(1)} = -\left[\mathbf{S}^{(1)} + \left(\mathbf{C}^{(1)} - \mathbf{C}^{(0)} \right)^{-1} \bullet \mathbf{C}^{(0)} \right]^{-1} : \boldsymbol{\varepsilon}_0 \tag{4.35}$$

$$\boldsymbol{\varepsilon}^{*(2)} = -\left\{ \mathbf{I} + \left(\mathbf{S}^{(1)} - \mathbf{S}^{(2)} \right) \bullet \left[\mathbf{S}^{(2)} + \left(\mathbf{C}^{(1)} - \mathbf{C}^{(0)} \right)^{-1} \bullet \mathbf{C}^{(0)} \right] \right\}^{-1} \bullet \left(\mathbf{S}^{(2)} - \mathbf{I} \right) \tag{4.36}$$

and

$$\mathbf{K} = \mathbf{S}^{(1)} + \left(\mathbf{C}^{(1)} - \mathbf{C}^{(0)} \right)^{-1} \bullet \mathbf{C}^{(0)} \tag{4.37}$$

$$\mathbf{J} = \frac{\mathbf{J}^*}{\rho} \equiv \left\{ \mathbf{I} + \left(\mathbf{S}^{(1)} - \mathbf{S}^{(2)} \right) \bullet \left[\mathbf{S}^{(2)} + \left(\mathbf{C}^{(1)} - \mathbf{C}^{(0)} \right)^{-1} \bullet \mathbf{C}^{(0)} \right]^{-1} \right\} \bullet \mathbf{E} \tag{4.38}$$

$$\mathbf{E} = \frac{\mathbf{E}^*}{\rho} = \lim_{\rho \to 0} \left(\mathbf{S}^{(2)} - \mathbf{I} \right) \Big/ \rho \tag{4.39}$$

Herein, f is the volume fraction of the single crack in a single fiber defined as

$$\begin{aligned} f &= \frac{\text{Area of An Elliptical-Shaped Void}}{\text{Area of A Cylindrical Fiber}} \\ &= \left(\frac{\pi(a_1)\left(a_2 = a_1/\alpha\right)}{\pi(a_1)^2} \right)_{\alpha \to \infty} = \left(\frac{1}{\alpha} \right)_{\alpha \to \infty} = (\rho)_{\rho \to 0} \end{aligned} \tag{4.40}$$

Hence, by using the overall eigenstrain in the damaged fiber and the average field equations from Ju and Chen's work (1994a, b), the effective elasticity tensor of a single-fiber composite can be reached

$$\begin{aligned} \bar{\mathbf{C}} = \underbrace{\mathbf{C}^{(0)}}_{\text{matrix}} &+ \underbrace{\phi^{(1)} \mathbf{C}^{(0)} \bullet \left[\mathbf{K} - \phi^{(1)} \mathbf{S} - \phi^{(2)} \mathbf{S}^{(1)} \bullet \mathbf{J}^{-1} \bullet \mathbf{K} \right]^{-1}}_{\text{intact fiber phase}} \\ &+ \underbrace{\phi^{(2)} \mathbf{C}^{(0)} \bullet \left[-\phi^{(2)} \mathbf{S}^{(1)} + \left(\mathbf{I} - \phi^{(2)} \mathbf{S}^{(1)} \bullet \mathbf{J}^{-1} \bullet \mathbf{K} \right) \bullet \mathbf{J} \right]^{-1}}_{\text{fiber breakage (void) phase}} \end{aligned} \tag{4.41}$$

4.4 Statistical Modeling of Damage Evolution in Fiber Reinforced Composites due to Fiber Breakage

4.4.1 Damage Evolution in Single-Fiber Composites

The averaged normal stress in the fiber longitudinal direction is the controlling factor in the fiber breakage evolution. This implies that fiber breakage occurs in a certain plane of the fiber if

the averaged normal stress perpendicular to that plane exceeds a critical value. As the applied strain increases, the number of fiber breaks (crack density) increases. Meanwhile, the fiber fragment length becomes smaller as the applied strain reaches a higher level. At a certain strain level, the crack density becomes constant and the fragment length achieves its minimum (Kim and Nairn, 2002). As a consequence, we introduce a quantity L represent the averaged fragment length. As the strain level increases, the averaged fragment length L decreases, whereas the number density of fiber breakages increases. Therefore, we adopted $1/L$ to quantify the crack number density evolution of fiber breakages. A two-parameter Weibull probability function is adopted to govern the fiber breakage evolution.

$$P_d = \begin{cases} 1-\exp\left[-\left(\dfrac{\bar{\sigma}_{11}^{(1)}-\sigma_{cri}}{S_{cr}}\right)^{M}\right], & \bar{\sigma}_{11}^{(1)} \geq \sigma_{cri} \\ 0, & \bar{\sigma}_{11}^{(1)} < \sigma_{cri} \end{cases} \tag{4.42}$$

where the Weibull parameters S_{cr} and M are related to the critical fracture strength of fibers and the fiber breakage evolution rate (Sun et al. 2003), respectively. σ_{cri} is the critical fracture stress. The volume-averaged internal fiber stress $\bar{\boldsymbol{\sigma}}^{(1)}$ can be determined by

$$\bar{\boldsymbol{\sigma}}^{(1)} = \mathbf{C}^{(0)} \bullet \left\{ \mathbf{I} + \left(\mathbf{I}-\mathbf{S}^{(1)}\right) \bullet \left[\mathbf{S}^{(1)} + \left(\mathbf{C}^{(1)}-\mathbf{C}^{(0)}\right)^{-1} \bullet \mathbf{C}^{(0)} \right]^{-1} \right\} : \boldsymbol{\varepsilon}^{\infty} \tag{4.43}$$

Therefore, the averaged post-breakage fiber length is defined as

$$L = L_0(1-P_d) \tag{4.44}$$

The volume fraction of the fiber breakages within a single-fiber composite is further modified as

$$f = \frac{\text{Area of An Elliptical-Shaped Void}}{\text{Area of A Cylindrical Fiber}}$$
$$= \left(\frac{\pi(a_1)(a_2 = a_1/\alpha)}{\pi(a_1)^2 L} \right)_{\alpha\to\infty} = \left(\frac{1}{\alpha L} \right)_{\alpha\to\infty} = \left(\frac{\rho}{L} \right)_{\rho\to 0} \tag{4.45}$$

4.4.2 Fiber-Dominated Damage Evolution in Multi-Fiber Composites

The failure of several fibers in the same plane may trigger the failure of the composite before the global onset of plastic deformation in the composite (Jeng et al., 1991). This damage mechanism is termed as the fiber-dominated damage is some literature. As the external loading increases, the volume fraction of intact fibers decreases, whereas the volume fraction of fractured fibers increases. The Weibull probability function is adopted to describe this damage evolutionary process.

$$P_d = \begin{cases} 1 - \exp\left[-\left(\dfrac{\bar{\sigma}_{11}^{(1)} - \tilde{\sigma}_{cri}}{S_{cr}} \right)^{\tilde{M}} \right], & \bar{\sigma}_{11}^{(1)} \geq \tilde{\sigma}_{cri} \\ 0, & \bar{\sigma}_{11}^{(1)} < \tilde{\sigma}_{cri} \end{cases} \tag{4.46}$$

where

$$\bar{\boldsymbol{\sigma}}^{(1)} = \mathbf{C}^{(0)} \bullet \left\{ \mathbf{I} + \left(\mathbf{I} - \mathbf{S}^{(1)} \right) \bullet \left[\mathbf{S}^{(1)} + \left(\mathbf{C}^{(1)} - \mathbf{C}^{(0)} \right)^{-1} \bullet \mathbf{C}^{(0)} \right]^{-1} \right\} : \boldsymbol{\varepsilon}^{\infty} \tag{4.47}$$

Therefore, the overall properties of a composite writes

$$\begin{aligned} \bar{\mathbf{C}} = \mathbf{C}^{(0)} &+ \phi^{(1)} \mathbf{C}^{(0)} \bullet \left[\mathbf{K} - \phi^{(1)} \mathbf{S} - \phi^{(2)} \mathbf{S}^{(1)} \bullet \mathbf{J}^{-1} \bullet \mathbf{K} \right]^{-1} \\ &+ \phi^{(2)} \mathbf{C}^{(0)} \bullet \left[-\phi^{(2)} \mathbf{S}^{(1)} + \left(\mathbf{I} - \phi^{(2)} \mathbf{S}^{(1)} \bullet \mathbf{J}^{-1} \bullet \mathbf{K} \right) \bullet \mathbf{J} \right]^{-1} \end{aligned} \tag{4.48}$$

4.5 Numerical Results and Discussions

Continuous fiber-reinforced epoxy matrix composites are adopted for illustration purpose with material properties and dimensions listed in Table 4.1. The prediction of the fiber breakage evolution in a single-fiber composite is plotted in comparison with experiment results. Good agreement is observed for both the AS4-Carbon and E-Glass fibers in Figure 4.6 and Figure 4.7, respectively. The number density of fiber breakages in the AS4-Carbon fiber increased rapidly after strain level of 1.5%. When the strain reached 2.7%, the fiber breakage number density shows a plateau. The critical length of the fiber fragment is obtained from this plateau region. For E-glass fibers, as expected, the fiber breakage number density plot demonstrates a similar fashion, but the plateau shifts into the higher strain region. The plateau is obtained after strain level about 3.2%.

Further, the stress-strain behavior of the multi-fiber composites is investigated. We adopt the same materials as those used in the single-fiber composite case. The total volume fraction of fibers is 15%. As clearly indicated in Figure 4.9, materials behave nonlinearly due to the existence of fiber breakages. The volume fraction evolution of the damaged fibers is plotted with respect to the applied strain in Figure 4.8. Two sets of Weibull parameters are considered to demonstrate the effect of Weibull parameters on the damage evolution. It is clear that M governs the evolution rate while S control the shape of the damage evolution curve.

4.6 Conclusions

In this chapter, we proposed a micromechanical damage framework to predict the overall elastic fiber-dominated damage behavior of continuous fiber-reinforced composites due to fiber breakage. The theory of double-inclusion was applied to derive the stress fields of a single fiber break embedded in a single fiber phase. First, the damage evolution due to fiber breakage in a SFC was investigated. An effective length L which signifies the averaged distance between two neighbored breakages was introduced to address the multiple fiber breakage inside a single fiber. The averaged length L decreases as loading increases. The total fiber breakage volume increases with the loading. A two-parameter Weibull distribution is adopted to govern the evolution of the averaged L upon the loading. In addition, the model was extended to investigate the overall fiber-dominated failure in a multi-fiber composite. In order to demonstrate the predictive capability of the proposed models, comparisons are made between our predictions and the available experimental data (Kim and Nairn, 2002). In general, good agreement has been observed.

Table 4.1 Material properties of composite materials used in the numerical examples.

	AS4-Carbon	E-Glass	Epoxy
Young's modulus (MPa)	231000	72500	2600
Poisson's Ratio	0.22	0.22	0.34
Length (mm)	25.4	25.4	
Radius ($\times 10^{-3}$ mm)	3.5	7	
Critical Tensile Strength (MPa)	4070	2000	

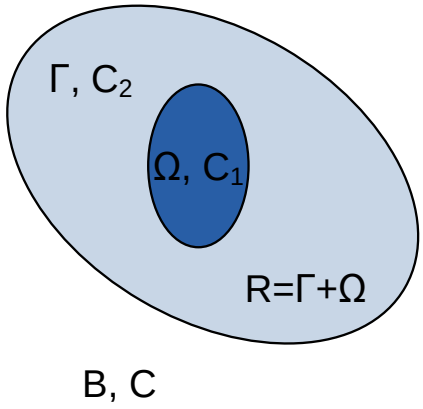

Figure 4.1 Illustration of a double-inclusion problem, in which a uniform infinite domain B with material properties $\mathbf{C}$ is embedded with a double inclusion $R = \Gamma + \Omega$ with material properties $\mathbf{C}^{(1)}$ and $\mathbf{C}^{(2)}$ for the inclusion and heterogeneity, respectively.

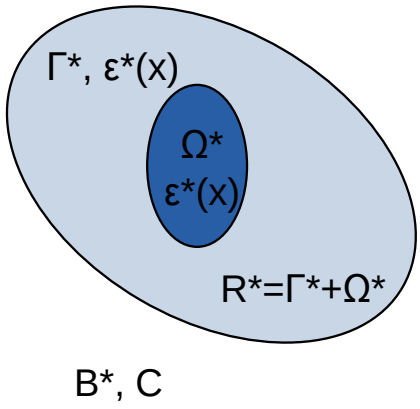

Figure 4.2 Illustration of the auxiliary problem to the double-inclusion problem, in which an equivalent, unbounded solid B^* with uniform material properties $\mathbf{C}$ is embedded with an equivalent inclusion $R^* = \Gamma^* + \Omega^*$ with homogenized eigenstrains $\boldsymbol{\varepsilon}^*(\mathbf{x})$.

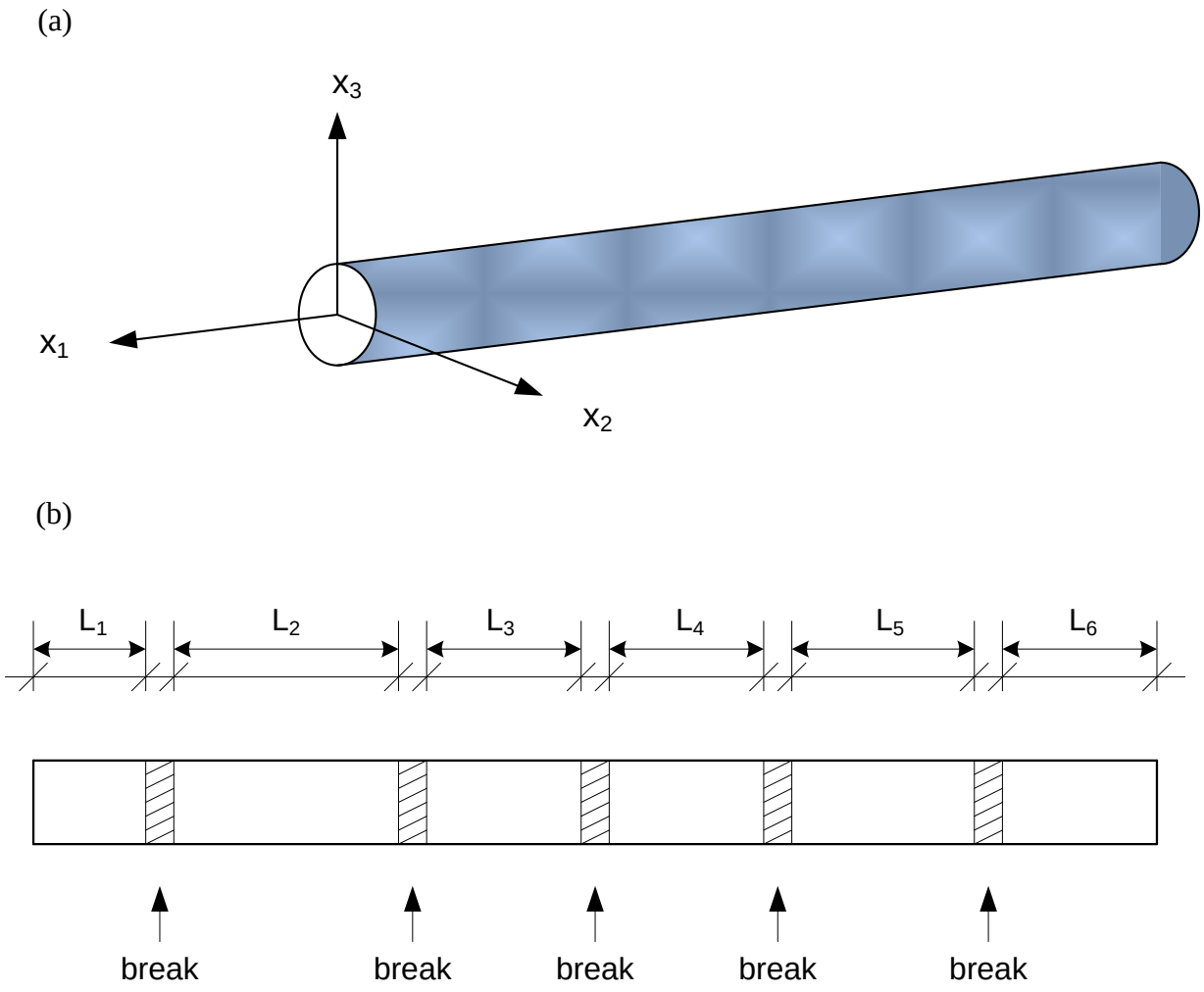

Figure 4.3 (a) Schematic of a three-dimensional intact fiber with original fiber length L_0 and (b) illustration of the multiple fiber breaks occurred in a single fiber.

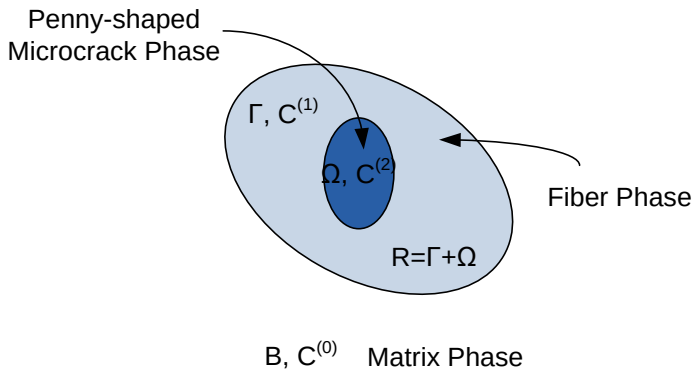

Figure 4.4 Illustration of the double-inclusion model for modeling of a single-fiber composite with a single fiber break.

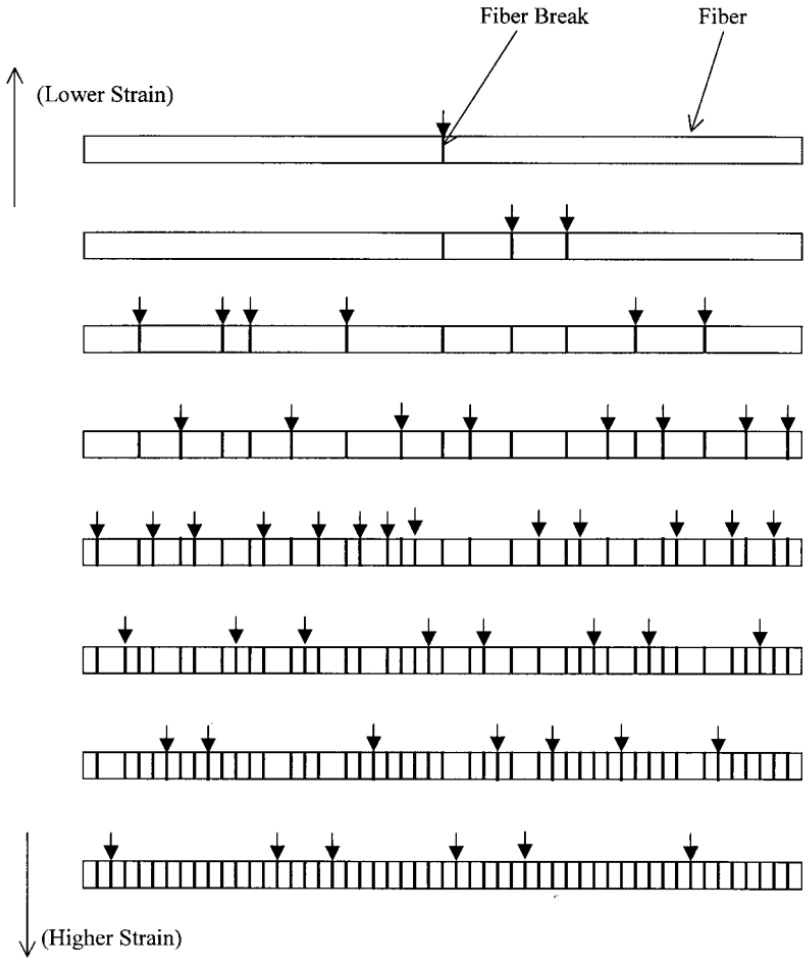

Figure 4.5 Illustration of the distribution of fiber breaks in single-fiber composites during tensile loadings (modified from Kim and Nairn 2002).

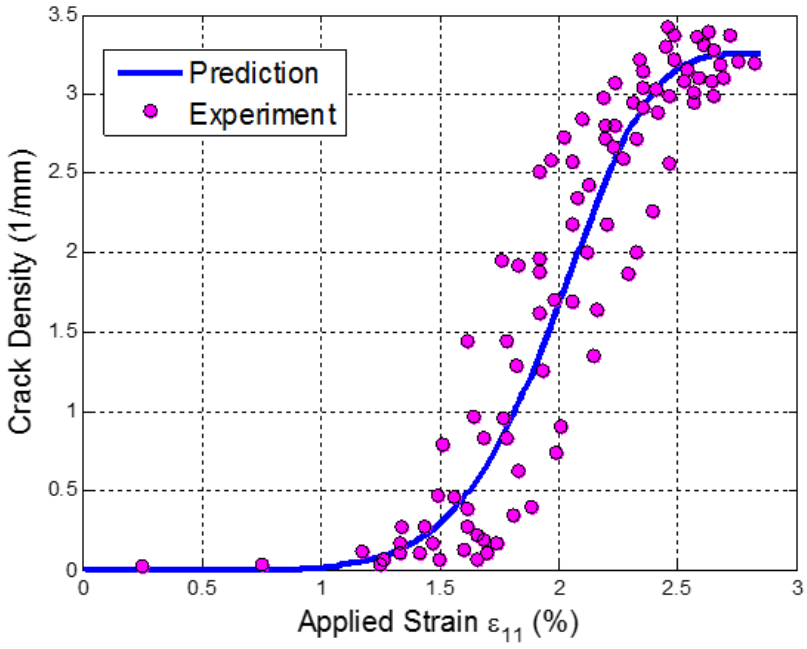

Figure 4.6 Numerically predicted fiber break density of AS4 carbon fiber as a function of the applied macroscopic strain.

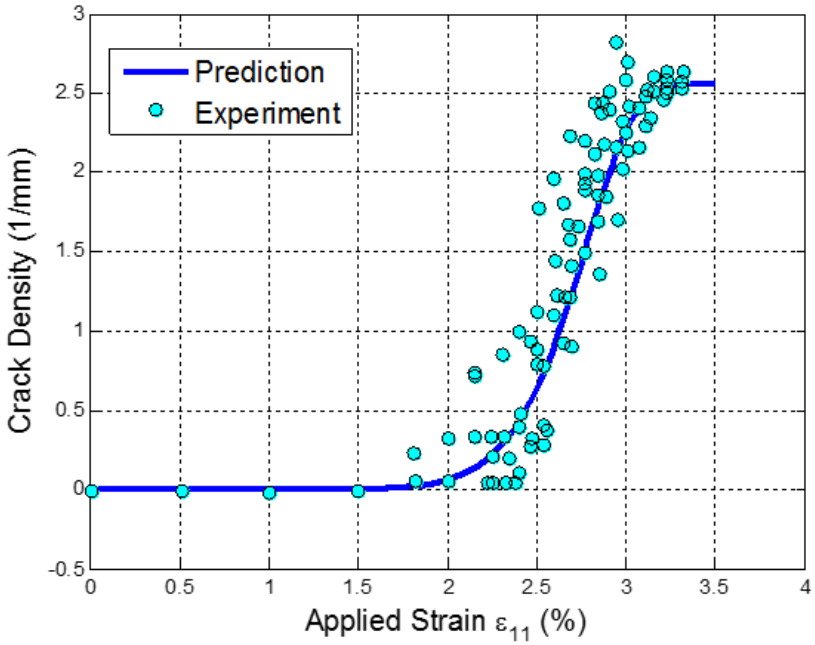

Figure 4.7 Numerically predicted fiber break density of E-glass fiber as a function of the applied macroscopic strain.

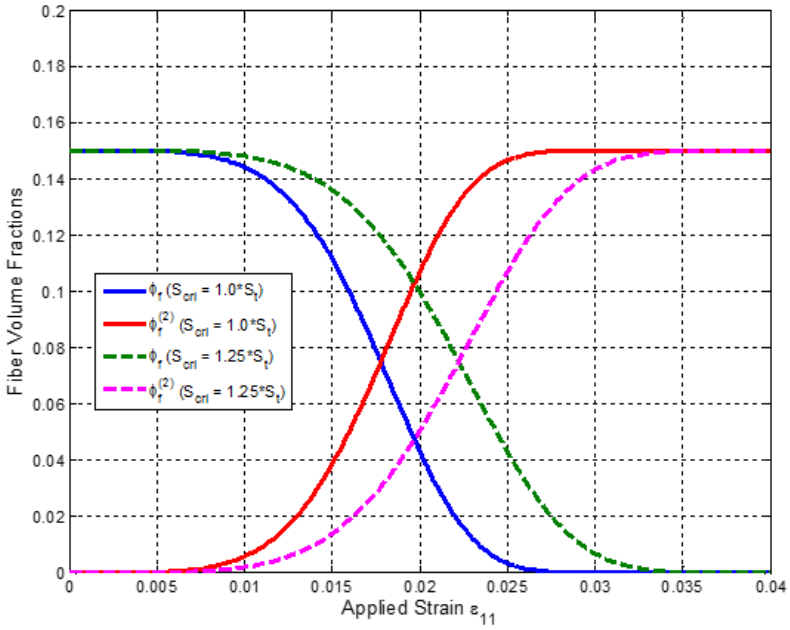

Figure 4.8 Numerically predicted volume fraction evolution of fiber breaking damage occurred in the fiber-reinforced composites with different values of Weibull parameter S_{cr} .

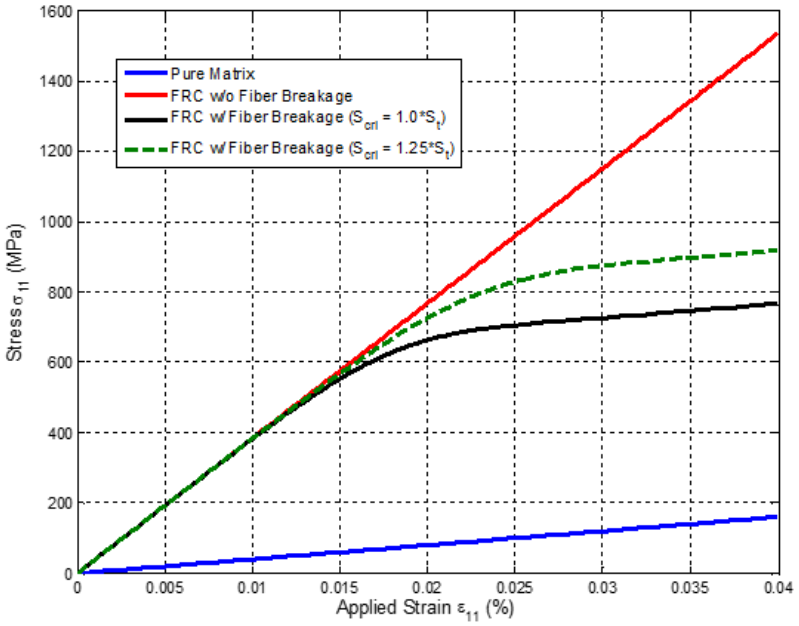

Figure 4.9 Numerically predicted stress-strain responses for pure matrix and for the fiber-reinforced composites without consideration of fiber breaking and with consideration of fiber breaking with different values of Weibull parameter S_{cr} .

CHAPTER 5 MICROMECHANICAL DAMAGE MODELING OF PROGRESSIVE ELASTIC FIBER BREAKAGE FOR LONGITUDINAL FIBER REINFORCED COMPOSITES

5.1 Introduction

Continuous fiber-reinforced metal matrix composites (MMCs) have been widely studied due to their highly specific mechanical properties and potential applications in various industries. The three phases of a continuous fiber-reinforced composite system, namely the fiber reinforcements, the matrix and the interface region between the fibers and matrix, together with the interfacial bonding condition control the failure mechanisms. In particular, experimental evidence reveals that although the interface zone between the fibers and matrix occupies a vanishing fraction of the total composite volume, it plays a key role in determining the overall composite properties and stress-strain relations related to damage (He et al., 1993; Curtin, 1998). It is generally agreed that the fiber fragmentation is the dominant damage mode leading to the catastrophic failure of the fiber reinforced composites, especially for the continuous fiber reinforced MMCs (Brindley et al., 1992). In a special case when i) the failure strain of the fiber phase is much lower than that of the matrix, and ii) the interphase zone between the fibers and matrix is relatively weak, damage is more likely to initiate from the interphase zone and propagate into the fiber causing fiber breaks at random locations. In other words, fiber breaks tend to appear prior to other damage scenarios such as the matrix cracking and massive matrix plastic deformation. In the present work, we concentrate our interests on the damage scenario of progressive fiber breakage in composite materials made of a tough matrix, and weak fibers with

relatively weak interfacial prosperities. In addition, the interfacial bonding condition between material phases is assumed to be perfect.

The fragmentation test on single-fiber composites (SFCs) serves as a means to investigate the local damage behavior within the multi-fiber composites. Considerable experimental evidences reveal that the number accumulation of fiber breaks in a SFC follows a Weibull statistic (Jeng et al., 1991; Zhao et al., 2000; Kim and Nairn, 2002). Moreover, the fiber breakage evolution and the fragmentation distribution can be used to derive the Weibull modulus, and to quantitatively extract the interfacial properties, such as the interfacial shear stress (Curtin, 1998). Although many features of the SFCs are preserved in the multi-fiber composites of practical interest, the evolution of fiber fragmentation in multi-fiber composites during loading is, in principle, different from that in the SFCs in many ways. For example, the sequence of damage initiation in each fiber can be characterized as a stochastic process since the fiber strength is non-uniform due to the manufacturing defects. Moreover, fiber damage in some local region increases the stresses in the surrounding fibers and drives further damage locally. The mechanism of this load transferring from broken fibers to intact fibers is difficult to be determined experimentally. In addition, the local microstructure of multi-fiber composites is more complex than that of the SFCs. Consequently, we assume in the current study that the composite failure becomes statistical and the fiber fragmentation evolution of multi-fiber composites follows certain probability distribution.

There are several schools of theories for estimating the damage effect of fiber breaks in multi-fiber composites. The shear-lag theory with different load transferring mechanisms is one

of the means. For example, the global load shearing (GLS) model assumes that the load originally taken by the broken fiber is equally redistributed over all the remaining intact fibers on the cross-section. Every cross-section becomes statistically identical, and therefore, a multi-fiber composite problem can be treated as an equivalent single-fiber composite problem (Curtin, 1998). The primary advantage of these models is their simplicity of applications. However, the load transfer mechanism in the local region is far more complicated in reality. Hence, the local load shearing (LLS) model was proposed assuming that the extra load associated with the failed fibers is transferred to the neighboring fibers (Smith, 1980; He et al., 1993; Zhou and Curtin, 1995; Ibnabdeljalil and Curtin, 1997; Okabe and Takeda, 2002). This group of models concerns the local microstructure, and the understanding on the load transfer from the broken fiber to the intact fibers is crucial. Both the GLS and LLS models allow the qualitative understanding of the mechanisms of forming discontinuities, as well as the interaction between the material phases. However, none of these approaches allows straightforward incorporation with the nonlinear models for describing complicated material behaviors (Mishnaevsky and Brøndsted, 2009).

Another school aims at formulating the explicit forms of the overall constitutive laws for heterogeneous materials considering various local damage modes (Ju, 1991; Ju and Tseng, 1992; Sun et al., 2003; Lee and Ju, 2008). Following the concept of eigenstrain introduced by Eshelby (1957, 1961), the effective properties of heterogeneous composites containing inhomogeneities and local damage can be then derived based on an ensemble-volume averaging process within a representative volume element (RVE). In particular, Sun and Ju (Sun et al., 2003) applied the double-inclusion theory (Hori and Nemat-Nasser, 1993; Shodia and Sarvestani, 2001) to investigate the particle-shaped fiber cracking problem. They explicitly derived the perturbed

stress field associated with a single crack embedded in a single fiber. The Weibull distribution was adopted to govern the accumulation of the crack number in the multi-fiber composite. Utilizing the innovative governing ensemble-volume average field equations developed by Ju and Chen (1994), the explicit form of the overall constitutive relations for short fiber reinforced composites with progressive fiber breaks were achieved. Ko and Ju (2013) further extended the application of the double-inclusion theory to predict the overall material behavior associated with fiber cracking in the continuous fiber reinforced composites, with the local cracking damage propagating along the longitudinal direction. The primary advantage of micromechanics is that the micromechanical models allow the explicit form of the overall constitutive relations of composites considering different material phases and various damage modes.

Moreover, numerical techniques have been applied extensively to simulate the fiber breakage process in MMCs. Finite element simulation is one of the most commonly-used methods (Nickolas and Ahmad, 1994; Shodja and Sarvestni, 2001; Xia et al., 2002; Ohno et al., 2004). Another widely adopted technique is the Monte Carlo simulation for prediction of the strength of the composite materials (Landis, 2000; Meyer et al., 2003; Liu and Zheng, 2006; Nazari et al., 2011). Most of the computational models are based on a pre-defined fiber micro-structural layout, which has the advantage of high accuracy of solutions by considering the geometry of reinforcements and local interactions among reinforcements. However, numerical models do not yield explicit forms for the overall constitutive relations, making them difficult to implement in the stress analyses at the macroscopic level.

The objective of this Chapter is to investigate the overall material behavior of continuous fiber reinforced composites with relatively ductile matrix and brittle continuous reinforcements under tensile loading. The primary interest focuses on the effect of fiber breaks on the overall material properties. The remainder of this Chapter is organized as follows. First, the micromechanical field equations are systematically presented with special consideration of fiber breaking effect. The computational algorithm of the progressive damage evolution is subsequently illustrated. The homogeneous damage evolution model is introduced to predict the mechanical properties of longitudinal fiber reinforced composites. Finally, numerical predictions by the proposed approach are validated with the available experimental data and a series of parametric studies are presented.

5.2 Micromechanical Formulation of Fiber Breakage Evolution in Longitudinal Fiber reinforced Composites

Consider a far-field macro strain $\boldsymbol{\varepsilon}^0$ applied on the boundary ∂D of a representative volume element (RVE) D embedded with an inhomogeneity Ω. The inhomogeneity is defined as inhomogeneous if there is an eigenstrain $\boldsymbol{\varepsilon}_{cr}^*$ inside the RVE. As a result, the total stress field $\boldsymbol{\sigma}^t$ in the composite material can be expressed as

$$\begin{cases} \boldsymbol{\sigma}^t = \mathbf{C}_1 : \left(\boldsymbol{\varepsilon}^0 + \boldsymbol{\varepsilon}' - \boldsymbol{\varepsilon}_{cr}^* \right) & \text{in } \Omega \\ \boldsymbol{\sigma}^t = \mathbf{C}_0 : \left(\boldsymbol{\varepsilon}^0 + \boldsymbol{\varepsilon}' \right) & \text{in D} - \Omega \end{cases} \tag{5.1}$$

where $\mathbf{C}_1$ and $\mathbf{C}_0$ are the elasticity tensors of the inhomogeneity (fiber) phase and the matrix phase, respectively, $\boldsymbol{\varepsilon}'$ is the perturbed strain due to the presence of the inhomogeneous

inhomogeneity, and $\boldsymbol{\varepsilon}_{cr}^{*}$ is the eigenstrain within the inhomogeneity. For a continuous fiber-reinforced composite with fiber breaks, $\boldsymbol{\varepsilon}_{cr}^{*}$ represents the eigenstrain caused by the fiber breaks in the fiber phase.

The inhomogeneous inhomogeneity problem can be analyzed by an equivalent inclusion problem using a homogeneous matrix with an elastic stiffness tensor $\mathbf{C}_0$, in which the total eigenstrain in the inclusion is $\boldsymbol{\varepsilon}^{**} = \boldsymbol{\varepsilon}^{*} + \boldsymbol{\varepsilon}_{cr}^{*}$. The corresponding total stress field $\boldsymbol{\sigma}^{t}$ of this equivalent inclusion problem is written as

$$\begin{cases} \boldsymbol{\sigma}^{t} = \mathbf{C}_0 : \left(\boldsymbol{\varepsilon}^{0} + \boldsymbol{\varepsilon}' - \boldsymbol{\varepsilon}_{cr}^{*} - \boldsymbol{\varepsilon}^{*} \right) & \text{in } \Omega \\ \boldsymbol{\sigma}^{t} = \mathbf{C}_0 : \left(\boldsymbol{\varepsilon}^{0} + \boldsymbol{\varepsilon}' \right) & \text{in } \mathrm{D} - \Omega \end{cases} \tag{5.2}$$

where $\boldsymbol{\varepsilon}^{*}$ is the conventional eigenstrain field accounting for the mismatch due to the inhomogeneity. Utilization of the equivalent inclusion principle leads to

$$\mathbf{C}_1 : \left(\boldsymbol{\varepsilon}^{0} + \boldsymbol{\varepsilon}' - \boldsymbol{\varepsilon}_{cr}^{*} \right) = \mathbf{C}_0 : \left(\boldsymbol{\varepsilon}^{0} + \boldsymbol{\varepsilon}' - \boldsymbol{\varepsilon}_{cr}^{*} - \boldsymbol{\varepsilon}^{*} \right) \qquad \text{in } \Omega \tag{5.3}$$

The perturbed strain $\boldsymbol{\varepsilon}'$ in Equation (5.3) can be related to the total eigenstrain $\boldsymbol{\varepsilon}^{**}$ based on the Eshelby solution:

$$\boldsymbol{\varepsilon}' = \mathbf{S} : \boldsymbol{\varepsilon}^{**} = \mathbf{S} : \left(\boldsymbol{\varepsilon}_{cr}^{*} + \boldsymbol{\varepsilon}^{*} \right) \tag{5.4}$$

where $\mathbf{S}$ is the interior-point Eshelby tensor which depends on the material properties of the matrix and the geometry of the fiber inclusion. For cylindrical embedded fibers, the Eshelby tensor can be expressed in a generalized isotropic fourth-order tensor form as

$$\mathbf{S}_{ijkl} = S^{(1)}_{IK}\delta_{ij}\delta_{kl} + S^{(2)}_{IJ}(\delta_{ik}\delta_{jl} + \delta_{il}\delta_{jk}) \tag{5.5}$$

where the second-rank coefficient tensors $S^{(1)}_{IK}$ and $S^{(2)}_{IJ}$ are

$$S^{(1)}_{11} = 0,\ \ S^{(1)}_{12} = S^{(1)}_{13} = 0,\ \ S^{(1)}_{21} = S^{(1)}_{31} = \frac{\nu_0}{2(1-\nu_0)},\ S^{(1)}_{22} = S^{(1)}_{33} = S^{(1)}_{32} = S^{(1)}_{23} = \frac{4\nu_0 - 1}{8(1-\nu_0)} \tag{5.6}$$

$$S^{(2)}_{11} = 0,\ \ S^{(2)}_{12} = S^{(2)}_{13} = S^{(2)}_{21} = S^{(2)}_{31} = \frac{1}{4},\ \ S^{(2)}_{22} = S^{(2)}_{33} = S^{(2)}_{23} = S^{(2)}_{32} = \frac{3-4\nu_0}{8(1-\nu_0)} \tag{5.7}$$

where ν_0 is the Poisson's ratio of the matrix. The ensemble-volume averaged strain $\langle \bar{\boldsymbol{\varepsilon}} \rangle$ can be determined by

$$\langle \bar{\boldsymbol{\varepsilon}} \rangle = \boldsymbol{\varepsilon}^0 + \mathbf{S} : \left(\sum_{r=1}^{n} \phi_r \langle \bar{\boldsymbol{\varepsilon}}^{**} \rangle_r \right) \tag{5.8}$$

where $\langle \bar{\bullet} \rangle$ denotes the ensemble-volume averaged operator; ϕ_r is the volume fraction of the *rth* phase inhomogeneity; and $< \bar{\boldsymbol{\varepsilon}}^{**} >_r$ is the ensemble volume-averaged total eigenstrain in the *rth* inclusion phase. Similarly, the ensemble-volume averaged stress is

$$\begin{aligned} \langle \bar{\boldsymbol{\sigma}} \rangle &= \frac{1}{V}\left[V_m \langle \bar{\boldsymbol{\sigma}} \rangle_m : + \sum_{r=1}^{n} V_r \langle \bar{\boldsymbol{\sigma}} \rangle_r \right] \\ &= \frac{1}{V}\left[V_m \mathbf{C}_0 : \langle \bar{\boldsymbol{\varepsilon}}_m \rangle + \sum_{r=1}^{n} \mathbf{C}_0 : \left(\langle \bar{\boldsymbol{\varepsilon}} \rangle_r - \langle \bar{\boldsymbol{\varepsilon}}^{**} \rangle_r \right) V_r \right] \\ &= \mathbf{C}_0 : \left[\langle \bar{\boldsymbol{\varepsilon}} \rangle - \sum_{r=1}^{n} \phi_r \langle \bar{\boldsymbol{\varepsilon}}^{**} \rangle_r \right] \end{aligned} \tag{5.9}$$

where V_m , V_r , and V are the volumes of the matrix phase, the *rth* inclusion phase, and the RVE, respectively. In order to determine the total eigenstrain $\langle \bar{\boldsymbol{\varepsilon}}^{**} \rangle$ in each fiber phase, we further

derive the expression for the portion of eigenstrain due to fiber breakage based on linear elastic fracture mechanics as presented in the following section.

5.3 Eigenstrain due to Fiber Breakage in Fiber Reinforced Composites

Experimental evidence indicated that the gap constituting the fiber break has a significant contribution to the longitudinal deformation of the composite. The presence of fiber breaks will cause the stress redistribution near the crack tips without further inducing extra stresses. Therefore, the strain caused by the fiber breaks is a stress-free strain, and it can be categorized as an additional eigenstrain $\boldsymbol{\varepsilon}_{cr}^{*}$ in the inhomogeneity phase. In the present work, we choose a composite reinforced with cylindrical-shaped fibers for illustration purpose. The ensemble-volume averaged eigenstrains in each fiber phase can be expressed as

$$\left\langle \boldsymbol{\varepsilon}_{cr}^{*} \right\rangle_{r} (\mathbf{x}) = f(\mathbf{x}) \cdot \frac{1}{2} \int_{S_i} \left\langle [\mathbf{u}] \otimes \mathbf{n} + \mathbf{n} \otimes [\mathbf{u}] \right\rangle (\mathbf{x}' | \mathbf{x}) \, dS_i \tag{5.10}$$

where $f(\mathbf{x})$ is the probability density function for a fiber break centered at $\mathbf{x}$; $\mathbf{n} = [0,0,1]^T$ is surface normal of the fiber break; $\mathbf{x}'$ denotes any point on the crack surface S_i; and $[\mathbf{u}]$ is the microcrack opening displacement vector based on the theory of linear elastic fracture mechanics as:

$$\begin{Bmatrix} [u_x] \\ [u_y] \\ [u_z] \end{Bmatrix} = \frac{8(1-\nu^2)}{\pi E(2-\nu)} \sqrt{c^2 - r^2} \begin{Bmatrix} 2s \\ 2t \\ (2-\nu)p \end{Bmatrix} \tag{5.11}$$

where E and ν are the Young's modulus and Poisson's ratio of the fiber; c is the radius of the fiber break; $r = |\mathbf{x}' - \mathbf{x}|$ is the distance of point $\mathbf{x}'$ away from the center of fiber break; and $p, s,$ and t are the *z*-direction *normal*, *x*-direction and *y*-direction *shear* stresses projected on the fiber microcrack surface in its local coordinates, respectively. Carrying out the integration in Equation (5.10) by using Equation (5.11) yields:

$$\left\langle \boldsymbol{\varepsilon}_{cr}^{*} \right\rangle_r (\mathbf{x}) = f(\mathbf{x}) \cdot \frac{16(1-\nu^2)}{3E(2-\nu)} \cdot c^3 \cdot \mathbf{g} \cdot \mathbf{K}_0 : \left\langle \boldsymbol{\sigma}_f \right\rangle_r \tag{5.12}$$

where $\left\langle \boldsymbol{\sigma}_f \right\rangle_r$ is the ensemble averaged fiber stress associated with the rth fiber phase; $\mathbf{g}$ and $\mathbf{K}_0$ are the transformation matrices with the forms:

$$\mathbf{g}^T = \begin{bmatrix} 0 & 0 & 2-\nu & 0 & 0 & 0 \\ 0 & 0 & 0 & 0 & 2 & 0 \\ 0 & 0 & 0 & 2 & 0 & 0 \end{bmatrix} \tag{5.13}$$

and

$$\mathbf{K}_0 = \begin{bmatrix} 0 & 0 & 1 & 0 & 0 & 0 \\ 0 & 0 & 0 & 0 & 1 & 0 \\ 0 & 0 & 0 & 1 & 0 & 0 \end{bmatrix} \tag{5.14}$$

The volume averaged eigenstrain due the existence of the fiber breaks in the rth fiber phase is

$$\left\langle \bar{\boldsymbol{\varepsilon}}_{cr}^{*} \right\rangle_r = \frac{16(1-\nu^2)}{3E(2-\nu)} \cdot c^3 \cdot \mathbf{g} \cdot \mathbf{K}_0 : \left\langle \bar{\boldsymbol{\sigma}}_f \right\rangle_r \cdot \frac{\int_{V_f} f(\mathbf{x}) d\mathbf{x}}{V_f} = \beta \cdot n \cdot \boldsymbol{\Gamma} : \left\langle \bar{\boldsymbol{\sigma}}_f \right\rangle_r \tag{5.15}$$

where $\beta = 16(1-\nu^2)c \Big/ \left[3E(2-\nu) L_f \right]$, n denotes the number of fiber breaks; L_f stands for the fiber length; and $\boldsymbol{\Gamma}$ is the 4[th] order tensor which has the form

$$\boldsymbol{\Gamma} = \begin{bmatrix} 0 & 0 & 0 & 0 & 0 & 0 \\ 0 & 0 & 0 & 0 & 0 & 0 \\ 0 & 0 & 2-\nu & 0 & 0 & 0 \\ 0 & 0 & 0 & 2 & 0 & 0 \\ 0 & 0 & 0 & 0 & 2 & 0 \\ 0 & 0 & 0 & 0 & 0 & 0 \end{bmatrix} = diag\left[0,0,2-\nu,2,2,0\right] \tag{5.16}$$

It can be easily seen from Equations (5.15) and (5.16) that the presence of the fiber breaks only contributes to the z-direction normal, *x*-direction and *y*-direction shear strain components of the eigenstrain field. Substituting the stresses of the fiber phase defined in Equation (5.2) into Equation (5.15), the volume averaged eigenstrain due to the multiple fiber breaks in the longitudinal direction is reached as the following

$$\left\langle \bar{\boldsymbol{\varepsilon}}_{cr}^{*} \right\rangle_r = \beta \cdot n \cdot \boldsymbol{\Gamma} : \left\langle \bar{\boldsymbol{\sigma}}_f \right\rangle_r = \beta \cdot n \cdot \boldsymbol{\Gamma} \bullet \left\{ \mathbf{C}_0 : \left[\boldsymbol{\varepsilon}^0 + \left\langle \bar{\boldsymbol{\varepsilon}}' \right\rangle - \left\langle \bar{\boldsymbol{\varepsilon}}^{**} \right\rangle_r \right] \right\} \tag{5.17}$$

Assume that the number evolution of fiber breaks is governed by the Weibull statistic:

$$n = p_1 \cdot n_{saturated} \tag{5.18}$$

and

$$p_1 = \begin{cases} 1 - \exp\left[-\left(\dfrac{\sigma - \sigma_{cr}}{S} \right)^M \right] & \text{if } \sigma \geq \sigma_{cr} \\ 0 & \text{if } \sigma < \sigma_{cr} \end{cases} \tag{5.19}$$

where $n_{saturated}$ and σ_{cr} are the saturated number of fiber breaks and stress threshold for fiber break initiation, respectively. Moreover, σ is the internal fiber stress in the longitudinal direction, and S and M are the two Weibull parameters, which can be quantitatively characterized from the fragmentation test of the single-fiber composite. Here, S is associated with the local fiber breaking strength, whereas M governs the damage evolution rate. Clearly,

the volume averaged eigenstrain due to fiber breaks depends on the material properties and geometry of the fiber phase, the geometry of the crack and the current stress level in the fiber.

Therefore, the expression for the ensemble-volume averaged total eigenstrains in the rth inclusion phase is obtained as follows:

$$\left\langle \bar{\boldsymbol{\varepsilon}}^{**} \right\rangle_r = \mathbf{T}_r : \boldsymbol{\varepsilon}^0 \tag{5.20}$$

The 4th order tensor $\mathbf{T}_r$ in Equation (5.20) relates the ensemble-volume averaged eigenstrains in the rth inclusion phase to the far-field macro strains as follows:

$$\mathbf{T}_r = -[\mathbf{C}_1 \bullet \mathbf{S} - \mathbf{C}_0 \bullet (\mathbf{S} - \mathbf{I}) - \beta \cdot (n)_r \cdot \mathbf{C}_1 \bullet \boldsymbol{\Gamma} \bullet \mathbf{C}_0 \bullet (\mathbf{S} - \mathbf{I})]^{-1} \bullet [\mathbf{C}_1 - (\mathbf{I} + \beta \cdot (n)_r \cdot \mathbf{C}_1 \bullet \boldsymbol{\Gamma}) \bullet \mathbf{C}_0] \tag{5.21}$$

where $\mathbf{I}_{ijkl} = \delta_{ij}\delta_{kl} + \frac{1}{2}(\delta_{ik}\delta_{jl} + \delta_{il}\delta_{jk})$ is the fourth-rank identity tensor. Clearly, the ensemble-volume averaged total eigenstrain in the inclusion phase is induced by both the mismatch due to the inhomogeneity and the fiber breaking effect. Readers interested in the detailed derivation of $\mathbf{T}_r$ can refer to **Appendix A**. Furthermore, with the aid of multiplication and inverse formulae and lengthy derivation, Equation (5.21) can be rewritten in the following generalized isotropic fourth-rank tensor form:

$$\left(\mathbf{T}_r\right)_{ijkl} = \left(T_r\right)^{(1)}_{IK} \delta_{ij}\delta_{kl} + \left(T_r\right)^{(2)}_{IJ} (\delta_{ik}\delta_{jl} + \delta_{il}\delta_{jk}) \tag{5.22}$$

where the expressions of the second-rank tensors $(T_r)^{(1)}_{IK}$ and $(T_r)^{(2)}_{IJ}$ are provided in **Appendix B**.

5.4 Overall Elastic Moduli of Fiber Reinforced Composites with Progressive Fiber Breakage

To derive the overall elastic moduli of the composites, we next seek the relationship between the ensemble-volume averaged stress and strain fields. Substituting Equation (5.20) into Equation (5.8) leads to the expression of the far-field strain in terms of the ensemble-volume averaged strain as follows:

$$\boldsymbol{\varepsilon}^0 = \mathbf{B}^{-1} : \langle \bar{\boldsymbol{\varepsilon}} \rangle \tag{5.23}$$

where the fourth-rank tensor $\mathbf{B}$ has the form

$$\mathbf{B} = \mathbf{I} + \sum_{r=1}^{n} \phi_r \cdot \mathbf{S} \bullet \mathbf{T}_r \tag{5.24}$$

Alternatively, the expression can be written in the following generalized isotropic fourth-rank tensor form:

$$\mathbf{B}_{ijkl} = B_{IK}^{(1)} \delta_{ij} \delta_{kl} + B_{IJ}^{(2)} (\delta_{ik} \delta_{jl} + \delta_{il} \delta_{jk}) \tag{5.25}$$

where

$$B_{IK}^{(1)} = \sum\nolimits_{r=1}^{n} \phi_r [2 S_{IK}^{(1)} (T_r)_{KK}^{(2)} + 2 S_{II}^{(2)} (T_r)_{IK}^{(1)} + \sum\nolimits_{R=1}^{3} S_{IR}^{(1)} (T_r)_{RK}^{(1)}] \tag{5.26}$$

$$B_{IJ}^{(2)} = \frac{1}{2} + \sum\nolimits_{r=1}^{n} 2 \phi_r S_{IJ}^{(2)} (T_r)_{IJ}^{(2)} \tag{5.27}$$

By combining Equations (5.20) and (5.23), we can reach the expression as follows:

$$\left\langle \bar{\boldsymbol{\varepsilon}}^{**} \right\rangle_r = \left(\mathbf{B}^{-1} \bullet \mathbf{T}_r \right) : \langle \bar{\boldsymbol{\varepsilon}} \rangle \tag{5.28}$$

With the aid of Equations (5.9) and (5.28), the ensemble-volume averaged strain and ensemble-volume averaged stress is

$$\langle \bar{\boldsymbol{\sigma}} \rangle = \left\{ \mathbf{C}_0 \bullet \left[\mathbf{I} - \sum_{r=1}^{n} \phi_r \left(\mathbf{B}^{-1} \bullet \mathbf{T}_r \right) \right] \right\} : \langle \bar{\boldsymbol{\varepsilon}} \rangle \tag{5.29}$$

Hence, based on the theory of micromechanics and linear elastic fracture mechanics, the overall homogenized elasticity moduli for the longitudinally fiber reinforced composites with progressive fiber breakage are derived:

$$\mathbf{C}^{*} = \mathbf{C}_0 \bullet \left[\mathbf{I} - \sum_{r=1}^{n} \phi_r \cdot \mathbf{B}^{-1} \bullet \mathbf{T}_r \right] \tag{5.30}$$

The above expression of the overall elasticity moduli can be recast into the following generalized isotropic fourth-rank tensor form:

$$\mathbf{C}^{*}_{ijkl} = C^{*(1)}_{IK} \delta_{ij} \delta_{kl} + C^{*(2)}_{IJ} (\delta_{ik} \delta_{jl} + \delta_{il} \delta_{jk}) \tag{5.31}$$

where

$$C^{*(1)}_{IJ} = \lambda_0 - \sum_{r=1}^{n} \phi_r (2\lambda_0 Z^{(2)}_{KK} + 2\mu_0 Z^{(1)}_{IK} + \lambda_0 \sum_{R=1}^{3} Z^{(1)}_{RK}), \quad C^{*(2)}_{IJ} = \mu_0 (1 - \sum_{r=1}^{n} 2\phi_r Z^{(2)}_{IJ}) \tag{5.32}$$

and

$$Z^{(1)}_{IK} = 2\left(B^{-1}\right)^{(1)}_{IK} \left(T_r\right)^{(2)}_{KK} + 2\left(B^{-1}\right)^{(2)}_{II} \left(T_r\right)^{(1)}_{IK} + \sum_{R=1}^{3} \left(B^{-1}\right)^{(1)}_{IR} \left(T_r\right)^{(1)}_{RK} \tag{5.33}$$

$$Z^{(2)}_{IJ} = 2\left(B^{-1}\right)^{(2)}_{IJ} \left(T\right)^{(2)}_{r\,IJ} \tag{5.34}$$

$$\left(B^{-1}\right)^{(1)}_{IK} = -Q_{IK} \big/ 2B^{(2)}_{II} \tag{5.35}$$

$$\left(B^{-1}\right)^{(2)}_{IJ} = 1 \big/ 4B^{(2)}_{IJ} \tag{5.36}$$

$$Q_{I1} = [(B_{22}^{(1)} + B_{22}^{(2)})B_{I1}^{(1)} - B_{21}^{(1)}B_{I2}^{(1)}] \big/ [(B_{22}^{(1)} + B_{22}^{(2)})(B_{11}^{(1)} + 2B_{11}^{(2)}) - B_{12}^{(1)}B_{21}^{(1)}] \tag{5.37}$$

$$Q_{I2} = Q_{I3} = [(B_{11}^{(1)} + 2B_{11}^{(2)})B_{I2}^{(1)} - B_{12}^{(1)}B_{I1}^{(1)}] \big/ 2[(B_{22}^{(1)} + B_{22}^{(2)})(B_{11}^{(1)} + 2B_{11}^{(2)}) - B_{12}^{(1)}B_{21}^{(1)}] \tag{5.38}$$

where λ_0 and μ_0 are the Lame constants of the matrix phase. The fiber stress in the *r*th phase inclusion for computing the damage evolution of fiber breakage as shown in Equation (5.19) can then be obtained by

$$\begin{aligned} \left\langle \bar{\boldsymbol{\sigma}}_f \right\rangle_r &= \mathbf{C}_0 : \left[\boldsymbol{\varepsilon}^0 + (\mathbf{S} - \mathbf{I}) : \left\langle \bar{\boldsymbol{\varepsilon}}^{**} \right\rangle_r \right] \\ &= \mathbf{C}_0 : \left[\mathbf{I} + (\mathbf{S} - \mathbf{I}) \bullet \mathbf{T}_r \right] : \boldsymbol{\varepsilon}^0 \\ &= \left\{ \mathbf{C}_0 \bullet \left[\mathbf{I} + (\mathbf{S} - \mathbf{I}) \bullet \mathbf{T}_r \right] \bullet \mathbf{B}^{-1} \right\} : \left\langle \bar{\boldsymbol{\varepsilon}} \right\rangle \end{aligned} \tag{5.39}$$

5.5 Computational Algorithm for Modeling of Progressive Damage of Fiber Breakage in Longitudinal Fiber Reinforced Composites

A strain-driven algorithm is employed to determine the overall stress history by the given overall strain history. Given the known state from the previous time step $t = t_\lambda$, the goal is to determine the unknown state $\left\{ \bar{\boldsymbol{\varepsilon}}_{(\lambda+1)}, \bar{\boldsymbol{\varepsilon}}^*_{cr(\lambda+1)}, \bar{\boldsymbol{\varepsilon}}'_{(\lambda+1)}, n_{(\lambda+1)}, \bar{\boldsymbol{\sigma}}_{(\lambda+1)} \right\}$ at the time step $t = t_{\lambda+1}$. The fiber stress and its induced fiber break number are computed by an internal numerical iteration at the (λ+1)th time step, with the following convergence criteria:

$$\left| n^{\nu}_{(\lambda+1)} - n^{\nu-1}_{(\lambda+1)} \right| \le TOL \tag{5.40}$$

and

$$(\bar{\boldsymbol{\sigma}}_f)^{\nu}_{(\lambda+1)} = \{ \mathbf{C}_0 \bullet [\mathbf{I} - \sum_{r=1}^{n} \phi_r ((\mathbf{B}^{\nu}_{(\lambda+1)})^{-1} \bullet (\mathbf{T}_r)^{\nu}_{(\lambda+1)})] \} : \bar{\boldsymbol{\varepsilon}}_{(\lambda+1)} \tag{5.41}$$

$$\left(n\right)_{r(\lambda+1)}^{\nu}=\left(p_1\right)_{(\lambda+1)}^{\nu}\cdot n_{saturated} \tag{5.42}$$

$$\left(p_1\right)_{(\lambda+1)}^{\nu}=1-\exp\left[-\left(\frac{\left(\bar{\sigma}_f\right)_{(\lambda+1)}^{\nu}-\sigma_{cr}}{S}\right)^{M}\right] \quad \text{if} \quad \left(\bar{\sigma}_f\right)_{(\lambda+1)}^{\nu}\geq\sigma_{cr} \tag{5.43}$$

where ν is the internal iteration index. Therefore, the overall elastic moduli at the current time step can be computed by

$$\mathbf{C}_{(\lambda+1)}^{*}=\mathbf{C}_0\bullet\left[\mathbf{I}-\sum_{r=1}^{n}\phi_r\cdot\mathbf{B}_{(\lambda+1)}^{-1}\bullet\left(\mathbf{T}_r\right)_{(\lambda+1)}\right] \tag{5.44}$$

Consequently, the overall stress $\bar{\boldsymbol{\sigma}}_{\lambda+1}$ at the current time step can be updated as

$$\bar{\boldsymbol{\sigma}}_{(\lambda+1)}=\bar{\boldsymbol{\sigma}}_{(\lambda)}+\mathbf{C}_{(\lambda+1)}^{*}:\Delta\bar{\boldsymbol{\varepsilon}}_{(\lambda+1)} \tag{5.45}$$

For convenience, Table 5.1 summarizes the above micromechanical iterative computational algorithm for the overall elastic responses of longitudinally fiber reinforced composites with progressive damages due to fiber breaks.

5.6 Numerical Results

First, we apply the newly proposed micromechanical damage framework to investigate the evolutionary fiber breaking process in single-fiber composites. The available experimental data of the single-fiber composite fragmentation tests provided by Zhao et al. (2000) are adopted for validation purpose. In their experimental study, the number of observed fiber breakages is recorded at each applied stress level until the specimen fragmentation reaches its critical length. In particular, SFCs with three surface treatments: the water-sized (untreated) E-glass fiber, γ-

GPS treated E-glass fiber, and γ-MPS treated E-glass fiber are used to account for the various interfacial bonding strengths. The following material and physical properties of composites are used in theoretical predictions: epoxy resin matrix with Young's modulus $E_m = 2600$ MPa, Poisson's ratio $\nu_m = 0.34$, E-glass fiber with Young's modulus $E_f = 72.5$ GPa, Poisson's ratio $\nu_f = 0.22$, fiber length $L_f = 25.4$ mm, fiber diameter $d_f = 14\ \mu$m. A two-parameter Weibull model as depicted in Equation (5.19) is employed to govern the damage evolution due to fiber breakage. The critical fiber breaking stress σ_{cr} and the number of fiber breakages at saturation $n_{saturated}$ are characterized by the nonlinear least-squares fitting. The theoretical predictions are summarized in Table 5.2 and Figure 4.1–Figure 5.3. The numerical results agree well with the available experimental data and the p-vales of the Kolmogorov-Smirmov (K-S) goodness-of-fit test are accepted at the 5% significance level for all the testing samples. Moreover, the predicted σ_{cr} and $n_{saturated}$ display good agreement with the experimental observations as shown in Table 5.3. Therefore, we conclude that the newly proposed micromechanical damage model is suitable for modeling of the progressive fiber breaking process in fiber reinforced composites.

Next, we apply the proposed model to investigate the tensile behavior of a multi-fiber reinforced titanium alloy matrix composite by considering the fiber breakage evolution with the homogeneous fashion. The parametric studies are performed thereafter to investigate the effects of material properties and matrix and fiber phases upon the predicted mechanical behaviors of the composite materials. The experimental data (Jeng et al., 1991) are available for three different titanium alloy matrix materials with unidirectional aligned SCS-6 fibers: Ti-6Al-4V (SCS-6/Ti-6-4), Ti-15V-3Al-3Cr-3Sn (SCS-6/Ti-15-3), and Ti-25Al-10Nb (SCS-6/Ti-25-10).

Fabricated condition is considered for all three cases, whereas a heat-treated condition with $500\ ^{\circ}\text{C}/12$ hrs heating rate is also examined for SCS-6/Ti-6-4 and SCS-6/Ti-25-10 composites. The material properties for the three composites are summarized as follows: Young's moduli $E_m^{Ti-6-4} = 113.8$ GPa , $E_m^{Ti-15-3} = 82$ GPa , $E_m^{Ti-25-10} = 113.3$ GPa $E_f^{SCS-6} = 400$ GPa; Poisson's ratios $\nu_m^{Ti-6-4} = 0.342$, $\nu_m^{Ti-15-3} = 0.33$, $\nu_m^{Ti-25-10} = 0.34$, $\nu_f^{SCS-6} = 0.25$, fiber volume fraction $\phi_f = 0.35$, fiber diameter $d_f = 142\ \mu$m , and fiber length $L_f = 125$ mm . Two Weibull parameters, S and M , the initial crack stress level σ_{cr} and the saturated number of fiber breaks $n_{saturated}$ are obtained through a nonlinear least-squares fit. For simplicity, the temperature effect is assumed to affect these four characterized parameters implicitly.

Table 5.3 summarizes the theoretical predictions for the tensile fragmentation behavior of the fiber reinforced titanium alloy matrix composites by the proposed micromechanical model. Figure 5.8–Figure 5.10 exhibit the comparisons of the stress-strain relationship between the numerical predictions and the experimental data. The numerical results are in general in good agreement with the experimental data below the yield strain (about 0.45~0.55 % as observed in the experiments), whereas the predictions deviate from the experimental observations slightly after the titanium alloy matrix reaches its yielding point, especially for the SCS-6/Ti-6-4 and SCS-6/Ti-15-3. The discrepancies may be due to the post-yielding plastic response of the matrix. This issue will be further taken into consideration in the next chapter.

To further investigate the effects of various material properties on the mechanical behaviors of the composites, we hereby perform the following parametric studies using the proposed micromechanical damage model. Due to the small-strain assumption, we only demonstrate the numerical predictions within the strain level of 1.5%. Figure 5.11–Figure 5.13 illustrate the overall stress-strain relations, the progressive damage evolution due to fiber breaking, and the overall effective elastic modulus along the loading direction with different volume fractions of reinforcing fibers ϕ_f. As the fiber volume fraction increases, the predicted macroscopic stress and the overall effective elastic modulus increase as well, resulting a greater resistance to the fiber breaking. This demonstrates the strengthening effect of the composites with longitudinally reinforcing fibers.

The effects of the fiber Young's modulus ratio E_f / E_m, fiber Poisson's ratio v_f, and matrix Poisson's ratio v_m upon the mechanical behaviors of composites with a constant fiber volume fraction of 30% are illustrated in Figure 5.14–Figure 5.16, Figure 5.17–Figure 5.19, and Figure 5.20–Figure 5.22, respectively. Although the stiffer reinforcement can increase the overall effective properties of the composites, it also increases the corresponding stress level in the fiber, thus the earlier initiation of fiber breaking. On the other hand, the increase in Poisson's ratio of both the matrix and fiber leads to the increase of the overall effective properties of the composites, thus the earlier damage initiation due to fiber breaking. Therefore, it is recommended in the design of fiber reinforced composites to carefully choose proper material properties of the matrix and fibers with a compromise between the enhancement of strength and the reduction of fiber-breaking resistance.

5.7 Conclusions

In this chapter, a computational micromechanics-based damage framework has been developed to predict the overall behavior and the damage evolution due to progressive fiber breakage in continuous fiber reinforced composites. The effect of the fiber breakage evolution is successfully quantified by an effective eigenstrain field based on the theories of linear elastic fracture mechanics and micromechanical damage mechanics. The accumulation of the break number is governed by a two-parameter Weibull probability function, which implicitly encloses the information of spatial distributions of the fiber breaks and the temperature effect on the damage evolution. The proposed model is validated with the experimental data of the single-fiber composite fragmentation tests from Zhao et al. (2000). Moreover, the proposed model is applied to investigate the fiber breakage evolution in multi-fiber composites with the homogeneous fashion. The predictions are validated with the overall stress-strain response of the titanium alloy matrix composites under the tensile fragmentation tests by Jeng et al. (1991). Numerical results indicate that the overall material response is sensitive to the fiber and matrix Young's modulus ratio. As a result, it is critical in the design of fiber reinforced composites to carefully choose proper material properties of the matrix and fibers for optimization between the reinforcement effect and the fiber-breaking resistance.

Table 5.1 Computational algorithm for the overall elastostatic damage response of fiber reinforced composites with fiber breakage evolution

Given: $\{\bar{\boldsymbol{\varepsilon}}_{(\lambda)}, \bar{\boldsymbol{\varepsilon}}^{*}_{cr(\lambda)}, \bar{\boldsymbol{\varepsilon}}'_{(\lambda)}, n_{(\lambda)}, \bar{\boldsymbol{\sigma}}_{(\lambda)}\}$ at the time step λ and with the strain increment $\{\Delta\bar{\varepsilon}_{(\lambda+1)}\}$

Solve: $\{\bar{\boldsymbol{\varepsilon}}_{(\lambda+1)}, \bar{\boldsymbol{\varepsilon}}^{*}_{cr(\lambda+1)}, \bar{\boldsymbol{\varepsilon}}'_{(\lambda+1)}, n_{(\lambda+1)}, \bar{\boldsymbol{\sigma}}_{(\lambda+1)}\}$ at the time step $(\lambda+1)$

i. Initialize: $\{\bar{\boldsymbol{\varepsilon}}_{(0)}=0, \bar{\boldsymbol{\varepsilon}}^{*}_{cr(0)}=0, \bar{\boldsymbol{\varepsilon}}'_{(0)}=0, n_{(0)}=0, \bar{\boldsymbol{\sigma}}_{(0)}=0\}$, and $(p_1)_{(0)}=0$

ii. Compute: $\bar{\boldsymbol{\varepsilon}}_{(\lambda+1)} = \bar{\boldsymbol{\varepsilon}}_{(\lambda)} + \Delta\bar{\boldsymbol{\varepsilon}}_{(\lambda+1)}$

iii. Compute: $\{\bar{\boldsymbol{\varepsilon}}^{*}_{cr(\lambda+1)}, n_{(\lambda+1)}, p_{1(\lambda+1)}\}$ with internal iterations until $|n^{\nu}_{(\lambda+1)} - n^{\nu-1}_{(\lambda+1)}| \le TOL$

$$(n)^{0}_{r(\lambda+1)} = (n)_{r(\lambda)}$$

$$(\mathbf{T}_r)^{\nu}_{(\lambda+1)} = -[\mathbf{C}_1 \bullet \mathbf{S} - \mathbf{C}_0 \bullet (\mathbf{S}-\mathbf{I}) - \beta \cdot (n)^{\nu}_{r(\lambda+1)} \cdot \mathbf{C}_1 \bullet \boldsymbol{\Gamma} \bullet \mathbf{C}_0 \bullet (\mathbf{S}-\mathbf{I})]^{-1} \bullet [\mathbf{C}_1 - (\mathbf{I} + \beta \cdot (n)^{\nu}_{r(\lambda+1)} \cdot \mathbf{C}_1 \bullet \boldsymbol{\Gamma}) \bullet \mathbf{C}_0]$$

$$\mathbf{B}^{\nu}_{(\lambda+1)} = \mathbf{I} + \sum\nolimits_{r=1}^{n} \phi_r \cdot \mathbf{S} \bullet (\mathbf{T}_r)^{\nu}_{(\lambda+1)}$$

$$(\bar{\boldsymbol{\sigma}}_f)^{\nu}_{(\lambda+1)} = \{\mathbf{C}_0 \bullet [\mathbf{I} - \sum_{r=1}^{n} \phi_r (\mathbf{B}^{-1}_{(\lambda+1)} \bullet (\mathbf{T}_r)^{\nu}_{\lambda+1})]\} : \bar{\boldsymbol{\varepsilon}}_{(\lambda+1)}$$

$$(< \bar{\boldsymbol{\varepsilon}}^{*}_{cr} >_r)^{\nu}_{(\lambda+1)} = \beta \cdot n^{\nu}_{(\lambda+1)} \cdot \boldsymbol{\Gamma} : (\bar{\boldsymbol{\sigma}}_f)^{\nu}_{(\lambda+1)}$$

$$(n)^{\nu}_{r(\lambda+1)} = (p_1)^{\nu}_{(\lambda+1)} \cdot n_{saturated}$$

$$(p_1)^{\nu}_{(\lambda+1)} = 1 - \exp[-((\bar{\sigma}_f)^{\nu}_{(\lambda+1)} - \sigma_{cr}/S)^{M}] \quad \text{if} \quad (\bar{\sigma}_f)^{\nu}_{(\lambda+1)} \ge \sigma_{cr}$$

iv. Compute: $\mathbf{C}^{*}_{(\lambda+1)} = \mathbf{C}_0 \bullet [\mathbf{I} - \sum\nolimits_{r=1}^{n} \phi_r \cdot \mathbf{B}^{-1}_{(\lambda+1)} \bullet (\mathbf{T}_r)_{(\lambda+1)}]$

v. Calculate: $\bar{\boldsymbol{\sigma}}_{(\lambda+1)} = \bar{\boldsymbol{\sigma}}_{(\lambda)} + \mathbf{C}^{*}_{(\lambda+1)} : \Delta\bar{\boldsymbol{\varepsilon}}_{(\lambda+1)}$

vi. Go to (ii) (next step computation)

Table 5.2 Summary of theoretical predictions and experimental data of the fragmentation tests of single-fiber composites.

		Water-sized fibers	γ-GPS treated fibers	γ-MPS treated fibers
S (MPa)		1475	2040	2467
M		2.026	1.334	2.949
σ_{cr} (MPa)	Theoretical Prediction	731	1954	843
	Experimental Observation	500~800	1700~2000	700~900
$n_{saturated}$ (in 20 mm gauge length)	Theoretical Prediction	81.27	63.26	60.28
	Experimental Observation	75~80	60	60

Table 5.3 Summary of theoretical predictions for the tensile test of fiber reinforced titanium alloy matrix composites.

	SCS-6/Ti-6-4		SCS-6/Ti-15-3	SCS-6/Ti-25-10	
	Fabricated	800 °C/12hrs	Fabricated	Fabricated	800 °C/12hrs
S (MPa)	1613.78	2595.47	1459.57	1659.60	1196.69
M	1.025	2.551	2.508	0.713	2.265
σ_{cr} (MPa)	258.54	257.07	1022.87	552.76	833.57
$n_{saturated}$	156.89	351.62	189.54	39.99	259.56

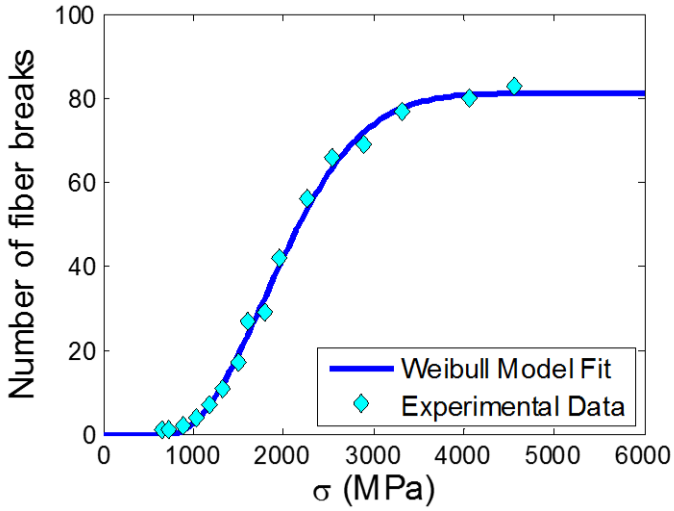

Figure 5.1 Comparisons of the number of observed fiber breaks versus applied stress between the theoretical prediction and the experimental data (water-sized fibers).

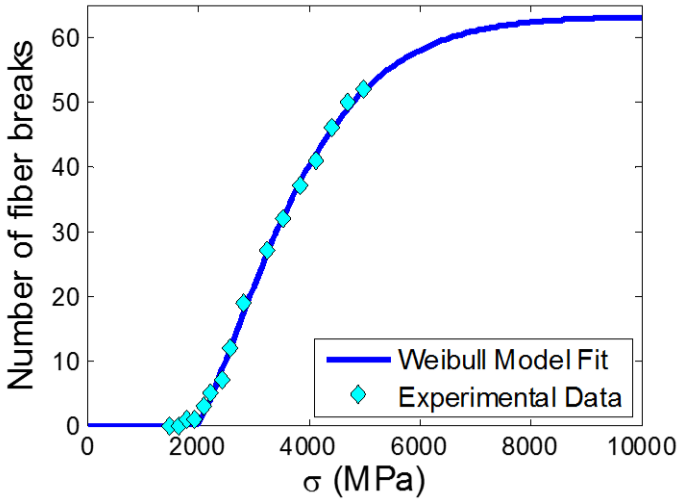

Figure 5.2 Comparisons of the number of observed fiber breaks versus applied stress between the theoretical prediction and the experimental data (γ-GPS fibers).

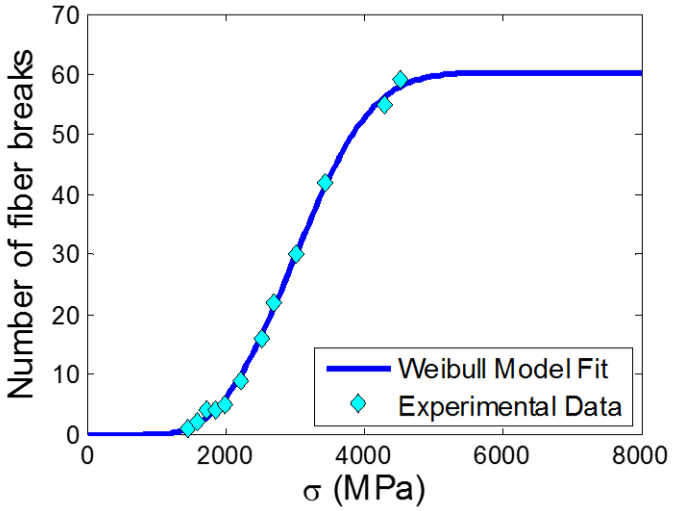

Figure 5.3 Comparisons of the number of observed fiber breaks versus applied stress between the theoretical prediction and the experimental data (γ-MPS fibers).

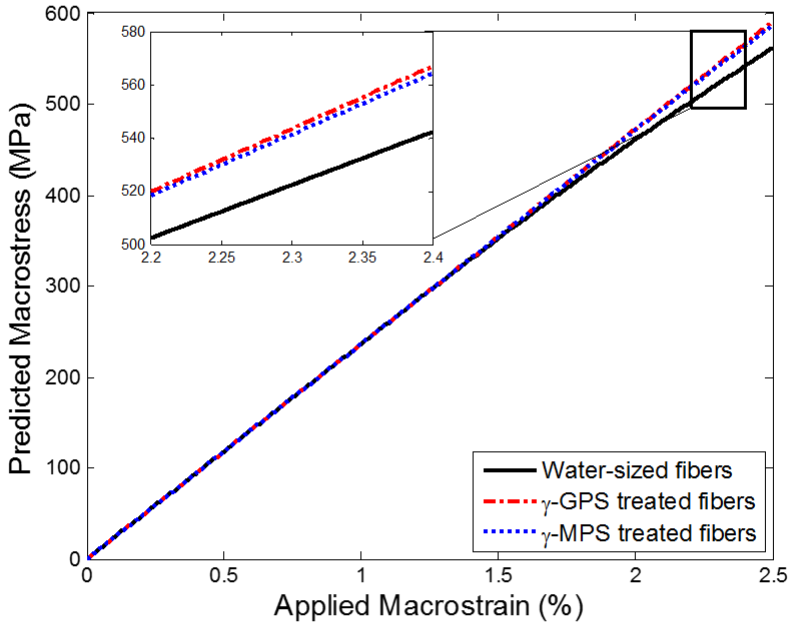

Figure 5.4 Comparisons of predicted behaviors of longitudinally fiber reinforced composites considering progressive fiber breaking with different surface treatments: predicted stress-strain relationships.

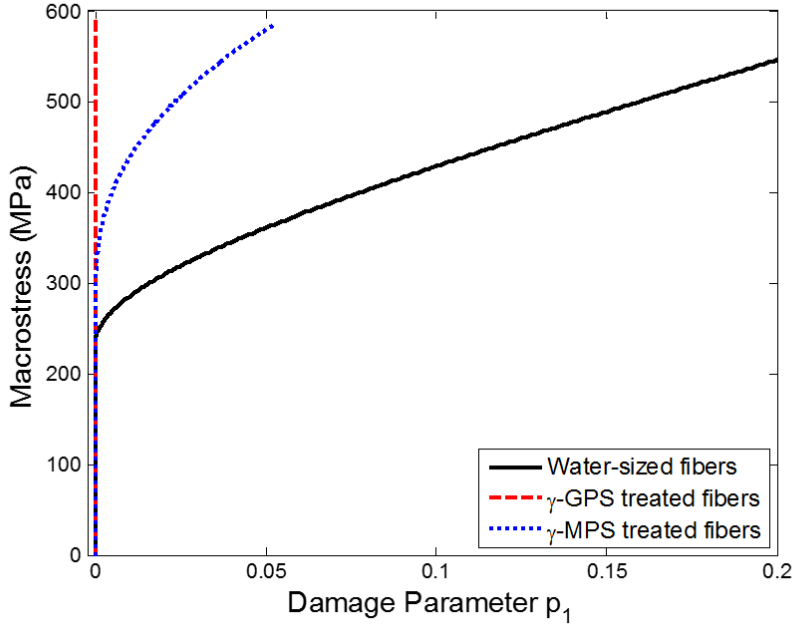

Figure 5.5 Comparisons of predicted behaviors of longitudinally fiber reinforced composites considering progressive fiber breaking with different surface treatments: predicted stress versus damage parameter p_1.

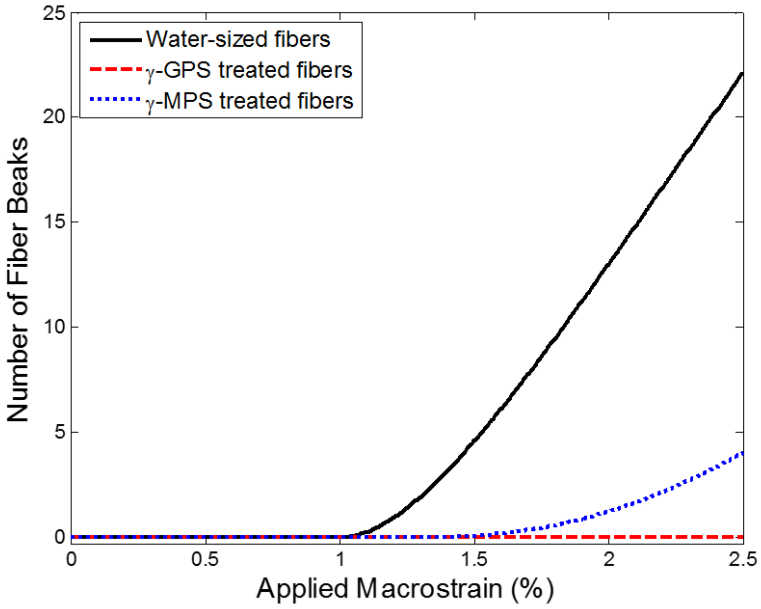

Figure 5.6 Comparisons of predicted behaviors of longitudinally fiber reinforced composites considering progressive fiber breaking with different surface treatments: predicted number of fiber breaks versus macroscopic strain.

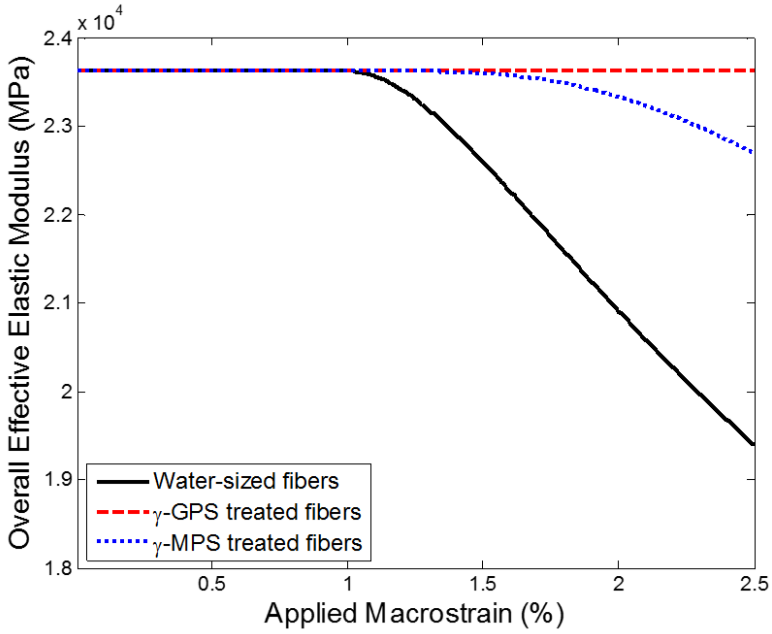

Figure 5.7 Comparisons of predicted behaviors of longitudinally fiber reinforced composites considering progressive fiber breaking with different surface treatments: overall effective elastic modulus versus macroscopic strain.

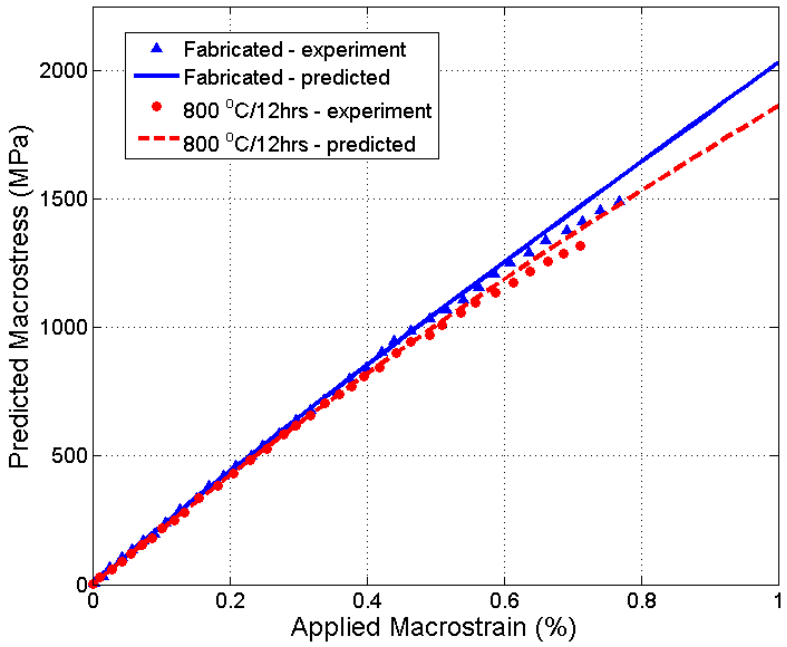

Figure 5.8 Comparisons between numerical predictions and experimental data of fiber reinforced titanium alloy matrix composites: SCS-6/Ti-15-3 composite.

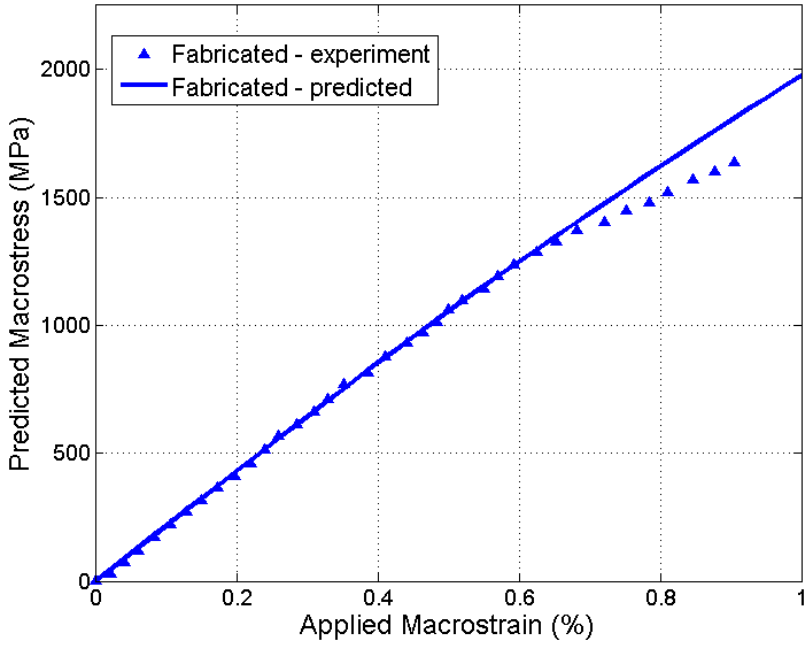

Figure 5.9 Comparisons between numerical predictions and experimental data of fiber reinforced titanium alloy matrix composites: SCS-6/Ti-6-4 composite.

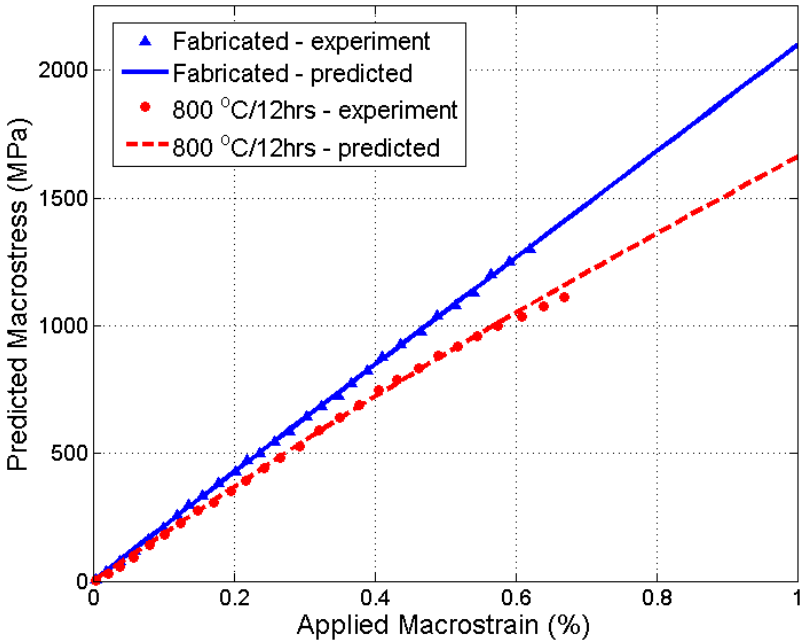

Figure 5.10 Comparisons between numerical predictions and experimental data of fiber reinforced titanium alloy matrix composites: SCS-6/Ti-25-10 composite.

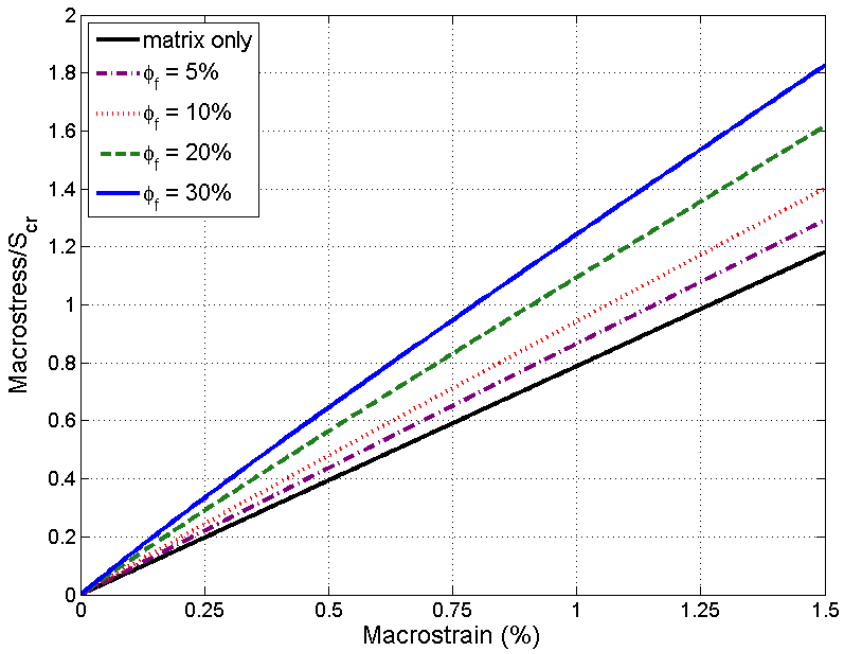

Figure 5.11 Comparisons of predicted behaviors of longitudinally fiber reinforced composites considering progressive fiber breaking with various volume fractions of fibers: predicted stress-strain relationships.

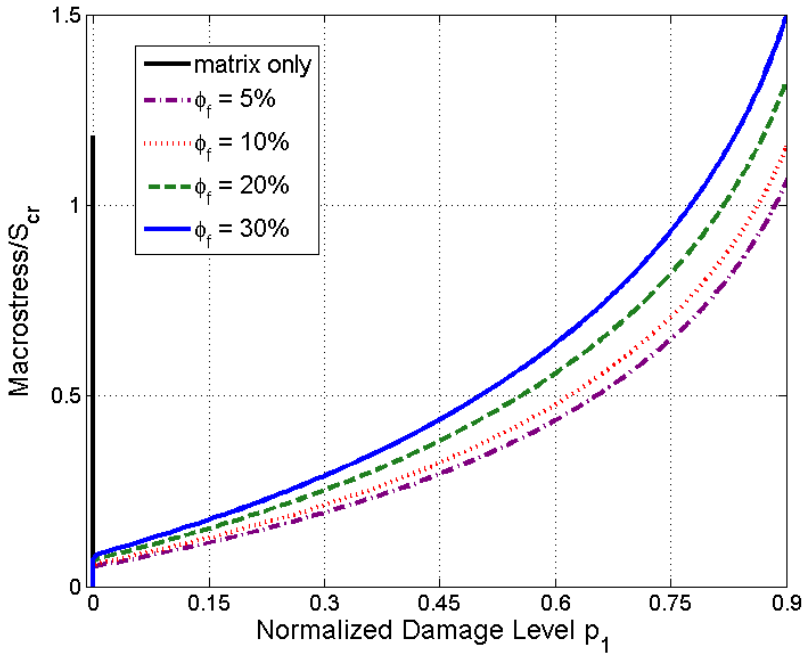

Figure 5.12 Comparisons of predicted behaviors of longitudinal fiber reinforced composites considering progressive fiber breaking with various volume fractions of fibers: predicted stress versus damage parameter.

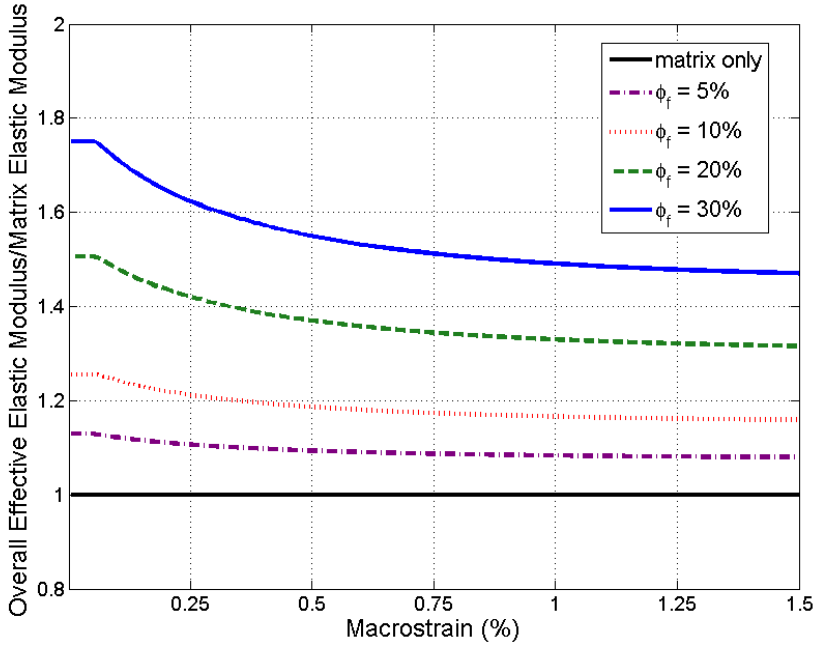

Figure 5.13 Comparisons of predicted behaviors of longitudinal fiber reinforced composites considering progressive fiber breaking with various volume fractions of fibers: overall effective elastic modulus versus macroscopic strain.

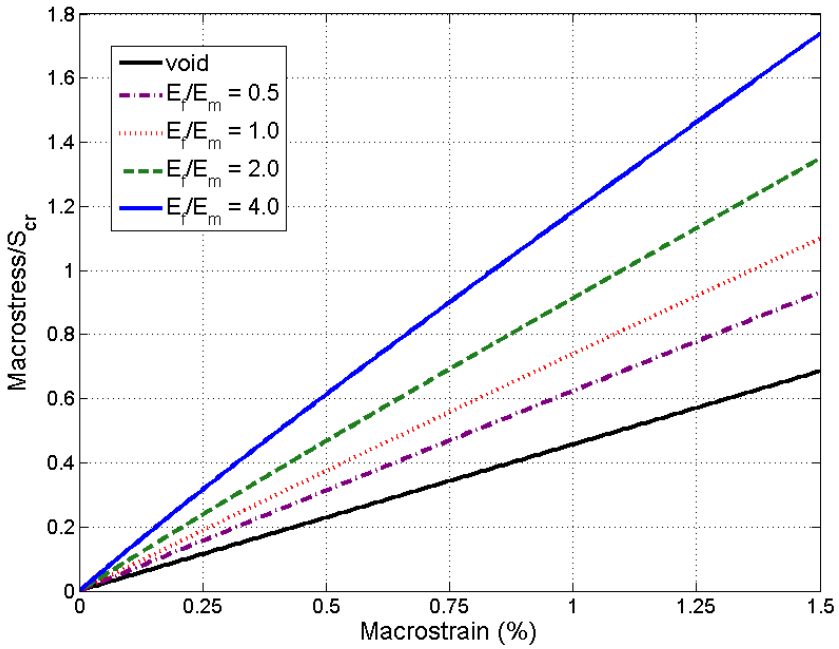

Figure 5.14 Comparisons of predicted behaviors of longitudinal fiber reinforced composites considering progressive fiber breaking with various Young's moduli of fibers: predicted stress-strain relationships.

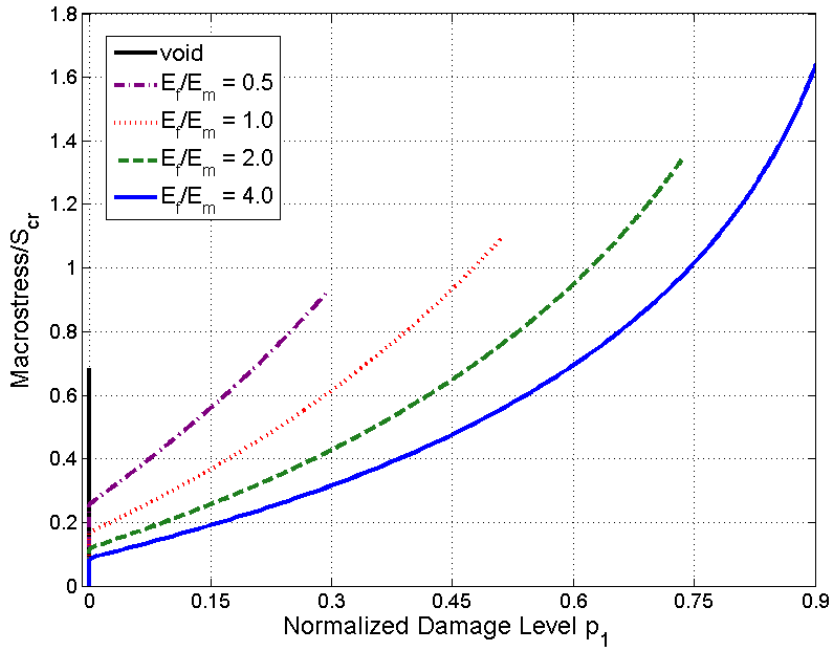

Figure 5.15 Comparisons of predicted behaviors of longitudinal fiber reinforced composites considering progressive fiber breaking with various Young's moduli of fibers: predicted stress versus damage parameter.

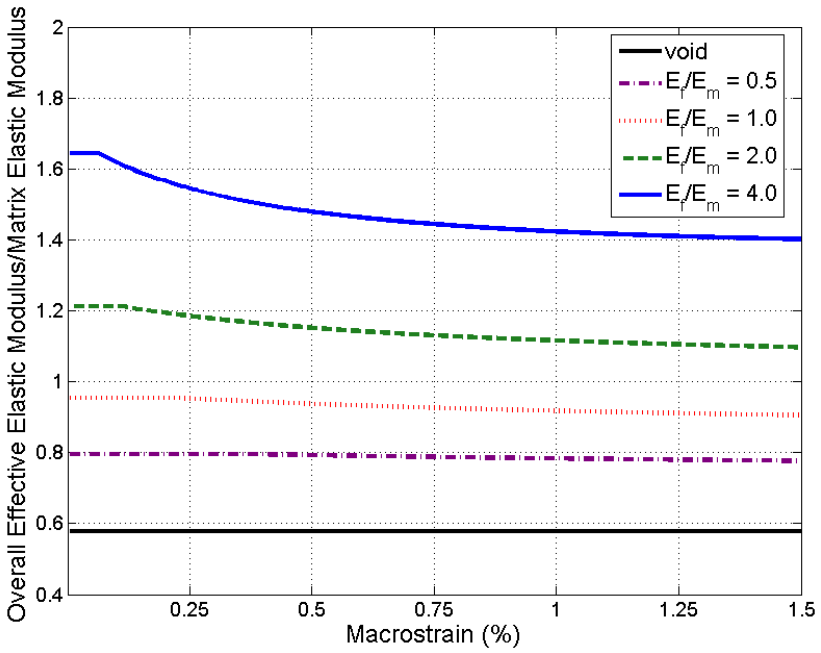

Figure 5.16 Comparisons of predicted behaviors of longitudinal fiber reinforced composites considering progressive fiber breaking with various Young's modulus values of fibers: overall effective elastic modulus versus macroscopic strain.

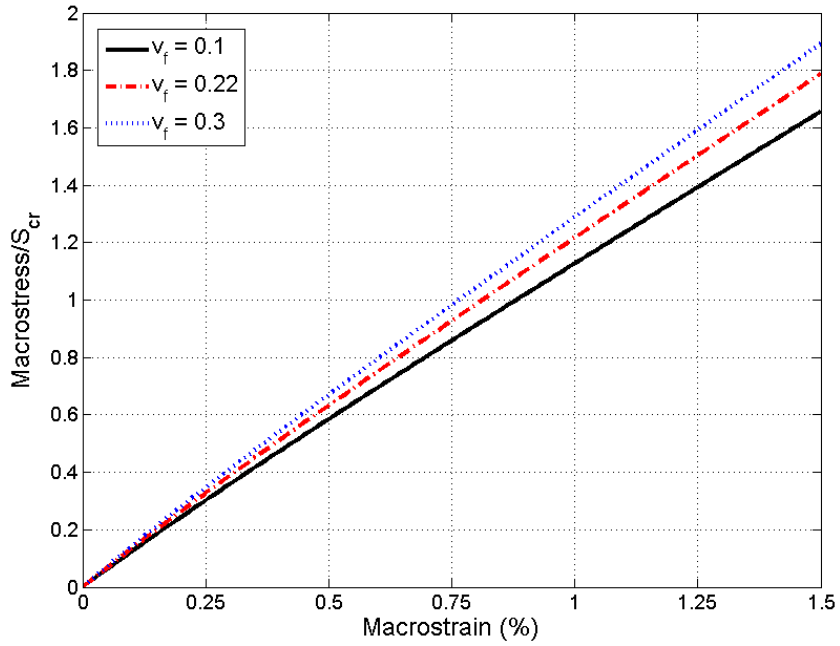

Figure 5.17 Comparisons of predicted behaviors of longitudinal fiber reinforced composites considering progressive fiber breaking with various Poisson's ratios of fiber: predicted stress-strain relationships.

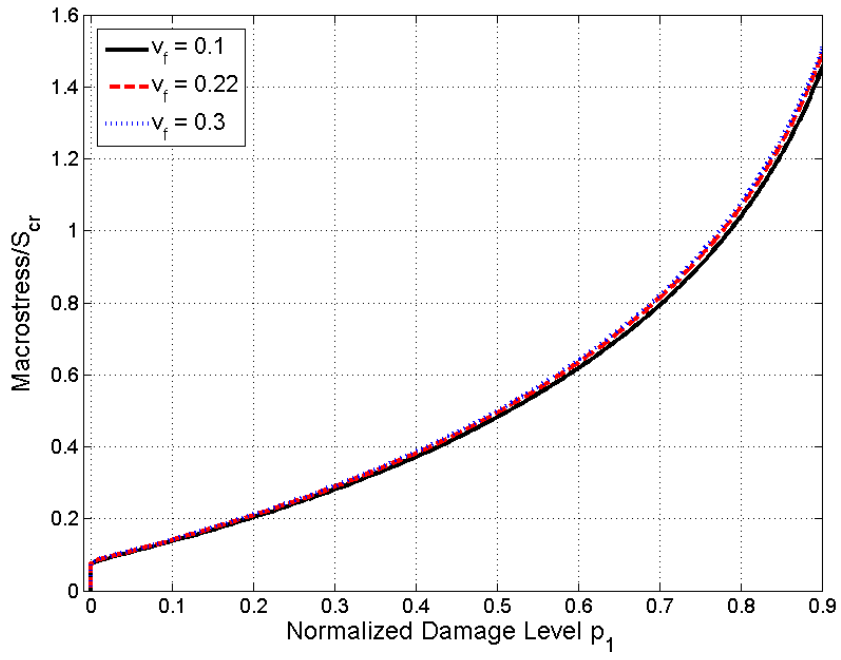

Figure 5.18 Comparisons of predicted behaviors of longitudinal fiber reinforced composites considering progressive fiber breaking with various Poisson's ratios of fiber: predicted stress versus damage parameter.

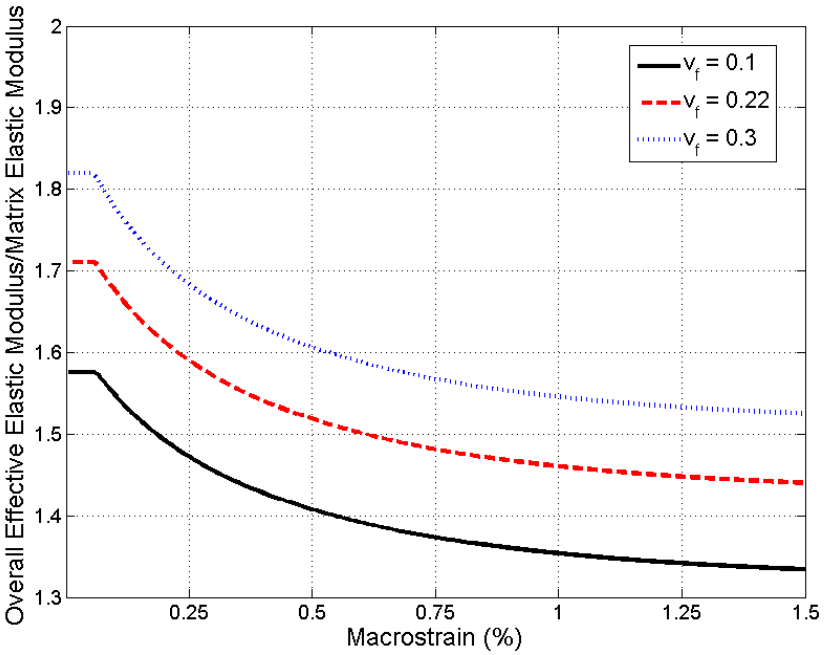

Figure 5.19 Comparisons of predicted behaviors of longitudinal fiber reinforced composites considering progressive fiber breaking with various Poisson's ratios of fiber: overall effective elastic modulus versus macroscopic strain.

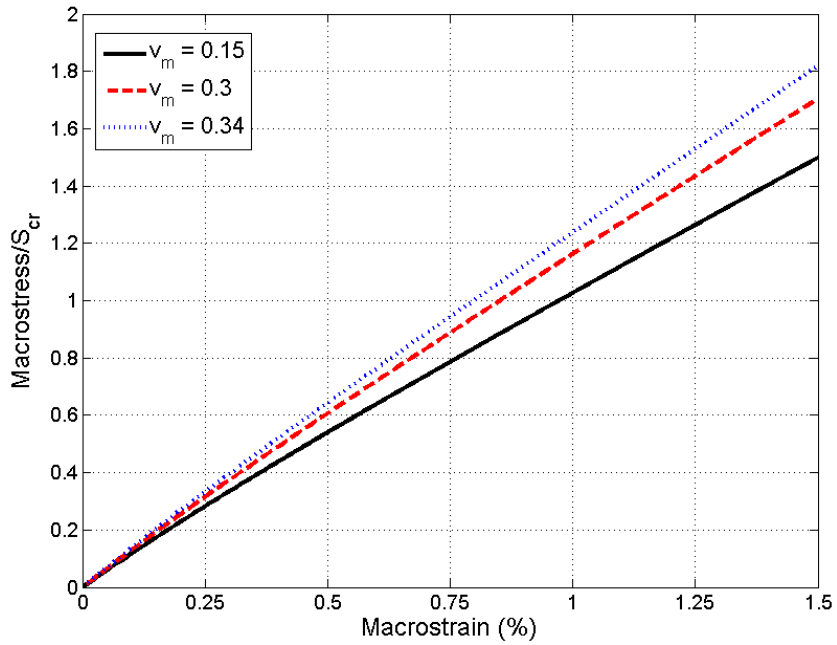

Figure 5.20 Comparisons of predicted behaviors of longitudinal fiber reinforced composites considering progressive fiber breaking with various Poisson's ratios of matrix: predicted stress-strain relationships.

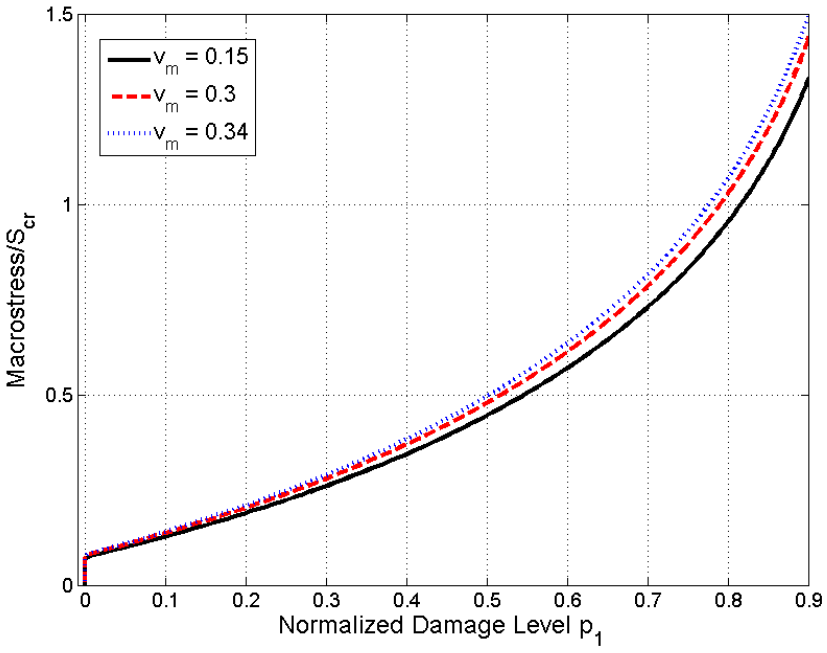

Figure 5.21 Comparisons of predicted behaviors of longitudinal fiber reinforced composites considering progressive fiber breaking with various Poisson's ratios of matrix: predicted stress versus damage parameter.

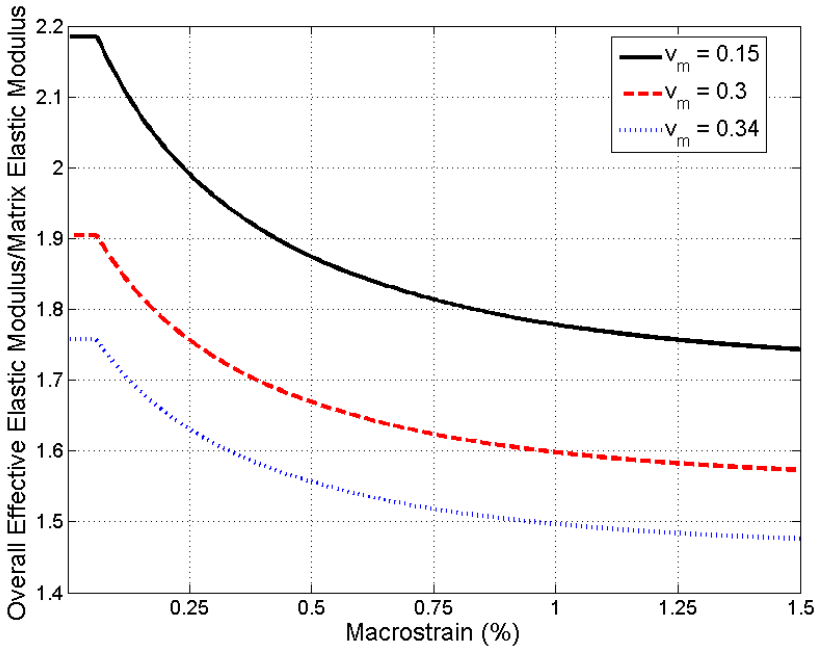

Figure 5.22 Comparisons of predicted behaviors of longitudinal fiber reinforced composites considering progressive fiber breaking with various Poisson's ratios of matrix ν_m : overall effective elastic modulus versus macroscopic strain.

CHAPTER 6 STOCHASTIC SIMULATIONS OF FIBER BREAKAGE EVOLUTION IN LONGITUDINAL MULTI-FIBER REINFORCED COMPOSITES

6.1 Introduction

The fiber fragmentation evolution in longitudinal multi-fiber reinforced composites is characterized as a stochastic process for several reasons. First of all, the fiber strength is not uniform due to manufacturing defects. Fibers fracture at random positions depending on their strength distributions. Second, the local microstructure of a multi-fiber reinforced composite is complex. The interactions among material phases are more complicated than that in a single-fiber composite. Third, the interfacial bonding conditions may not be perfect due to the limitations of the current manufacturing techniques. More importantly, once a fiber breakage occurs, the stress around the breakage region increases and drives further damage locally. The mechanism of the load transferring from broken fibers to intact fibers is difficult to be determined analytically. As a result, the composite failure becomes statistical and the fiber fragmentation evolution follows some probability distribution.

The objective of this chapter is to investigate the fiber breakage evolution in a longitudinal multi-fiber reinforced composite with an inhomogeneous fashion based on the micromechanical framework proposed in the previous chapter. The following assumptions are adopted for this study: i) the failure strain of the embedded fibers is much lower than that of the matrix, ii) the bonding conditions are perfect. In other words, we herein focus on composites with brittle fibers,

relatively ductile matrix, and perfectly bonded interface. The remainder of this chapter is organized as follows. First, the stochastic unit cell approach is introduced for the modeling of fiber breakage evolution. Two stochastic risk-competing models are proposed subsequently to simulate the fiber breakage evolution in an inhomogeneous fashion considering different load sharing mechanisms. The first risk-competing model states that the nearest neighboring fibers of the damaged fiber with the dominant weakness will fracture with some probability, while the second model assumes that all surrounding fibers associated with the broken fibers have an equal chance to fracture with some probability. Finally, numerical simulations of the proposed approach are performed.

6.2 Stochastic Unit Cell Approach on Modeling of Fiber Breakage Evolution

The microstructural characteristics, such as the mechanical properties of constituent phases, volume fractions, spatial distributions, and micro-geometries (shapes, orientations and sized) of inhomogeneities, have effects on the overall nonlinear behaviors (Jeng et al., 1991). However, for a continuous fiber reinforced composite subjected to a tensile loading along the fiber direction, neither the cross-section geometry nor the distribution of the fibers has noticeable effect on the constitutive response (Brockenbrough and Sureash, 1990). Therefore, periodic unit cell models are suitable in studying the continuous fiber reinforced composites. The periodic unit cell model is used widely in micromechanics analyses due to its simplicity and well-representation. In this chapter, a planar periodic unit cell structure as shown in Figure 6.1 is adopted to simulate the damage accumulation in a multi-fiber composite. Each sub-unit represents a matrix material embedded with a single fiber. The evolution of fiber fragmentation in multi-fiber composites during loading is, in principle, different from that in the single-fiber

composites. In a multi-fiber composite, each fiber experiences a non-uniform stress due to the uniform applied stress plus stresses transferred from other broken fibers in the composites. Fiber damage in some local region increases the stresses in the surrounding neighborhood and drives further damage locally. As a consequence, the composite failure becomes statistical, with some probability distribution. In this sense, the evolution of fiber damage depends crucially on the nature of the load transfer from broken or slipping fibers to intact fibers. The key to describe the fragmentation process in a multi-fiber composite is to understand how the local loading sharing influences the composite behavior. Figure 6.2 illustrates the computational algorithm for the numerical simulation of the fiber breakage process in a multi-fiber composite. In particular, two risk-competing models are implemented in the algorithm to simulate the load sharing mechanism in a composite system for arbitrary spatial locations of fiber breakages.

6.3 Simulation Mechanism of Fiber Breakage – Dominant Weakness Selection

A risk-competing model based on the fiber weakness is proposed to describe the non-uniform and inhomogeneous damage evolution as illustrated in Figure 6.3. The computational procedure for the fiber breaking process within the periodic unit cell is described as follows:

(1) Assign an initial value of weakness to each cell based on a normal distribution.

(2) Choose the first fiber to fracture at random.

(3) Degrade the strength intensity of the four nearest fibers with a factor ρ.

(4) Determine the fiber with the dominant weakness value (yellow cycle in Figure 6.3) and fracture this fiber *j* with the following probability:

$$p_j = \frac{weakness_j}{\sum_{i=1}^{4} weakness_i} \tag{6.1}$$

6.4 Simulation Mechanism of Fiber Breakage – All Surrounding Neighboring Fiber Selection

The second risk-competing model is proposed as illustrated in Figure 6.4, and the corresponding computational procedure is exhibited below:

(1) Assign an initial value of weakness to each cell based on a normal distribution.

(2) Choose the first fiber to fracture at random.

(3) Degrade the strength intensity of the nearest four fibers with a factor ρ.

(4) Select a fiber among all the neighboring fibers with an equal probability and fracture fiber *j* with the following probability:

$$p_j = \frac{weakness_j}{\sum_{i \in V} weakness_i} \tag{6.2}$$

where set V contains all the fiber sub-units surrounding the fractured fibers.

6.5 Numerical Investigation

To investigate the fragmentation process and local load sharing mechanism in a multi-fiber reinforced composite system, we perform stochastic simulations of progressive fiber breakage within a representative unit cell by implementing the two proposed risk-competing models. For

each model, 50 independent simulations are carried out with an incremental strain of 0.005%. Each fiber sub-unit is assigned an initial weakness value based on a normal distribution $\mathcal{N}(0.5, 0.01)$ to account for the quality variation in fibers. As one fiber sub-unit experiences a breakage, a reduction factor ρ of 0.95 is adopted to reduce the strength intensity of the neighboring fiber sub-units associated with the damaged fiber. Meanwhile, the local fiber stress of the broken fiber sub-unit decreases by 10%, and the extra load is equally redistributed in the nearest neighboring fiber sub-units. The material properties and Weibull parameters adopted in the stochastic simulations are: E_m =114 GPa, v_m = 0.34, E_f = 400 GPa, , v_f = 0.25, L_f = 125 mm, d_f = 142 μm, $\phi_f = 0.3$ ($\phi_{f_i} = \phi_f / N_{sub-unit}$), S = 1460 MPa, M = 2.51, $\sigma_{cr} = 1020$ MPa , $n_{saturated} = 1.52/\text{mm}$.

The predicted macroscopic stress and the total number of fiber cracks in a 12×12 unit cell model versus the applied macroscopic strain by the proposed two stochastic modeling methods are rendered in Figure 6.5-Figure 6.6 and Figure 6.7-Figure 6.8, respectively. At the applied macroscopic strain level of 1.0%, fiber breakage Mechanism 1 yields the predicted macroscopic stress with the mean of 2,051.3 MPa and the standard deviation of 17.8 MPa, and the total number of fiber breaks with the mean of 79.01 and a standard deviation of 3.48. On the other hand, fiber breakage Mechanism 2 produces the results of $\sigma_{macro} = 1{,}943.8 \text{ MPa} \pm 28.4 \text{ MPa}$ and $n_{cracks} = 100.3 \pm 16.2$ at the macroscopic strain level of 1.0%.

The typical damage patterns for the corresponding failure mechanisms are illustrated in Figure 6.9 and Figure 6.10, respectively. Figure 6.11 and Figure 6.12 exhibit the typical intensity

pattern obtained by Model 1 and Model 2, respectively. As observed in Figure 6.11 and Figure 6.12, Model 1 tends to generate a concentrated damage pattern with broken fibers clustering in a T-shape or cross type shape, whereas Model 2 generally yields a more diffused damage pattern. Therefore, it is reasonable to assume that Model 1 is more appropriate in simulating the damage evolution in a stiffer material, while Model 2 is more suitable in describing the damage pattern of a softer composite.

To investigate the effect of the unit cell size on the numerical predictions, we further perform the stochastic simulations by applying various unit cell sizes: 8×8, 10×10, 12×12 and 15×15. The predicted macroscopic stress versus applied macroscopic strain relationships by using the two risk-competing models are illustrated in Figure 6.13 and Figure 6.14, respectively. Less than 5% variation is observed as the size of the unit cell models varies for both risk-competing models, indicating that our proposed approaches are statistically robust and suitable for stochastic modeling of fiber breakage evolution in longitudinal fiber reinforced composites.

6.6 Conclusions

To account for the realistic damage accumulation in a multi-fiber reinforced composite system, two risk-competing models have been proposed to simulate the local load sharing mechanism and the damage evolution of fiber breakage. In the absence of sufficient experimental observations, the proposed risk-competing models demonstrate the possible fiber breakage evolution patterns in a multi-fiber reinforced composite. In general, the stochastic modeling results are capable of capturing the salient characteristics and responses of the composite

materials. Thorough validations will be performed as the associated experimental data become available.

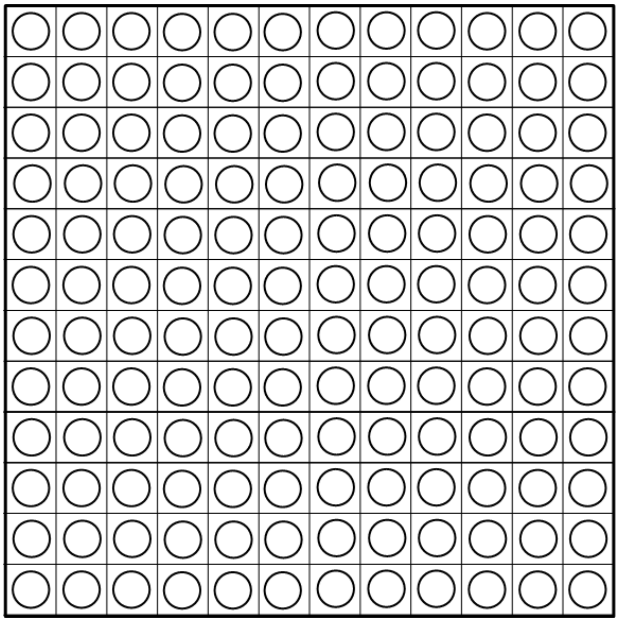

Figure 6.1 Schematic representation of a unit cell of 12x12 fiber sub-units for stochastic simulation of fiber breakage evolution in multi-fiber reinforced composites.

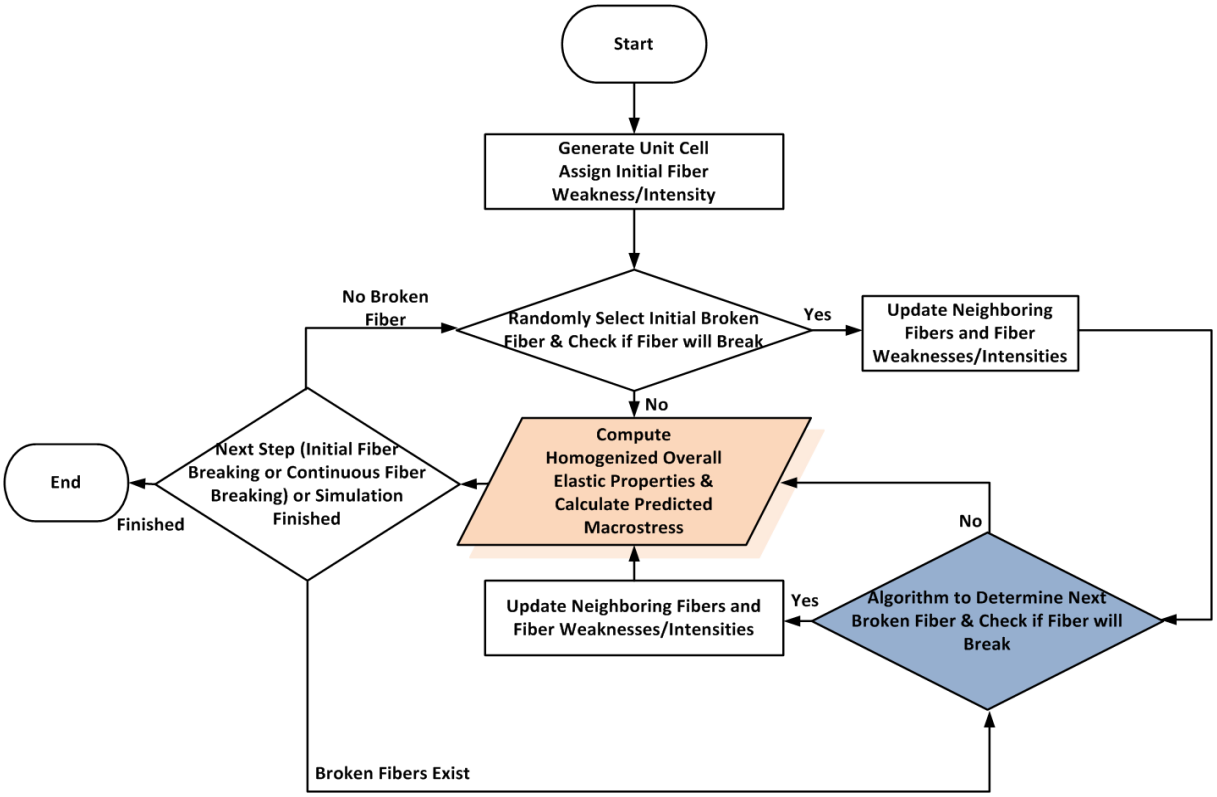

Figure 6.2 Flowchart of computational algorithm for stochastic simulation of fiber breakage evolution in multi-fiber reinforced composites.

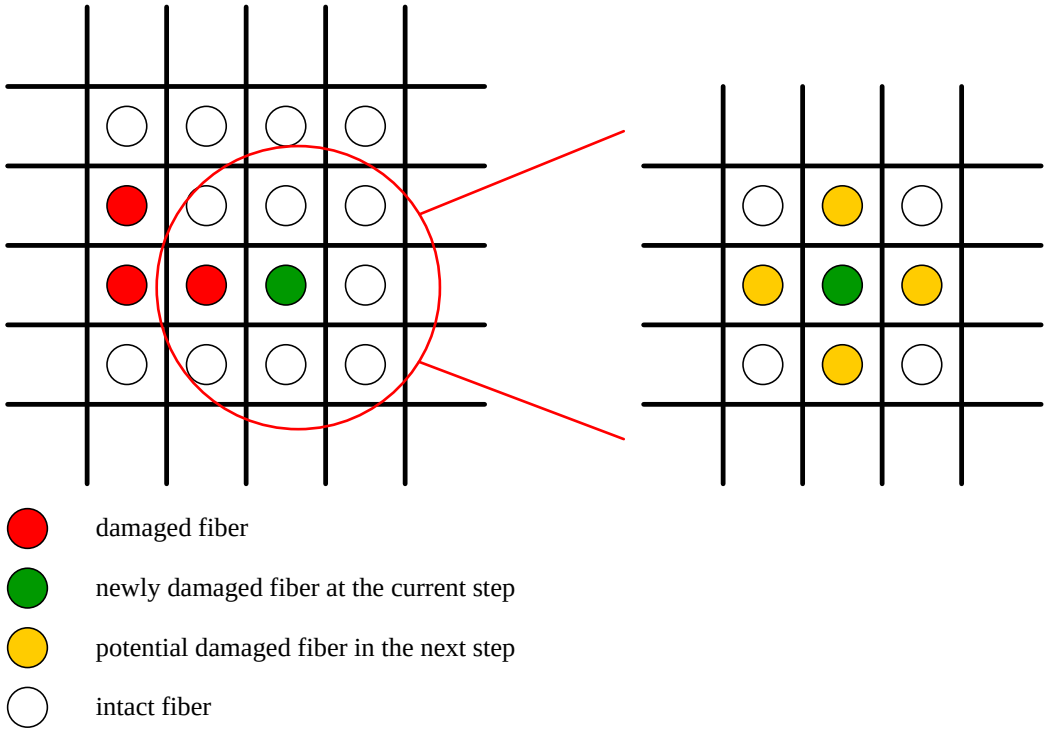

Figure 6.3 Schematic diagram of risk-competing model 1 – dominant weakness selection.

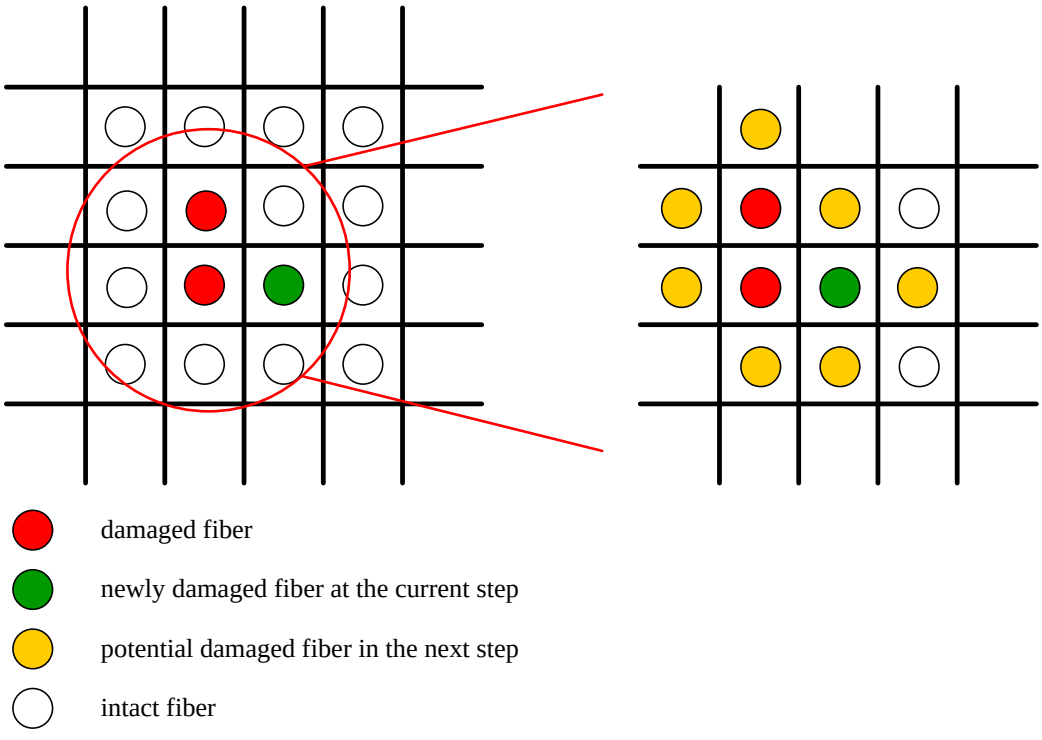

Figure 6.4 Schematic diagram of risk-competing model 2 – all surrounding fiber selection.

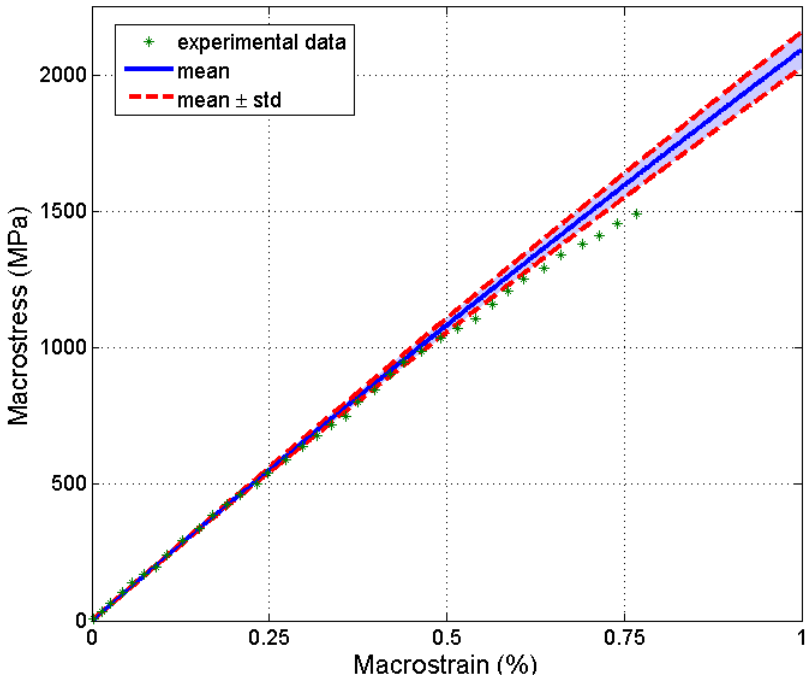

Figure 6.5 Results of stochastic modeling of progressive fiber breaking in multi-fiber reinforced composites by Failure Mechanism 1: simulated stress-strain curves (mean ± 1.0 standard deviation).

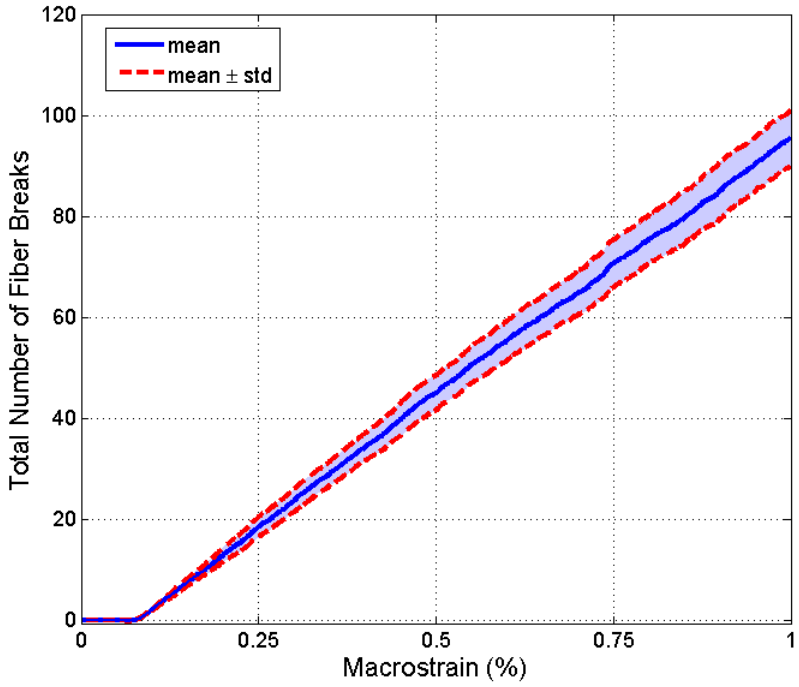

Figure 6.6 Results of stochastic modeling of fiber breakage evolution in multi-fiber reinforced composites by Failure Mechanism 1: simulated total number of fiber breakages versus strain curves (mean ± 1.0 standard deviation).

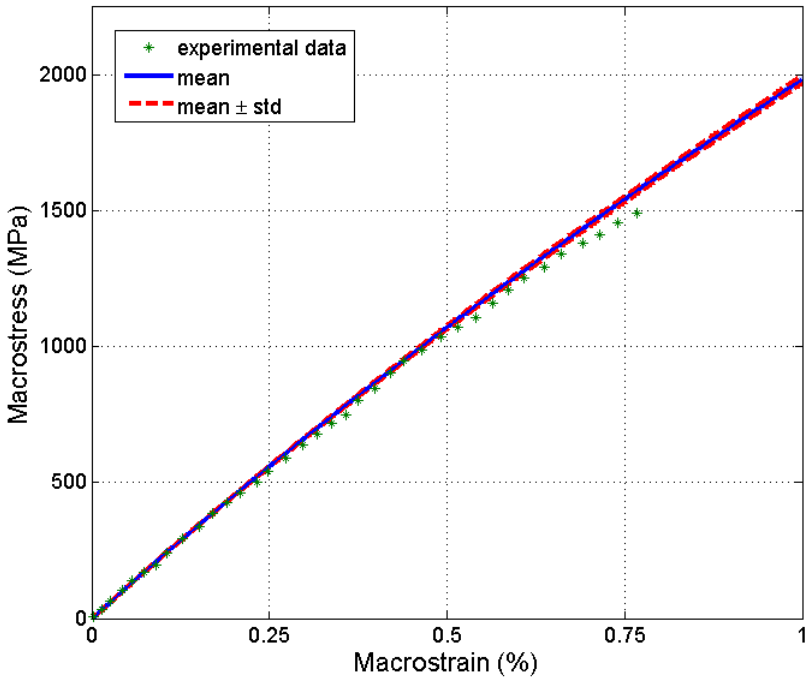

Figure 6.7 Results of stochastic modeling of fiber breakage evolution in multi-fiber reinforced composites by Failure Mechanism 1: simulated stress-strain curves (mean ± 1.0 standard deviation).

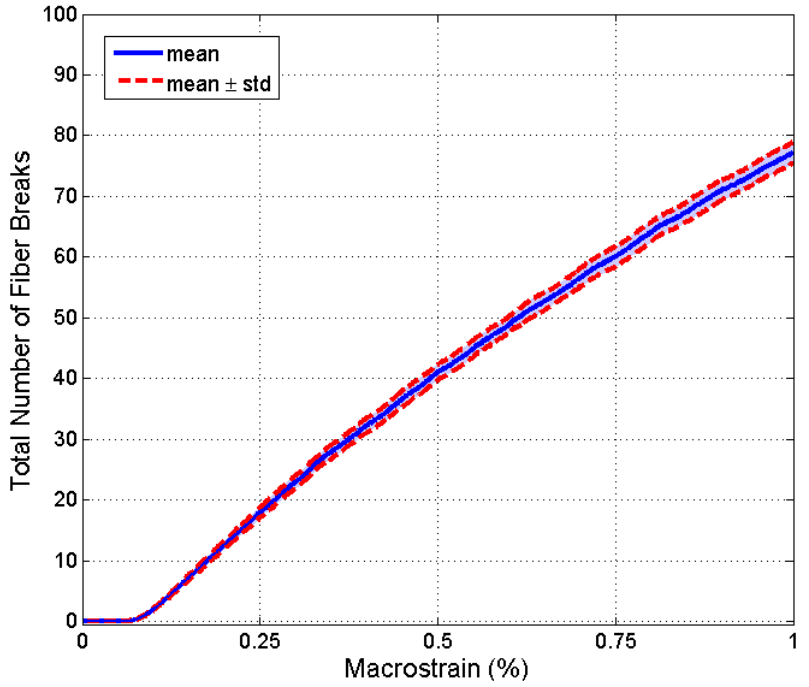

Figure 6.8 Results of stochastic modeling of fiber breakage evolution in multi-fiber reinforced composites by Failure Mechanism 2: simulated total number of fiber breakages versus strain curves (mean ± 1.0 standard deviation).

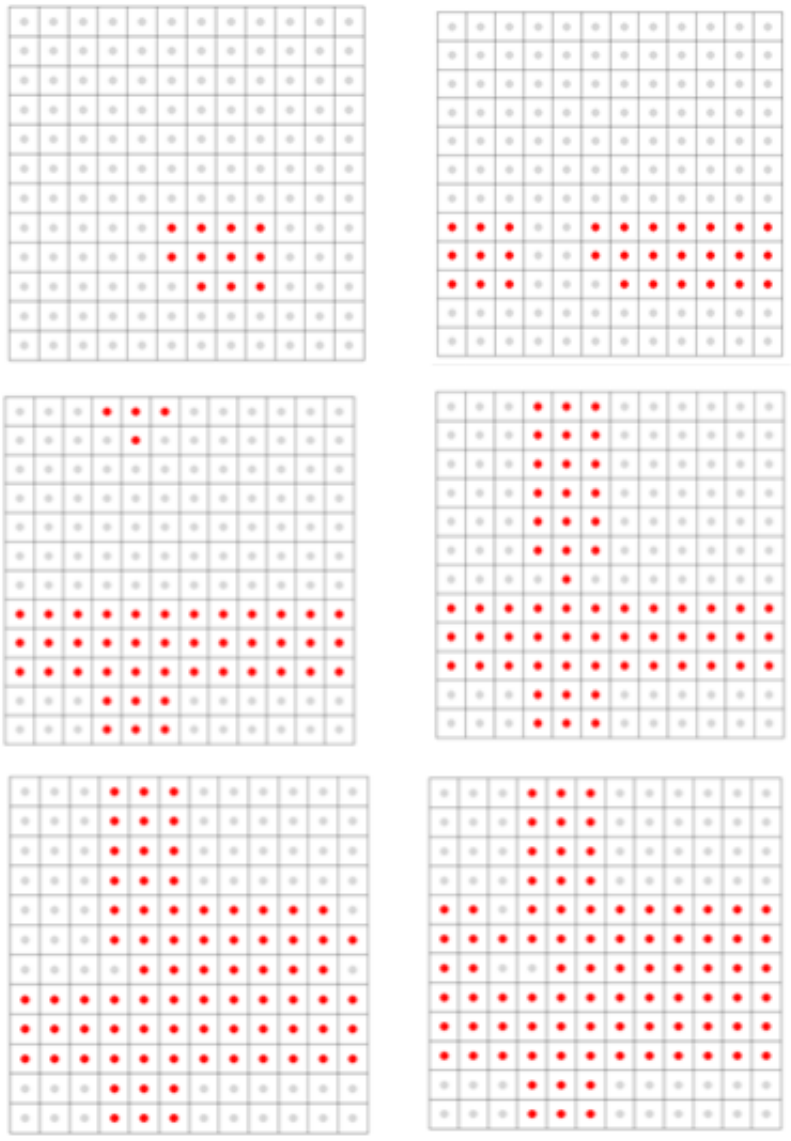

Figure 6.9 Typical progressive damage pattern of broken fibers in multi-fiber reinforced composites by Failure Mechanism 1.

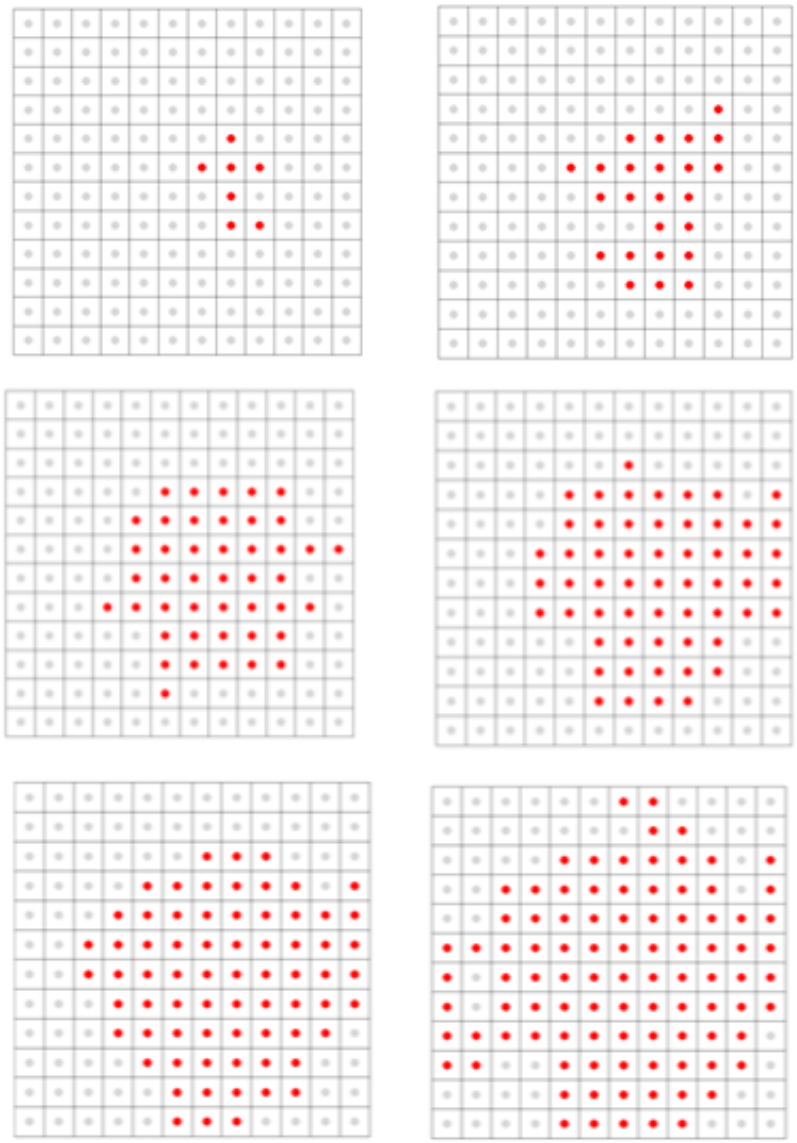

Figure 6.10 Typical progressive damage pattern of broken fibers in multi-fiber reinforced composites by Failure Mechanism 2.

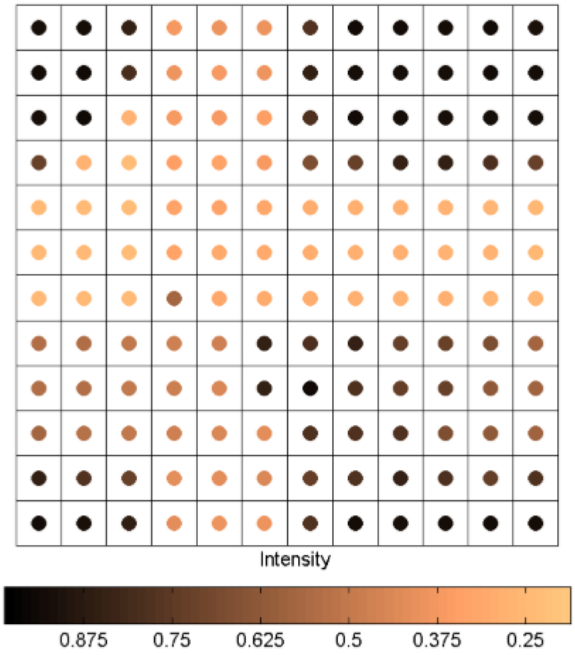

Figure 6.11 Comparisons of typical intensity patterns of the stochastic simulation results: Failure Mechanism 1.

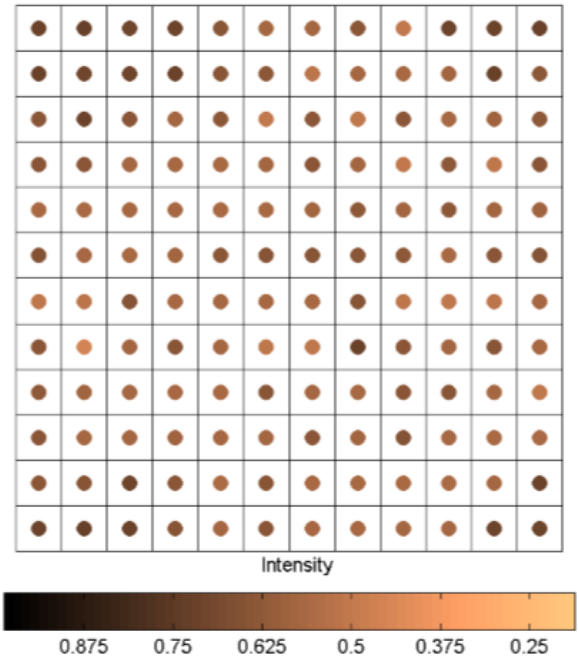

Figure 6.12 Comparisons of typical intensity patterns of the stochastic simulation results: Failure Mechanism 2.

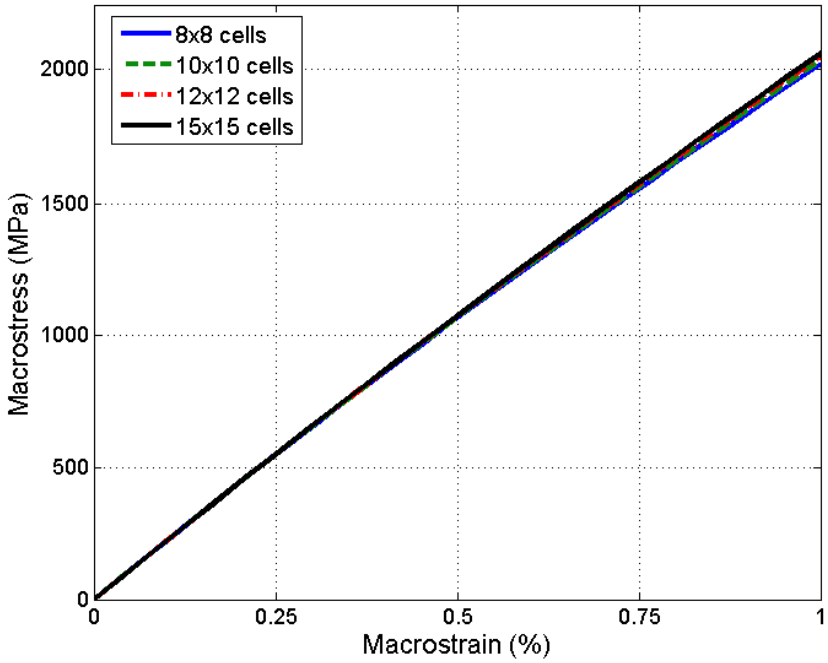

Figure 6.13 Comparisons of averaged stress-strain curves of 50 simulations for multi-fiber reinforced composites considering progressive fiber breakage with various unit cell sizes: Failure Mechanism 1.

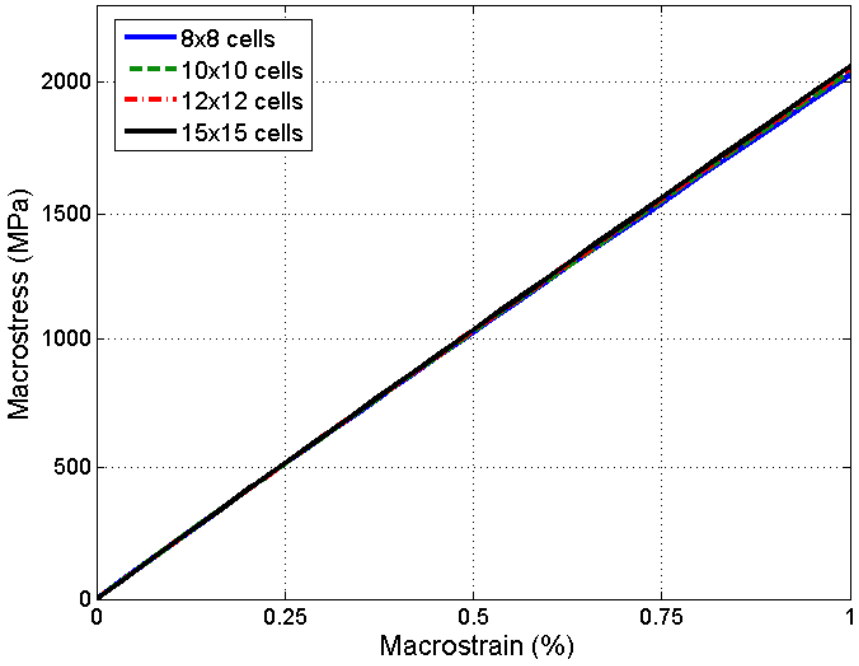

Figure 6.14 Comparisons of averaged stress-strain curves of 50 simulations for multi-fiber reinforced composites considering progressive fiber breakage with various unit cell sizes: Failure Mechanism 2.

CHAPTER 7 ELASTOPLASTIC DAMAGE MICROMECHANICS FOR CONTINUOUS FIBER REINFORCED DUCTILE MATRIX COMPOSITES WITH FIBER BREAKAGE EVOLUTION

7.1 Introduction

Continuous fiber reinforced metal matrix composites (MMCs) are attractive candidate materials for aerospace, automotive and many other industry applications for their superb mechanical properties, such as low density, high strength, and high stiffness (Brindley et al., 1992; Draper et al., 1989). In practice, a thin interface layer is normally formed between the matrix and the fibers due to chemical reactions during fabrication. The interface layer, although occupies a vanishing fraction of the total composite volume, plays a key role in determining the overall composite properties and characterizing the composite failure mechanisms (Eldridge and Brindley, 1989; Jeng et al., 1991; He et al., 1993; Curtin, 1998; Zhao et al., 2000; Kim and Nairn, 2002). The interfacial bonding strength between adjacent material phases, such as the bonding strength between the fiber and the interface zone and the bonding strength between the matrix and the interface zone, is critical in controlling the damage evolution. For a composite made of a ductile matrix and weak fibers with high interfacial bonding strength under tensile loading, microcracks first initiate in the interfacial layer due to its brittleness and low fracture strength comparing to that of the matrix and the fibers. Consequently, stress concentration occurs near these crack tips, which in turn results in the microyielding of the matrix and further leads to the blunting of the cracks. These microcracks extend into the fibers at random locations causing fiber fracture due to the statistical scattering of the fiber strength. Upon further loading, fiber

breakage evolution occurs in accompany with global matrix yielding. Therefore, both the progressive fiber breakage evolution and the matrix inelastic deformation has significant contributions to the overall nonlinear material behaviors of fiber reinforced MMCs.

The inelastic behaviors of MMCs under tensile loadings are complex in many ways. On one hand, the stress and strain fields in the matrix material vary substantially from one point to another. For instance, local damage in the interfacial reaction layer leads to the microyielding of the matrix to blunt the cracks. However, this local plastic yielding does not control the onset of the global yielding. The overall yield stress of metal matrix composites is governed by the average stress in the matrix that is sufficient for the global yielding (Clyne and Withers, 1993). As a result, a number of models use the von Mises and the Tresca type yield criterion, assuming that when the average stress in the matrix exceeds a threshold value, the overall plastic flow of the composite occurs. On the other hand, the microstructural characteristics, such as the mechanical properties of constituent phases, volume fractions, spatial distributions, and micro-geometries (shapes, orientations and sized) of inhomogeneities, have effects on the overall nonlinear behaviors (Jeng et al., 1991). However, for a continuous fiber reinforced composite subjected to a tensile loading along the fiber direction, neither the cross-section geometry nor the distribution of the fibers has noticeable effect on the constitutive response (Brockenbrough and Sureash, 1990). Therefore, unit cell models have been widely used in the prediction of the continuous fiber reinforced composites.

A group of models focused on the prediction of the effective elastoplastic behavior of MMCs accounting for the microstructural characteristics. Important analytical models includes Tandon

and Weng (1988), Christman and his coworks (1989), Zhao and Weng (1990), Qiu and Weng (1991, 1992, 1995), Dednarcykand Arnold (2001). Further, Ju and his coworkers (1994a; 1997; 2001; 2003a) performed a series of studies on prediction of the elastoplasitc behavior of two-phase metal matrix composites with different microstructural characteristics. The local stress field in any matrix point can be computed directly by using of the exterior-point Eshelby's tensor. The ensemble-area-averaging method can then be employed directly to obtain the effective yield function for the fiber-reinforced MMCs with various evolutionary damage modes, such as matrix cracking, interfacial debonding and reinforcement cracking (Ju and Chen 1994b; Sun and Ju, 2001; Sun et al., 2003b; Ju and Yanase, 2008; Ju et al., 2008).

Computational approaches such as the finite element analysis and Monte Carlo simulations have also been performed extensively to capture the nonlinear behaviors of MMCs (Lienkamp and Schwartz, 1993; Durham et al., 1997; Landis et al., 2000; Park and Padgett, 2006; Okabe et al., 2010; 2012). For example, Allen and his coworkers (1994) simulated the inelasticity of a matrix material by using a rate-dependent viscoplasticity model. The interface fracture was modeled by using a nonlinear interface constitutive model. Zhang and his coworkers (2010) proposed a hierarchical multiscale model to simulate the failure mechanism in a unidirectional fiber-reinforced MMC. Monte Carlo simulations were conducted at the macroscale level with a representative volume model established in the mesoscale and the residual stress derived in the mircoscale level to obtain the ultimate tensile strength.

Taking advantage of the continuum mechanics approach, another group of researchers treated MMCs as single-phase anisotropic materials with different properties along different directions,

such as the continuum model by Mulhern et al. (1967), the failure criteria proposed by Hashin (1980), and the bi-modal plasticity analysis by Dvorak and Bahei-El-Din (1987) and the fiber reinforced MMCs analysis by Dvorak et al. (1988). Hansen et al. (1991) and Schmidt et al. (1993) proposed a modified Hill model (1948) to calculate the plastic behavior of transversely isotropic composites. Further, Voyiadjis and Thiagarajan (1995) proposed a new anisotropic pressure-dependent continuum yield surface for directional fiber-reinforced MMCs.

This chapter focuses upon the prediction of the overall elastoplastic material properties of continuous fiber reinforced MMCs under external loadings. We assume that the fracture strength of the fiber is much lower than that of the matrix. Furthermore, the interfacial bonding condition is assumed to be perfect. Hence, the local damage due to interfacial debonding is neglected in the current study. First of all, an elastic damage micromechanical framework is introduced to derive the overall stress fields taking account of fiber breakage evolution. The effective damaged moduli of continuous fiber reinforced MMCs are formulated systematically. Further, the effective yield function which controls the global plastic deformation is presented based on the ensemble-volume averaging technique. The computational algorithm of the elastoplastic damage modeling is subsequently illustrated. Finally, comparisons of the stress-strain behaviors are performed between the numerical predictions and the available experimental data to demonstrate the capability of our proposed methodology.

7.2 Micromechanics and Damage Mechanics of MMCs with Fiber Breakage

Consider a unidirectionally aligned yet randomly distributed continuous fiber reinforced ductile matrix composite with fiber breakages as shown in Figure 7.1. The elasticity tensors of the matrix and the fiber are $\mathbf{C}_0$ and $\mathbf{C}_1$, respectively. The Eshelby's equivalent equation can be derived as

$$\mathbf{C}_1 : \left(\boldsymbol{\varepsilon}^0 + \boldsymbol{\varepsilon}' - \boldsymbol{\varepsilon}_{cr}^*\right) = \mathbf{C}_0 : \left(\boldsymbol{\varepsilon}^0 + \boldsymbol{\varepsilon}' - \boldsymbol{\varepsilon}_{cr}^* - \boldsymbol{\varepsilon}^*\right) \qquad \text{in } \Omega \tag{7.1}$$

where $\boldsymbol{\varepsilon}'$ is the perturbed strain due to the presence of the fiber phase; $\boldsymbol{\varepsilon}^*$ is the conventional eigenstrain field accounting for the mismatch between the matrix and the fiber; and $\boldsymbol{\varepsilon}_{cr}^*$ is the eigenstrain proposed in Chapter 5 to quantify the effect of fiber breakages. The eigenstrain $\boldsymbol{\varepsilon}_{cr}^*$ together with $\boldsymbol{\varepsilon}^*$ compose the total eigenstrain $\boldsymbol{\varepsilon}^{**}$.

Theoretically, the perturbed strain $\boldsymbol{\varepsilon}'$ in Equation (7.1) can be related to the total eigenstrain $\boldsymbol{\varepsilon}^{**}$ by

$$\boldsymbol{\varepsilon}' = \mathbf{S} : \boldsymbol{\varepsilon}^{**} = \mathbf{S} : \left(\boldsymbol{\varepsilon}_{cr}^* + \boldsymbol{\varepsilon}^*\right) \tag{7.2}$$

where $\mathbf{S}$ is the fourth-rank interior-point Eshelby's tensor which depends on the Poisson's ratio of the matrix phase and the geometry of the fiber phase. The expression of the Eshelby's tenor $\mathbf{S}$ writes (Sun and Ju, 2001)

$$\mathbf{S}_{ijkl} = S_{IK}^{(1)} \delta_{ij} \delta_{kl} + S_{IJ}^{(2)} (\delta_{ik} \delta_{jl} + \delta_{il} \delta_{jk}) \tag{7.3}$$

where $S_{IK}^{(1)}$ and $S_{IJ}^{(2)}$ are the second-rank tensors with the components of an elliptic cylindrical inclusion provided in **Appendix C**.

In the present work, a penny-shaped crack model considering the crack thickness u is adopted to simulate the fiber breakage. The crack surface is assumed to be perpendicular to the longitudinal direction (X_1). Based on linear elastic fracture mechanics, the thickness of a fiber breakage is predicted by averaging the mode I crack opening displacement over the crack surface. By using the ensemble-volume average technique, the volume-averaged eigenstrain due to multiple fiber breakages in the fiber phase can be quantified as follows:

$$\bar{\boldsymbol{\varepsilon}}_{cr}^{*} = \beta \cdot n \cdot \boldsymbol{\Gamma} \bullet \mathbf{C}_0 : \left[\boldsymbol{\varepsilon}^0 + \boldsymbol{\varepsilon}' - \boldsymbol{\varepsilon}^{**} \right] \tag{7.4}$$

where $\beta = 16(1-\nu_0^2)c\phi \big/ \left[3E_0(2-\nu_0)L_f \right]$, $\boldsymbol{\Gamma} = diag\left[0, 0, 2-\nu, 2, 2, 0\right]$, and n denotes the number of fiber breakages.

Further, we employ a two-parameter Weibull's probability function to govern the number evolution of fiber breakages as follows:

$$P_1 = \frac{n}{\bar{n}} = 1 - \exp\left[-\left(\frac{\bar{\sigma}_f - \sigma_{cr}}{S} \right)^M \right] \tag{7.5}$$

where P_1 is a damage parameter which describes the current state of the fiber breakage evolution; $\bar{n}$ represents the saturated number of fiber breakage; σ_{cr} signifies the stress threshold of fiber breakage; and M and S are the two Weibull parameters, which can be quantitatively characterized from a fragmentation test of a single-fiber composite (Zhao et al., 2000). In the present model, S is associated with the local fiber breakage strength, whereas M governs the damage evolution rate. The Weibull parameters implicitly include the temperature effect on the

material behavior. $\bar{\sigma}_f$ denotes the average internal fiber stress along the longitudinal direction. The expression of $\bar{\boldsymbol{\sigma}}_f$ is determined by

$$\bar{\boldsymbol{\sigma}}_f = \left\{ \mathbf{C}_0 \bullet \left[\mathbf{I} + \left(\mathbf{I} - \mathbf{S} \right) \bullet \mathbf{B} \right] \right\} : \boldsymbol{\varepsilon}^0 \tag{7.6}$$

Clearly, the ensemble-volume averaged eigenstrain $\boldsymbol{\varepsilon}_{cr}^{*}$ explicitly encloses the information of the mechanical properties of the matrix (Poisson's ratio ν_0 and Young's modulus E_0), the physical properties of the fiber (the radius of fiber break c, volume fraction of fiber ϕ, and fiber length L_f), the local fiber breakage strength, and the current internal stress level in the fiber.

In consequence, the ensemble-volume averaged total eigenstrain within the fiber phase can be related to the applied far-field strains $\boldsymbol{\varepsilon}^0$ by

$$\boldsymbol{\varepsilon}^{**} = \mathbf{B} : \boldsymbol{\varepsilon}^0 \tag{7.7}$$

where

$$\mathbf{B} = \left[\mathbf{A} + \mathbf{S} + \beta \cdot n \left(\mathbf{A} \bullet \boldsymbol{\Gamma} \bullet \mathbf{C}_1 \right) \right]^{-1} \tag{7.8}$$

$$\mathbf{A} = \left[\left(\mathbf{C}_1 - \mathbf{C}_0 \right) - \beta \cdot n \left(\mathbf{C}_1 \bullet \boldsymbol{\Gamma} \bullet \mathbf{C}_0 \right) \right]^{-1} \cdot \mathbf{C}_0 \tag{7.9}$$

It is interesting to note that Equations (7.8) and (7.9) are reduced to Equations (20) and (21) in Sun and Ju (2001) if no fiber breakage is presented, that is, $\beta \cdot n = 0$. The component form of the fourth-rank tensor **B** is given in **Appendix C**.

7.3 Effective Elastic Moduli of Continuous Fiber Reinforced MMCs with Evolutionary Fiber Breakage

The ensemble-volume averaged strain $\overline{\boldsymbol{\varepsilon}}$ and stress $\overline{\boldsymbol{\sigma}}$ can be determined by

$$\overline{\boldsymbol{\varepsilon}} = \boldsymbol{\varepsilon}^0 + \phi \mathbf{S} : \overline{\boldsymbol{\varepsilon}}^{**} \tag{7.10}$$

and

$$\overline{\boldsymbol{\sigma}} = \mathbf{C}_0 : \left(\overline{\boldsymbol{\varepsilon}} - \phi \overline{\boldsymbol{\varepsilon}}^{**} \right) \tag{7.11}$$

Therefore, the overall macroscopic stress-strain relationship writes

$$\overline{\boldsymbol{\sigma}} = \mathbf{C}^* : \overline{\boldsymbol{\varepsilon}} \tag{7.12}$$

where $\mathbf{C}^*$ is the effective elastic stiffness tensor of a continuous fiber reinforced MMC with evolutionary fiber breakage. It is determined based on the framework of micromechanics and damage mechanics by

$$\mathbf{C}^* = \mathbf{C}_0 \bullet \left(\mathbf{I} + \phi \mathbf{M}^{-1} \bullet \mathbf{B} \right) = \mathbf{C}_0 \bullet \left\{ \mathbf{I} + \phi \mathbf{M}^{-1} \bullet \left[\mathbf{A} + \mathbf{S} + \beta \cdot n \left(\mathbf{A} \bullet \boldsymbol{\Gamma} \bullet \mathbf{C}_1 \right) \right]^{-1} \right\} \tag{7.13}$$

and

$$\mathbf{M} = \mathbf{I} + \phi \mathbf{S} \bullet \mathbf{B} \tag{7.14}$$

The detailed component form of the fourth-rank tensor $\mathbf{C}^*$ are provided in **Appendix C**.

7.4 Homogenization Procedure for the Effective Yield Function

The deformation of a two-phase metal matrix composite can be decomposed into the elastic deformation of both the matrix and the fibers along with the stress-free plastic deformation in the

metallic matrix only. A homogenization (ensemble-volume averaging) procedure is typically performed within the RVE, in which *elastic* fibers are embedded in an *elastoplastic* matrix material, to obtain the overall constitutive equations of composites. In this research, the current stress $\boldsymbol{\sigma}(\mathbf{x})$ is assumed to satisfy the von Mises yield criterion for any material point $\mathbf{x}$ in the matrix phase:

$$F\left(\boldsymbol{\sigma}, \bar{\mathrm{e}}_m^p\right) = \sqrt{\boldsymbol{\sigma} : \mathbf{I}_d : \boldsymbol{\sigma}} - K\left(\bar{\mathrm{e}}_m^p\right) \le 0 \tag{7.15}$$

where $\bar{\mathrm{e}}_m^p$ is the equivalent plastic strain; $K\left(\bar{\mathrm{e}}_m^p\right)$ is the isotropic hardening function; and $\mathbf{I}_d = \frac{1}{2}(\delta_{ik}\delta_{jl} + \delta_{ij}\delta_{kl}) - \frac{1}{3}\delta_{ij}\delta_{kl}$ signifies the deviatoric part of the fourth-rank identity tensor. We then denote the square of the current stress norm associated with the local material point and a given inclusion configuration $\mathscr{g}$ as $H(\mathbf{x}\,|\,\mathscr{g}) \triangleq \boldsymbol{\sigma}(\mathbf{x}\,|\,\mathscr{g}) : \mathbf{I}_d : \boldsymbol{\sigma}(\mathbf{x}\,|\,\mathscr{g})$. Following Ju and Chen (1994a) and Sun and Ju (2001), the ensemble-volume averaged square of the stress norm over all possible realizations can be obtained with the first-order approximation by

$$\left\langle H \right\rangle_m (\mathbf{x}) \approx H_0 + \int_{\mathbf{x}' \notin \Xi(\mathbf{x})} \left[H\left(\mathbf{x}\,|\,\mathbf{x}^{(1)}\right) - H^0 \right] p\left(\mathbf{x}^{(1)}\right) d\mathbf{x}^{(1)} \tag{7.16}$$

where $H^0 = \boldsymbol{\sigma}^0 : \mathbf{I}_d : \boldsymbol{\sigma}^0$ denotes the square of the far-field stress norm, and $\Xi\left(\mathbf{x}\right)$ defines the exclusion zone of material point $\mathbf{x}$ associated with the inclusion centered at $\mathbf{x}^{(1)}$ with the probability density function $p(\mathbf{x}^{(1)})$. The above approximation neglects the interactions among neighboring inclusions and $p(\mathbf{x}^{(1)})$ is assumed to be statistically homogeneous, isotropic, and uniform, that is, $p(\mathbf{x}^{(1)}) = N / V$, where N and V are the number of inclusions and the volume of the RVE, respectively. After carrying out lengthy derivation, we can evaluate the ensemble-volume averaged square of the stress norm as

$$\langle H \rangle_m (\mathbf{x}) \approx \boldsymbol{\sigma}^0 : \mathbf{T} : \boldsymbol{\sigma}^0 \tag{7.17}$$

where the fourth-rank tensor **T** has the form:

$$T_{ijkl} = T_{IK}^{(1)} \delta_{ij} \delta_{kl} + T_{IJ}^{(2)} \left(\delta_{ik} \delta_{jl} + \delta_{il} \delta_{jk} \right) \tag{7.18}$$

The detailed expressions for $T_{IK}^{(1)}$ and $T_{IJ}^{(2)}$ can be found in Sun and Ju (2001). Alternatively, $\langle H \rangle_m (\mathbf{x})$ can be written in terms of the macroscopic stress $\bar{\boldsymbol{\sigma}}$ as follows:

$$\langle H \rangle_m (\mathbf{x}) \approx \bar{\boldsymbol{\sigma}} : \bar{\mathbf{T}} : \bar{\boldsymbol{\sigma}} \tag{7.19}$$

where

$$\boldsymbol{\sigma}^0 = \mathbf{P} : \bar{\boldsymbol{\sigma}} \tag{7.20}$$

$$\bar{\mathbf{T}} = \mathbf{P}^T \bullet \mathbf{T} \bullet \mathbf{P} \tag{7.21}$$

$$\mathbf{P} = \left\{ \mathbf{C}_0 \bullet \left[\mathbf{I} + \phi \left(\mathbf{I} - \mathbf{S} \right) \bullet \mathbf{B} \right] \bullet \mathbf{C}_0^{-1} \right\}^{-1} \tag{7.22}$$

Readers can refer to **APPENDIX C** for the component forms of the fourth-rank tensor **P**. Equation (7.19) reduces to Equation (58) in Sun and Ju (2001) if no fiber breakage presents in the composites. In addition, the above-mentioned ensemble averaged square of the stress norm degenerates to the classical J_2 invariant as $\phi = 0$ (special case with matrix phase only).

7.5 Computational Modeling of Elastoplastic Behaviors of MMCs with Fiber Breakage Evolution

Based on continuum plasticity, the total macroscopic strain $\bar{\boldsymbol{\varepsilon}}$ can be decomposed into elastic and plastic parts as follows:

$$\overline{\boldsymbol{\varepsilon}} = \overline{\boldsymbol{\varepsilon}}^{e} + \overline{\boldsymbol{\varepsilon}}^{p} \tag{7.23}$$

Upon loading, the MMCs behave as purely elastic materials or yield and behave plastically depending on the current stress state. After the ensemble-volume averaging process presented in the previous section, the macroscopic yield criterion of the composite material can be written as:

$$\overline{F}\left(\overline{\boldsymbol{\sigma}}, \overline{\mathrm{e}}_{m}^{p}\right) = \left(1-\phi\right)\sqrt{\overline{\boldsymbol{\sigma}} : \overline{\mathbf{T}} : \overline{\boldsymbol{\sigma}}} - K\left(\overline{\mathrm{e}}_{m}^{p}\right) \le 0 \tag{7.24}$$

where the fourth-rank tensor $\overline{\mathbf{T}}$ is defined in Equation (7.21), and $K(\overline{\mathrm{e}}_{m}^{p})$ denotes the isotropic hardening function expressed as

$$K\left(\overline{\mathrm{e}}_{m}^{p}\right) = \sqrt{\frac{2}{3}}\left[\sigma_{Y} + h \cdot \left(\overline{e}^{p}\right)^{q}\right] \tag{7.25}$$

Herein, σ_{Y} represents the yield strength of the matrix material; and h and q signify the isotropic hardening parameters. Moreover, the overall ensemble-volume averaged *associative* flow rule is considered in the current study, and the plastic strain rate can be determined by

$$\dot{\overline{\boldsymbol{\varepsilon}}}^{p} = \dot{\lambda}\frac{\partial \overline{F}}{\partial \overline{\boldsymbol{\sigma}}} = \dot{\lambda}\left(1-\phi\right)\frac{\overline{\mathbf{T}} : \overline{\boldsymbol{\sigma}}}{\sqrt{\overline{\boldsymbol{\sigma}} : \overline{\mathbf{T}} : \overline{\boldsymbol{\sigma}}}} \tag{7.26}$$

where $\dot{\lambda}$ is the plastic consistency parameter. Furthermore, the rate of the effective equivalent plastic strain writes

$$\dot{\overline{e}}^{p} = \sqrt{\frac{2}{3}}\left(1-\phi\right)\dot{\lambda} \tag{7.27}$$

The plastic consistency parameter $\dot{\lambda}$ together with the effective yield function $\overline{F}\left(\boldsymbol{\sigma}, \overline{\mathrm{e}}_{m}^{p}\right)$ must satisfy the Kuhn-Tucker loading and unloading conditions as well as the consistency requirement:

$$\dot{\lambda} \ge 0,\ \overline{F}\left(\boldsymbol{\sigma}, \overline{\mathrm{e}}_{m}^{p}\right) \le 0,\ \dot{\lambda}\overline{F}\left(\boldsymbol{\sigma}, \overline{\mathrm{e}}_{m}^{p}\right) = 0 \quad \text{(Kuhn-Tucker loading/unloading condition)} \tag{7.28}$$

$$\dot{\lambda}\dot{\bar{F}}\left(\boldsymbol{\sigma},\bar{\mathrm{e}}_m^p\right)=0 \quad \text{(consistency requirement)} \tag{7.29}$$

Hence, the plastic consistency condition can be calculated by

$$\dot{\lambda}=\frac{\left[\left(\bar{\mathbf{T}}:\bar{\boldsymbol{\sigma}}\right):\mathbf{C}^*:\dot{\bar{\boldsymbol{\varepsilon}}}\right]}{\left[\frac{\partial\bar{F}}{\partial\bar{\boldsymbol{\sigma}}}:\left(\mathbf{C}^*\bullet\bar{\mathbf{T}}\right):\bar{\boldsymbol{\sigma}}\right]-\left[\frac{2}{3}\left(1-\phi\right)\cdot h\cdot q\cdot\left(\bar{e}^p\right)^{q-1}\right]} \tag{7.30}$$

The overall macroscopic stress rate tensor is related to the overall macroscopic strain rate tensor by

$$\dot{\bar{\boldsymbol{\sigma}}}=\mathbf{C}^{*ep}\dot{\bar{\boldsymbol{\varepsilon}}} \tag{7.31}$$

where the elastoplastic tangent stiffness tensor $\mathbf{C}^{*ep}$ takes the form

$$\mathbf{C}^{*ep}=\begin{cases}\mathbf{C}^* & \text{if} \quad \dot{\lambda}=0 \text{ (elastic)}\\ \mathbf{C}^*\bullet\left(\mathbf{I}-\mathbf{U}\right) & \text{if} \quad \dot{\lambda}>0 \text{ (plastic)}\end{cases} \tag{7.32}$$

Herein, the fourth-rank tensor $\mathbf{U}$ reads

$$\mathbf{U}=\frac{\left(\bar{\mathbf{T}}:\bar{\boldsymbol{\sigma}}\right)\otimes\left(\mathbf{C}^*\bullet\bar{\mathbf{T}}:\bar{\boldsymbol{\sigma}}\right)}{\bar{\boldsymbol{\sigma}}:\left[\bar{\mathbf{T}}\bullet\mathbf{C}^*\bullet\bar{\mathbf{T}}+\frac{2h\cdot q\cdot\left(\bar{e}^p\right)^{q-1}}{3\left(1-\phi\right)}\bar{\mathbf{T}}\right]:\bar{\boldsymbol{\sigma}}} \tag{7.33}$$

Therefore, an elastoplastic damage micromechanical constitutive model for MMCs with evolutionary fiber breakage has been explicitly formulated. The extension of the proposed model to accommodate the kinematic hardening, anisotropic hardening, and non-associative overall flow rule is feasible within the micromechanical homogenization framework.

In the following section, several applications of the proposed elastoplastic constitutive model are performed to illustrate the predictability of the present approach. In each simulation, an incremental macroscopic stress tensor $\Delta\bar{\boldsymbol{\sigma}}$ is provided as well as the current total macroscopic stress tensor $\bar{\boldsymbol{\sigma}}_{\nu+1} = \bar{\boldsymbol{\sigma}}_{\nu} + \Delta\bar{\boldsymbol{\sigma}}$. Based on Equations (7.26)-(7.27) and (7.30)-(7.31), the incremental plastic strain tensor $\Delta\bar{\boldsymbol{\varepsilon}}^{p}$, incremental plastic consistency parameter $\Delta\lambda$, incremental equivalent plastic strain $\Delta\bar{e}^{p}$, and the incremental total strain tensor $\Delta\bar{\boldsymbol{\varepsilon}}$ are computed. The current state solutions at increment $\nu+1$ are updated by $\bar{\boldsymbol{\varepsilon}}^{e}_{\nu+1} = \mathbf{C}^{*-1} : \bar{\boldsymbol{\sigma}}_{\nu+1}$, $\bar{\boldsymbol{\varepsilon}}_{\nu+1} = \bar{\boldsymbol{\varepsilon}}_{\nu} + \Delta\bar{\boldsymbol{\varepsilon}}$, $\bar{\boldsymbol{\varepsilon}}^{p}_{\nu+1} = \bar{\boldsymbol{\varepsilon}}^{p}_{\nu} + \Delta\bar{\boldsymbol{\varepsilon}}^{p}$, $\bar{e}^{p}_{\nu+1} = \bar{e}^{p}_{\nu} + \Delta\bar{e}^{p}$, and $\lambda_{\nu+1} = \lambda_{\nu} + \Delta\lambda$, whereas the current total number of fiber breaks $(n)_{\nu+1}$ is determined with a local iteration as summarized in Table 7.1.

7.6 Numerical Simulations

In the following study, unless noted otherwise, the matrix material is taken as the titanium alloy with Young's modulus $E_m = 82$ GPa, Poisson's ratio $v_m = 0.342$, initial uniaxial yield stress $\sigma_Y = 430$ MPa, and the strain hardening parameters $h = 14.4$ GPa and $q = 0.685$. For the reinforcement material, we adopt Young's modulus $E_f = 400$ GPa, Poisson's ratio $v_f = 0.25$ which are similar to the elastic properties of SiC materials. The critical strength that governs the fiber breakage is $\sigma_{cr} = 255$ MPa, and the Weibull parameters are $M = 1.54$ and S = 3200 MPa.

7.6.1 Uniaxial Stress-Strain Behavior

Consider a uniaxial tensile loading along the X_1 (fiber longitudinal) direction, the applied macroscopic stress $\bar{\boldsymbol{\sigma}}$ can be expressed by

$$\bar{\sigma}_{11} > 0, \quad \text{all other } \bar{\sigma}_{ij} = 0 \tag{7.34}$$

With a simple isotropic hardening law, the overall yield function is derived as

$$\bar{F}\left(\bar{\boldsymbol{\sigma}}, \bar{e}^{\,p}\right) = (1-\phi)\sqrt{\bar{T}_{11}^{(1)} + 2\bar{T}_{11}^{(2)}}\,\bar{\sigma}_{11} - \sqrt{\tfrac{2}{3}}\left[\sigma_y + h \cdot (\bar{e}^{\,p})^q\right] \tag{7.35}$$

where the component forms of the second-rank tensors $\bar{\mathbf{T}}^{(1)}$ and $\bar{\mathbf{T}}^{(2)}$ can be determined from Equation (7.21). The macroscopic incremental elastic strains and overall incremental plastic strain can be determined by

$$\left[\Delta\bar{\varepsilon}_{ij}^{e}\right] = \Delta\bar{\sigma}_{11}\begin{bmatrix} D_{11} & 0 & 0 \\ 0 & D_{12} & 0 \\ 0 & 0 & D_{12} \end{bmatrix} \tag{7.36}$$

$$\left[\Delta\bar{\varepsilon}_{ij}^{p}\right] = (1-\phi)\frac{\Delta\lambda}{\sqrt{\bar{T}_{11}^{(1)} + 2\bar{T}_{11}^{(2)}}}\begin{bmatrix} \bar{T}_{11}^{(1)} + 2\bar{T}_{11}^{(2)} & 0 & 0 \\ 0 & \bar{T}_{12}^{(1)} & 0 \\ 0 & 0 & \bar{T}_{12}^{(1)} \end{bmatrix} \tag{7.37}$$

where $\Delta\lambda$ is the incremental plastic consistency parameter and D_{ij} denotes the component of the compliance tensor $\mathbf{D} = \mathbf{C}^{*-1}$. For a *monotonic* uniaxial loading condition, the overall stress-strain relationship can be obtained by integrating Eq. (7.36) as follows:

$$\begin{Bmatrix} \bar{\varepsilon}_{11} \\ \bar{\varepsilon}_{22} \\ \bar{\varepsilon}_{33} \\ \bar{\varepsilon}_{23} \\ \bar{\varepsilon}_{13} \\ \bar{\varepsilon}_{12} \end{Bmatrix} = \bar{\sigma}_{11}\begin{Bmatrix} D_{11} \\ D_{12} \\ D_{12} \\ 0 \\ 0 \\ 0 \end{Bmatrix} + (1-\phi)\frac{\lambda}{\sqrt{\bar{T}_{11}^{(1)} + 2\bar{T}_{11}^{(2)}}}\begin{Bmatrix} \bar{T}_{11}^{(1)} + 2\bar{T}_{11}^{(2)} \\ \bar{T}_{12}^{(1)} \\ \bar{T}_{12}^{(1)} \\ 0 \\ 0 \\ 0 \end{Bmatrix} \tag{7.38}$$

where the positive plastic consistency parameter $\lambda = \sum \Delta\lambda$ is determined by solving the nonlinear equation $\bar{F} = 0$ with the plastic consistency condition:

$$\lambda = \frac{1}{\sqrt{2/3}(1-\phi)}\left[\frac{(1-\phi)\sqrt{\frac{3}{2}\left(\bar{T}_{11}^{(1)}+2\bar{T}_{11}^{(2)}\right)}\bar{\sigma}_{11}-\sigma_y}{h}\right]^{-q} \tag{7.39}$$

To illustrate the capability of the proposed elastoplastic-damage formulation, we compare our analytical predictions with the available experimental data of uniaxial tension tests reported by Jeng et al. (1991). Figure 7.2 and Figure 7.3 demonstrate the comparisons between the predictions and the experimental data of the stress-strain relationships of Ti-15-3 composites under the as-fabricated condition and the 800^{o}C/12 hrs condition, respectively. The prediction is in general in good agreement with the experimental observation. The proposed elastoplastic damage model is able to capture the plastic behavior of the material, yielding a more accurate prediction than the effective elastic damage formulation (Ju and Wu, 2013). The temperature effect is assumed to be implicitly enclosed using the Weibull parameters with $h = 12.1$ GPa, $q = 0.624$ for 800^{o}C/12 hrs condition. As observed, extensive thermal exposure at 800^{o}C degrades the material properties. The yielding point of the Ti-15-3 composite with the as-fabricated state is slightly higher than that after the heat treatment at 800^{o}C. Good agreement is also observed between the prediction and experimental result for Ti-6-4 composites under as-fabricated condition as shown in Figure 7.4. It is interesting to notice in Figure 7.5 that the fiber breakage process evolves at a slower rate beyond 0.6% macroscopic strain in the elastoplastic-damage model than that in the elastostatic-damage counterpart, as certain amount of energy is dissipated in the form of plastic deformations once the matrix yields.

Figure 7.6 shows that the Young's modulus, the initial yield strength and the plastic hardening modulus increase as the volume fraction of fibers increases. This serves as the

evidence of the fiber-strengthening effect on MMCs. Figure 7.7 displays the effect of the reinforcement shape (fiber aspect ratio) on the mechanical behavior of MMCs with a constant fiber volume fraction. It is clear that fibers with larger aspect ratio have stronger strengthening effect in the longitudinal direction. Figure 7.8 illustrates the elastoplastic behavior of MMCs with different contrast ratios in Young's modulus between the matrix and fiber constituents. Fibers with higher Young's modulus lead to higher elastic and plastic stress-strain responses, thus more pronounced stiffening effects. In contrast, no significant differences are observed in the stress-strain responses as the Poisson's ratio of fibers varies as presented in Figure 7.9.

Next, we investigate the effects of various parameters on the evolutionary fiber breakage process. Figure 7.10 illustrates the effect of the fiber volume fraction on the number of cumulative fiber breakages. The probability of having manufactory imperfections increases as the volume fraction of fibers increases. Therefore, composites with larger fiber volume fraction are likely to have more fiber breakages as shown in Figure 7.10. Similarly, as the length of the fiber increases, the chance that the fiber possesses imperfections increases. Thus, composites with fibers in longer length tend to have more fiber cracks during the damage evolution as demonstrated in Figure 7.11. Figure 7.12 indicates that higher Young's modulus of fibers is also one of the reasons that lead to greater number of cracks. This is primarily due to the fact that fibers with higher Young's modules are generally more brittle. Moreover, the Poisson's ratio of the fiber phase is found to have insignificant effects on the crack number as shown in Figure 7.13.

7.6.2 Mechanical Behaviors of MMCs under Asymmetric Loadings

Under asymmetric tension, the overall stress state can be expressed by

$$\bar{\sigma}_{11} > 0, \quad \bar{\sigma}_{22} = \bar{\sigma}_{33} = R\bar{\sigma}_{11}, \quad \text{all other } \bar{\sigma}_{ij} = 0 \tag{7.40}$$

where R is the ratio of the stress along the longitudinal direction to that in the radial direction. Specifically, if $R=0$, the previously discussed uniaxial loading case will be recovered; on the other hand, if R=1, it results in a pure hydrostatic loading condition. The corresponding yield function writes

$$\bar{F}\left(\bar{\boldsymbol{\sigma}}, \bar{e}^{\,p}\right) = (1-\phi)\,\Upsilon(R)\,\bar{\sigma}_{11} - \sqrt{\tfrac{2}{3}}\left[\sigma_y + h\cdot(\bar{e}^{\,p})^q\right] \tag{7.41}$$

where $\Upsilon(R) = \sqrt{\bar{T}_{11}^{(1)} + 2\bar{T}_{11}^{(2)} + 4R\bar{T}_{12}^{(1)} + 4R^2(\bar{T}_{22}^{(1)} + \bar{T}_{22}^{(2)})}$. The incremental elastic strains and incremental plastic strains can then be computed by

$$\left[\Delta\bar{\varepsilon}_{ij}^{e}\right] = \Delta\bar{\sigma}_{11}\begin{bmatrix} D_{11}+2RD_{12} & 0 & 0 \\ 0 & D_{12}+RD_{22} & 0 \\ 0 & 0 & D_{12}+RD_{22} \end{bmatrix} \tag{7.42}$$

and

$$\left[\Delta\bar{\varepsilon}_{ij}^{p}\right] = \frac{(1-\phi)\Delta\lambda}{\Upsilon(R)}\begin{bmatrix} \bar{T}_{11}^{(1)} + 2\bar{T}_{11}^{(2)} + 2R\bar{T}_{12}^{(1)} & 0 & 0 \\ 0 & \bar{T}_{12}^{(1)} + 2R\bar{T}_{22}^{(1)} + 2R\bar{T}_{22}^{(2)} & 0 \\ 0 & 0 & \bar{T}_{12}^{(1)} + 2R\bar{T}_{22}^{(1)} + 2R\bar{T}_{22}^{(2)} \end{bmatrix} \tag{7.43}$$

Since there is no experimental data available for this asymmetric loading case, we consider the same MMCs in the previous section for demonstration purpose. Figure 7.14 and Figure 7.15 show the stress-strain responses of MMCs under various stress ratios (R = 0, 0.4, 0.7, 0.85, 1.25,

1.5, and 2.0). It is observed that the stress ratio affects the overall responses of the MMCs significantly. The stress-strain curves exhibit less non-linearity as *R* increases until the negative strain, since the stress in the radial direction becomes dominant in the overall elastoplastic responses. Therefore, a proper selection of the stress ratio *R*, fiber volume fraction ϕ , and the aspect ratio of the fiber can help the design of the MMCs with *better performance* under asymmetric loadings.

7.6.3 Initial Yield Surface of MMC's with Fiber Breakage

For general loading conditions, the initial yield surface of MMCs can be obtained by

$$\bar{F}_0^2(\bar{\boldsymbol{\sigma}}) = \bar{F}^2(\bar{\boldsymbol{\sigma}}, \bar{e}^p = 0) = (1-\phi)^2(\bar{\boldsymbol{\sigma}} : \bar{\mathbf{T}} : \bar{\boldsymbol{\sigma}}) - \tfrac{2}{3}\sigma_y^2 = 0 \tag{7.44}$$

Carrying out the tensor contraction, we arrive at

$$\begin{aligned}(\bar{T}_{11}^{(1)} + 2\bar{T}_{11}^{(2)})\bar{\sigma}_{11}^2 + (\bar{T}_{22}^{(1)} + 2\bar{T}_{22}^{(2)})(\bar{\sigma}_{22}^2 + \bar{\sigma}_{33}^2) + 4\bar{T}_{12}^{(2)}(\bar{\sigma}_{12}^2 + \bar{\sigma}_{13}^2) + 4\bar{T}_{22}^{(2)}\bar{\sigma}_{23}^2 + \\ 2\bar{T}_{12}^{(1)}\bar{\sigma}_{11}(\bar{\sigma}_{22} + \bar{\sigma}_{33}) + 2\bar{T}_{22}^{(1)}\bar{\sigma}_{22}\bar{\sigma}_{33} = \frac{2\sigma_y^2}{3(1-\phi)^2}\end{aligned} \tag{7.45}$$

Alternatively, the initial yield surface can be expressed in terms of the mean stress and the effective deviatoric stress as follows:

$$\bar{\sigma}_m = \tfrac{1}{3}\left(\bar{\sigma}_{11} + \bar{\sigma}_{22} + \bar{\sigma}_{33}\right) \tag{7.46}$$

$$\bar{\sigma}_e = \sqrt{\tfrac{3}{2}\left[\left(\bar{\sigma}_{11}^2 - \bar{\sigma}_m\right)^2 + \left(\bar{\sigma}_{22}^2 - \bar{\sigma}_m\right)^2 + \left(\bar{\sigma}_{33}^2 - \bar{\sigma}_m\right)^2 + 2\left(\bar{\sigma}_{12}^2 + \bar{\sigma}_{13}^2 + \bar{\sigma}_{23}^2\right)\right]} \tag{7.47}$$

The predictions of the overall normalized initial yield surfaces at various damage levels for the MMCs with harder ($E_f > E_m$) reinforcements and softer ($E_m > E_f$) reinforcements are shown

in Figure 7.16 and Figure 7.17, respectively. The initial yield surface in the middle region undergoes more expansion away from the origin as more damage cumulating in the composite, indicating that a larger amount of the energy is dissipated in the form of fiber breaks rather than incurring the plastic deformations. Figure 7.18–Figure 7.20 exhibit the overall normalized initial yield surfaces with various fiber volume fractions at three levels of fiber breakage damage for the MMCs with harder fibers. It is noted that the initial yielding point in terms of pure $\bar{\sigma}_m$ or pure $\bar{\sigma}_e$ increases or decreases, respectively, as increasing fiber volume fraction. On the other hand, the effects of the fiber aspect ratio on the initial yield surface at various stages of fiber breaking damage for the MMCs with harder fibers are demonstrated in Figure 7.21–Figure 7.23.

7.7 Conclusion

Emanating from the elastic damage micromechanical framework proposed in Chapter 5, the effective elastoplastic formulations have been derived to capture the nonlinear behaviors of continuous fiber reinforced ductile matrix composites under various loadings. In this chapter, the total eigenstrain field is a summation of the conventional eigenstrain due to the mismatch between the inclusion and the matrix and the effective eigenstrain due to fiber. In addition, the effective elastoplastic deformations are predicted by means of the effective yield surface derived from a representative microstructure with purely elastic fibers embedded in the elastoplastic matrix. Several numerical applications of the proposed model to fiber reinforced MMCs under external loadings are presented. In particular, the overall uniaxial and axisymmetric elastoplastic stress-strain responses of the continuous fiber reinforced MMCs are investigated. Studies of the initial yield surfaces at various damage levels are performed.

In summary, the proposed model is capable of predicting the elastoplastic stress-strain responses of the continuous fiber reinforced MMCs under tensile loadings. Reinforcements with the larger aspect ratio, the higher volume fraction, or the higher Young's modulus result in better strengthening effects at the expense of accelerating the fiber breakage evolution rate. On the other hand, the plastic deformation in the matrix tends to slow the rate of fiber breakage evolution in the form of energy dissipation. In addition, the transverse loading has significant effect on the material behavior.

Table 7.1 Computational algorithm for determination of the total number of fiber breakages.

Given the state solutions at the previous increment ν : $\{\bar{\boldsymbol{\varepsilon}}_\nu, \bar{\boldsymbol{\varepsilon}}_\nu^e, \bar{\boldsymbol{\varepsilon}}_\nu^p, \bar{e}_\nu^p, \lambda_\nu, (n)_\nu\}$ and current total macroscopic stress tensor $\bar{\boldsymbol{\sigma}}_{\nu+1}$

To compute $(n)_{\nu+1}$ with the following local iteration scheme with the iteration count $\eta = 0$, and $(n)_{\nu+1}^0 = (n)_\nu$:

(i) Obtain $(\mathbf{B})^\eta = [\mathbf{A} + \mathbf{S} + \beta \cdot (n)_{\lambda+1}^\eta (\mathbf{A} \bullet \boldsymbol{\Gamma} \bullet \mathbf{C}_1)]^{-1}$

(ii) Calculate $(\bar{\boldsymbol{\sigma}}_f)^\eta = \left[\mathbf{I} + (\mathbf{I} - \mathbf{S}) \bullet (\mathbf{B})^\eta\right] : \bar{\boldsymbol{\sigma}}_{\nu+1}$

(iii) Determine $(n)_{\nu+1}^\eta / \bar{n} = 1 - \exp\{-[(\bar{\sigma}_f)^\eta - \sigma_{cr} / S]^M\}$

(iv) Check if $|(n)_{\nu+1}^\eta - (n)_{\nu+1}^{\eta-1}| \leq TOL$

YES: terminate local iteration and return

$(n)_{\nu+1} = (n)_{\nu+1}^{\eta_{\text{converged}}}$, $(\mathbf{B})_{\nu+1} = (\mathbf{B})^{\eta_{\text{converged}}}$, $(\mathbf{M})_{\nu+1} = \mathbf{I} + \phi \mathbf{S} \bullet (\mathbf{B})_{\nu+1}$,

$(\mathbf{P})_{\nu+1} = \{\mathbf{C}_0 \bullet [\mathbf{I} + \phi (\mathbf{I} - \mathbf{S}) \bullet (\mathbf{B})_{\nu+1}] \bullet \mathbf{C}_0^{-1}\}^{-1}$, $(\bar{\mathbf{T}})_{\nu+1} = (\mathbf{P})_{\nu+1}^T \bullet \mathbf{T} \bullet (\mathbf{P})_{\nu+1}$, and

$\mathbf{C}_{\nu+1}^* = \mathbf{C}_0 \bullet \{\mathbf{I} + \phi \cdot (n)_{\nu+1} (\mathbf{M})_{\nu+1}^{-1} \bullet [\mathbf{A} + \mathbf{S} + \beta \cdot (n)_{\nu+1} (\mathbf{A} \bullet \boldsymbol{\Gamma} \bullet \mathbf{C}_1)]^{-1}\}$

NO: go to step (i)

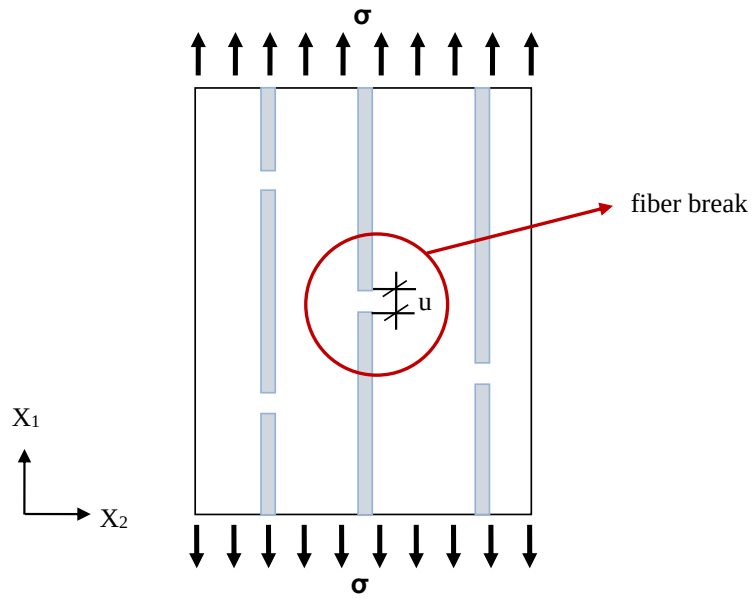

Figure 7.1 Schematic representation of a continuous fiber reinforced metal matrix composite subjected to external loadings with fiber breakages.

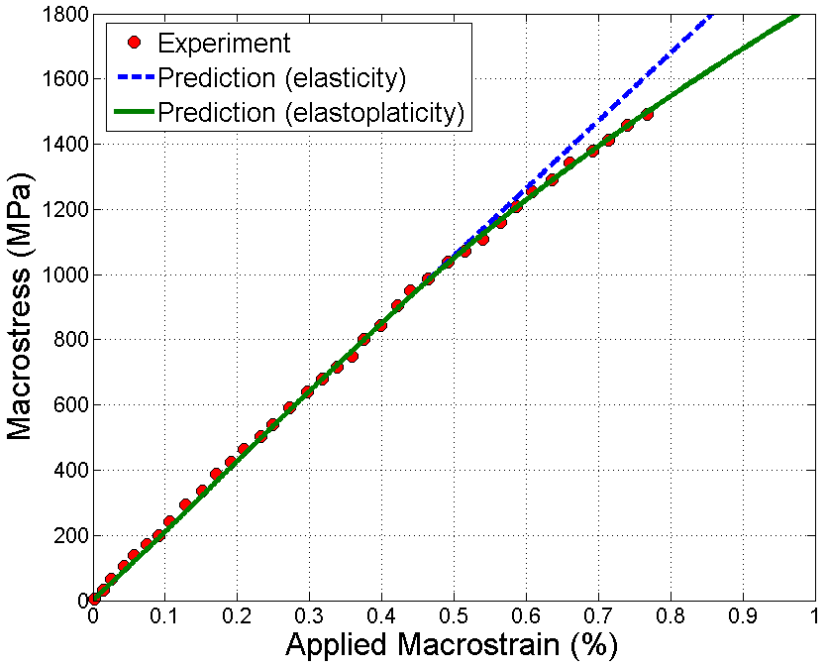

Figure 7.2 Comparison of the uniaxial stress-strain responses between the analytical predictions (elastostatic damage model and elastoplastic damage model) and the experimental data (Jeng et al., 1991) for Ti5-3 composites in the as fabricated condition.

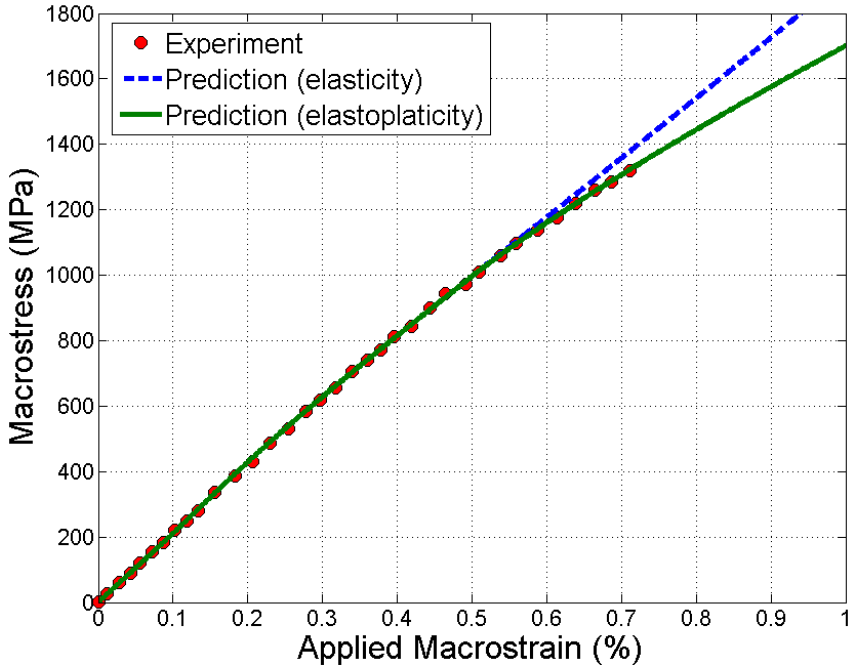

Figure 7.3 Comparison of the uniaxial stress-strain responses between the analytical predictions (elastostatic damage model and elastoplastic damage model) and the experimental data (Jeng et al., 1991) for Ti5-3 composites in the 800°C/12hrs condition.

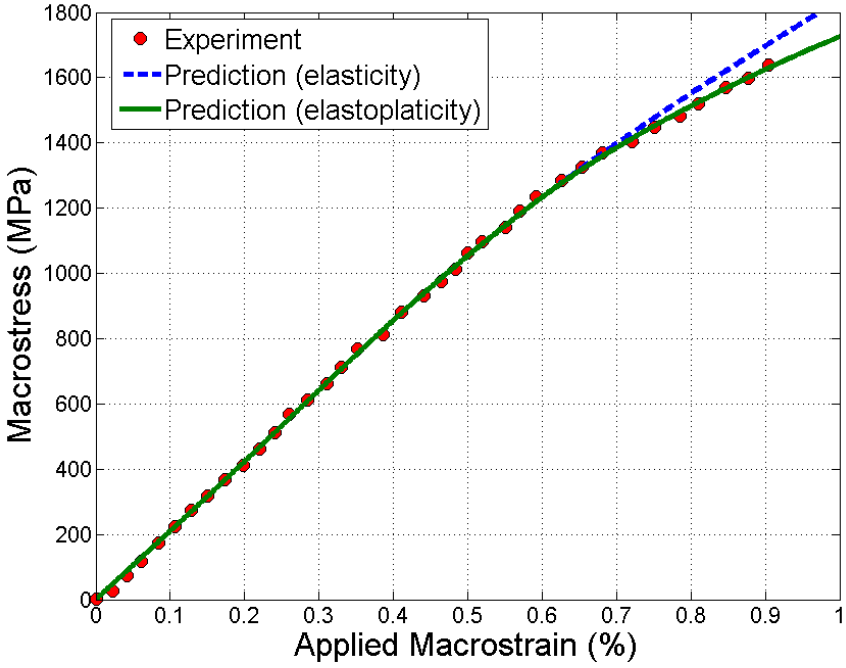

Figure 7.4 Comparison of the uniaxial stress-strain response between the analytical predictions (elastostatic damage model and elastoplatic damage model) and the experimental data (Jang et al., 1991) for Ti-6-4 composites.

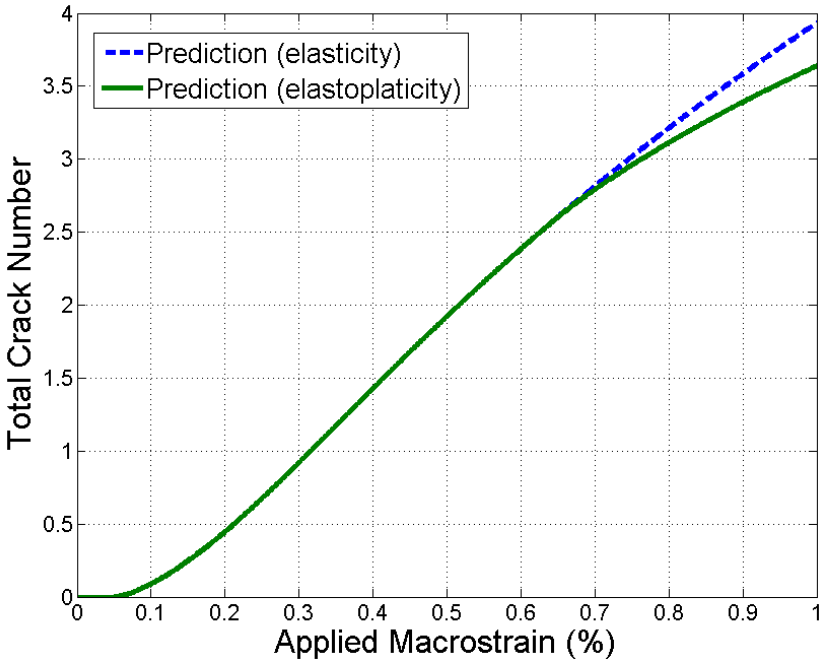

Figure 7.5 Comparison of the predicted evolutionary numbers of fiber breakages in the Ti-6-4 composites between the elastostatic damage model and elastoplastic damage model.

E_m = 82 GPa, ν_m = 0.342, E_f = 400 GPa,
ν_f = 0.25, σ_{cr} = 250 MPa, S = 3200 Mpa, α = 10,
M = 1.54, σ_Y = 430 MPa, h = 14400 MPa, q = 0.685

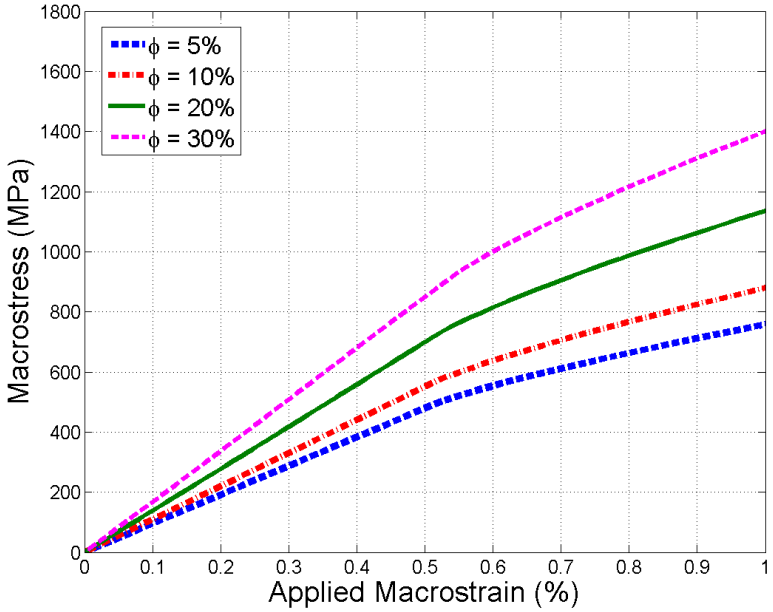

Figure 7.6 Parametric studies on the effects of fiber volume fraction on the uniaxial stress-strain behavior of the continuous fiber reinforced MMCs.

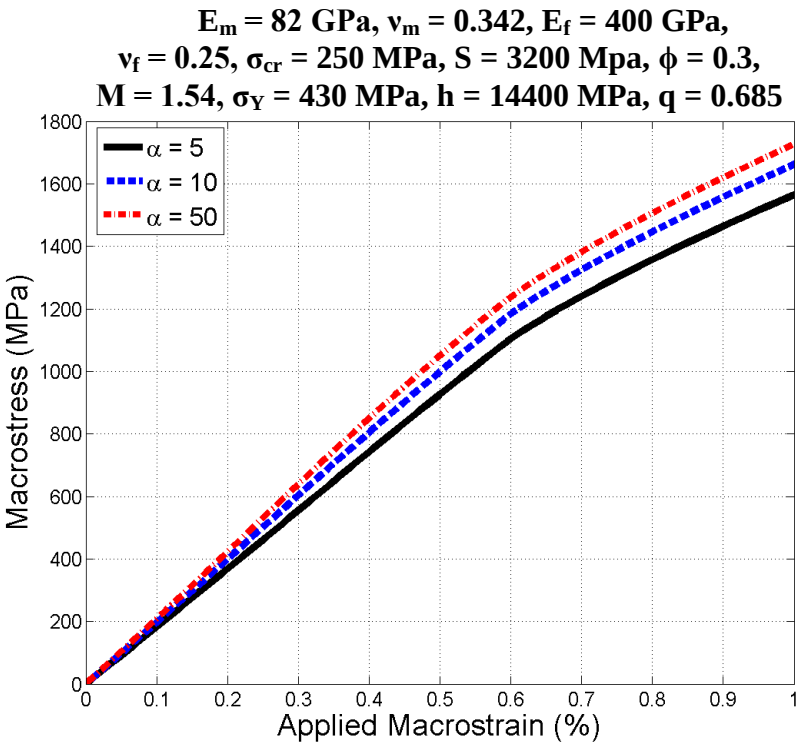

Figure 7.7 Parametric studies on the effects of fiber aspect ratio on the uniaxial stress-strain behavior of the continuous fiber reinforced MMCs.

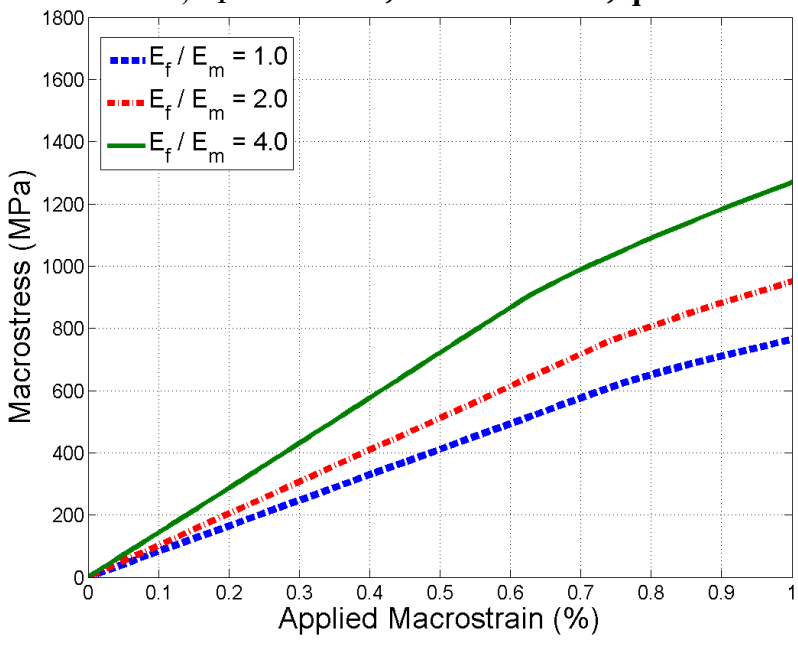

Figure 7.8 Parametric studies on the effects of fiber Young's modulus on the uniaxial stress-strain behavior of the continuous fiber reinforced MMCs.

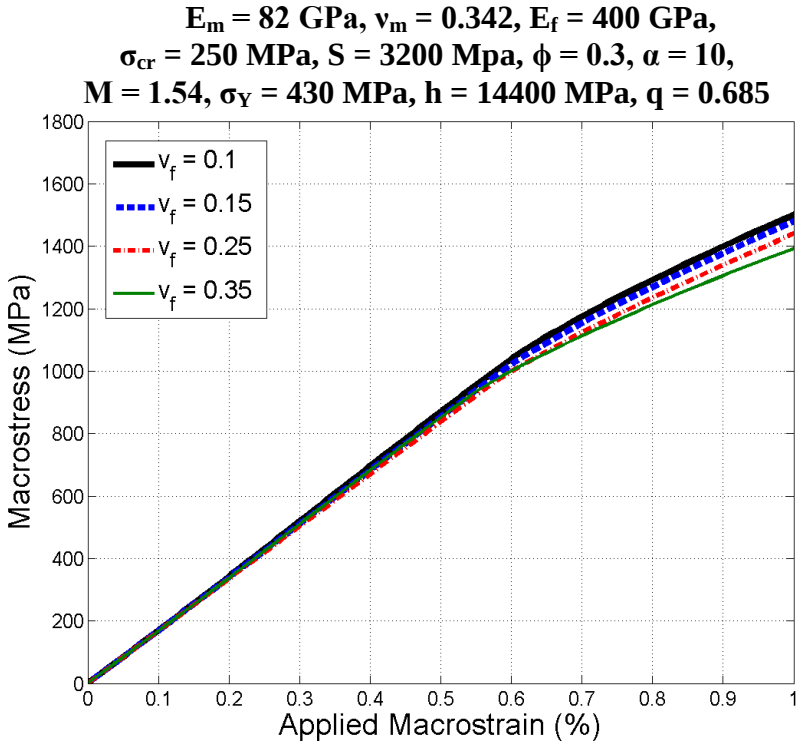

Figure 7.9 Parametric studies on the effects of matrix Poisson's ratio on the uniaxial stress-strain behavior of the continuous reinforced MMCs.

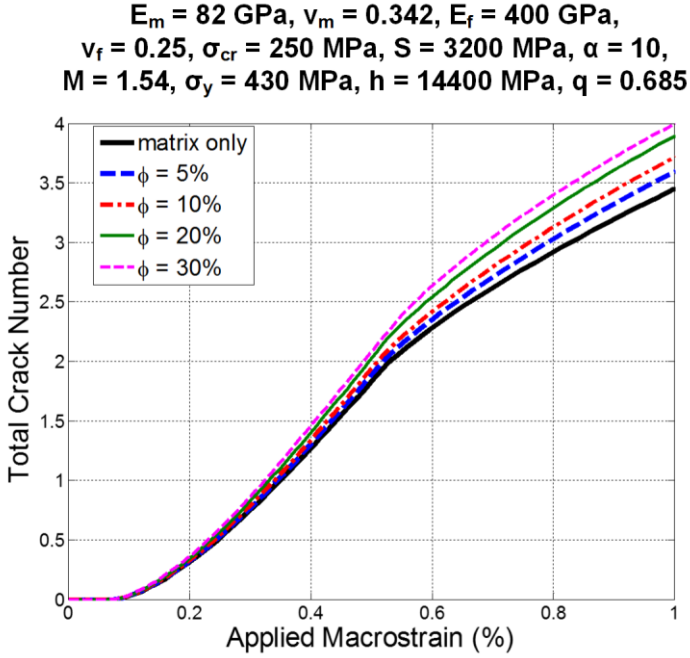

Figure 7.10 Parametric studies on the effects of fiber volume fraction on the number of evolutionary fiber breakages in the continuous fiber reinforced MMCs.

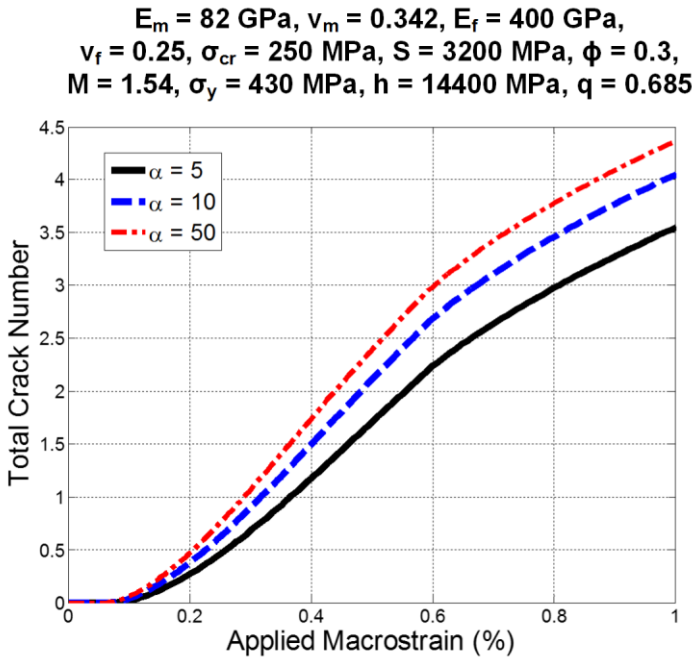

Figure 7.11 Parametric studies on the effects of fiber aspect ratio on the number of evolutionary fiber breakages in the continuous fiber reinforced MMCs.

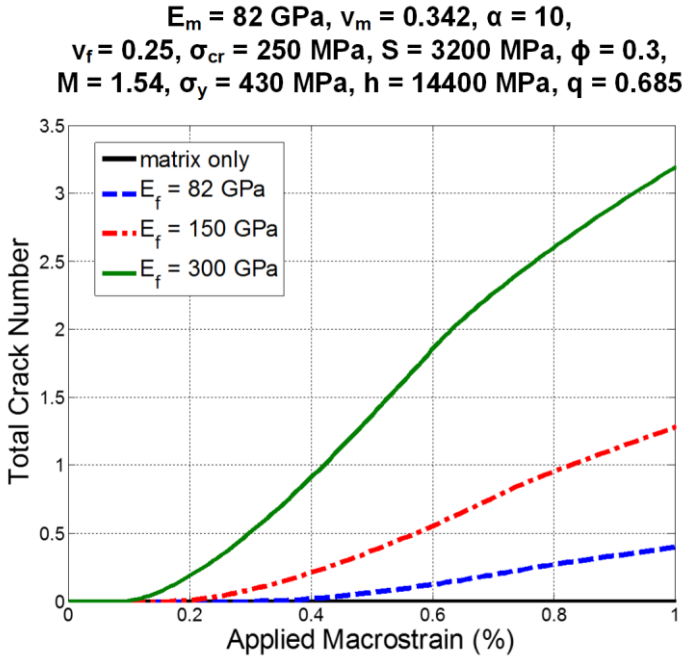

Figure 7.12 Parametric studies on the effects of fiber Young's modulus on the number of evolutionary fiber breakages in the continuous fiber reinforced MMCs.

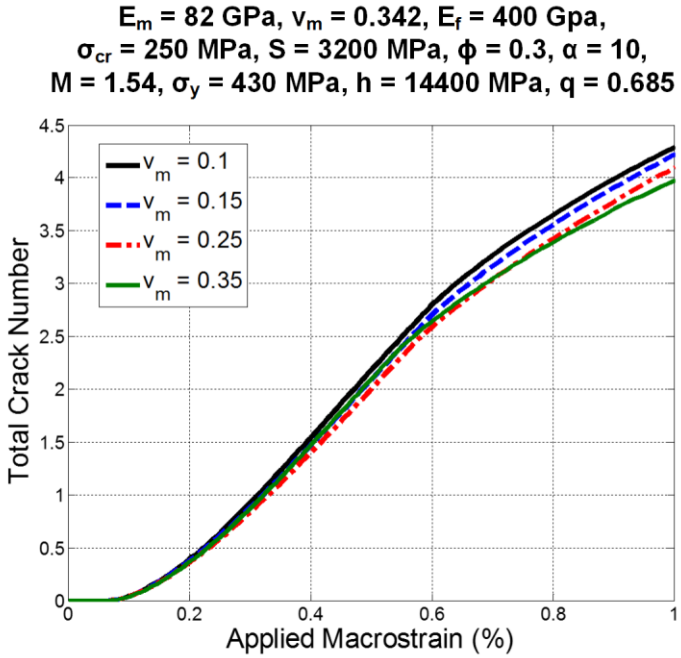

Figure 7.13 Parametric studies on the effects of matrix Poisson's ratio on the number of evolutionary fiber breakages in the continuous fiber reinforced MMCs.

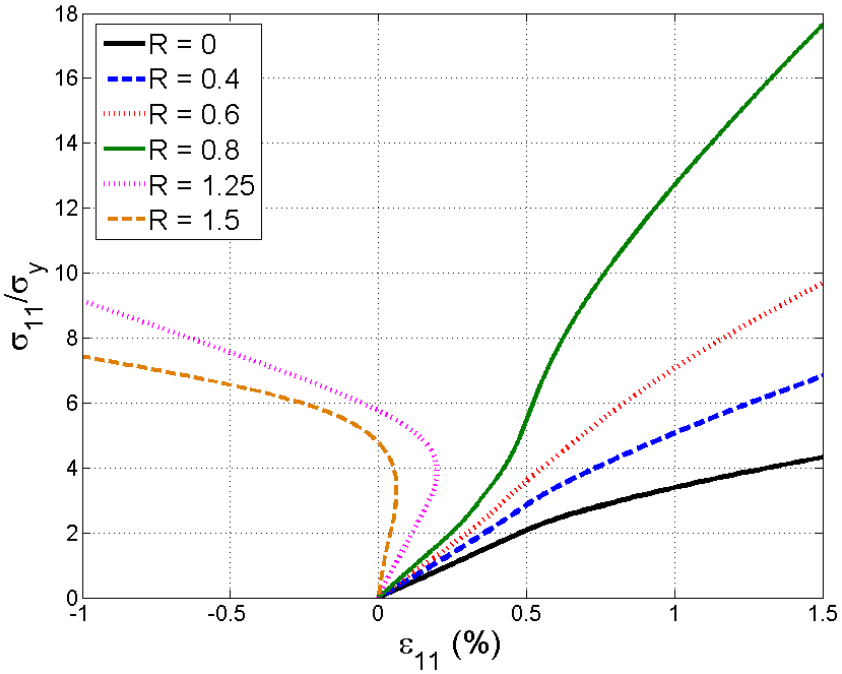

Figure 7.14 Effects of the stress ratio on the normalized overall elastoplastic-damage responses in the X_1 (longitudinal) direction with the material properties: E_m = 82 GPa, ν_m = 0.342, E_f = 400 GPa, α = 25, ν_f = 0.25, σ_{cr} = 250 MPa, S = 3200 MPa, ϕ = 0.3, M = 1.54, σ_Y = 430 MPa, h = 14400 MPa, q = 0.685).

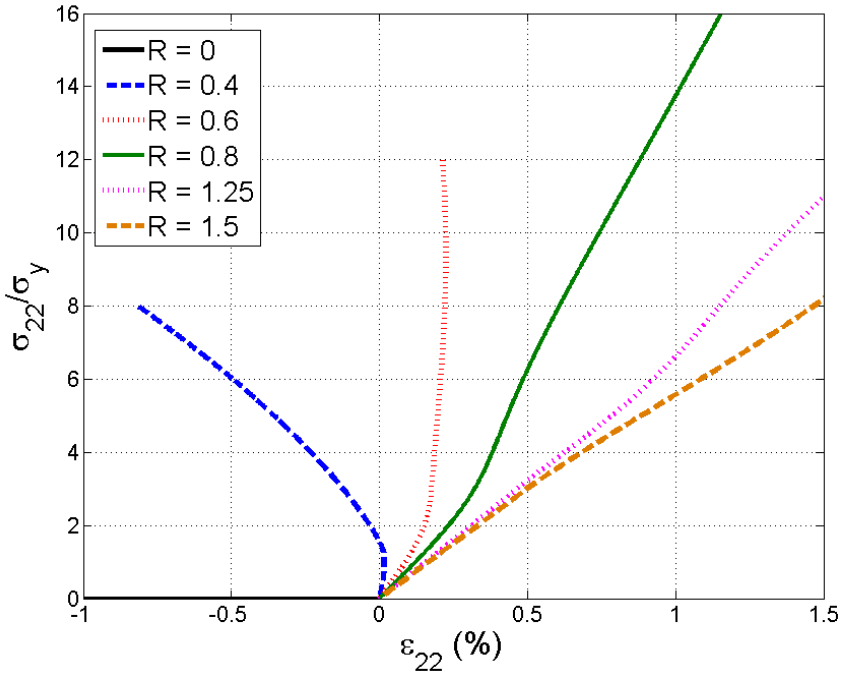

Figure 7.15 Effects of the stress ratio on the normalized overall elastoplastic-damage responses in the X_2 (radial) direction with the material properties: E_m = 82 GPa, ν_m = 0.342, E_f = 400 GPa, α = 25, ν_f = 0.25, σ_{cr} = 250 MPa, S = 3200 MPa, ϕ = 0.3, M = 1.54, σ_Y = 430 MPa, h = 14400 MPa, q = 0.685).

E_m = 82 GPa, ν_m = 0.342, E_f = 400 GPa, ν_f = 0.25, ϕ = 0.2, α = 25

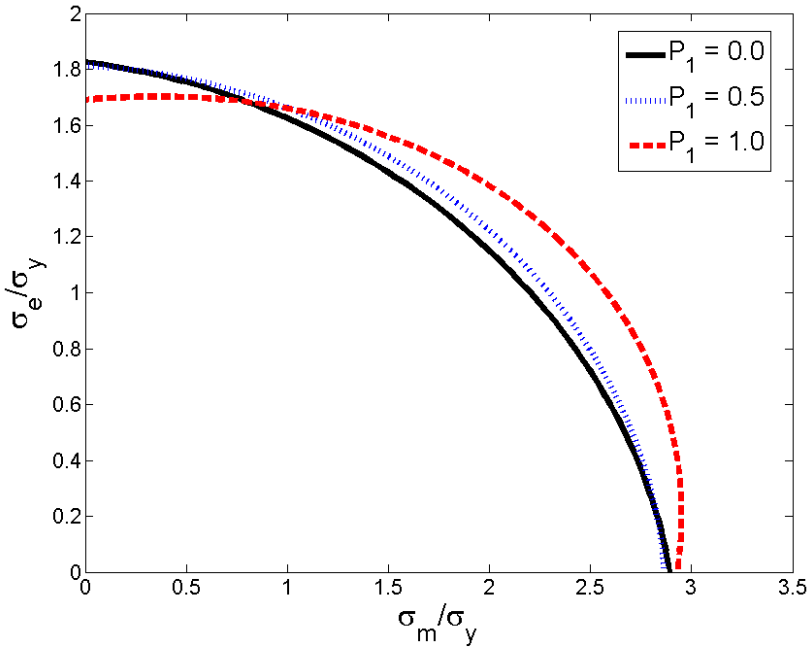

Figure 7.16 Effects of the fiber Young's modulus on the initial yield surface at various levels of fiber breakage damage in harder fiber inclusion.

E_m = 82 GPa, ν_m = 0.342, E_f = 30 GPa, ν_f = 0.25, ϕ = 0.2, α = 25

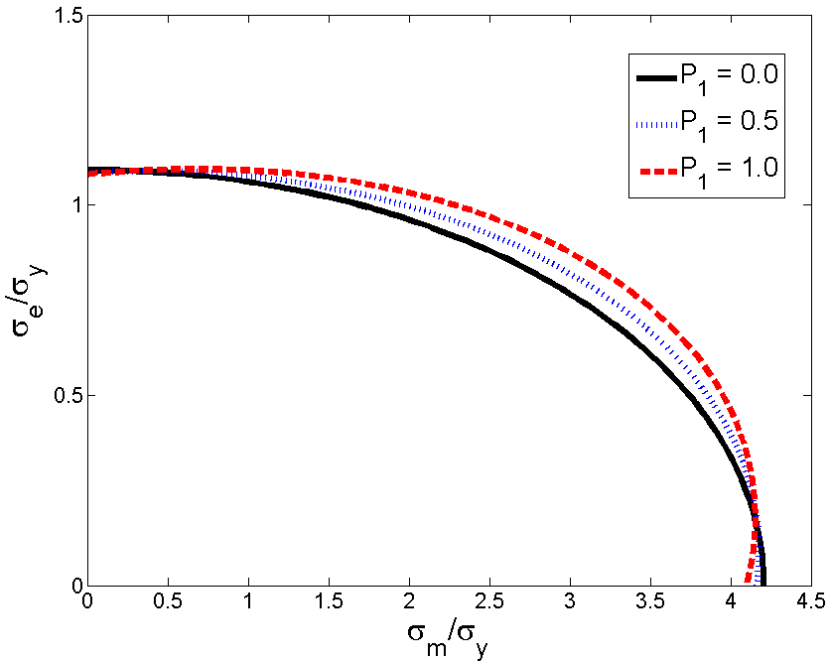

Figure 7.17 Effects of the fiber Young's modulus on the initial yield surface at various levels of fiber breakage damage in softer fiber inclusion.

E_m = 82 GPa, ν_m = 0.342, E_f = 400 GPa, ν_f = 0.25, ϕ = 0.2, α = 25, P_1 = 0.0

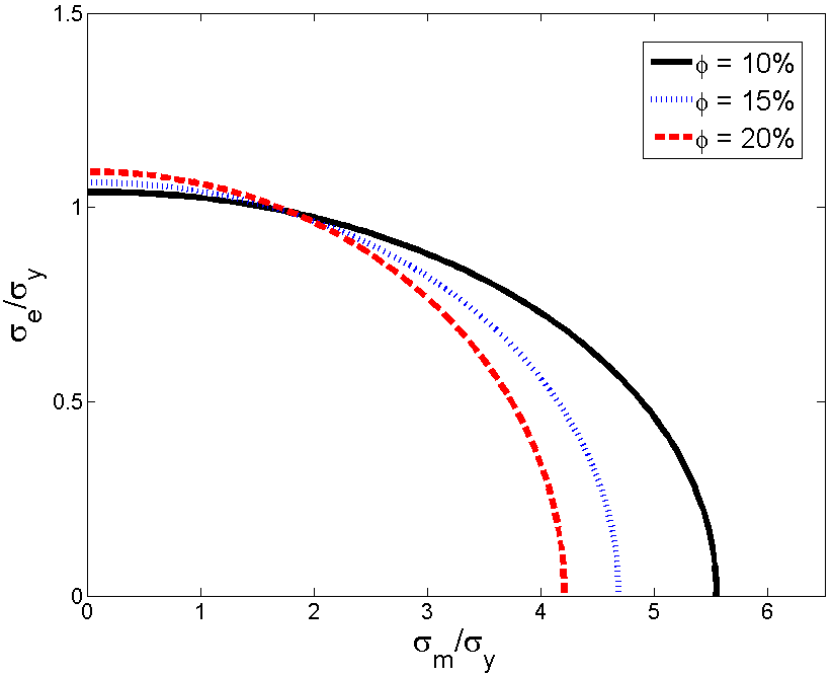

Figure 7.18 Effects of the fiber volume fraction on the initial yield surface at various levels of fiber breakage damage (damage parameter P_1 = 0).

E_m = 82 GPa, ν_m = 0.342, E_f = 400 GPa, ν_f = 0.25, ϕ = 0.2, α = 25, P_1 = 0.5

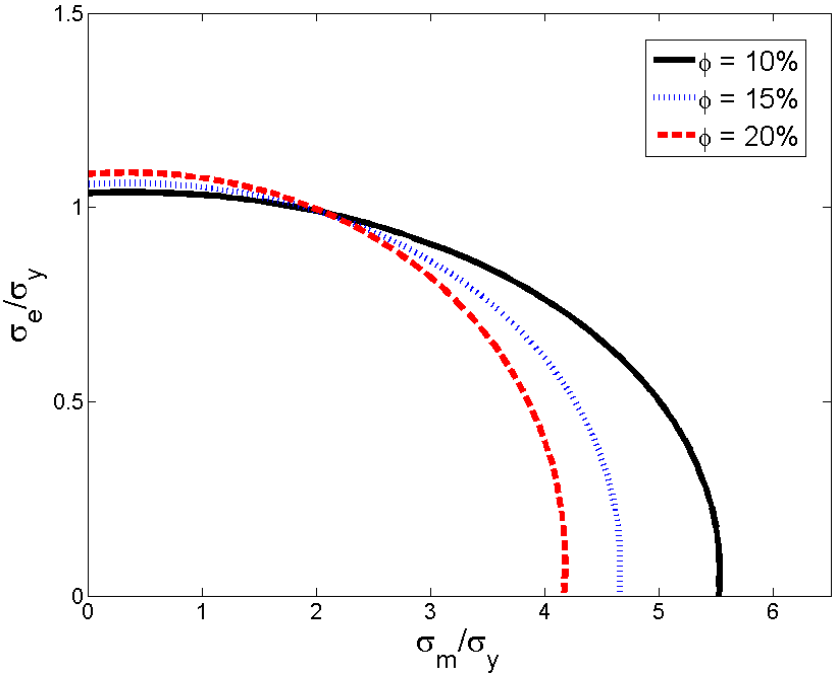

Figure 7.19 Effects of the fiber volume fraction on the initial yield surface at various levels of fiber breakage damage (damage parameter P_1 = 0.5).

E_m = 82 GPa, ν_m = 0.342, E_f = 400 GPa, ν_f = 0.25, ϕ = 0.2, α = 25, P_1 = 0.5

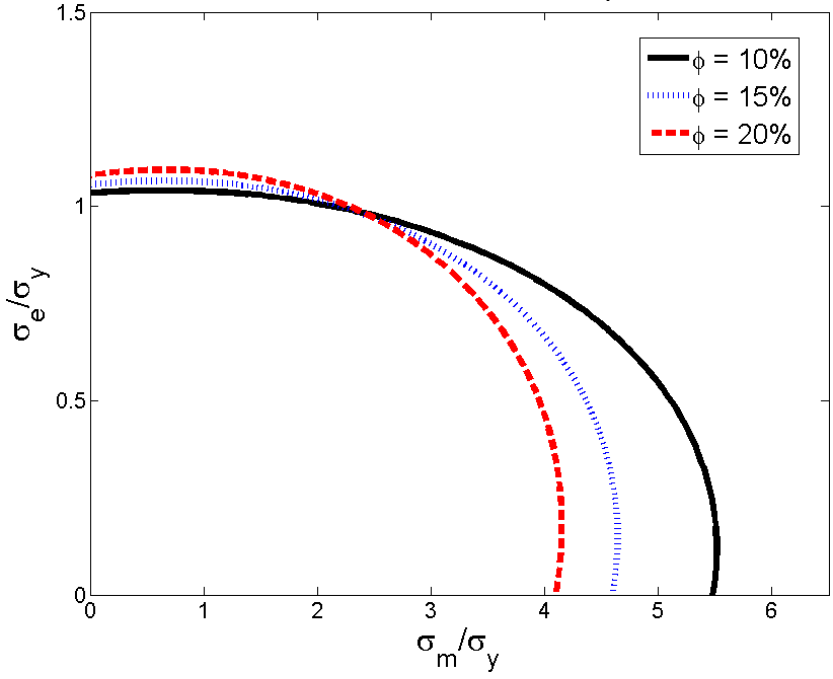

Figure 7.20 Effects of the fiber volume fraction on the initial yield surface at various levels of fiber breakage damage (damage parameter P_1 = 1.0).

E_m = 82 GPa, ν_m = 0.342, E_f = 400 GPa, ν_f = 0.25, ϕ = 0.2, α = 25, P_1 = 0.0

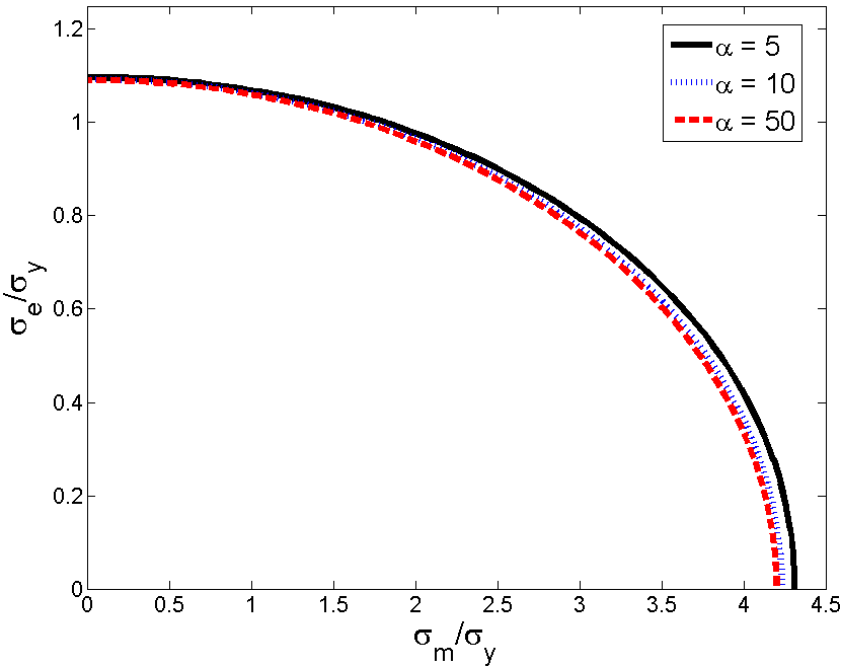

Figure 7.21 Effects of the aspect ratio on the initial yield surface at various levels of fiber breakage damage (damage parameter P_1 = 0).

E_m = 82 GPa, ν_m = 0.342, E_f = 400 GPa, ν_f = 0.25, ϕ = 0.2, α = 25, P_1 = 0.5

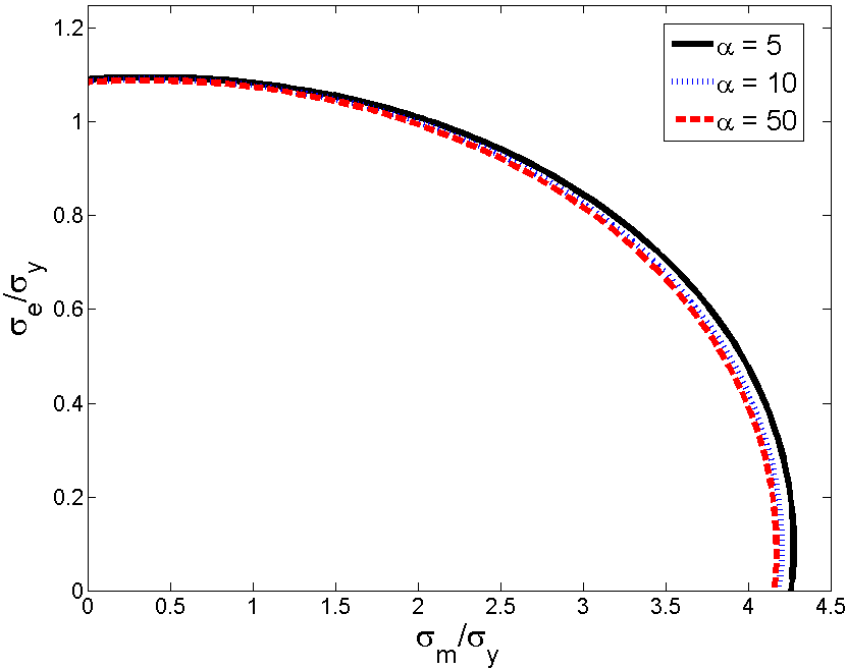

Figure 7.22 Effects of the aspect ratio on the initial yield surface at various levels of fiber breakage damage (damage parameter P_1 = 0).

E_m = 82 GPa, ν_m = 0.342, E_f = 400 GPa, ν_f = 0.25, ϕ = 0.2, α = 25, P_1 = 0.5

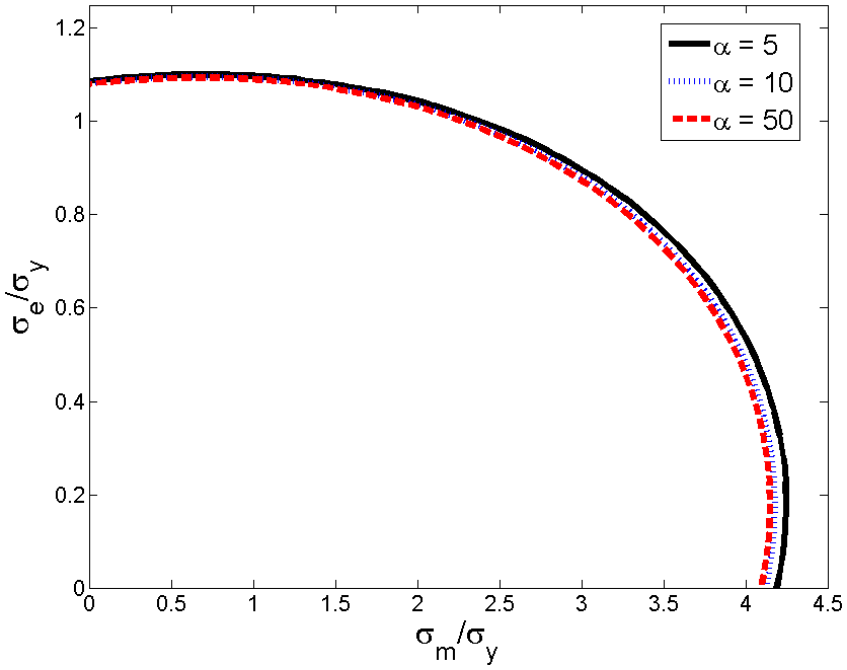

Figure 7.23 Effects of the aspect ratio on the initial yield surface at various levels of fiber breakage damage (damage parameter P_1 = 0).

CHAPTER 8 CONCLUSIONS AND FUTURE WORKS

8.1 Conclusions

In this dissertation, modeling on the elastic and the elastoplastic material behaviors of continuous fiber reinforced composites is investigated. A major part of the work conducted involves the investigation of the effective damage responses due to damage evolutions of matrix microcracks and fiber breakages.

Chapter 3 presents the effective elastic damage behavior of continuous fiber reinforced composites with evolutionary matrix microcracks. A cohesive penny-shape microcrack model is proposed within a two-step homogenization framework to achieve the effective elastic damage behavior of continuous fiber reinforced composites. In the present model, the size and the number density of microcracks are defined as two damage parameters to control the damage evolution. In addition, the thermal effect has been taken into account in the proposed model by taking advantage of the thermal eigenstrain and the Eshelby's equivalent inclusion principle. The overall coefficient of thermal expansion (CTE) of a fiber reinforced composite is derived systematically under the framework of micromechanics to describe the overall damage behavior of composites due to the matrix microcrack evolution under temperature changes.

Chapter 4 proposes a micromechanical evolutionary damage framework capable of predicting the overall mechanical behavior of and damage evolution in continuous fiber reinforced composites. In the presented framework, the effective stress fields in a single fiber due

to an embedded penny-shaped fiber break are systematically derived by applying the double-inclusion theory. An effective length denoting the distance between two adjacent cracks is then introduced as a damage parameter while determining the damage evolution within a single fiber. This enables the modeling of the effective damage behavior of a single fiber-reinforced composite. As an application of the proposed framework, a micromechanical damage model is further proposed to simulate the fiber-dominated failure mechanism within a continuous fiber reinforced composite. A Weibull probability function is adopted to estimate the varying volume fractions of damaged fibers and intact fibers. Numerical simulations are presented to demonstrate the effectiveness of the proposed methodology.

In Chapter 5, based on the linear elastic fracture mechanics (LEFM) and ensemble-volume averaging technique, an effective eigenstrain is newly proposed to quantify the homogenized stress fields in a single fiber due to multiple breaks. In the proposed model, the number density evolution of fiber breaks is characterized by a two-parameter Weibull statistic with the temperature effect implicitly enclosed by properly adjusting the Weibull parameters. In particular, the damage criterion in the evolutionary model is theoretically. Base on the proposed damage framework, a homogeneous damage evolution model capable of simulating the material behavior of multi-fiber reinforced composite materials is developed.

Chapter 6 presents two stochastic risk-competing models to simulate the fiber breaking evolution in a multi-fiber composite in an inhomogeneous fashion by considering different load sharing mechanisms. A unit cell model is adopted with each cell being assigned an initial weakness based on a normal distribution. Damage evolution inside each individual cell structure

follows the micromechanical model presented in Chapter 5. Two risk competing models are then introduced to determine the damage sequence within the multi-fiber composite by computing the fracture probability based on the weakness of cells at each time step. It is observed that one risk-competing model tends to generate a concentrated damage pattern with broken fibers clustering in a T-shape or a cross-shape, while the other model yields a more diffused damage pattern. Finally, the overall stress-strain responses and the fiber break evolution are s predicted and verified against experimental data.

Chapter 7 examines the effective elastoplastic behavior of MMCs containing unidirectionally aligned continuous fibers. A homogenization procedure is utilized to derive the overall yield function for the composite based on the probabilistic spatial distribution of aligned inclusions. Based on continuum plasticity, a plastic flow rule and a hardening law are postulated. These laws together with the proposed overall yield function then characterized the macroscopic elastoplastic behavior of the composite under three-dimensional arbitrary loading/unloading histories. The overall uniaxial elastoplastic stress-strain behavior of MMCs with aligned continuous fibers is investigated. Comparisons between theoretical predictions and experimental data for the composite are performed to illustrate the capability of the proposed method.

8.2 Future works

To further enhance the proposed models, the following improvements can be accomplished in the future.

(1) *Combined effect of fiber breakage and fiber/matrix interfacial debonding*

Experimental investigations reveal that interfacial debonding between the fiber and the matrix normally occurs simultaneously along with fiber fracture. It is crucial to consider the combined effect due to both fiber breaking and the fiber/matrix debonding. On one hand, the stress distribution near the fiber breakage is affected significantly by the existence of the fiber/matrix debonding. On the other hand, the load-sharing capability of a fiber that is partially or completely debonded from the matrix will degrade to different levels. Therefore, a debonded fiber is less likely to have multiple fiber breakages comparing to an intact fiber. The number density of fiber breakages and the debonding length are intrinsically related. Their quantitative relationship depends on the material properties, loading conditions and bonding conditions. To account for the combined effect of these two damage modes, we can extend the framework developed in Chapter 6 by proposing a risk-competing model to simulate the competition between fiber breakage evolution and interfacial debonding evolution. Once the effective elastic damage constitutive relations are achieved, the overall yielding function can be further derived to capture the elastoplastic damage behavior of a fiber reinforced MMC considering both fiber breakage and interfacial debonding.

(2) *Damage behavior of functionally graded composites*

In reality, an interface region possesses functionally graded multi-layer structure, which is formed primarily due to the chemical reaction between the fiber and the matrix. In addition, the carbon coating technique, which is a commonly used to protect the fiber from strength degradation during fabrication, e.g., double-layer carbon coating, will also introduce additional layers between the fiber and interfacial layer. As a consequence, fiber/matrix

interfacial debonding may take place at different locations including the interfaces between the carbon coating layers, the outer carbon layer and reaction zone, and the reaction zone and matrix alloy. In the future research, the geometry and material properties of the interfacial layer can be taken into account while investigating the damage behavior of fiber reinforced composites. The effect of interfacial debonding at various locations on the overall material behavior can be investigated in details under the framework of micromechanics.

(3) *Fiber-dominated damage mechanism considering higher-order interactions*

The fiber-dominated damage mechanism in a multi-fiber reinforced composite has been investigated in Chapter 4. However, some experimental studies indicate that the fiber-dominated failure mechanism is more likely to be observed in composite with a high fiber volume fraction. As a result, the interactions among inclusions become significant, and further studies need to be performed to include the higher-order interaction effect. Based on the micromechanical models proposed by Ju and Lin (2001), Ju and Lee (2004) and Ju and Ko (2006), the proposed fiber-dominated damage mode in Chapter 4 can be further extended to include the effect of higher-order interactions among inclusions.

(4) *Nanocomposites*

Nanocomposites are materials filled with nano-sized inclusions. In other words, inclusions have at least one dimension in the nanometer scale. They become more and more popular in various application fields due to their capability of improving mechanical properties with a small amount of reinforcements. However, the nanocomposite is still a nascent field of

material science and technology in the development stage. Some of the critical issues hindering realizations of their full potential are dispersion and alignment, and interfacial bonding of nano-inclusions. Moreover, due to the nano-size of the inclusion, some of the micromechanics analysis models may not be valid because of the size-effect. Therefore, a new micromechanical/nanomechanical model needs to be developed to account for the influence of size, shape, volume fraction, and distribution of these nano-scaled reinforcements. In addition, a better understanding is necessary for the composition, microstructure, properties of nano-scaled reinforcements, and the influence of heat treatment or manufacturing process on the nano-structure and the overall properties of composites. The elucidation of these effects on the mechanical properties and deformation behaviors of nano-size particle/fiber reinforced composites through theoretical and experimental investigations will open a door for the development of the performance-based design of composite materials for a wide range of engineering applications.

APPENDIX A DETAILED DERIVATION OF THE RELATIONSHIP BETWEEN FIBER-BREAKAGE INDUCED EIGENSTRAIN AND MACROSCOPIC STRAIN

The ensemble-volume averaged perturbed strain $\left\langle \bar{\boldsymbol{\varepsilon}}' \right\rangle_r$ in the *rth* fiber phase is related to the ensemble-volume averaged total eigenstrain $\left\langle \bar{\boldsymbol{\varepsilon}}^{**} \right\rangle_r$ based on the Eshelby's solution as follows

$$\left\langle \bar{\boldsymbol{\varepsilon}}' \right\rangle_r = \mathbf{S} : \left\langle \bar{\boldsymbol{\varepsilon}}^{**} \right\rangle_r \tag{A.1}$$

where **S** is the interior Eshelby tensor, and the total eigenstrain $< \bar{\boldsymbol{\varepsilon}}^{**} >_r = < \bar{\boldsymbol{\varepsilon}}^{*}_{cr} >_r + < \bar{\boldsymbol{\varepsilon}}^{*} >_r$ which accounts for both the eigenstrain presents in the inhomogeneity $< \bar{\boldsymbol{\varepsilon}}^{*} >_r$ and the eigenstrain due to fiber breaking $< \bar{\boldsymbol{\varepsilon}}^{*}_{cr} >_r$. Based on the micromechanical formulation presented in Ju and Chen (1994), the ensemble volume averaged eigenstrain in the *rth* fiber phase due to fiber breaking can be expressed by

$$\left\langle \bar{\boldsymbol{\varepsilon}}^{*}_{cr} \right\rangle_r = \beta \cdot n \cdot \boldsymbol{\Gamma} \bullet \left\{ \mathbf{C}_0 : \left[\boldsymbol{\varepsilon}^0 + \left\langle \bar{\boldsymbol{\varepsilon}}' \right\rangle_r - \left\langle \bar{\boldsymbol{\varepsilon}}^{**} \right\rangle_r \right] \right\} \tag{A.2}$$

The consistency condition based on the Eshelby equivalent inclusion principle reads

$$\mathbf{C}_1 : \left(\boldsymbol{\varepsilon}^0 + \left\langle \bar{\boldsymbol{\varepsilon}}' \right\rangle_r - \left\langle \bar{\boldsymbol{\varepsilon}}^{*}_{cr} \right\rangle_r \right) = \mathbf{C}_0 : \left(\boldsymbol{\varepsilon}^0 + \left\langle \bar{\boldsymbol{\varepsilon}}' \right\rangle_r - \left\langle \bar{\boldsymbol{\varepsilon}}^{*}_{cr} \right\rangle_r - \left\langle \bar{\boldsymbol{\varepsilon}}^{*} \right\rangle_r \right) \tag{A.3}$$

Combining Eqns. (A.1) and (A.3) and utilizing Eq. (A.2) lead to

$$\mathbf{C}_1 : \boldsymbol{\varepsilon}^0 + \mathbf{C}_1 \bullet \mathbf{S} : \left\langle \bar{\boldsymbol{\varepsilon}}^{**} \right\rangle_r - \beta \cdot n \cdot \boldsymbol{\Gamma} \bullet \mathbf{C}_0 : \boldsymbol{\varepsilon}^0 - \beta \cdot n \cdot \boldsymbol{\Gamma} \bullet \mathbf{C}_0 \bullet (\mathbf{S} - \mathbf{I}) : \left\langle \bar{\boldsymbol{\varepsilon}}^{**} \right\rangle_r = \mathbf{C}_0 : \boldsymbol{\varepsilon}^0 + \mathbf{C}_0 \bullet (\mathbf{S} - \mathbf{I}) : \left\langle \bar{\boldsymbol{\varepsilon}}^{**} \right\rangle_r \tag{A.4}$$

or

$$\left[\mathbf{C}_1-\left(\mathbf{I}+\beta\cdot n\cdot\boldsymbol{\Gamma}\right)\bullet\mathbf{C}_0\right]:\boldsymbol{\varepsilon}^0=-\left[\mathbf{C}_1\bullet\mathbf{S}-\mathbf{C}_0\bullet\left(\mathbf{S}-\mathbf{I}\right)-\beta\cdot n\cdot\boldsymbol{\Gamma}\bullet\mathbf{C}_0\bullet\left(\mathbf{S}-\mathbf{I}\right)\right]:\left\langle\bar{\boldsymbol{\varepsilon}}^{**}\right\rangle_r \quad \text{(A.5)}$$

Therefore, we reach the following expression which relates the ensemble volume averaged total eigenstrain in the *rth* fiber phase to the macroscopic strain

$$\left\langle\bar{\boldsymbol{\varepsilon}}^{**}\right\rangle_r=\mathbf{T}_r:\boldsymbol{\varepsilon}^0 \quad \text{(A.6)}$$

and

$$\mathbf{T}_r=-\left[\mathbf{C}_1\bullet\mathbf{S}-\mathbf{C}_0\bullet\left(\mathbf{S}-\mathbf{I}\right)-\beta\cdot n\cdot\boldsymbol{\Gamma}\bullet\mathbf{C}_0\bullet\left(\mathbf{S}-\mathbf{I}\right)\right]^{-1}\bullet\left[\mathbf{C}_1-\left(\mathbf{I}+\beta\cdot n\cdot\boldsymbol{\Gamma}\right)\bullet\mathbf{C}_0\right] \quad \text{(A.7)}$$

Noted that $\mathbf{T}_r$ reduces to Eqn. (20) in Ju and Sun (2001) with no presence of fiber breaks as follows:

$$\begin{aligned}\mathbf{T}_r&=-\left[\mathbf{C}_1\bullet\mathbf{S}-\mathbf{C}_0\bullet\left(\mathbf{S}-\mathbf{I}\right)\right]^{-1}\bullet\left[\mathbf{C}_1-\mathbf{C}_0\right]\\&=-\left[\mathbf{S}+\left(\mathbf{C}_1-\mathbf{C}_0\right)\bullet\mathbf{C}_0\right]^{-1}\\&\triangleq-\left[\mathbf{S}+\mathbf{A}\right]^{-1}\end{aligned} \quad \text{(A.8)}$$

APPENDIX B COMPONENTS OF THE FOUR-RANK TENSORS (T_r) IN CHAPTER 5

The coefficient tensors $(T_r)_{IK}^{(1)}$ and $(T_r)_{IJ}^{(2)}$ of the generalized isotropic fourth-rank tensor $\mathbf{T}_r$ shown in Equation (5.21) are provided as follows:

$$(T_r)_{I1}^{(1)} = -[\delta_2(Y_1 + S_{I1}^{(1)} + G_{I1}^{(1)}) - 2\delta_4(Y_1 + S_{I2}^{(1)} + G_{I2}^{(1)})]/2\omega_{II}(\delta_1\delta_2 - \delta_3\delta_4) \tag{B.1}$$

$$(T_r)_{I2}^{(1)} = (T_r)_{I3}^{(1)} = [\delta_3(Y_1 + S_{I1}^{(1)} + G_{I1}^{(1)}) - \delta_1(Y_1 + S_{I2}^{(1)} + G_{I2}^{(1)})]/2\omega_{II}(\delta_1\delta_2 - 2\delta_3\delta_4) \tag{B.2}$$

$$(T_r)_{IJ}^{(2)} = 1/4(Y_2 + S_{IJ}^{(2)} + G_{IJ}^{(2)}) \triangleq 1/2\omega_{IJ} \tag{B.3}$$

where

$$\omega_{IJ} = 2\left(Y_2 + S_{IJ}^{(2)} + F_{IJ}^{(2)}\right) \tag{B.4}$$

$$\delta_1 = (Y_1 + S_{11}^{(1)} + G_{11}^{(1)}) + \omega_{11},\ \delta_2 = 2(Y_1 + S_{22}^{(1)} + G_{22}^{(1)}) + \omega_{22},\ \delta_3 = Y_1 + S_{12}^{(1)} + G_{12}^{(1)},\ \delta_4 = Y_1 + S_{21}^{(1)} + G_{21}^{(1)} \tag{B.5}$$

$$G_{IK}^{(1)} = \beta \cdot (n)_r\,(2\mu_1 H_{IK}^{(1)} + 2\lambda_1 H_{II}^{(2)} + \lambda_1 \sum_{R=1}^{3} H_{RK}^{(1)}),\quad G_{IJ}^{(2)} = 2\beta \cdot (n)_r\,\mu_1 H_{IJ}^{(2)} \tag{B.6}$$

$$H_{IK}^{(1)} = 2Y_1\Gamma_{KK}^{(2)} + 2Y_2\Gamma_{IK}^{(1)} + Y_1 \sum_{R=1}^{3} \Gamma_{RK}^{(1)},\quad H_{IJ}^{(2)} = 2Y_2\Gamma_{IJ}^{(2)} \tag{B.7}$$

$$Y_1 = (\lambda_0\mu_1 - \lambda_1\mu_0)/(\mu_1 - \mu_0)[2(\mu_1 - \mu_0) + 3(\lambda_1 - \lambda_0)],\ \ Y_2 = \mu_0/2(\mu_1 - \mu_0) \tag{B.8}$$

where λ_i and μ_i are the Lame constants of the ith phase ($i = 0$ for matrix and $i = 1$ for fiber), respectively.

APPENDIX C COMPONENTS OF THE FOUR-RANK TENSORS (B, P, C*) IN CHAPTER 7

With the aid of the inversion formula for the *generalized isotropic* fourth-rank tensor provided in Appendix B, the **B** tensor in Equation (7.8) can be expressed as

$$B_{ijkl} = B_{IK}^{(1)}\delta_{ij}\delta_{kl} + B_{IJ}^{(2)}\left(\delta_{ik}\delta_{jl} + \delta_{il}\delta_{jk}\right) \tag{C.1}$$

with

$$B_{IJ}^{(2)} = \frac{1}{4\left(Z_2 + S_{IJ}^{(2)} + F_{IJ}^{(2)}\right)} \triangleq \frac{1}{2\alpha_{IJ}} \tag{C.2}$$

$$B_{I1}^{(1)} = -\frac{1}{2\alpha_{II}}\left[\frac{\gamma_2\left(Z_1 + S_{I1}^{(1)} + F_{I1}^{(1)}\right) - 2\gamma_4\left(Z_1 + S_{I2}^{(1)} + F_{I2}^{(1)}\right)}{\gamma_1\gamma_2 - \gamma_3\gamma_4}\right] \tag{C.3}$$

$$B_{I2}^{(1)} = B_{I3}^{(1)} = -\frac{1}{2\alpha_{II}}\left[\frac{-\gamma_3\left(Z_1 + S_{I1}^{(1)} + F_{I1}^{(1)}\right) + \gamma_1\left(Z_1 + S_{I2}^{(1)} + F_{I2}^{(1)}\right)}{\gamma_1\gamma_2 - 2\gamma_3\gamma_4}\right] \tag{C.4}$$

and

$$\alpha_{IJ} = 2\left(Z_2 + S_{IJ}^{(2)} + F_{IJ}^{(2)}\right) \tag{C.5}$$

$$\gamma_1 = \left(Z_1 + S_{11}^{(1)} + F_{11}^{(1)}\right) + \alpha_{11} \tag{C.6}$$

$$\gamma_2 = 2(Z_1 + S_{22}^{(1)} + F_{22}^{(1)}) + \alpha_{22} \tag{C.7}$$

$$\gamma_3 = Z_1 + S_{12}^{(1)} + F_{12}^{(1)} \tag{C.8}$$

$$\gamma_4 = Z_1 + S_{21}^{(1)} + F_{21}^{(1)} \tag{C.9}$$

$$F_{IK}^{(1)} = \beta \cdot n \cdot \left(2\mu_1 E_{IK}^{(1)} + 2\lambda_1 E_{II}^{(2)} + \lambda_1 \sum_{R=1}^{3} E_{RK}^{(1)} \right) \tag{C.10}$$

$$F_{IJ}^{(2)} = 2\beta \cdot n \cdot \mu_1 E_{IJ}^{(2)} \tag{C.11}$$

$$E_{IK}^{(1)} = 2Z_1 \Gamma_{KK}^{(2)} + 2Z_2 \Gamma_{IK}^{(1)} + Z_1 \sum_{R=1}^{3} \Gamma_{RK}^{(1)} \tag{C.12}$$

$$E_{IJ}^{(2)} = 2Z_2 \Gamma_{IJ}^{(2)} \tag{C.13}$$

$$Z_1 = \frac{\lambda_0 \mu_1 - \lambda_1 \mu_0}{\left(\mu_1 - \mu_0\right)\left[2\left(\mu_1 - \mu_0\right) + 3\left(\lambda_1 - \lambda_0\right)\right]} \tag{C.14}$$

$$Z_2 = \frac{\mu_0}{2\left(\mu_1 - \mu_0\right)} \tag{C.15}$$

where λ_0 and μ_0 are the Lame constants of the matrix-phase material, and λ_1 and μ_1 are the Lame constants of the fiber-phase material. Therefore, we can derive the component form for the fourth-rank tensor **P** defined in Equation (7.17) as follows:

$$P_{ijkl} = P_{IK}^{(1)} \delta_{ij} \delta_{kl} + P_{IJ}^{(2)} (\delta_{ik} \delta_{jl} + \delta_{il} \delta_{jk}) \tag{C.16}$$

$$P_{IK}^{(1)} = -\frac{Y_{IK}}{2Q_{II}^{(2)}} \tag{C.17}$$

$$P_{IJ}^{(2)} = \frac{1}{4Q_{IJ}^{(2)}} \tag{C.18}$$

with

$$Q_{IK}^{(1)} = -2\phi S_{IK}^{(1)} B_{KK}^{(2)} + \phi\left(1-2S_{IJ}^{(2)}\right) B_{IK}^{(1)} + \sum_{R=1}^{3}\left(-\phi S_{IR}^{(1)} B_{RK}^{(1)}\right) \tag{C.19}$$

$$Q_{IJ}^{(2)} = \frac{1}{2} + \phi\left(1-2S_{IJ}^{(2)}\right) B_{IJ}^{(2)} \tag{C.20}$$

$$Y_{I1} = \frac{(Q_{22}^{(1)} + Q_{22}^{(2)})Q_{I1}^{(1)} - Q_{21}^{(1)}Q_{I2}^{(1)}}{\left[\left(Q_{22}^{(1)} + Q_{22}^{(2)}\right)\left(Q_{11}^{(1)} + 2Q_{11}^{(2)}\right) - Q_{12}^{(1)}Q_{21}^{(1)}\right]} \tag{C.21}$$

$$Y_{I2} = Y_{I3} = \frac{\left(Q_{11}^{(1)} + 2Q_{11}^{(2)}\right)Q_{I2}^{(1)} - Q_{12}^{(1)}Q_{I1}^{(1)}}{2\left[\left(Q_{22}^{(1)} + Q_{22}^{(2)}\right)\left(Q_{11}^{(1)} + 2Q_{11}^{(2)}\right) - Q_{12}^{(1)}Q_{21}^{(1)}\right]} \tag{C.22}$$

Similarly, the overall effective moduli tensor $\mathbf{C}^*$ in Equation (7.19) can be explicitly expressed by

$$C_{ijkl}^{*} = C_{IK}^{*(1)}\delta_{ij}\delta_{kl} + C_{IJ}^{*(2)}\left(\delta_{ik}\delta_{jl} + \delta_{il}\delta_{jk}\right) \tag{C.23}$$

and

$$C_{IJ}^{*(1)} = \lambda_0 + 2\phi\lambda_0 \mathrm{X}_{KK}^{(2)} + 2\phi\mu_0 \mathrm{X}_{IK}^{(1)} + \phi\lambda_0 \sum_{R=1}^{3} \mathrm{X}_{RK}^{(1)} \tag{C.24}$$

$$C_{IJ}^{*(2)} = \mu_0\left(1 + 2\phi \mathrm{X}_{IJ}^{(2)}\right) = \mu_0\left[1 + \frac{\phi}{2\left(W_{IJ}^{(2)} - \phi S_{IJ}^{(2)}\right)}\right] \tag{C.25}$$

$$\mathrm{X}_{IJ}^{(2)} = \frac{1}{4\left(W_{IJ}^{(2)} - \phi S_{IJ}^{(2)}\right)} \tag{C.26}$$

$$\mathrm{X}_{I1}^{(1)} = \frac{-\left[\left(W_{22}^{(1)} - \phi S_{22}^{(1)}\right) + \left(W_{22}^{(2)} - \phi S_{22}^{(2)}\right)\right]\left(W_{I1}^{(1)} - \phi S_{I1}^{(1)}\right) + \left(W_{21}^{(1)} - \phi S_{21}^{(1)}\right)\left(W_{I2}^{(1)} - \phi S_{I2}^{(1)}\right)}{2D} \tag{C.27}$$

$$\mathrm{X}_{I2}^{(1)} = \mathrm{X}_{I3}^{(1)} = \frac{\left(W_{12}^{(1)} - \phi S_{12}^{(1)}\right)\left(W_{I1}^{(1)} - \phi S_{I1}^{(1)}\right)\left[\left(W_{11}^{(1)} - \phi S_{11}^{(1)}\right) + 2\left(W_{11}^{(2)} - \phi S_{11}^{(2)}\right)\right]\left(W_{I2}^{(1)} - \phi S_{I2}^{(1)}\right)}{4D} \tag{C.28}$$

$$\begin{aligned} D = {} & (W_{II}^{(2)} - \phi S_{II}^{(2)}) \times \\ & \{[(W_{I1}^{(1)} - \phi S_{11}^{(1)}) + 2(W_{11}^{(2)} - \phi S_{11}^{(2)})][(W_{2I}^{(1)} - \phi S_{22}^{(1)}) + (W_{22}^{(2)} - \phi S_{22}^{(2)})] - (W_{12}^{(1)} - \phi S_{12}^{(1)})(W_{21}^{(1)} - \phi S_{21}^{(1)})\} \end{aligned} \tag{C.29}$$

where ϕ is the volume fraction of the reinforcements, and $S_{IK}^{(1)}$ and $S_{IJ}^{(2)}$ are the coefficient tensors of the Eshelby tensor **S** for a cylindrical inclusion. **S** is dependent on the geometry of the inclusion and the Poisson's ratio of the matrix with each component explicitly described as follows

$$S_{11}^{(1)} = 0 \tag{C.30}$$

$$S_{12}^{(1)} = S_{13}^{(1)} = 0 \tag{C.31}$$

$$S_{21}^{(1)} = S_{31}^{(1)} = \frac{\nu_0}{2\left(1-\nu_0\right)} \tag{C.32}$$

$$S_{22}^{(1)} = S_{33}^{(1)} = S_{32}^{(1)} = S_{23}^{(1)} = \frac{4\nu_0 - 1}{8\left(1-\nu_0\right)} \tag{C.33}$$

$$S_{11}^{(2)} = 0 \tag{C.34}$$

$$S_{12}^{(2)} = S_{13}^{(2)} = S_{21}^{(2)} = S_{31}^{(2)} = \frac{1}{4} \tag{C.35}$$

$$S_{22}^{(2)} = S_{33}^{(2)} = S_{23}^{(2)} = S_{32}^{(2)} = \frac{3-4\nu_0}{8\left(1-\nu_0\right)} \tag{C.36}$$

APPENDIX D MULTIPLICATION FORMULA FOR TWO GENERALIZED ISOTROPIC FOURTH-RANK TENSORS

Consider a generalized isotropic fourth-rank tensor **C** as the multiplication of another two generalized isotropic fourth-rank tensors **A** and **B**

$$C_{ijkl} = C_{IK}^{(1)}\delta_{ij}\delta_{kl} + C_{IJ}^{(2)}\left(\delta_{ik}\delta_{jl} + \delta_{il}\delta_{jk}\right) = A_{ijmn}B_{mnkl} \tag{D.1}$$

$$A_{ijkl} = A_{IK}^{(1)}\delta_{ij}\delta_{kl} + A_{IJ}^{(2)}\left(\delta_{ik}\delta_{jl} + \delta_{il}\delta_{jk}\right) \tag{D.2}$$

$$B_{ijkl} = B_{IK}^{(1)}\delta_{ij}\delta_{kl} + B_{IJ}^{(2)}\left(\delta_{ik}\delta_{jl} + \delta_{il}\delta_{jk}\right) \tag{D.3}$$

where $(\bullet)_{IK}^{(1)}$ and $(\bullet)_{IJ}^{(2)}$ are the second-rank tensors. By carrying out the multiplication on the R.H.S of Eq. (D.1) and using the fact that $(\bullet)_{IJ}^{(2)}$ is symmetric, it can be easily shown that the second-rank tenors $C_{IK}^{(1)}$ and $C_{IJ}^{(2)}$ have the form:

$$C_{IK}^{(1)} = 2A_{IK}^{(1)}B_{KK}^{(2)} + 2A_{II}^{(2)}B_{IK}^{(1)} + \sum_{R=1}^{3} A_{IR}^{(1)}B_{RK}^{(1)} \tag{D.4}$$

and

$$C_{IJ}^{(2)} = 2A_{IJ}^{(2)}B_{IJ}^{(2)} \tag{D.5}$$

where the repeated capital indices *II* and *KK* follow the notation in Mura (1987) that do not imply summation,.

APPENDIX E INVERSE FORMULA FOR A GENERALIZED ISOTROPIC FOURTH-RANK TENSOR

Consider a generalized isotropic fourth-rank tensor **Z** with the following component form:

$$Z_{ijkl} = Z_{IK}^{(1)}\delta_{ij}\delta_{kl} + Z_{IJ}^{(2)}\left(\delta_{ik}\delta_{jl} + \delta_{il}\delta_{jk}\right) \tag{E.1}$$

where $Z_{IK}^{(1)}$ and $Z_{IJ}^{(2)}$ are second-rank tensors and $Z_{IJ}^{(2)}$ is symmetric. After lengthy derivations, it can be shown that the inverse of the above fourth-rank tensor has the form:

$$Z_{ijkl}^{-1} = \hat{Z}_{IK}^{(1)}\delta_{ij}\delta_{kl} + \frac{1}{4Z_{IJ}^{(2)}}\left(\delta_{ik}\delta_{jl} + \delta_{il}\delta_{jk}\right) \tag{E.2}$$

where the second-rank tensor $\hat{Z}_{IK}^{(1)}$ can be calculated by the following expressions:

$$\hat{Z}_{I1}^{(1)} = -\frac{1}{2Z_{II}^{(2)}}\left[\frac{\left(Z_{22}^{(1)} + Z_{22}^{(2)}\right)Z_{I1}^{(1)} - Z_{21}^{(1)}Z_{I2}^{(1)}}{\left(Z_{22}^{(1)} + Z_{22}^{(2)}\right)\left(Z_{11}^{(1)} + 2Z_{11}^{(2)}\right) - Z_{12}^{(1)}Z_{21}^{(1)}}\right] \tag{E.3}$$

$$\hat{Z}_{I2}^{(1)} = \hat{Z}_{I3}^{(1)} = -\frac{1}{2Z_{II}^{(2)}}\left[\frac{\left(Z_{11}^{(1)} + Z_{11}^{(2)}\right)Z_{I2}^{(1)} - Z_{12}^{(1)}Z_{I1}^{(1)}}{2\left(Z_{22}^{(1)} + Z_{22}^{(2)}\right)\left(Z_{11}^{(1)} + 2Z_{11}^{(2)}\right) - 2\left(Z_{12}^{(1)}Z_{21}^{(1)}\right)}\right] \tag{E.4}$$

REFERENCES

Allen, D.H., Jones, R.H. and Boyd, J.G. (1994). Micromechanical analysis of a continuous fiber metal matrix composite including the effects of matrix viscoplasticity and evolving damage, *Journal of the Mechanics and Physics of Solids*, **42**(3): 505-529.

Arsenault, R.J. (1984). The strengthening of aluminum alloy 6061 by fiber and platelet silicon carbide, *Materials Science and Engineering*, **64**(2):171-181.

Brindley, P.K., Draper, S.L., Eldridge, J.I., Nathal, M.V. and Arnold, S.M. (1991). The effect of temperature on the deformation and fracture of SiC/Ti-24Al-11Nb, *Metallurgical and Materials Transactions A*, **23**: 2527-2540.

Brockenbrough, J.R. and Suresh, S. (1990). Plastic deformation of continuous fiber-reinforced metal matrix composites: effects of fiber shape and distribution, *Scripta Metallurgica et Materialia*, **24**: 325-330.

Budiansky, B. (1965). On the elastic moduli of some heterogeneous materials, *Journal of the Mechanics and Physics of Solids*, **13**(4): 223-227.

Budiansky, B. and O'Connell, R.J. (1976). Elastic moduli of a cracked solid, *International Journal of Solids and Structures*, **12**(2): 81-97.

Castaneda, P.P. (1991). The effective mechanical properties of nonlinear isotropic composites, *Journal of the Mechanics and Physics of Solids*, **39**(1): 45-71.

Castaneda, P.P. and Willis, J.R. (1988). On the overall properties of nonlinearly viscous composites, *Proceedings of the Royal Society of London, Series A: Mathematical and Physical Sciences*, **416**(1850): 217-244.

Chen, W.R. and Keer, L.M. (1993). Mixed-mode fatigue crack propagation of penny-shaped cracks, *Journal of Engineering Materials and Technology*, **115**(4): 365-372.

Christensen, R.M. and Lo, K.H. (1979). Solutions for effective shear properties in three phase sphere and cylinder models, *Journal of the Mechanics and Physics of Solids*, **27**(4): 315-330.

Christensen, R.M. (1990). A critical evaluation for a class of micro-mechanics models, *Journal of the Mechanics and Physics of Solids*, **38**(3): 379-404.

Christman, T., Needleman, A., Nutt, S. and Suresh, S. (1989). On microstructural evolution and micromechanical modeling of deformation of a whisker-reinforced metal-matrix composite, *Materials Science and Engineering: A*, **107**: 49-61.

Clyne, T.W. and Withers, P.J. (1993). *An Introduction to Metal Matrix Composites*, Cambridge, Cambridge University Press.

Curtin, W.A. (1998). Stochastic damage evolution and failure in fiber-reinforced composites, *Advances in Applied Mechanics*, **36**: 163-253.

Dednarcyk, B.A. and Arnold, S.M. (2001). Micromechanics-based deformation and failure prediction for longitudinally reinforced titanium composites, *Composites Science and Technology*, **61**: 705-729.

Divecha, A.P., Fishman, S.G. and Karmarkar, S.D. (1981). Silicon carbide reinforced aluminum - a formable composite, *Journal of Metals*, **33**:12-17.

Draper, S.L., Brindley, P.K. and Nathal, M.V. (1989). Factors which influence tensile strength of a SiC/Ti-24Al-11Nb, *Proceedings of 1989 TMS Fall Meeting*, Indianapolis, IN.

Durham, S.D., Lynch, J.D., Padgett, W.J., Horan, T.J. and Owen, W.J. (1997). Localized load-sharing rules and Markov-Weibull fibers: a comparison of microcomposite failure data with Monte Carlo simulations, *Journal of Composite Materials*, **31**:1856-1882.

Dvorak, G.J. and Bahei-El-Din, Y.A. (1987). A bimodal plasticity theory of fibrous composite materials, *Acta Mechanica*, **69**(1-4): 219-241.

Dvorak, G.J., Bahel-el-Din, Y.A., Macheret, Y. and Liu, C.H. (1988). An experimental study of elastic-plastic behavior of a fibrous boron-aluminum composite, *Journal of the Mechanics and Physics of Solids*, **36**(6): 655-687.

Eldridge, J.I. and Brindley, P.K. (1989). Investigation of interfacial shear strength in SiC fibre/Ti-24Al-11Nb composite by a fibre pus-out technique, *Journal of Materials Science Letters*, **8**: 1451-1454.

Eshelby, J.D. (1957). The determination of the elastic field of an ellipsoidal inclusion and related problems, *Proceedings of the Royal Society of London, Series A: Mathematical and Physical Sciences*, **241**: 376-396.

Eshelby, J.D. (1961). Elastic inclusions and inhomogeneities, in *Progress in Solid Mechanics* (Editor: Sneddon, L.N. and Hill, R.), North-Holland Publisher Company.

Garrett, K.W. and Bailey, J.E. (1977). Multiple transverse fracture in 90° cross-ply laminates of a glass fibre-reinforced polyester, *Journal of Materials Science*, **12**(1): 157-168.

Hansen, A.C., Blackketter, D.M. and Walrath, D.E. (1991). An invariant-based flow rule for anisotropic plasticity applied to composite materials, *Journal of Applied Mechanics*, **58**(4): 881-888.

Hashin, Z. (1965). On elastic behaviour of fibre reinforced materials of arbitrary transverse phase geometry, *Journal of the Mechanics and Physics of Solids*, **13**(3): 119-134.

Hashin, Z. and Shtrikman, S. (1962a). On some variational principles in anisotropic and nonhomogeneous elasticity, *Journal of the Mechanics and Physics of Solids*, **10**(4): 335-342.

Hashin, Z. and Shtrikman, S. (1962b). A variational approach to the theory of the elastic behaviour of polycrystals, *Journal of the Mechanics and Physics of Solids*, **10**(4): 343-352.

Hashin, Z. and Shtrikman, S. (1963). A variational approach to the theory of the elastic behaviour of multiphase materials, *Journal of the Mechanics and Physics of Solids*, **11**(2): 127-140.

Hashin, Z. (1980). *Fatigue Failure Criteria for Unidirectional Fiber Composites* (No. TR-5), Department of Materials Science and Engineering, University of Pennsylvania.

Hashin, Z. (1988). The differential scheme and its application to cracked materials, *Journal of the Mechanics and Physics of Solids*, **36**(6): 719-734.

Hatta, H., Takei, T. and Taya, M. (2000). Effects of dispersed microvoids on thermal expansion behavior of composite materials, *Materials Science and Engineering A*, **285**(1-2): 99-110.

He, M.Y., Evans, A.G. and Curtin, W.A. (1993). The ultimate tensile strength of metal and ceramic-matrix composites, *Acta Metallurgica et Materialia*, **41**: 871-878.

Hill, R. (1963). Elastic properties of reinforced solids: Some theoretical principles, *Journal of the Mechanics and Physics of Solids*, **11**(5): 357-372.

Hori, M. and Nemat-Nasser, S. (1987). Interacting micro-cracks near the tip in the process zone of a macro-crack, *Journal of the Mechanics and Physics of Solids*, **35**(5): 601-629.

Hori, M. and Nemat-Nasser, S. (1993). Double-inclusion model and overall moduli of multi-phase composites, *Mechanics of Materials*, **14**(3): 189-206.

Ibnabdeljalil, M. and Curtin, W.A. (1997). Strength and reliability of fiber-reinforced composites: localized load sharing and associated size effects, *International Journal of Solids and Structures*, **34**: 2649-2668.

Jeng, S.M., Yang, J.M. and Yang, C.J. (1991). Fracture mechanisms of fiber-reinforced titanium alloy matrix composites, part II: tensile behavior, *Material Science and Engineering A*, **138**: 169-180.

Ju, J.W. (1991a). On two-dimensional self-consistent micromechanical damage models for brittle solids, *International Journal of Solids and Structures*, **27**: 227-258.

Ju, J. and Lee, X. (1991b). On three-dimensional self-consistent micromechanical damage models for brittle solids. part I: tensile loadings, *Journal of Engineering Mechanics*, **117**(7): 1495-1515.

Ju, J. and Lee, X. (1991c). On Three-dimensional self-consistent micromechanical damage models for brittle solids. part II: compressive loadings, *Journal of Engineering Mechanics*, **117**: 1516-1537.

Ju, J. W. (1991d). A micromechanical damage model for uniaxially reinforced composites weakened by interfacial arc microcracks, *Journal of Applied Mechanics*, **58**(4): 923-930.

Ju, J.W. and Tseng, K.H. (1992). A three-dimensional statistical micromechanical theory for brittle solids with interacting microcracks, *International Journal of Damage Mechanics*, **1**(1): 102-131.

Ju, J.W. and Chen, T.M. (1994a). Micromechanics and effective moduli of elastic composites containing randomly dispersed ellipsoidal inhomogeneities, *Acta Mechanica*, **130**: 103-121.

Ju, J.W. and Chen, T.M. (1994b). Effective elastic moduli of two-phase composites containing randomly dispersed spherical inhomogeneities, *Acta Mechanica*, **103**: 123-144.

Ju, J.W. and Chen, T.M. (1994c). Effective elastic moduli of two-dimensional brittle solids with interacting microcracks, part 1: basic formulations, *Journal of Applied Mechanics*, **61**: 349-357.

Ju, J.W. and Chen, T.M. (1994d). Effective moduli of two-dimensional solids with interacting microcracks part II: evolutionary damage models, *Journal of Applied Mechanics*, **61**: 358-366.

Ju, J.W. and Tseng, K.H. (1997). Effective elastoplastic behavior algorithms for ductile matrix composites, *Journal of Engineering Mechanics*, **123**(3): 260-26.

Ju, J.W. and Zhang, X.D. (1998). Micromechanics and effective transverse elastic moduli of composites with randomly located aligned circular fibers, *International Journal of Solids and Structures*, **35**(9-10): 941-960.

Ju, J.W., Ko, Y.F. and Ruan, H.N. (2008). Effective elastoplastic damage mechanics for fiber reinforced composites with evolutionary partial fiber debonding, *International Journal of Damage Mechanics*, **17**(6): 493–537.

Ju, J.W. and Yanase, K. (2008). Elastoplastic damage micromechanics for elliptical fiber composites with progressive partial fiber debonding and thermal residual stresses, *Theoretical and Applied Mechanics*, **35**(1–3): 137–170.

Ju, J.W. and Wu, Y. (2013). Stochastic Micromechanical Damage Modeling of Progressive Fiber Breaking for Longitudinally Fiber-Reinforced Composites, *International Journal of Damage Mechanics*, in submission.

Kachanov, M. (1987). Elastic solids with many cracks: a simple method of analysis, *International Journal of Solids and Structures*, **23**(1): 23-43.

Keer, L.M. and Mura, T. (1965). Stationary crack and continuous distribution of dislocations, *Processing of The First International Conference on Fracture, The Japanese Society for Strength and Fracture of Materials 1*: 99-115, Sendai, Japan.

Kim, B.W. and Nairn, J.A. (2002). Observations of fiber fracture and interfacial debonding phenomena using the fragmentation test in single-fiber composites, *Journal of Composite Materials*, **36**(15): 1825-1858.

Ko, Y.F. and Ju, J.W. (2012). Effect of fiber cracking on elastoplastic-damage behavior of fiber-reinforced metal matrix composites, *International Journal of Damage Mechanics*, **22**(1): 48-67.

Krasnikovs, A. and Megnis, M. (2005). Fatigue damage accumulation in unidirectional composite under applied cycling tension load, *International Conference on Fracture* (ICF11), Italy.

Landis, C.M., Beyerlein, I.J. and McMeeking, R.M. (2000). Micromechanical simulation of the failure of fiber reinforced composites, *Journal of the Mechanics and Physics of Solids*, **48**: 621-648.

Lee, H.K. and Ju, J.W. (2008). 3D micromechanics and effective moduli for brittle composites with randomly located interacting microcracks and inclusions, *International Journal of Damage Mechanics*, **17**: 377-417.

Liao, K. and Kenneth, L.R. (2000). A tensile strength model for unidirectional fiber-reinforced brittle matrix composite, *International Journal of Fracture*, **106**(2): 95-115.

Lienkamp, M. and Schwartz, P. (1993). A Monte Carlo simulation of the failure of a seven fiber microcomposite, *Composites Science and Technology*, 4**6**: 139-146.

Liu, H.T. and Sun, L.Z. (2004). Effects of thermal residual stresses on effective elastoplastic behavior of metal matrix composites, *International Journal of Solids and Structures*, **41**(8): 2189-2203.

Liu, P.F. and Zheng, J.Y. (2006). A Monte Carlo finite element simulation of damage and failure in SiC/Ti-Al composites, *Material Science and Engineering: A*, **425**: 260-267.

Matthews, F.L. and Rawlings, R.D. (1993). *Composite Materials: Engineering and Science*, Woodhead Publishing Limited, Cambridge, England.

McLaughlin, R. (1977). A study of the differential scheme for composite materials, *International Journal of Engineering Science*, **15**(4): 237-244.

Moës, N., Dolbow, J. and Belytschko, T. (1999). A finite element method for crack growth without remeshing, *International Journal for Numerical Methods in Engineering*, **46**: 131-150.

Moes, N. and Belytschko, T. (2002). Extended finite element method for cohesive crack growth, *Engineering Fracture Mechanics*, **69**(7): 813-833.

Mori, T. and Tanaka, K. (1973). Average stress in matrix and average elastic energy of materials with misfitting inclusions, *Acta Metallurgica*, **21**(5): 571-574.

Meyer, S., Bruckner-Foit, A., and Moslang, A. (2003). A stochastic simulation model for microcrack initiation in a martensitic steel, *Computational Material Science*, **26**: 102-110.

Mishnaevsky, L. and Brondsted, P. (2008). Micromechanical modeling of damage and fracture of unidirectional fiber reinforced composites: a review, *Computational Materials Science*, **44**: 1351-1359.

Mulhern, J.F., Rogers, T.G. and Spencer, A.J.M. (1967). A continuum model for fibre-reinforced plastic materials, *Proceedings of the Royal Society of London. Series A. Mathematical and Physical Sciences*, **301**(1467): 473-492.

Mura, T. (1987). *Micro-mechanics of Defects in Solids*, Kluwar Academic Publisher, Netherlands.

Narin, J.A. and Hu, S. (1994). Micromechanics of damage: a case study of matrix microcracking, in *Damage Mechanics of Composite Materials*: 197-243.

Nazari, A., Milani, A.A., and Zakeri, M. (2011). Modeling ductile to brittle transition temperature of functionally graded steels by artificial neural networks, *Computational Material Science*, **50**: 2028-2037.

Netravali, A.N., Henstenburg, R.B., Phoenix, S.L., and Schwartz, P. (1989). Interfacial shear strength studies using the single-filament-composite test. I: experiments on graphite fibers in epoxy, *Polymer Composites*, **10**: 226-241.

Nicholas, T. and Ahmad, J. (1994). Modeling fiber breakage in a metal-matrix composite, *Composites Science and Technology*, **52:** 29-38.

Nishikawa, M., Okabe, T., Takeda, N. and Curtin, W.A. (2008). Micromechanics of the fragmentation process in single-fiber composites, *Modelling and Simulation in Materials Science and Engineering*, **16**(5): 055009.

Oguni, K. and Ravichandran, G. (2000). An energy-based model of longitudinal splitting in unidirectional fiber-reinforced composites, *Journal of Applied Mechanics*, **67**(3): 437-443.

Ohno, N., Okabe, S. and Okabe, T. (2004). Stress concentrations near a fiber break in unidirectional composites with interfacial slip and matrix yielding, *International Journal of Solids and Structures*, **41**: 4263-4277.

Okabe, T. and Takeda, N. (2002). Elastoplastic shear-lag analysis of single-fiber composites and strength prediction of unidirectional multi-fiber composites, *Composites Part A: Applied Science and Manufacturing*, **33**: 1327-1335.

Okabe, T., Ishii, K., Nishikawa, M. and Takeda, N. (2010). Prediction of tensile strength of unidirectional CFRP composites, *Advanced Composite Materials*, **19**: 229-241.

Okabe, T., Motani, T., Nishikawa, M. and Hashinoto, M. (2012). Numerical simulation of microscopic damage and strength of fiber-reinforced plastic composites, *Advanced Composite Materials*, **21**(2): 147-163.

Park, C. and Padgett, W.J. (2006) Analysis of strength distributions of multi-modal failures using the EM algorithm, *Journal of Statistical Computation and Simulation*, **76** (7): 619-636.

Povirk, G.L., Needleman, A. and Nutt, S.R. (1991). An analysis of the effect of residual stresses on deformation and damage mechanisms in Al---SiC composites, *Materials Science and Engineering: A*, **132**: 31-38.

Qiu, Y.P. and Weng, G.J. (1991). Elastic constants of a polycrystal with transversely isotropic grains, and the influence of precipitates, *Mechanics of materials*, **12**(1): 1-15.

Qiu, Y.P. and Weng, G.J. (1992). A theory of plasticity for porous materials and particle-reinforced composites, *Journal of Applied Mechanics*, **59**: 261.

Qiu, Y.P. and Weng, G.J. (1995). An energy approach to the plasticity of a two-phase composite containing aligned inclusions, *Journal of applied mechanics*, **62**(4): 1039-1046.

Schmidt, R.J., Wang, D.Q. and Hansen, A.C. (1993). Plasticity model for transversely isotropic materials, *Journal of engineering mechanics*, **119**(4): 748-766.

Shodja, H.M. and Sarvestni, A.S. (2001). Elastic fields in double inhomogeneity by the equivalent inclusion method, *Journal of Applied Mechanics*, **68**: 3-10.

Smith, R.L. (1980). A probability model for fibrous composites with local load sharing, *Proceedings of the Royal Society of London, Series A: Mathematical and Physical Sciences*, **372**: 530-553.

Steif, P.S. (1984). Stiffness reduction due to fiber breakage, *Journal of Composite Materials*, 18(2): 153-172.

Sun, L.Z. and Ju, J.W. (2001). Effective elastoplastic behavior of metal matrix composites containing randomly located aligned spheroidal inhomogeneities. part II: applications, *International Journal of Solids and Structures*, **38**: 203-225.

Sun, L.Z., Ju, J.W. and Liu, H.T. (2003a). Elatoplastic modeling of metal matrix composites with evolutionary particle debonding, *Mechanics of Materials*, **35**: 559-569.

Sun, L.Z., Liu, H.T. and Ju, J.W. (2003b). Effect of particle cracking on elastoplastic behavior of metal matrix composites, *International Journal for Numerical Method in Engineering*, **56**: 3183-2198.

Takao, Y. and Taya, M. (1985). Thermal expansion coefficients and thermal stresses in an aligned short fiber composite with application to a short carbon fiber/aluminum, *Journal of Applied Mechanics*, **52**(4): 806-810.

Takao, Y. and Taya, M. (1987). The effect of variable fiber aspect ratio on the stiffness and thermal expansion coefficients of a short fiber composite, *Journal of Composite Materials*, **21**(2): 140-156.

Talbot, D.R.S. and Willis, J.R. 1(985). Variational principles for inhomogeneous non-linear media, *IMA Journal of Applied Mathematics*, **35**(1): 39-54.

Tandon, G.P. and Weng, G.J. (1988). A theory of particle-reinforced plasticity, *Journal of Applied Mechanics*, **55**(1): 126-135.

Voyiadjis, G.Z. and Thiagarajan, G. (1997). Micro and macro anisotropic cyclic damage-plasticity models for MMCS, *International journal of engineering science*, **35**(5): 467-484.

Wang, B.L., Sun, Y.G. and Zhang, H.Y. (2008). Multiple cracking of fiber/matrix composites--Analysis of normal extension, *International Journal of Solids and Structures*, **45**(14-15): 4032-4048.

Wakashima, K., Otsuka, M. and Umekawa, S. (1974). Thermal expansions of heterogeneous solids containing aligned ellipsoidal inclusions, *Journal of Composite Materials*, **8**(4): 391-404.

Wang, G. and Li, S.F. (2004). A penny-shaped cohesive crack model for material damage, *Theoretical and Applied Fracture Mechanics*, **42**(3): 303-316.

Weng, G.J. (1990). The theoretical connection between Mori-Tanaka's theory and the Hashin-Shtrikman-Walpole bounds, *International Journal of Engineering Science*, **28**(11): 1111-1120.

Xia, Z., Okabe, T. and Curtin, W.A. (2002). Shear-lag versus finite element models for stress transfer in fiber-reinforced composites, *Composites Science and Technology*, **62**: 1141-1149.

Zhao, Y., Tandon, G. and Weng, G. (1989). Elastic moduli for a class of porous materials, *Acta Mechanica*, **76**(1): 105-131.

Zhao, F.M., Okabe, T., and Takeda, N. (2000). The estimation of statistical fiber strength by fragmentation tests of single-fiber composites, *Composites Science and Technology*, **60**: 1965-1974.

Zhang, B.M., Yang, Z., Wu, Y.F. and Sun, H.W. (2010). Hierarchical multiscale modeling of failure in unidirectional fiber-reinforced plastic matrix composite, *Material and Design*, **31**: 2312-2318.

Zhou, S.J. and Curtin, W.A. (1995). Failure of fiber composites: a lattice green function model, *Acta Metallurgica er Materialia*, **43**: 3093-3104.